

# Electrochemical Oxidation of H<sub>2</sub>,CO Gas Mixtures in Polymer-Electrolyte-Membrane Fuel Cells

## Dissertation

zur Erlangung des akademischen Grades

## Doktoringenieur (Dr.-Ing.)

von Dipl. Phys. Sebastian Kirsch

geb. am 23.09.1982 in Plauen

genehmigt durch die Fakultät für Verfahrens- und Systemtechnik  
der Otto-von-Guericke-Universität Magdeburg

Promotionskommission:	Prof. Dr. rer. nat.	Helmut Weiß	(Vorsitzender)
	Prof. Dr.-Ing.	Kai Sundmacher	(Gutachter)
	Prof. Dr. rer. nat.	Katharina Krischer	(Gutachter)
	Prof. Dr. rer. nat.	Andreas K. Friedrich	(Gutachter)

eingereicht am: 26.8.2013

Promotionskolloquium am: 3.4.2014



# Contents

<b>Kurzfassung</b>	<b>vi</b>
<b>Abstract</b>	<b>viii</b>
<b>Acknowledgments</b>	<b>x</b>
<b>List of Symbols</b>	<b>xii</b>
<b>1 Introduction</b>	<b>1</b>
1.1 PEMFC: Setup and Fundamentals . . . . .	2
1.1.1 Components . . . . .	2
1.1.2 Working Principle . . . . .	5
1.1.3 Loss Mechanisms and Efficiency . . . . .	6
1.2 State of the Art . . . . .	8
1.2.1 Applications . . . . .	9
1.2.2 Institutions and Targets . . . . .	10
1.2.3 The Obstacle: Degradation . . . . .	11
1.2.4 New Materials . . . . .	13
1.2.5 Heat and Water Management . . . . .	15
1.2.6 Present Challenges . . . . .	16
1.3 CO Contamination . . . . .	17
1.3.1 The Conventional Process Chain . . . . .	18
1.3.2 Potentiostatic PEMFC Operation with CO Containing Fuel . . . . .	19
1.3.3 Galvanostatic PEMFC Operation with CO Containing Fuel . . . . .	21
1.4 Aims of the Work and Proceeding . . . . .	24
<b>2 H<sub>2</sub>,CO Oxidation in a PEMFC: The Homogeneous System</b>	<b>27</b>
2.1 Nonlinear Dynamics in Electrochemical Systems: Fundamentals in a Nutshell . . . . .	28
2.1.1 The Homogeneous Electrochemical System . . . . .	28
2.1.2 The Stability of the Steady State . . . . .	31
2.1.3 Two Different Saddles . . . . .	33
2.1.4 Adjacent to the Saddle . . . . .	35
2.1.5 Bistability, Oscillations and Excitability . . . . .	36
2.1.6 Adaption to PEMFCs . . . . .	39
2.2 H <sub>2</sub> ,CO Oxidation in a Homogeneous PEMFC - Theory . . . . .	40
2.2.1 Modeling . . . . .	40
2.2.2 Model Predictions . . . . .	44
2.3 H <sub>2</sub> ,CO Oxidation in an Homogeneous PEMFC - Experiments . . . . .	51
2.3.1 Experimental . . . . .	51
2.3.2 Results and Discussion . . . . .	53
2.4 Summary . . . . .	58

<b>3</b>	<b>H<sub>2</sub>,CO Oxidation in a PEMFC: The Inhomogeneous System</b>	<b>61</b>
3.1	The Role of the Electric Field . . . . .	62
3.2	Nonlinear Dynamics in Inhomogeneous Electrochemical Systems . . . . .	66
3.2.1	Phenomena in Non-Oscillatory Media . . . . .	68
3.2.2	Phenomena in Oscillatory Media . . . . .	70
3.2.3	Preliminary Expectations . . . . .	74
3.3	H <sub>2</sub> ,CO Oxidation in an Inhomogeneous PEMFC - Theory . . . . .	74
3.3.1	Modeling . . . . .	75
3.3.2	Model Predictions . . . . .	78
3.4	H <sub>2</sub> ,CO Oxidation in an Inhomogeneous PEMFC - Experiments . . . . .	89
3.4.1	Experimental . . . . .	89
3.4.2	Results and Discussion: Galvanostatic Control . . . . .	92
3.4.3	Results and Discussion: Potentiostatic Control . . . . .	100
3.5	Summary . . . . .	107
<b>4</b>	<b>Conclusions and Outlook</b>	<b>109</b>
	<b>Appendix A: Model Reduction via Quasistationarity</b>	<b>111</b>
	<b>Appendix B: Derivation of Eq. (72)</b>	<b>114</b>
	<b>References</b>	<b>115</b>
	<b>Publications and Statements on Authorship</b>	<b>125</b>
	<b>Student Theses</b>	<b>126</b>
	<b>Curriculum Vitae</b>	<b>127</b>
	<b>Schriftliche Erklärung</b>	<b>128</b>



*“Technology also follows life in a cosmic scale migration towards greater complexity, diversity, and energy density. So we can think of the technium [technology as a whole, S.K.] as a 7th kingdom of life. As such the technium tends to be in alignment with the rest of the 6 kingdoms of life. Technology is inherently at home with other life, rather than contrary to it.”*

Kevin Kelly



## Kurzfassung

In der vorliegenden Arbeit werden Phänomene der Selbstorganisation untersucht, welche während der elektrochemischen Oxidation von  $H_2$ ,  $CO$ -Gemischen in Polymer-Elektrolyt-Membran Brennstoffzellen (im folgenden als Brennstoffzellen bezeichnet) auftreten. Dabei stehen zwei Ziele im Mittelpunkt. Zum einen soll das Verhalten einer sehr kleinen Brennstoffzelle verstanden werden. Hier treten Phänomene wie Bistabilität und autonome Oszillationen auf. Zum anderen soll aber auch das Verhalten von Brennstoffzellen mit erheblicher örtlicher Ausdehnung analysiert werden. In diesem System werden neben synchronisierten Oszillationen auch Raumzeitturbulenz und Pulse gefunden. Ein umfassendes Verständnis der beobachteten Phänomene könnte wesentlich sein, um bestehende technische Hürden bei der elektrochemischen Oxidation von  $H_2$ ,  $CO$ -Gemischen zu überwinden. Derzeit muss mit- $CO$ -verunreinigter Wasserstoff aufwendig gereinigt werden, bevor er in Brennstoffzellen zur Erzeugung elektrischer Energie umgesetzt werden kann.

Um das Verhalten einer sehr kleinen Brennstoffzelle während der elektrochemischen  $H_2$ ,  $CO$ -Oxidation zu verstehen, wird im ersten Teil der Arbeit zuerst ein örtlich homogenes mathematisches Modell entwickelt und analysiert. Anschließend werden auf die Ergebnisse abgestimmte Validierungsexperimente durchgeführt. Um der kleinen Zellfläche während der Modellierung Rechnung zu tragen, wird davon ausgegangen, dass Transportprozesse parallel zu den Elektroden vernachlässigt werden können. Das vorausgesagte Verhalten (Oszillationen und Bistabilität) ist daher geprägt vom lokalen Reaktionsnetzwerk und dem Gastransport rechtwinklig zur Zellfläche.

Die entscheidende Schlussfolgerung der Modellanalyse ist, dass das beobachtete Verhalten Ausdruck zweier Instabilitäten unterschiedlichen Ursprungs ist. Die Ursache einer der beiden Instabilitäten liegt in der Überspannungs-abhängigen Bildung einer passivierenden  $OH$ -Schicht, welche die elektrochemische  $H_2$ -Oxidation behindert. Die zweite Instabilität beruht auf der autokatalytischen Verarmung von  $CO$  in der Reaktionszone. Weil dieser Prozess ebenfalls  $OH$  benötigt, überlagern sich beide Instabilitäten in weiten Parameterbereichen. Wesentliche Vorhersagen der Modellanalyse werden von den (im Rahmen dieser Arbeit durchgeführten) Experimenten bestätigt. In bestimmten Widersprüchen zwischen Vorhersagen und experimentellen Ergebnissen zeigt sich aber auch die Notwendigkeit zur Modellierung des örtlich ausgedehnten Systems.

Im zweiten Teil der Arbeit wird die elektrochemische  $H_2$ ,  $CO$ -Oxidation in einer örtlich ausgedehnten Brennstoffzelle untersucht. Dazu wird zuerst ein weiteres mathematisches Modell entwickelt und analysiert. Dieses zweite Modell berücksichtigt, im Gegensatz zum ersten Modell, auch Transportprozesse parallel zur Zellfläche. Komplexeres Verhalten, verglichen zu den Vorhersagen des ersten Modells, wird vorausgesagt. Im Anschluss an die Modellierung werden abermals Validierungsexperimente durchgeführt. Dabei kommt eine eigens entwickelte Brennstoffzelle zum Einsatz, welche es erlaubt die Stromdichteverteilung entlang einzelner gerader Kanäle in Echtzeit zu messen.

Als wichtigstes Ergebnis der zweiten Modellanalyse wird geschlussfolgert, dass elektrische Migrationsströme in der Membran, Ströme aufgrund der globalen Kopplung (vermittelt durch die externe elektrische Beschaltung) und der  $CO$  Transport entlang des Kanals die wesentlichen Transportprozesse parallel zur Elektrode darstellen. In Abhängigkeit ihres relativen Einflusses werden im Modell verschiedene Verhalten gefunden, nämlich homogene Oszillationen, Wellen und Raumzeitturbulenz. In den folgenden Experimenten werden die vorhergesagten Muster mit Hilfe der

eigens entwickelten Brennstoffzelle gesucht: Neben den homogenen Oszillationen und der Raumzeitturbulenz werden zusätzlich auch Pulse gefunden. Das untersuchte System scheint erst das zweite bekannte elektrochemische System zu sein, welches raumzeitturbulentes Verhalten zeigt.

## Abstract

This work investigates self-organization phenomena which occur during the electrochemical oxidation of  $H_2$ ,  $CO$ -mixtures in Polymer-Electrolyte-Membrane Fuel Cells (PEMFCs). The work is focused on two aims. The first aim is to understand the behavior of a very small PEMFC. Here, phenomena like oscillations and bistability appear. The second aim is to analyze pattern formation in PEMFCs with considerable lateral extension. In these systems, apart from the mentioned phenomena, also spatio-temporal turbulence and pulses are found. A comprehensive understanding of these phenomena might be essential to overcome present hurdles in the electrochemical oxidation of  $H_2$ ,  $CO$  mixtures. Yet,  $CO$ -contaminated hydrogen can only be fed into a PEMFC for electric power generation if the  $CO$  is removed beforehand to a level of 10 ppm.

In order to understand the behavior of a very small PEMFC during the electrochemical  $H_2$ ,  $CO$  oxidation, in the first part of the work, initially, a spatially homogeneous mathematical model is developed and analyzed. Afterwards, experiments, dedicated to the verification of the model results, are carried out. To account for the small cell area during the modeling, it is assumed that transport processes parallel to the cell area can be neglected. Accordingly, the predicted behavior (oscillations and bistability) is dominated by the local reaction network and transport perpendicular to the cell area.

The main conclusion of the model analysis is that the complex behavior of the small PEMFC is caused by two instabilities of different origin. Thereby, the origin of one of the instabilities lies in the overvoltage-dependent formation of a passivating  $OH$  layer, leading to a blockage of the electrochemical  $H_2$  oxidation. The other instability originates from the autocatalytic depletion of  $CO$  in the reaction zone. As the autocatalytic  $CO$  depletion also depends on the  $OH$  species, both instabilities overlap in wide parameter ranges. The experiments, carried out subsequently, confirm crucial predictions of the model. However, deviations between predictions and experimental results point towards the necessity to model in addition the spatially extended system.

In the second part of the work the electrochemical  $H_2$ ,  $CO$  oxidation in a spatially extended PEMFC is investigated. Initially, another mathematical model is developed and analyzed. This second model takes into account, oppositely to the first model, also the transport processes parallel to the cell area. More complex behavior, compared to the predictions of the first model, is anticipated. Subsequent to the modeling part, again experiments, dedicated to the verification of the model results, are reported. Thereby, the experiments are accomplished with the help of a specific PEMFC design, which allows to measure the current distribution alongside individual straight gas channels with real-time resolution.

The main conclusion of the second model analysis is that the  $CO$  transport along the channel, the electric migration currents and currents due to a global coupling (mediated by the external circuit) are the most important transport processes parallel to the cell area. Depending on the relative impact of the processes, different behavior is found in the simulations, namely homogeneous oscillations, waves and spatio-temporal turbulence. In the subsequent experiments the predicted patterns were searched with the help of the specific PEMFC design: Apart from the homogeneous oscillations and spatio-temporal turbulence, also pulses are found. Thereby, the investigated system seems to be the second example for an electrochemical system that expresses spatio-temporal turbulence.



## Acknowledgments

The presented thesis was prepared during the time that I spent as a PhD student in the Process Systems Engineering group at the Max-Planck-Institute for the Dynamics of Complex Technical Systems Magdeburg. Here, I would like to thank everybody who contributed to this work.

Initially, I thank Professor Dr. Kai Sundmacher for his continuous interest and support. In his group, I found excellent scientific working conditions as well as enriching friends and colleagues. I also thank him for guidance in the field of Process Systems Engineering. Especially, the mathematical modeling means a lot to me.

I thank the International Max Planck Research School for the continuous financial support.

I thank my mentor Dr. Richard Hanke-Rauschenbach who had the idea for this work and who supported me in three different ways. Firstly, his scientific eagerness, his support and his interest in this specific topic motivated me continuously. Secondly, his sound advices were essential for me to take my first steps into the scientific world. And thirdly, I also acknowledge his truth-speaking and very humanely nature that guaranteed a great atmosphere since the beginning.

I thank Professor Dr. Katharina Krischer for her guidance in the wide field of nonlinear dynamics. Apart from her continuous interest and support she also induced the detailed investigation of the homogeneous system and she served as the second reviewer for this manuscript.

I thank Professor Dr. Andreas Friedrich for resuming the responsibility of the third review.

I thank Ralf Kraume for the development and preparation of a new measurement device. Without this tool, a large part of the experimental investigations would not have been possible. I also acknowledge his immediate support with multiple problems that appeared during operation.

Furthermore, I would like to thank my colleagues Boris Bensmann, Astrid Bornhöft, Ivonne Peña Arias and Richard Hanke-Rauschenbach for careful proof-reading of this manuscript. I thank Ali el-Sibai for his enthusiasm and his will to progress during the time when he was a master student. I thank other people for enlightening scientific debates, these are Thomas Kadyk, Dietrich Flockerzi and Philipp Bauer.

I greatly thank Bianka Stein for her incredible precision while working in the lab. She prepared the investigated membrane-electrode-assemblies and she helped me in all lab-aspects. Her reliability is surely one of the pillars of this thesis. I thank Thorsten Schröder not only for his continuous technical support, but also for his help during the acquisition of the FuelCon test-stand. I thank other people from the technical staff that supported me in various aspects. These are Markus Ikert, Rainer Könning and Klaus-Dieter Stoll, Detlef Franz and his team, as well as the library-team and the IT-team.

I found many friends in Magdeburg. These friends made me feel home. I therefore express special thanks to Boris Bensmann, Astrid Bornhöft, Mike Darlong, Ivonne Darlong, Melanie Fachel, Thomas Kadyk, Maik Kraus, Richard Hanke-Rauschenbach and André Sommer. I also enjoyed the time with the other members of the Process Systems Engineering group as well as the time with the International Max Planck Research School.

Finally, I would like to thank Conny Möller and my family. Conny continuously supported me with patience, friendship and love and ensured that I also enjoy the non-scientific aspects of life. I thank my parents Thomas and Sylvia Kirsch and my brother Alexander for supporting me at any opportunity.





# List of Symbols

greek symbols		unit
$\alpha_{\text{H}_2\text{O,dis}}$	transfer coefficient for water dissociation	1
$\alpha_{\text{H,ox}}$	transfer coefficient for hydrogen oxidation	1
$\alpha_{\text{CO,ox}}$	transfer coefficient for carbon monoxide oxidation	1
$\alpha_c$	transfer coefficient for oxygen reduction	1
$\gamma$	catalyst surface per geometric area	$\text{m}_{\text{PtRu}}^2 \text{m}^{-2}$
$\Delta\varphi$	double layer voltage of working electrode	V
$\Delta\varphi_{a,c}$	anodic, cathodic double layer voltage	V
$\Delta\varphi_{a,c}^0$	anodic, cathodic equilibrium double layer voltage	V
$\Delta_R G^\theta$	Gibbs free reaction enthalpy at standard pressure	$\text{J mol}^{-1}$
$\epsilon$	fuel cell efficiency	1
$\epsilon_{\text{td}}$	thermodynamic efficiency	1
$\epsilon_{\text{ec}}$	electrochemical efficiency	1
$\epsilon_{\text{fu}}$	fuel utilization efficiency	1
$\epsilon_C$	Carnot efficiency	1
$\zeta$	spatial non-dimensional coordinate: $\zeta = z/L$	1
$\eta_{a,c}$	anodic, cathodic overpotential	V
$\theta_0$	fraction of free surface sites	1
$\theta_{\text{H,CO,OH}}$	surface coverage of $\text{H}, \text{CO}, \text{OH}$	1
$\kappa$	membrane conductivity	$\text{S m}^{-1}$
$\kappa_{y,z}$	control parameter for mean-field, migration coupling	$\text{S m}^{-1}$
$\varphi$	absolute potential in the electrolyte	V
$\varphi_{a,c}$	absolute potential of the anode, cathode	V
$\phi, \psi$	potential of the outer anodic, cathodic Helmholtz plane	V
$\phi_n, \psi_n$	Fourier transform of n'th order of $\phi, \psi$	V

latin symbols		unit
$A$	PEMFC area (in Sec. 2.1: the Jacobian)	$\text{m}^2 \text{(V)}$
$A_n, B_n$	hyperbolic decay functions	1
$b$	width of the PEMFC	m
$c_{\text{dl,(a,c)}}$	specific electric capacity of the anode, cathode	$\text{F m}^{-2}$
$C_{\text{dl,(a,c)}}$	electric capacity of the anode, cathode	F
$c_t^*$	specific molar capacity of the anode	$\text{mol m}_{\text{PtRu}}^{-2}$
$C$	molar capacity of the anodic double layer	$\text{mol m}^{-2}$
$d_m$	thickness of the PEMFC membrane	m
$f, g$	arbitrary functions	different
$F$	Faraday constant	$\text{As mol}^{-1}$
$F_{\text{in,out}}$	volumetric flow rate at the inlet, outlet	sccm
$h_{\text{ga}}$	height of the anode gas chamber	m

latin symbols		unit
$i$	current density defined by the load	$\text{A m}^{-2}$
$I$	total current	A
$i_{F,(a,c)}$	Faradaic anodic, cathodic current density	$\text{A m}^{-2}$
$J_F$	Faradaic current of working electrode	A
$J_{F,(a,c)}$	Faradaic current of the anode, cathode	A
$k_{\text{H}_2,\text{ad}}$	reaction constant for $\text{H}_2$ adsorption	$\text{mol m}^{-2} \text{Pa}^{-1} \text{s}^{-1}$
$K_{\text{H}_2,\text{ad}}$	equilibrium constant for $\text{H}_2$ adsorption-desorption	Pa
$k_V$	reaction constant for $\text{H}_2$ oxidation	$\text{mol m}^{-2} \text{s}^{-1}$
$k_{\text{CO},\text{ad}}$	reaction constant for $\text{CO}$ adsorption	$\text{mol m}^{-2} \text{Pa}^{-1} \text{s}^{-1}$
$K_{\text{CO},\text{ad}}$	equilibrium constant for $\text{CO}$ adsorption-desorption	Pa
$k_{\text{CO},\text{ox}}$	reaction constant for $\text{CO}$ oxidation	$\text{mol m}^{-2} \text{s}^{-1}$
$k_{\text{H}_2\text{O},\text{dis}}$	reaction constant for $\text{H}_2\text{O}$ dissociation	$\text{mol m}^{-2} \text{s}^{-1}$
$K_{\text{OH}}$	equilibrium constant for $\text{H}_2\text{O}$ dissociation	$\text{mol m}^{-2} \text{s}^{-1}$
$L$	length of the PEMFC	m
$N_{\text{H}_2,\text{consumed}}$	volumetric rate of $\text{H}_2$ consumption	$\text{mol s}^{-1}$
$N_{\text{H}_2,\text{supplied}}$	volumetric feed flow rate of $\text{H}_2$	$\text{mol s}^{-1}$
$p$	total system pressure	Pa
$p_{\text{H}_2}$	$\text{H}_2$ partial pressure at the anode catalyst	$\text{N m}^{-2}$
$p_{\text{H}_2\text{O}}$	$\text{H}_2\text{O}$ partial pressure at the anode catalyst	$\text{N m}^{-2}$
$p_{\text{O}_2}$	$\text{O}_2$ partial pressure at the cathode catalyst	$\text{N m}^{-2}$
$p^\theta$	standard pressure	$\text{N m}^{-2}$
$Q_{1,2,3,4}$	help variables	1
$r_V$	rate of hydrogen oxidation	$\text{mol m}^{-2} \text{s}^{-1}$
$r_T$	rate of hydrogen adsorption	$\text{mol m}^{-2} \text{s}^{-1}$
$r_{\text{H}_2\text{O},\text{dis}}$	rate of water dissociation	$\text{mol m}^{-2} \text{s}^{-1}$
$r_{\text{CO},\text{ad}}$	rate of carbon monoxide adsorption	$\text{mol m}^{-2} \text{s}^{-1}$
$r_{\text{CO},\text{ox}}$	rate of carbon monoxide oxidation	$\text{mol m}^{-2} \text{s}^{-1}$
$R$	Ohmic system resistance (or ideal gas constant)	$\Omega \text{ (J mol}^{-1} \text{K}^{-1}\text{)}$
$R^*$	uncompensated electrolyte resistance	$\Omega$
$R_\Omega$	membrane resistance in PEMFC	$\Omega$
$R_{\text{ext}}$	external resistance in PEMFC control circuit	$\Omega$
$t$	time	s
$T$	total system temperature	K
$U$	voltage used by load for control of the circuit	V
$U_{\text{cell}}$	PEMFC voltage	V
$U_{\text{ocv}}$	open circuit voltage of the PEMFC	V
$v$	gas velocity	$\frac{\text{m}}{\text{s}}$
$x_{\text{H}_2,\text{CO}}$	$\text{H}_2, \text{CO}$ mole fraction at the anodic double layer	1
$x_{\text{CO},\text{in}}$	$\text{CO}$ mole fraction at the inlet	1
$x_{\text{O}_2}$	$\text{O}_2$ mole fraction at the cathodic double layer	1
$y, z$	spatial coordinate perpendicular to, along the channel	m

# 1 Introduction

Always when a new technology enters successfully its commercialization the producers as well as the consumers benefit in a win-win situation. But once the technique is widely accepted and when through extensive spread and application a dependence on it has emerged the drawbacks appear. This is the story of many inventions of humankind, especially since the time when the industrialization started. Now, living 250 years later, the global climate change is in full progress and the majority of people do not wonder anymore if humankind has an influence on the climate (what was the status when the author of this thesis was young) but whether humankind can stop the change.

In the past a lot of drawbacks of industrialization (e.g. water pollution and the emission of cancerous species from industrial plants) were alleviated by new inventions. But the challenge that we face at present is of different quality. The objective is not to change a side product of some technology but the feedstock of our welfare. It includes the change of the feed of a lot of technological processes from fossil to regenerative resources. Thereby, the big problem is that due to the tremendous economic importance of fossil resources it cannot be expected that the climate change can be altered considerably by global political action. It appears that the only way that can be gone is through more inventions, such that sustainable ecologic technology becomes economic, too.

In a solo attempt, the present German's and Switzerland's government decided to reduce the portion of conventional energy supply in Germany from today 80 % to less than 20 % in 2050 [1] (including the phasing out of nuclear power until 2022). It can therefore be expected that in 2050 the energy infrastructure of Germany will be totally different from today: Likely, the energy will be generated from wind turbines, solar panels, geothermal power plants, etc. at the positions with the highest emergence of the respective energy form, while the consumers live in urban areas. Apart from a totally different electric grid, also new storage and energy conversion techniques will be needed by then.

For mobility applications theoretically also synthetic fuel could be produced from the electric energy delivered by the new plants. But a lot of energy would be lost during the generation of these rather complex molecules. Accordingly, the importance of less complex fuel-molecules, like  $H_2$ , will likely increase. This anticipated fuel change offers a unique chance for the implementation of polymer electrolyte membrane fuel cells (PEMFCs) in transportation. PEMFCs base on a direct electrochemical conversion of  $H_2$  with the  $O_2$  contained in the ambient air under the production of pure water. Thereby, the emission of all harmful gases is avoided. Compared with other energy conversion systems that are (or might become) important for automobile applications (combustion engines, batteries and other fuel cell types) PEMFCs show a rather high energy density, a large power density as well as quick start up and load change behavior. However, a couple of material issues hinder the breakthrough of PEMFCs, such that their implementation is not economically, yet. All of them are related to cost and lifetime.

One of these hurdles appears if the  $H_2$ -rich fuel is generated from carbon-containing molecules. In the reformation process certain amounts of  $CO$  can not be avoided. If these traces enter the PEMFC they accumulate at the catalyst and passivate it. The beforehand almost loss free electrochemical  $H_2$  oxidation becomes tremendously lossy and renders the whole fuel cell operation inefficient. Therefore, in the past, two different routes were followed to tackle this issue. The one path heads for the deep removal of  $CO$  from the reformat and the subsequent feed of the "clean" gas into a  $CO$  sensitive PEMFC. The other path leads toward the development of  $CO$  tolerant catalysts, the PEMFC

could then be fed with  $CO$ -containing gas. Nevertheless, both techniques have their drawbacks: While during deep  $CO$  removal, some  $H_2$  - the fuel - is lost, the best  $CO$ -tolerant catalysts today (alloys of platinum and ruthenium/molybdenum:  $PtRu$  and  $PtMo$ ) are not good enough to consider the  $CO$  challenge solved. In the present work an alternative approach is investigated.

In 2002 two researchers from the Polytechnical Institute of Worcester/Massachusetts investigated the electrochemical oxidation of  $H_2, CO$  mixtures in a PEMFC under galvanostatic control [2]. They found that the cell voltage started to oscillate once a certain critical current was exceeded and noticed that due to the non-sinusoidal shape of the oscillations the cell voltage loss in the temporal mean was far lower compared to potentiostatic control, where no oscillations were seen [3]. This observation directly translates into an enhanced  $CO$  tolerance of a PEMFC if the  $H_2, CO$  mixture is oxidized in the formerly unused galvanostatic operation mode. Later the researchers proposed to consider this specifically operated PEMFC as a new device that should be optimized for deep  $CO$  removal and called it electrochemical preferential oxidation of  $CO$  (ECP<sub>ro</sub>Ox-reactor) [4]. Therefore, the exploitation of the oscillation-phenomenon might finally contribute either to an enhanced  $CO$  tolerance of PEMFC or to an improved deep  $CO$  removal. However, before a specific technical implementation can be discussed, first the fundamentals of the oscillatory phenomenon and other related phenomena need to be elucidated, which is the objective of this thesis.

This first chapter is organized as follows: Initially, the principal PEMFC setup is introduced and the essential processes are depicted. Afterwards, the state of the art in PEMFC technology is presented in order to arrange the thesis in this wider context. Subsequently, the problem of  $CO$  contamination is explained and the benefit of the oscillations, occurring under galvanostatic control, is sketched. Finally, the aims of the work are explained and the approach followed in this manuscript is outlined.

## 1.1 PEMFC: Setup and Fundamentals

The design of the PEMFC, as it is today, was established in the course of the last 150 years through stepwise improvement (see [5] for an overview). As the setup and the working principle of PEMFCs is well presented in a couple of standard textbooks, here only a short outline is given which comprises an introduction of the components, the illustration of the working principle and the evaluation of the efficiency. For a more detailed introduction the reader is referred to [6–8].

### 1.1.1 Components

The PEMFC setup and its components are depicted in Fig. 1. The “heart” of the PEMFC is formed by the electrolyte membrane and the attached electrodes, the so-called membrane-electrode-assembly (MEA). The MEA is assembled between gas diffusion layers and flow fields. Together with the electric circuit they provide an electron conducting path between the electrodes. In industrial applications several cells are stacked, meaning that the  $O_2$ -containing side of the one cell is electrically contacted to the  $H_2$ -containing side of another cell. The power output of the stack is then simply the sum of the power outputs of the individual cells.

The membrane has to fulfill two different tasks: Firstly, it should prevent the mixing of the anodic and cathodic gases. Secondly, it needs to act as a proton conductor and inhibit electron conduction. The most established membrane material is Nafion, a perfluorated ionomer out of the group of polyperfluorosulfonic acids (PFSAs). The chemical structure is depicted in Fig. 2.

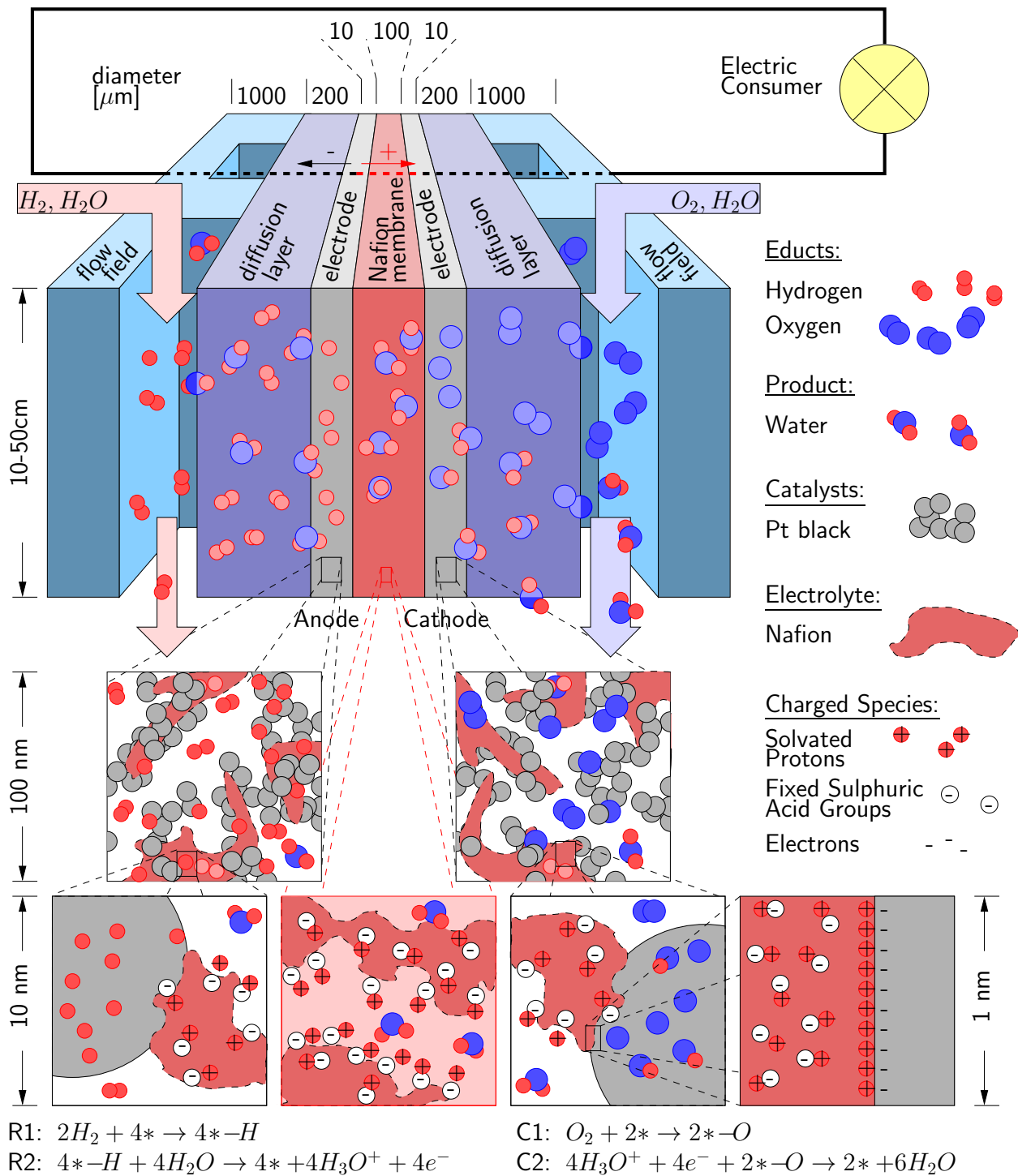


Figure 1: A PEMFC consists of a proton conducting membrane that is covered with porous electrodes and embraced between electron conducting gas diffusion layers and flow fields. Protons and electrons that form through the splitting of hydrogen at the anodic catalyst take individual routes (through the electrolyte and the electronic circuit, respectively) to approach the cathode side where they combine with oxygen to form water. The energy of the overall reaction (R1 + R2 + C1 + C2:  $2\text{H}_2 + \text{O}_2 \rightarrow 2\text{H}_2\text{O}$ ) is released in the electric consumer. "\*" represents a catalyst site of the Pt surface.

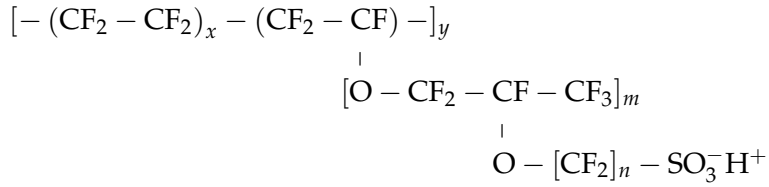


Figure 2: Chemical structure of Nafion - the most common material for PEMFC membranes.  $x = 5 - 13.5$ ,  $y \approx 10^3$ ,  $m = 1$  and  $n = 1$  [9,10].

The long backbone of the polymer and the fluorination lead to a large mechanical as well as chemical stability which is essential to hinder the mixing of the gases. The ability to conduct protons is established by the sulfonated acid groups at the end of the side chains. At sufficient humidification of the electrolyte, the attached protons dissociate (and solvate), while the negative charges remain fixed in the polymer. The resulting much higher mobility of the solvated protons compared to the acid groups makes Nafion a proton conductor<sup>1</sup>. However, depending on the humidification of the Nafion, the Nafion structure (and accordingly also the details of the proton conduction mechanism) change. At high humidification levels essentially a segregation of polymeric and water clusters leads to the development of liquid paths through which protons can easily travel (as indicated in the excerpt of Fig. 1 showing the membrane). Thereby, each proton drags its solvent shell with it, leading to an effective water drag in case of macroscopic proton motion, also referred to as “vehicular mechanism”. The behavior especially at low humidification levels is addressed in the review of Paddison [12], while an overview about the present overall understanding is given in the latest review article of Hickner [13].

The task of the electrodes is four-fold. Firstly, they need to support a good gas transport from the gas diffusion layers to the reaction regions (catalyst particles). Secondly, the electrodes should support the charge-supplying reactions (need good catalysts). Thirdly, they need to provide a proton conducting path from the reaction zone to the electrolyte membrane. And fourthly, they also need to provide an electron conducting path from the reaction zone to the gas diffusion layer. As a result the electrodes are highly porous structures (for gas transport), in which the solid phase consists of 10 – 30 % Nafion (for proton conduction) and the catalyst (for electron conduction and catalysis). In the easiest case the catalyst is a fine *Pt* powder. In acidic environments (like here) *Pt* has outstanding catalytic properties for the Hydrogen Oxidation Reaction (HOR: reactions R1-R2 in Fig. 1) and serves at least as a benchmark for the Oxygen Reduction Reaction (ORR: reactions C1-C2 in Fig. 1), even if *Pt* shows about six orders worse ORR activity compared to HOR activity. Often also electron conducting carrier particles (e.g.: graphitized carbon, nanotubes, titaniumoxide, etc.) are used to increase the *Pt* utilization. A good picture of how the electrodes can be imagined is to look at them as field of rocks soaked with air and honey [14].

The other components are the gas diffusion layers, the flow fields and the electric circuit. The gas diffusion layers and the flow fields serve for the transport of educt gases to the electrodes as well as the transport of product water from the electrodes. They are also part of the electron pathway and therefore need to be highly conductive. Due to cost optimization and corrosion problems carbon is

<sup>1</sup>Oppositely, metals show a large electron conductivity due to the fixed positively charged metal ions and free moving electrons (see the “free electron model” of Drude and Sommerfeld, e.g. in [11]).

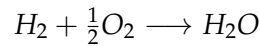
the most established material for both. In addition, the gas diffusion layers have a large porosity in order to homogenize the current distribution. The electric circuit consists of metal wires (of a specific ohmic resistance) and an electric consumer (e.g. Ohmic resistor, bulb, etc.).

### 1.1.2 Working Principle

During supply of the educt gases the following happens: At the anodic three phase boundary, at which the catalyst particles intersect with the  $H_2$  gas and the electrolyte network, a certain number of the adsorbed atoms (reaction R1, see bottom of Fig. 1 - also referred to as "Tafel reaction") undergo a dissociation (reaction R2 at the bottom of Fig. 1 - also referred to as "Volmer reaction") until an equilibrium is established. The resulting structure of protons (solvated by water) in the electrolyte and electrons at the interface of the metal catalyst is called "double layer" (see excerpt in Fig. 1 with highest resolution). The electric field across the double layer is linked to a electric potential difference, named "equilibrium double layer voltage"  $\Delta\varphi_a^0$ . At the catalyst-electrolyte interface that is in contact with  $O_2$  a similar structure is formed. The same charge carriers (protons and electrons) but different adsorbates are involved (reactions C1-C2 at the bottom of Fig. 1). The related equilibrium double layer voltage is referred to as  $\Delta\varphi_c^0$ . If the circuit is open, such that no electric current can pass, the difference in the potential of the two electric terminals yields the so-called "open circuit voltage"  $U_{ocv}$ . It specifies the difference in the equilibrium double layer voltages of the two electrodes

$$U_{ocv} = \Delta\varphi_c^0 - \Delta\varphi_a^0 \quad (1)$$

and is directly related to the oxidation potential of the reaction educts  $H_2$  and  $O_2$ . As the  $O_2$  has a higher oxidation potential it acts as the electron acceptor. The related side of the PEMFC is named "cathode", while the side with the  $H_2$  is referred to as "anode". At the cathode, the  $O_2$  reacts with arriving electrons and protons to form water. The overall reaction (that follows from summing up the reactions R1-C2) reads



and therefore the only chemical product of a PEMFC is pure water. The value of the open circuit voltage can be derived from fundamental thermodynamics (e.g. [6]): The Nernst equation for the given reaction reads<sup>2</sup>

$$U_{ocv} = -\frac{\Delta_R G(T, p_{H_2O}, p_{H_2}, p_{O_2})}{2F} = -\frac{\Delta_R G^\theta(T)}{2F} - \frac{RT}{2F} \cdot \ln \frac{p_{H_2O} \sqrt{p^\theta}}{p_{H_2} \sqrt{p_{O_2}}}. \quad (2)$$

The symbol  $\Delta_R G^\theta(T)$  stands for the Gibbs free enthalpy of the reaction at standard pressure, while  $F$ ,  $R$ ,  $T$  and  $p^\theta$  represent the Faradaic constant, the gas constant, the temperature in the cell and the standard pressure. The variables  $p_{H_2}$ ,  $p_{O_2}$  and  $p_{H_2O}$  represent the partial pressures of  $H_2$ ,  $O_2$  and  $H_2O$  in the respective electrodes. Assuming that water is formed in liquid state, Eq. (2) yields about  $\approx 1.23V^3$  at standard conditions, pure  $H_2$  and fully humidified  $O_2$ .

However, the above derived cell voltage value is only valid as long as the cell is in equilibrium - as long as the current is zero. Once the circuit is closed and a current is passing through the components of the cell the individual steps that are involved in the PEMFC's charge transfer undergo losses that

<sup>2</sup>It is assumed that the fugacity coefficient is one, an assumption that is well fulfilled close to standard conditions.

<sup>3</sup>If water is formed in vapor state (higher heating value) the condensation energy would decrease the Gibbs free enthalpy and lead to a value of about 1.19 V.



reduce the cell voltage. A typical polarization curve and the individual component losses are shown in Fig. 3.

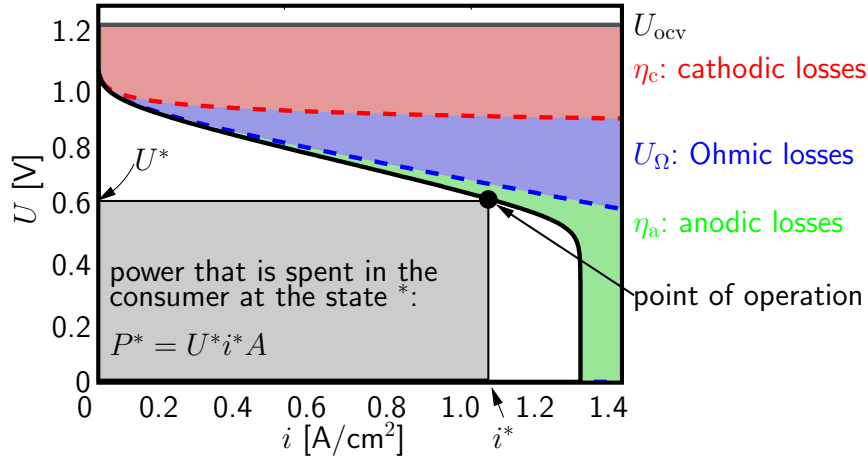


Figure 3: The polarization curve is used to characterize the technical performance of the PEMFC. It yields the cell voltage  $U$  as a function of the applied current density  $i$ . The curve monotonically decreases due to increasing losses in the electrode reactions and the charge transfer in the rest of the electric circuit.

### 1.1.3 Loss Mechanisms and Efficiency

As can be seen in Fig. 3, the cell voltage decreases with increasing current density due to losses caused by the electrode reactions and the charge transfer (ionic charge transfer in the electrolyte and electronic charge transfer in the circuitry). Thereby, the cathodic loss is usually dominant, especially at low current densities. The charge transfer loss can only at highest currents get into in the range of the cathodic loss. It is usually of Ohmic nature<sup>4</sup> and therefore constantly decreases with decreasing current. The anodic loss is usually very small, indicating the quality of the  $Pt$  catalyst to support the  $H_2$  oxidation. However, in Fig. 3 at highest current densities a quick onset in the anodic loss is indicated which limits the current to a maximal value. Such a scenario might for example arise in the case of  $H_2$  starvation, once the Faradaic limit is reached (full conversion of all fuel gas). Of course, also the cathode could starve  $O_2$  (maybe due to flooding or due to insufficient supply).

The voltage loss across the electrode double layer is referred to as “overvoltage”  $\eta_{a,c}$ , the index indicates anode and cathode, respectively. The overvoltage is given as the difference in the double layer voltage at a state far from equilibrium and the open circuit (equilibrium) value

$$\eta_{a,c} = \Delta\varphi_{a,c} - \Delta\varphi_{a,c}^0. \quad (3)$$

It acts as a driving force for the electrochemical reactions as can be seen, for example, in the Volmer reaction (R2 in Fig. 1)

$$r_V = k_V \theta_H \exp\left(\frac{F}{2RT} \eta_a\right), \quad (4)$$

<sup>4</sup>At low humidity the membrane can not be described as Ohmic resistor. However, this case is not important in the framework of the thesis.



in which  $k_V$  is a reaction constant,  $\theta_H$  is the portion of the surface covered with the hydrogen adsorbate and the exponential term represents the influence of the electric field across the double layer. Basically, each mole of positive and negative charge-pairs get the energy  $\frac{F}{2RT}\eta_a$  from the field, therefore minimizing the activation energy and supporting the creation of charges with increasing overvoltage. For a more detailed discussion the reader is referred to the theory of transition states [15].

At a large reaction rate (high current density), when it eventually comes to  $H_2$  starvation,  $\theta_H$  tends to zero. The steep increase in  $\eta_a$  is a direct consequence, indicating that not enough fuel arrives at the anode.

The Ohmic losses, to the largest part, are caused by the resistance of the electrolyte against proton transport. As the conductivity of the metal components is about seven orders larger ( $10^6 \text{ S m}^{-1}$ ), the electronic losses in the metal (and graphite) parts are almost negligible. However, contact resistances between different components of the electronic circuit (catalyst  $\rightarrow$  gas diffusion layer  $\rightarrow$  flow field  $\rightarrow$  cable) also might have a small contribution.

The gray box in Fig. 3 indicates the power that is spent in the electric consumer in the state of operation. The state of operation is characterized by the current density  $i^*$  (and the related voltage  $U^*$ ). Evidently, in this point, about 50% of the energy, that is theoretically available at the given current is spent in the consumer. The related efficiency is named “electrochemical efficiency”. The electrochemical efficiency accounts for all the loss mechanisms discussed earlier

$$\epsilon_{ec} = \frac{U^* i^*}{U_{ocv} i^*} = -\frac{U^* \cdot 2F}{\Delta_R G(p, T)}. \quad (5)$$

However, to calculate the overall PEMFC efficiency  $\epsilon$ , in addition also the “thermodynamic efficiency” ( $\epsilon_{td}$ ) and the “fuel utilization efficiency” ( $\epsilon_{fu}$ ) need to be taken into account. The thermodynamic efficiency expresses how much electrical energy can be generated at maximum from the available reaction enthalpy

$$\epsilon_{td} = \frac{\Delta_R G(p, T)}{\Delta_R H(p, T)}, \quad (6)$$

while the fuel utilization efficiency is the ratio of the amount of consumed fuel ( $N_{H_2, \text{consumed}}$ ) divided by the amount of supplied fuel ( $N_{H_2, \text{supplied}}$ )

$$\epsilon_{fu} = \frac{N_{H_2, \text{consumed}}}{N_{H_2, \text{supplied}}} = \frac{i^* A}{2F N_{H_2, \text{supplied}}}. \quad (7)$$

The overall efficiency can then be evaluated according to

$$\epsilon = \epsilon_{td} \cdot \epsilon_{ec} \cdot \epsilon_{fu} = -\frac{U^* i^* A}{\Delta_R H(p, T) N_{H_2, \text{supplied}}}. \quad (8)$$

A comparison of the efficiency of the fuel cell conversion with combustion cycle processes is depicted in Fig. 4. In Fig. 4a only the thermodynamic efficiencies of the fuel cell process and the optimal combustion cycle are compared. The thermodynamic efficiency of the optimal combustion cycle process is given by the Carnot efficiency  $\epsilon_C$

$$\epsilon_C = 1 - \frac{T_{\text{cold}}}{T_{\text{hot}}}. \quad (9)$$

$T_{\text{cold}}$  and  $T_{\text{hot}}$  represent herein the temperature of the cold and the hot reservoir, respectively. As can be seen from Fig. 4a, the big advantage of PEMFCs is that, especially at ambient conditions, the

direct conversion yields a much higher  $\epsilon_{td}$  compared to the combustion process. Then,  $\epsilon_{td}$  decreases with increasing temperature because more energy is needed to compensate the change in entropy of the hotter gases. Oppositely, the thermodynamic efficiency of the optimal combustion process  $\epsilon_C$  increases with increasing temperature of the hot reservoir (the temperature at which the heat is provided). These opposite trends lead to the fact that fuel cells (these types in which the reactions R1-C2 happen, see Fig. 1) are less desirable at high temperatures. However, in addition also the heat of the fuel cell might be used via e.g. a additional Carnot process. The related thermodynamic efficiency of this combined process is also shown in Fig. 4a. It is the maximal possible value for the heat-to-electric-energy conversion and tends to unity (as the Carnot efficiency does) for a temperature approaching infinity.

Fig. 4b compares different techniques for stationary power generation (based on estimations). It depicts the overall system efficiency  $\epsilon$  as a function of the systems power class. It can be seen that, generally, fuel cells provide the biggest advantages at small power outputs. In accordance with the discussion above, these benefit arise especially due to thermodynamic fundamentals because small systems naturally work at lower operation temperatures. This advantage becomes less important at higher temperatures (power classes). However, also at high temperatures the direct conversion of fuel to electricity can be advantageous, but it then requires “High Temperature Fuel Cells” (fuel cells of very different design that can withstand these conditions) and, as argued above, additional turbines which exploit the process heat.

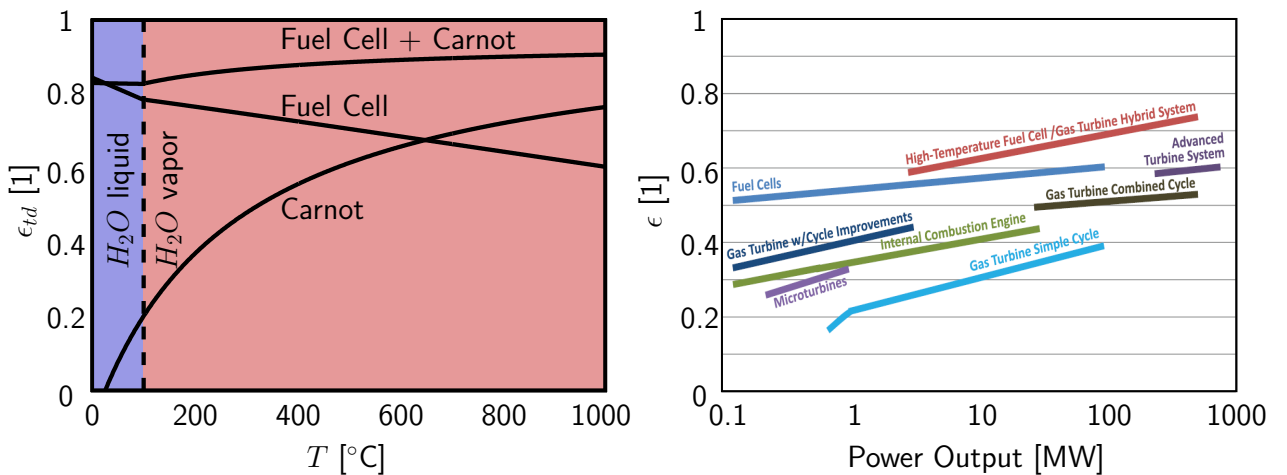


Figure 4: a: Comparison of the thermodynamic efficiency  $\epsilon_{td}$  (Eq. (6)) between the direct conversion of chemical into electrical energy, the optimal combustion cycle process and a combined system. In the figure, the cold reservoir was assumed to have a temperature of 25 °C. b: Comparison of system efficiencies  $\epsilon$  (Eq. (8)) for stationary power generation (Figure taken from [16]). Note that, the efficiency calculated in a) refers to the higher heating value (formation of liquid water), yielding therefore smaller thermodynamic efficiencies as the values that are used in b), where the lower heating value (formation of water vapor) was used.

## 1.2 State of the Art

Evidently from Fig. 4b, PEMFCs can show higher performance than conventional combustion cycle processes and can therefore be operated more profitable. The reasons why PEMFCs today still have

only a limited share in different markets is their high investment cost and their low durability. The attempts to lower the costs and enhance durability involve the investigation of degradation mechanisms, the invention of new materials as well as the development of sophisticated heat, water and contamination management strategies.

Due to the tremendous diversity, progress and specialization in the PEMFC world, the following section can not give a complete overview. Its purpose is to serve as orientation about present developments in the field in order to arrange the present thesis and its impact. The section starts with the state of present applications and future application targets. Afterwards, the fields of degradation research, material research and heat and water management are discussed individually, with highlights sketched in each field. Finally, the challenges that follow from the state of the art in order to support PEMFC commercialization are collected.

### 1.2.1 Applications

The PEMFC is the type of fuel cell with the overwhelming shipping contribution (83 % in numbers) compared to all other fuel cell types [17] (see [18] for state of the art of the other fuel cell types). The highest potential for PEMFCs lies in the automobile application, especially because its impact on green house gas emissions. But also decentralized stationary as well as portable power generation are promising application areas, in part commercialization has already started. In the following, the state in these three areas is sketched. More detailed overviews can be found in recent reviews [17, 19, 20].

Vehicles that are operated with PEMFCs are bicycles, boats, forklifts, buses, trucks and submarines [20]. Of course, the most promising vehicles for PEMFC application are light duty vehicles. Car manufacturers work to the largest extend with PEMFCs due their high current density and good load change behavior compared to other fuel cell types. Almost all big companies in that area have proven concept cars (Honda: FCX-V3; Hyundai: Santa Fe FCV; Chevrolet: Fuel Cell EV; Mercedes-Benz: B-Class F-CELL; VW: Bora-Motion; GM: Hydrogen 1; Toyota: CHV-4; Nissan: XTERRA FCV; BMW: Hydrogen 7; Audi: Q5; and others [21]). Typical fuel cell system sizes are in the range of 80 kW (110 PS). All cars are fueled with hydrogen, stored either under high pressure, in metal or complex hydrides or under cryo-compressed conditions [22]. The “standard” today is to store  $H_2$  at pressures up to 700 bar in polymer-lined, fiber-wound tanks [17]. On board reformation of liquid hydrocarbons is presently considered to be less efficient - basically because during the reformation CO is formed, which is very harmful for PEMFCs, and this CO can not be sufficiently removed economically (see Sec. 1.3 for detailed discussion). Often the PEMFCs are hybridized with batteries (e.g. Mercedes-Benz) or super capacitors (e.g. Honda) that provide peak powers, such that smaller PEMFC systems can be implied [7]. That the technology is in place for commercialization was also signaled by a group of large European companies (Linde, Daimler, Total, Shell and others) that signed a memorandum of understanding in September 2009. The memorandum states that “from 2015 onwards a quite significant number of fuel cell vehicles could be commercialized” and urges the oil and energy industry to deploy the necessary hydrogen infrastructure in Europe and elsewhere [23].

Usually, natural gas is used as fuel resource for stationary applications. As for PEMFC devices the natural gas has first to be reformed and then to be cleaned laboriously, as PEMFCs require a sophisticated water management and as quick load changes are less important also other fuel cell types are interesting for stationary applications. In the field of low electric power generation 1 – 15 kW<sub>el</sub> in combination with heat and hot water supply (CHP) a couple of companies have designed sys-

tems based on PEMFCs, high temperature PEMFCs (HT-PEMFCs) and solid oxide fuel cells (SOFCs) that are either in the test state (PEMFCs: Baxi Innotech, Vaillant, Viessmann, Toshiba, RBZ; HT-PEMFC: Vaillant, Elcore; SOFC: Hexis, Vaillant) or already commercially available (PEMFC: Panasonic, Eneos; SOFC: Ceramic Fuel Cells). For back-up power solutions and decentralized power supply at larger power classes, several companies (Onsi, Ballard, MTU, Vaillant, Inhouse Engineering, Sulzer Hexis, Vaillant) have developed systems based on a larger variety of fuel cells [24] from which also some may be purchased (e.g.: Bloom Energy (SOFC), UTC Power (PAFC), FuelCell Energy (MCFC) [17]). Stationary systems have seen a tremendous increase in shipping numbers in the last year (94 % from 2010 to 2011 [17]).

The application of fuel cells in future portable devices is mainly driven by the speculation that the expected energy demands can not be fulfilled with batteries due to their lower energy capacity and long charging times. The most promising applications are the usage in laptops and mobile phones. Due to the more difficult handling of  $H_2$  in portable systems also “Direct Methanol Fuel Cells” are commonly applied in this field. Many Asian companies have own in-house fuel cell research departments (e.g. Toshiba, Sony, Motorola, LG, Samsung). The typical power output lies between 5 – 50  $W_{el}$  [20]. Recently, portable PEMFCs have shown the highest increase in shipping numbers [17, 19].

### 1.2.2 Institutions and Targets

Worldwide, there are several major institutions that support the progress of fuel cell and  $H_2$  economy. In Europe [25], the European Commission for Research and Innovation spent almost 700 Mio. US\$ since 1968, while the German government will invest more than 900 Mio. US\$ in the framework of the “Nationales Wasserstoff und Brennstoffzellen Innovationsprogramm”. The Japanese government spent about 300 Mio. US\$ annually since 2006. In addition, the Japanese Ministry of Economy, Trade and Industry (METI) in cooperation with industry demonstrated more than 60 fuel cell electric vehicles and over 3.300 stationary residential fuel cells. Also, the US government spent 1.5 Bio. US\$ in the years between 2004 and 2009 [26]. Thereby, especially the US PEMFC research (universities, national laboratories, industry partners) is strong due to its close cooperation with the US Department of Energy (DOE), which in the past provided steady guidance in PEMFC advancement through continuously updated economic studies and long term road maps. To evaluate the state of the art in PEMFC technology it is therefore reasonable to focus on the point of view of the DOE. Links to the targets of the Japanese and European activities can be found in [27].

In 2007 the DOE targeted investment costs<sup>5</sup> of 30 \$  $kW^{-1}$  for a complete automotive PEMFC system in 2015, including an anticipated  $Pt$  loading of 0.15  $mg\ cm^{-2}$  [28] (see also the cost breakdown in Fig. 1 in [20]). While the status in 2002 was about 275 \$  $kW^{-1}$ , in 2009 systems with 0.3  $mg\ cm^{-2}$  and investment costs of 61 \$  $kW^{-1}$  [20] (0.15  $mg\ cm^{-2}$  [29] and 49 \$  $kW^{-1}$  [26] in 2011) have been realized. Similarly, lifetimes have expanded drastically from 950 h (2006) to 2500 h (2009) for automobile and 20000 h for stationary applications, compared to the goals of the DOE of 5000 h and 40000 h, respectively [20, 30]. In lab environment the company 3M has presented even PEMFCs for automobile application with more than 7000 h lifetime [20, 21], meeting the DOE target for 2015 today.

The new DOE target for automobile PEMFC systems in 2017 is set to a value of 0.125  $g\ cm^{-2}$  of platinum group metals (PGM) [26], yielding 8  $kW\ g_{PGM}^{-1}$ , which in total would lead to a total amount

<sup>5</sup>All costs resemble projections to at most  $5 \cdot 10^5$  units per year

of 8 g<sub>PGM</sub> per car - about the same amount that today is implied in the catalytic converters. Debe, a researcher from the company 3M, believes that the search for better and better catalysts is coming to an end and that instead the focus should be set on high performance catalysts that can be forwarded to mass production [31].

### 1.2.3 The Obstacle: Degradation

A decade ago the durability of PEMFCs was limited due to a series of degradation phenomena. The investigation of the specific mechanisms has been in the focus of ambitious research since. Generally, great progress has been achieved through the implementation of Accelerated Stress Tests (ACTs), operation protocols specifically developed to support a certain degradation mechanism (for a recent overview in ACTs see [32]). Today, the mechanisms of several phenomena are rather clear. The most comprehensive review article in the field of degradation was published by a large group of almost thirty authors from the United States and Japan in 2007, showing the importance of these field worldwide [27]. As commonly the different degradation phenomena are related to the component that is concerned, here first membrane degradation is discussed and then the durability of the catalyst layers and the support particles are considered. Finally, freezing is introduced separately, because it implies degradation of all components.

#### *Nafion*

In the case of membranes it is differentiated between chemical and physical/mechanical degradation. The major cause for chemical PFSA degradation is provoked through *OH* and *OOH* radicals, usually depicted as  $\bullet OH$  and  $\bullet OOH$ , respectively. The species might either form directly at the cathode or from chemical decomposition of  $H_2O_2$ , which is a side product of the ORR (and forms as well at the anode after  $O_2$  diffusion). Also other radicals might play an important role. The radicals attack the polymer and dissolve it, leading to a cleavage of the polymer backbone and unzipping of the side chains [33–35]. Rare amounts of metal cations (e.g.  $Fe^{2+}$ ,  $Cu^{2+}$ ) that are dissolved from components of the PEMFC periphery and that accumulate in the cell even support radical formation and catalyze therefore the membrane decomposition. Strategies against this mechanism are the implementation of so-called radical quenchers -  $Mn^{2+}$ ,  $Cr^{3+}$  ions - which can bind the radicals (see [36] and sources therein) and improved fluorination [37].

Physical PFSA membrane degradation occurs either as a result of alternating mechanical stresses or as result of membrane creep. Due to the swelling of the membranes (to more than 50 % of volume change) severe stresses appear at the edges at which the membrane is fixed (e.g. between channel and land area of the flow field aside). Through varying humidity (changed operation) especially these places are mechanically weakened and the membranes start to crack [38]. The effect can be lowered by simply keeping the humidity constant. But even without changing humidity pinholes might form. Due to the visco-elastic properties of the membrane, it can also undergo thinning under the constant application of high clamping pressures (named creep), especially when the water content in the membrane is high [27]. New developed reinforced membranes shall mitigate these mechanisms (e.g. [39–41]).

Physical membrane degradation can also be caused by too high temperatures (which also sets the upper temperature limit for PEMFCs operated with Nafion). Although the chemical structure of Nafion is stable at temperatures higher than 150 °C [42], the order in the ionic clusters starts to be



irreversibly destroyed above 120 °C leading to losses in conductivity [43].

#### *Pt-Cathode*

The most severe degradation phenomenon occurring at the *Pt* cathode under oxygen operation is the dissolution of the particles [35,44]. Dissolved  $Pt^{2+}$  diffuses into the membrane and recrystallizes upon interaction with  $H_2$  diffusing from the anode. Typically, a band of re-crystallized *Pt* can be found between the electrodes in micro-section images. In addition, Ostwald ripening is observed which describes the recrystallization of  $Pt^{2+}$  at larger particles. Both effects reduce the electrochemical active surface area and depend mainly on the size of the nanoparticles, the cathode double layer potential and the cell temperature. Therefore, *Pt* particles with diameters below 3 nm are highly unstable [27]. Degradation is worse for high temperatures and high double layer potentials ( $> 0.9V$  — at ocv!).

It should also be said that some gas traces, typically released in larger amounts in urban areas, can harm the cathode, too. The most severe influence was found for  $SO_2$ ,  $H_2S$ ,  $O_3$  and  $NO_x$  [45].

#### *PtRu-Anode*

If the *Pt* anodes double layer voltage exceeds a value of about 0.8 V in the presence of water, surface oxides are formed. On the one hand the oxides passivate the catalyst for  $H_2$  oxidation, on the other hand a short-term surface area enhancement is observed when the double layer voltage falls below 0.8 V (for introduction see [46]). In *PtRu* alloys the same phenomena can be observed, but the critical voltage lies at  $\approx 0.55$  V (e.g. [47]). A well known degradation effect for *PtRu* anodes is *Ru* dissolution. It is major in the presence of these oxides [48]. Usually, when PEMFCs are fed with clean  $H_2$  the anode double layer potential is less than 50 mV and these effects are unimportant. However, with regard to the present work, where  $H_2$  is contaminated with  $CO$ , the phenomena of oxide formation plays a crucial role. Therefore, also some impact of *Ru* dissolution is likely.

As hydrogen is mainly generated by steam reformation of hydrocarbons, apart from  $CO$  also other impurities are always present. Special care need also to be taken upon  $NH_3$ ,  $H_2S$  and  $SO_2$ .  $CO_2$  itself is not believed to be poisonous, but  $CO$  is formed via the reverse water gas shift reaction. Hydrocarbon impurities might form  $CO$ , too.  $N_2$  might form ammonia [45,49]. Typical concentrations, above which the influence of these species is recognized lie between 0.01 and 1 ppm at ambient conditions [27] but strongly depends on temperature.

#### *Carbon Support*

Another very important degradation mechanism is the electrochemical corrosion of the carbon support particles that carry the *Pt* nano-catalyst [27,35,44]. The equilibrium double layer potential for the oxidation of a carbon support according to the following reaction



is 0.207 V at room conditions and therefore thermodynamically allowed at the cathode for all relevant operation conditions. However, due to the slow reaction kinetics it has in practice almost no importance below a double layer voltage of  $\approx 1$  V (Indeed, the long term behavior of the cell might be affected.). On first glance a double layer voltage larger than 1 V seems to be unreachable. But during  $H_2$  starvation in a cell of a whole stack or during start-stop cycling (when the anode is flushed with  $H_2$  after it has been in air contact) it can be reached in parts of the fuel cell easily [50,51]. When a

few percent of the carbon support have been oxidized, the catalyst layer collapses, reducing the void volume and rendering transport inefficient. Yet, the strategy to handle carbon support corrosion is to avoid the highly corrosive situations. But in parallel the search for other catalyst support materials is in progress.

### *Freezing*

Apart from the yet described effects of operation, degradation can also occur under freezing conditions. This scenario was explored in the last years due to the necessity to create automobile PEMFC systems that survive these conditions. The DOE target temperature for unassisted freeze start in the year 2030 is  $-30^{\circ}\text{C}$  [26]. Literature reports on freezing experiments seem to be rather contradictory, indicating that the observed effects strongly depend on the preparation protocol of the PEMFC [27]. Apart from the groups that have not noticed any degradation events, often an increase in the high frequency resistance accompanied with a loss in electrochemical surface area was observed [27]. These effects are attributed to delamination of the electrodes, the alteration of membrane structure as well as to ice-formation and related blockage.

### **1.2.4 New Materials**

The main focus in material research is concentrated on better catalysts for the ORR. As the activity of usual *Pt* is rather poor for this reaction, the ORR causes major losses and costs (such that in fact the DOE targets could never be reached with conventional *Pt* [31]). After introducing recent research in ORR catalysis the progress in the development of new membranes is depicted. New membranes were heavily investigated to increase the resistance to chemical degradation as well as creep and crack. Finally, the progress in the field of catalyst support materials is sketched. The research in this field is mainly driven by the necessity to improve the corrosion resistance.

### *New Cathode Catalysts*

One way to increase the ORR activity is through application of extended surface area catalysts. Instead of nano-particles on carbon support, nano-structured thin films (NTFS) of non-conducting organic whiskers are sputter coated with the catalyst, that forms at the same time an electron conducting film. Other (presently less practicable) surface area enhanced catalysts comprise porous metal membranes and *Pt* skins. NTFS electrodes are usually  $1\ \mu\text{m}$  in diameter and have shown to improve the activity, the surface area utilization, the stability and also the corrosion resistance of the support. Additionally, they can be produced in large volumes [31] and the implementation of sophisticated catalyst compositions is, due to the sputter-coating, straight forward. At present, the most NTFS electrodes incorporate a  $\text{Pt}_{68}\text{Co}_{29}\text{Mn}_3$  composition. Highly promising is also the development of  $\text{Pt}_{1-x}\text{Ni}_x$  surfaces that show a sharp 100 fold increase in activity at  $x \approx 0.7$  compared to pure *Pt* [29].

Apart from different compositions also shape control can lead to activity improvement. Capping agents are applied to control the facet growth rates and support highly active facets [52]. Also the particle size influences the activity leading for example to an optimal particle size of 4.5 nm in case of *PtCo* [52]. The third method in the field of shape control is the structuring of the outermost particle layers as was shown through depletion of *Ni* from homogeneously alloyed *PtNi* particles [53], leading to *Pt*-skeleton structures. *Pt* utilization can also be increased upon use of core-shell technique by which either the core is produced empty [54] or filled with less noble materials [55].

An route for improving the ORR is the development of non-precious metal (NPM) catalysts (see [18] for small overview). Especially in this field recently breakthroughs with iron based NPM catalysts lead to a 100 fold increase in activity in 2011 [56] ( $0.75 \text{ W cm}^{-2}$  at 0.6 V) compared to 2008 [57]. However, as for the shape controlled particles, durability is the main issue of present research [31].

#### *New Membranes*

Membranes of pure PFSA (Nafion) are prone to mechanical degradation. Composite membranes as the GORE-SELECT material have greatly increased the mechanical durability and lifetime [58]. In this membrane, the PFSA polymer is reinforced with a thin, porous, and strong matrix (e.g. PTFE) at micro scale [39]. Thus, thinner GORE-SELECT membranes (down to  $5 \mu\text{m}$ ) can replace thicker non-reinforced membranes, thereby decreasing membrane resistance (specific conductance up to  $80 \text{ S cm}^{-2}$  at room temperature [59] compared to  $6 \text{ S cm}^{-2}$  for Nafion 117) while simultaneously increasing mechanical durability. Additionally, for the thin membranes the backdiffusion of water to the anode is enhanced, yielding higher currents and supporting PEMFC operation with dry gases (and therefore PEMFC system simplification). The most sophisticated reinforced Nafion membranes, offered by Du Pont today have diameters well below  $30 \mu\text{m}$  (e.g. Nafion-NR211:  $25 \mu\text{m}$ ). A different (yet less successful) approach, that also leads to improved mechanical properties, is the application of shorter sulfonated side chains in the PFSA [27].

To increase the chemical resistance, commercial available state of the art membranes base on an improved fluorination of the ionomer chains (as *H*-containing terminal bonds are most prone to cleavage) and thus reduce the amount of reactive centers [37, 60]. The most recent product release of Du Pont for increased chemical and physical stability is named Nafion XL. Other, more recently developed membranes contain additionally inorganic additives that are effective in limiting dimensional change and in improving fuel cell performance under high temperatures (above  $100 \text{ }^\circ\text{C}$ ) and low relative humidity conditions [61]. An example of such a system is the nano-fiber supported Polyfluoro-Imide-Acid (PFIA) membrane with chemically stabilizing additives [62]. The membrane shows conductivities higher than  $0.1 \text{ S cm}^{-1}$  for humidities larger than 40% at  $120 \text{ }^\circ\text{C}$  cell temperatures. It is prepared with a diameter of about  $15 - 20 \mu\text{m}$  (specific conductance higher than  $50 \text{ S cm}^{-2}$  at  $rH > 40\%$ ) and fulfills all DOE targets for  $\text{H}_2$  and  $\text{O}_2$  diffusion, as well as for chemical and mechanical durability.

Another method to extend the operation regime to high temperatures, that was proposed already in 1996, is the implementation of *Pt* particles in the interior of the membrane with the aim to produce water from diffusive  $\text{H}_2$  and  $\text{O}_2$  fluxes [63]. The idea of this so-called self-humidifying membranes has been further developed to incorporate hygroscopic (inorganic) materials like  $\text{SO}_2$  into the membrane that keep it wet [64]. However, durable high performance automotive application under dry gas inlet conditions has (to my knowledge) not been presented yet.

#### *New Catalyst Supports*

In order to enhance the *Pt* utilization and to tackle the carbon support corrosion a lot of research has focused on various forms of carbon (and other) materials, their macromolecular structure as well as their surface modification. New catalyst supports comprise graphitized carbon blacks, carbon nanotubes (nano-fibers, nano-horns, etc.), electron conducting diamond, metal oxides, silicon or electron conducting polymers. The main drawbacks of silicon structures and boron doped diamond is their cost. What hinders metal oxides yet is their poor electric conductivity. And the limit to conducting



polymers is set by their rather quick oxidation [27,65]. At present the most promising materials are the graphitized carbon and the nano-tubes.

At temperatures above 2000 °C carbon is converted into graphite, yielding improved durability and electric resistance. Graphitized carbons are the most established materials upon the sophisticated supports. Single wall carbon nanotubes (SWNT) can be understood as sheets of graphene that are rolled to form hollow cylinders. Generally, the properties of the nanotube depend on the discrete angle upon which the graphene sheet was rolled, yielding conducting, semiconducting or non-conducting tubes. Multi wall carbon nanotubes (MWNT) comprise many SWNTs. The conductance of the outer tube is affected by the inner tubes. Generally, the benefit of nanotubes, compared to conventional carbon supports, lies in the better (overall) electronic conductivity and the enhanced interaction with the catalyst particles (increasing the catalyst activity) [65]. Furthermore, they are more resistant to oxidation [49] and allow to form ordered electrode structures [66]. However, these improvements are yet not sufficient for straight forward commercialization, especially with respect to their more costly production.

### 1.2.5 Heat and Water Management

As a result of the material component properties, the cell temperature and the water content are the most important parameters and they are strongly connected. But their optimal values also depend on the choice of feed flow rates and system pressure. Accordingly, understanding these interactions is a pre-requisite for discussing control strategies. Therefore, this subsection starts with summarizing the impacts of temperature and humidity, it then proceeds via the control of the feed flow rates as well as heat and it finishes with the discussion of several water management strategies.

The only aspect that supports low cell temperatures is the thermodynamic efficiency (see Fig. 4a). But alone the improved reaction kinetics at higher cell temperatures by far outbalance the thermodynamic losses. In automobiles, where radiator size is an issue, higher temperatures are also encouraged to allow smaller radiators [67]. Generally, also the electrolytes show larger conductivities at higher temperature (for a given relative humidity  $rH$ ). However, for a high conductivity a large  $rH$  is even more important [68,69]. As above 80 °C the gas need to be pressurized in order to keep the partial pressure of the saturated fuel sufficiently high, most present PEMFCs operate at about 80 °C. Future membranes that show high conductivity at lower  $rH$  might resolve this limitation but are not implemented yet.

A certain humidity in the cell is important not only for the membrane. Water is also essential at the anode in order to allow  $H_2$  oxidation (reaction R2 in Fig. 1). But the humidity in the cell is hardly a constant but a three dimensional distribution, determined by a variety of phenomena: Firstly, a considerable amount of water is dragged with the protons to the cathode (2 – 3 water molecules per proton [6]), leading eventually to a dry out of the anode [68]. Secondly, water at the cathode is not only arriving due to drag but is also produced (reaction C2 in Fig. 1). Thirdly, backdiffusion from the cathode to the anode due to the water concentration gradient counteracts the drag. Difficulties arise because the saturation level might be easily exceeded at the cathode (especially at the outlets), leading to the formation of liquid water. The liquid causes clogging of the electrode pores and related transport losses. Liquid water can also enhance degradation because its high purity supports leaching of elements in the environment that can be carried easily into the electrodes and the sensitive membrane [70].

Typically, in automobile and stationary applications the feed flow rates of the gases are fixed to the electrical PEMFC current. That has two advantages. Firstly, an effective fuel utilization is guaranteed. Secondly, a simple water management strategy is realized<sup>6</sup>. The applied stoichiometry of the fuel is as low as 1.02 in case of pure hydrogen [67] and 1.1 in case of reformat gas [71] (in order to compensate transport losses due the lower hydrogen concentration). The air stoichiometry typically ranges from 1.4 to 2 [67,71]. Portable PEMFCs usually work in anodic dead end mode and use air in large excess to avoid active heat and water management [72,73].

The necessary control of the cell temperature in stationary and automobile devices (when high power densities are demanded) is rather straight forward. Proper insulation and heat removal are important. Heat is usually removed with the help of coolants which flow in separate channels hidden in the flow fields. Mixtures of glycol and water that are anti-corrosive and withstand freezing seem to be most suited [67].

Compared to the heat management, water management is more difficult. In principal, system humidification strategies divide into active and passive methods. While active strategies rely on external humidifiers, passive methods head for the skillful reuse of product water. The most used active humidifier for laboratory experiments and stationary applications is the so-called bubbler, a water filled vessel of a certain temperature through which the gas stream passes and thereby saturates. As the bubbler performance depends on its alignment, it is not suited for automotive application. Instead, membrane humidifiers [74], direct injection [75], humidification wheels [76] and porous bipolar plates [77] are in use. The water balance in the system, under the constraint to avoid flooding, can be obtained by choosing the inlet  $rH$  such that for the given stoichiometry saturation is reached at the outlets. However, this approach might lead to local dry out in the inlet region which enhances degradation [78]. Additionally, the cost of the system is increased when external humidification is used, a fact that can be circumvented with passive methods.

Passive methods comprise counter-flow arrangements that are specifically engineered. Implied temperature gradients help to increase the saturation vapor pressure at positions that are prone to flooding. Differences in the temperature distribution can be as high as 15 °C [8]. Similarly, pressure gradients might be implemented via proper flow field design. A decreasing pressure profile allows the gas to pick up water more efficient at the outlet than at the inlet [8]. Also, hydrophobic micro-porous layers ( $\approx 10 \mu\text{m}$  thick, 100 – 500 nm pore sizes) are placed between the electrodes (10 – 50 nm pore sizes) and gas diffusion layers (100 – 500  $\mu\text{m}$  pore sizes). The micro-porous layers act as evaporation resistances for water that is produced between them (in the cathode), therefore improving water diffusion from cathode to anode and increasing the membrane  $rH$  value. But in addition also water transport into the cathode channel, and a related drainage of the gas diffusion layer seem to be supported [8].

### 1.2.6 Present Challenges

The present challenges, according to what is depicted above, can be divided into needs on fundamental and applied research. But no matter which of the two fields is concerned the embracing issue at the time is to enhance durability and reduce costs.

<sup>6</sup>As the amount of product water scales with the current, a gas feed excess that also increases with the current keeps the molar water fraction stable and counteracts condensation [8].

With the help of fundamental research recently a variety of highly active catalysts and electrode structures have been proven at lab scale. Nano-structured thin film technology, crystal shaping and alloying are the most promising developments. The new catalysts reduce the amount of noble metals into the range of  $0.1 \text{ mg cm}^{-2}$  without performance losses. However, the corrosion of present catalyst supports and dissolution of *Pt* limit the durability of most of them under practical conditions. Also non-noble catalysts quickly caught up but they suffer from degradation, too. Therefore, new durable supports and mitigation strategies for active area loss are highly in need. An eye need to be held on the possible upscale of the catalyst and MEA production.

New reinforced, chemically stabilized and very thin membranes, like self-humidifying Nafion or nano-fiber supported Polyfluoro-Imide-Acid (PFIA), promise to diminish Ohmic losses, reduce anodic dry out and simplify water management. However, due to lifetime issues they are not established yet and it remains an obstacle to find and mitigate the specific degradation mechanisms.

Research that seems promising (as long as liquid water is an issue) is also the investigation of two-phase mass transport in the porous catalyst, micro-porous and gas diffusion layers of different hydrophobicity/hydrophilicity. These investigations should include modeling studies as well as experiments. Yet, it is not clear what an optimal distribution of pores and hydrophobicity/hydrophilicity would be like.

Another important question arises about the optimal handling of impurities. Under certain circumstances considerable losses can be induced in the PEMFC operation by contaminations in the fuel and the air as well as internal reaction by-products. Two prominent examples are  $H_2O_2$  that forms at the electrodes and  $CO$  that is present in reformat. How can such contamination be handled without reducing system efficiency?

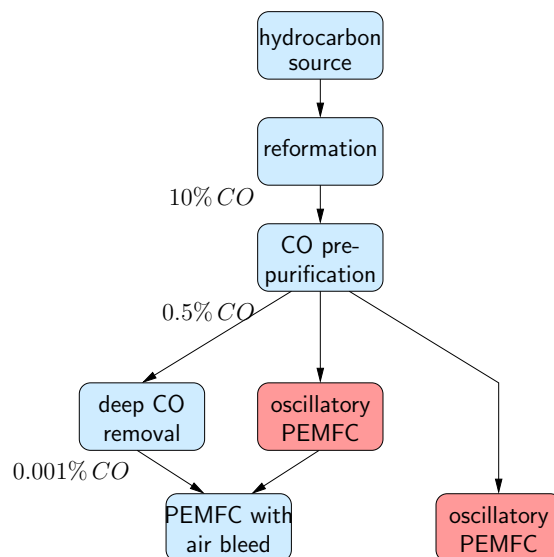
### 1.3 CO Contamination

Yet, an overview of the variety of problems (and their mitigation strategies) that hinder the large-scale implementation of PEMFCs was presented. Thereby, the overview was started with material problems. Afterwards, the difficulties in heat and water management were described. However, one specific problem was not introduced yet and this is the blockage of the anodic catalyst by  $CO$  molecules - a problem that occurs if the PEMFC is operated with  $H_2$  that was generated from hydrocarbon sources (e.g. via steam reforming, autothermal reforming or partial oxidation). This problem was left to be discussed at the end of the introduction, because it motivates the body of this thesis.

Fig. 5 presents an overview of the processes which are involved in the conversion of chemical energy (stored in the form of hydrocarbons) into electrical energy with a PEMFC. The path along the blue boxes represents the conventional process chain. It involves the production of a reformat mixture from the hydrocarbon source (first process), the cleaning of the reformat from  $CO$  (next three processes) and the conversion of the resulting gas in the PEMFC. The red boxes are potential new processes which are motivated by the behavior of a specifically controlled,  $CO$ -poisoned PEMFC. Namely in the case of galvanostatic control, the PEMFC shows oscillation of the cell voltage that have an interesting technical aspect.

The section starts with the depiction of the conventional process chain. Then, the behavior of a  $CO$ -poisoned PEMFC is described. Firstly, the operation under the conventional, potentiostatic control is explained. Thereby, the present mechanistic understanding of  $H_2$ ,  $CO$  conversion in PEM-

Figure 5: Scheme of the processes which are involved in the conversion of chemical energy (stored in the form of hydrocarbons) into electrical energy with a PEMFC. The scheme is valid for stationary applications only. The path along the blue boxes stands for the conventional process chain. The red boxes represent altered processes for which this work tries to establish the fundamentals. Both “new” processes are motivated by the same phenomena, namely autonomous cell voltage oscillations under the galvanostatic operation of a PEMFC with CO containing feed gas.

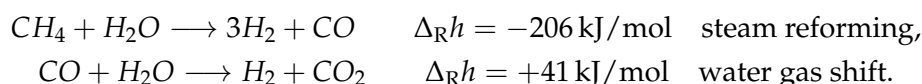


FCs is introduced. Afterwards, secondly, the behavior under galvanostatic control is sketched. The oscillation-phenomenon is depicted and its technical impact is highlighted.

### 1.3.1 The Conventional Process Chain

#### *Reformat Production and CO Pre-Purification*

There are three main techniques to generate reformat from hydrocarbon sources (e.g. natural gas): Steam reforming, autothermal reforming and partial oxidation [79]. As during the last two processes clean  $O_2$  is desired as oxidant, instead of air (in order to avoid  $N_2$  dilution of the reformat stream), steam reforming is the process that is usually applied in industry. It bases on the endothermic oxidation of the hydrocarbon source with water and desires high temperatures ( $> 500^\circ\text{C}$ ) [79]. However, in a steam reformer also the water gas shift reaction (WGSR) occurs, converting some CO into  $CO_2$ :



Typical CO concentrations at the outlet of a steam reformer are in the range of 5 – 15% [79]. As CO is causing a blockage of the anodic PEMFC catalyst, it is conventionally believed that the CO concentration of the fuel should not exceed 10 ppm<sup>7</sup>. A beneficial first cleaning process is a one or two step WGSR. It works at temperatures that are lower than in the steam reformer (high-temp. shift:  $450^\circ\text{C}$ ; low-temp. shift:  $220^\circ\text{C}$ ) and reduces the amount of CO into the range of 0.5%. Lower CO concentrations can, with a WGSR working at even lower temperatures, hardly be achieved due to the insufficient activity of present catalysts.

#### *Deep CO Removal and Air Bleed*

Processes that reduce the CO content further, to below 10 ppm, are collected under the term “deep CO removal”. The presently most effective strategy for deep CO removal is the preferential oxidation of CO (PrOx). The PrOx bases on the oxidation of CO with well dosed  $O_2$  (or air) at a Pt containing surface. However, in the oxidation also some  $H_2$  is consumed and, in that way, fuel is wasted.

<sup>7</sup>Indeed, this value serves only as a crude estimate, because the CO tolerance of a PEMFC depends drastically on operation temperature and catalyst loading - see the next subsection.

The amount of lost  $H_2$  lies in the same range as oxidized  $CO$ , e.g. [80]. Other less important deep- $CO$ -removal techniques are the selective  $CO$  methanation and separation techniques like cryogenic separation, pressure swing adsorption and selective  $CO$  diffusion through membranes [81,82]. Recently a promising alternative approach for deep  $CO$  removal was proposed by Balasubramanian et al. [83]. In this study two PEMFCs were applied, intended to work as  $CO$  filters that can be cleaned occasionally through application of an electric square pulse.

Finally, please note that even smallest  $CO$  concentrations (below 10 ppm) can lead to high PEMFC performance losses, especially at low operation temperatures and large current densities. Then, strategies to deal with  $CO$  in the PEMFC are needed on top of the deep  $CO$  removal. Today, the major technique to clean PEMFC anodes from  $CO$  is "air bleed". Thereby, some  $O_2$  (air) is added to the fuel stream in order to oxidize the  $CO$  adsorbate. The typical air fraction for fuels containing 10 – 100 ppm  $CO$  and state-of-the-art MEAs ( $0.4 - 0.5 \text{ mg}_{PtRu} \text{ cm}^{-2}$ ) is 2 – 3 % (vol.% referred to the total reformat stream) [84]. A second (yet not so established) method relies on pulsing the anodic double layer voltage to oxidize  $CO$  once in a while. The method was first presented by Carette et al. [85] and further developed in [86] and [87] where the pulse form and the frequency were optimized.

### 1.3.2 Potentiostatic PEMFC Operation with $CO$ Containing Fuel

Presently, the most suitable strategy to allow the conversion of reformates in PEMFCs relies on the implementation of the PrOx and the air bleed. However, both processes waste some fuel and induce costs. It is desirable to improve the PEMFC in such a way that  $H_2$  can, even in the presence of  $CO$ , be consumed effectively. Here, the behavior of a  $CO$ -poisoned PEMFC is depicted under the conventional potentiostatic control. Thereby, the mechanisms behind the losses are introduced whose understanding is fundamental to improve the PEMFCs  $CO$  tolerance.

The negative impact of  $CO$  contamination on the electrochemical  $H_2$  oxidation has been studied in rotating disk electrode (RDE) experiments since the 70's [88,89]. The research was not only important with respect to reformat consumption but also in relation to direct methanol conversion, in which  $CO$  plays the role as main intermediate [90,91]. Among other results, one main outcome of this research is the network of the essential catalyst reactions, depicted in Tab. 1.

The key point of this network is this: Compared to the highly active electrochemical oxidation of pure  $H_2$  at  $Pt$  electrodes (reactions R1-R2), the presence of  $CO$  can lead to major losses as it forms a very dense [91] and stable [89,93] adsorbate layer (reaction R3) that reduces the available free surface for the  $H_2$  adsorption (reaction R1). This  $CO$  layer can, at  $Pt$ , only be electro-oxidized when the voltage across the anodic reaction zone (anodic double layer voltage) is larger than 500 mV [94] (by the reactions R4 and R5). The polarization curves (green, black and red), illustrated in Fig. 6, are a consequence of the reaction network. The blue curve, corresponding to the electrochemical oxidation of clean  $H_2$ , is given as a reference. It is dominated by Ohmic losses alone - the logarithmic shape follows from the scaling of the current axis.

Taking the black curve as an example, the  $CO$ -influenced polarization curves can be understood as follows: Although the  $CO$  adsorbate is very dense, the few remaining free sites (1 – 2 %) at the  $CO$ -covered catalyst are sufficient for a rather unhindered electrochemical  $H_2$  oxidation at low current densities. Accordingly, at low current densities the cell voltage is almost not influenced by the presence of  $CO$  ( $< 0.04 \text{ A cm}^{-2}$ ). However, once a certain critical current density is approached, the small



R1:	$\frac{1}{2}H_2 + *$	$\leftrightarrow$	$*H$
R2:	$*H$	$\leftrightarrow$	$* + H^+ + e^-$
R3:	$CO + *$	$\leftrightarrow$	$*CO$
R4:	$H_2O + *$	$\leftrightarrow$	$*OH + H^+ + e^-$
R5:	$*CO + *OH$	$\leftrightarrow$	$2* + CO_2 + H^+ + e^-$

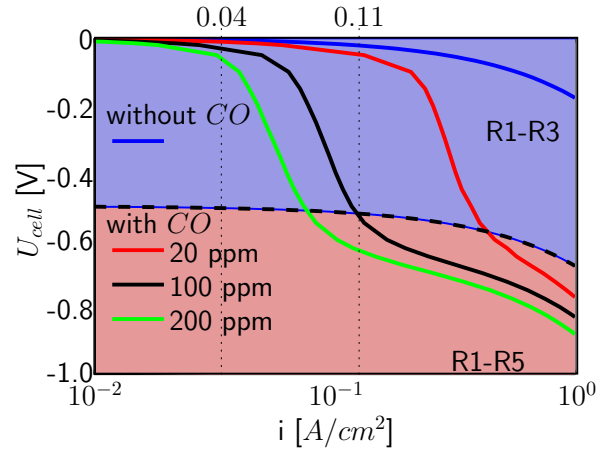


Table 1: Major reactions during the electrochemical oxidation of  $H_2$ ,  $CO$  mixtures. “\*” represents a catalyst site of the  $Pt$ -alloy considered.

Figure 6: Potentiostatic polarization curves for the electrochemical oxidation of  $H_2$ ,  $CO$  mixtures in a PEMFC (conditions:  $80^\circ C$ , ambient pressure, 100 ppm  $CO$ , feed in excess ( $H_2, CO / H_2$ )). The data is taken from [92]. The red (blue) area indicates in which voltage region R4 and R5 occur (do not occur).

amount of free surface sites starts to limit the electrochemical  $H_2$  oxidation ( $\approx 0.04 \text{ A cm}^{-2}$ ). This limitation is evident by a steep increase in the anodic double layer voltage. Consequently, the cell voltage decreases dramatically at this current value. At currents above a threshold current ( $\approx 0.11 \text{ A cm}^{-2}$ ), some surface is freed from  $CO$ , because the  $CO$  layer is continuously electrochemical oxidized (reaction R5). Then, the polarization curve tends to follow a parallel trend compared to the curve related to the absence of  $CO$  (blue curve). Therefore, the region at the right hand side of  $0.11 \text{ A cm}^{-2}$  is the regime in which  $CO$  is electrochemically oxidized, while left of it no  $CO$  is oxidized.

The bottleneck of the electrochemical  $CO$  oxidation (reaction R5) at  $Pt$ , is the simultaneous consumption of an  $OH$  adsorbate.  $OH$  only forms when the anodic double layer voltage is sufficiently high for water dissociation (reaction R4). For  $Pt$ , this critical value is approximately 500 mV - the value mentioned above. Similarly, water dissociation is also the bottleneck when  $PtRu$  is used (presently the best  $CO$ -tolerant catalyst) instead of  $Pt$  although the mechanism at  $PtRu$  is believed to be different. Namely, it is believed that the  $OH$  forms at the  $Ru$  compound at double layer voltages as low as 200 mV and then diffuses to the  $Pt$  sites, where it removes the  $CO$  [47, 91]. Therefore, at  $PtRu$  the electrochemical  $CO$  oxidation does not start at 500 mV, but already at 350 mV [95].

Finally, let us consider the influence of a decreasing  $CO$  feed gas content. It has two positive consequences [92], both can be examined from Fig. 6. On the one hand, a lower  $CO$  content in the fuel shifts the threshold current (at which the free catalyst sites start to limit the electrochemical  $H_2$  oxidation) towards larger current densities. And on the other hand, in the presence of less  $CO$ , the cell voltage loss in the electrochemical  $CO$  oxidation regime is lower. However, even for a small  $CO$  content of 20 ppm (red curve), similar to the concentration in a deeply- $CO$ -cleaned reformat, the  $H_2, CO$  conversion undergoes large losses as soon as the amount of free surface sites starts to limit  $H_2$  adsorption at  $\approx 200 \text{ mA}$ . This is the reason why, even after the deep  $CO$  removal, air bleed is needed in the conventional scheme.

### 1.3.3 Galvanostatic PEMFC Operation with CO Containing Fuel

Typically, the anodic voltage loss in the absence of CO is smaller than 30 mV [96]. During potentiostatic PEMFC operation in the presence of CO, even with the most-CO-tolerant catalyst *PtRu*, the loss is at least 10 times larger. Interestingly, the PEMFC has the intrinsic capability to reduce this loss under galvanostatic operation considerably. Then, the cell voltage exhibits autonomous oscillations. This phenomenon is depicted at next.

Sustained cell voltage oscillations during the galvanostatic electro-oxidation of  $H_2, CO$  mixtures at *Pt* electrodes in conventional electrochemical setups are reported since the 70's [97, 98]. Afterwards, they have also been found in PEMFCs with a *PtRu* anode [99, 100] but the first complete article dedicated to them was published by Zhang and Datta in 2002 [2]. Later, many others have followed [3, 4, 86, 101–108]. The article of 2002 [2] focused on the origin of the oscillations and presented a very important mathematical model for an anode comprising *PtRu*. This model reproduces the phenomenon almost quantitatively. Later, the oscillations have also been found with *PtPd* [109] and *Pt* [92] PEMFC anodes.

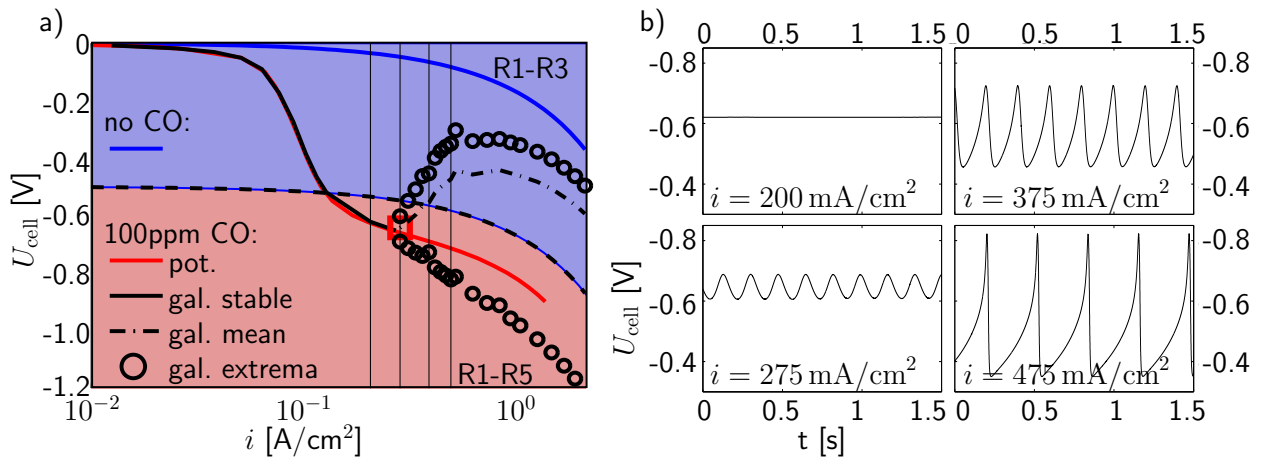


Figure 7: Galvanostatic  $H_2, CO$  oxidation in a differential PEMFC with a *Pt* anode (conditions:  $80^\circ C$ , ambient pressure, 100 ppm CO, feed in excess ( $H_2, CO/H_2$ )). a: The overall polarization curve, including minimum, maximum and mean double layer voltages. In addition, the potentiostatic curve as well as the polarization curve due to absent CO is plotted. The positions of the time series in b) is marked. The red (blue) area indicates in which voltage region R4 and R5 occur (do not occur). b: Time series of the cell voltage at specific current densities. The data is taken from [92].

#### Phenomenology

Fig. 7a depicts two measured polarization curves in the presence of 100 ppm CO. The blue curve serves as reference. It corresponds to the electrochemical oxidation of humidified, but otherwise clean,  $H_2$  and is dominated by Ohmic losses. Or in other words, electrode-related losses are negligible due to the superior reaction kinetics of the anodic hydrogen oxidation and the cathodic hydrogen evolution<sup>8</sup>. Differences between the blue and the other curves can be attributed to a change in the anodic double layer voltage alone that arise when 100 ppm CO are added to the  $H_2$  feed stream.

Looking at the black and red polarization curves (Fig. 7a), the anodic double layer voltage shows only a small increase with current density up to current densities of  $\approx 0.04 \text{ A cm}^{-2}$ . The following

<sup>8</sup> $H_2$  evolution is only used to unmask the anode. The principal anodic behavior remains the same also during cathodic  $O_2$  reduction.

steep increase marks the region in which  $H_2$  adsorption lacks sufficient free surface sites due to the almost complete  $CO$  blockage. As depicted previously, the start of the plateau marks the onset of  $OH$  formation and the related electrochemical  $CO$  oxidation. Up to this point, potentiostatic and galvanostatic experiments match each other. However, once a certain critical current density in the high current regime is exceeded, then the anodic double layer voltage (and the cell voltage, too) starts to oscillate (Fig. 7b). At 200 mA, when the oscillations appear first, the shape is sinusoidal. But the further the current is increased, the more non-sinusoidal becomes the shape. In parallel the temporally averaged double layer voltage is decreasing, too (Fig. 7b). As a consequence the temporally averaged cell voltage (dash-dotted black curve) approaches, with increasing current, the polarization curve related to no- $CO$  (Fig. 7a). This effect - the decreasing cell voltage loss in the presence of the oscillations - is technically interesting.

Indeed, in [110] it was shown that the oscillations can be understood as an autonomous cyclic self-cleaning process of the surface. By analyzing the time series, derived with the model of Zhang and Datta [2], it was illustrated that each oscillation period can be divided into a  $CO$  poisoning and a  $CO$  oxidation (reactivation) phase: Caused by an accumulation of  $CO$  in the poisoning phase, the double layer voltage continuously increases to the value required for electrochemical  $CO$  oxidation. The length of the poisoning phase depends on the amount of  $CO$  that is fed into the cell but is far apart from the bifurcation (at high current densities) much longer than the oxidation phase. In the oxidation phase, when the critical double layer potential is reached, water dissociates and removes a part of the  $CO$ .

#### *Technical Implications and Challenges*

The oscillations motivate two new processes in the conventional conversion chain (see Fig. 5). On the one hand, the oscillatory phenomenon directly increases the  $CO$  tolerance of the PEMFC, such that a process for deep  $CO$  removal might become superfluous (the lower red box in Fig. 5). But on the other hand, it was argued that, if the  $CO$  could be oxidized selectively, the oscillatory PEMFC might also be seen as an alternative process for the deep  $CO$  removal, thereby replacing the PrOx unit (the upper red box in Fig. 5). Speculating about the both processes, different questions arise.

The idea to look at the oscillatory PEMFC as a reactor for deep  $CO$  removal was first mentioned by Zhang and Datta in 2005 [4]: “*With further improvement and optimization, the ECPrOx [electrochemical preferential oxidation of  $CO$ , S.K.] technology may be a promising alternative to the conventional preferential oxidation of  $CO$* ”. Approaching from this standpoint, Lu et al. compared a parallel connection of two such operating PEMFCs (ECPrOx cells) with a single ECPrOx cell by means of  $H_2$  recovery degree and  $CO$  conversion [105]. The  $H_2$ ,  $CO$  mixture leaving the anode of the first cell served as the inlet stream for the second cell when two cells were used. It was found that in case of the parallel electric connection the overall performance was the same as if only one cell was used, indicating that the first cell of the parallel connection was so heavily  $CO$  blocked that all the current passed through the second cell. The study therefore rises the question if a part of the single cell is “dead”, too and if there is an optimal system length for the ECPrOx cell. It also left the question open whether this kind of deep  $CO$  removal is more costly than the established PrOx process.

Considering the case, in which a  $H_2$ ,  $CO$ -fed PEMFC shall be optimized for electricity production (the lower red box in Fig. 5), the main question is: How can the anodic losses be further reduced? Presently, with the help of the oscillations sketched above, it is possible to reduce the anodic losses to 200 mV in case of pure  $Pt$  and to 100 mV in case of  $PtRu$  [95], compared to 500 mV for non-oscillatory



operation at *Pt*. How can the losses be lowered further? Several other questions are directly linked to this main question: Yet, it is unclear which processes control the oscillatory behavior and which operating conditions (feed flow rate, applied current density, temperature, etc.) are optimal. Furthermore, as will be shown later in this work, a variety of phenomena can be expected apart from the oscillation shown above. These phenomena play a major role in PEMFCs of a certain spatial extension. Is it possible to exploit them technically?

### *The Interest in Nonlinear Dynamics*

There are several other systems that exhibit autonomous oscillations, too. Most relevant for this work are other oscillating electrochemical systems. However, in these other systems, often oscillations are only one phenomenon out of several. Systems that express (temporal) oscillations often also show bistable behavior and complex spatial patterns. The patterns can be stationary or undergo temporal variations (e.g. waves and chaos). All phenomena together are often referred to as “nonlinear phenomena”. Nonlinear phenomena are studied within the research field “nonlinear dynamics”.

Yet, the oscillations depicted in Fig. 7 have not been embedded into the framework of nonlinear dynamics adequately. But this connection is promising, because nonlinear dynamics provide a variety of methods that can help to investigate the oscillations during the electrochemical  $H_2$ ,  $CO$  oxidation (e.g.: time-series analysis, phase space analysis, bifurcation diagrams). And if these oscillations would be understood in terms of nonlinear dynamics, then a bunch of related phenomena could be predicted (and understood) immediately. In order to be more precise with the expected phenomena, initially a quick note on terminology is needed.

Most fundamentally, research in nonlinear dynamics bases on the development and analysis of mathematical models. Hereby, the differentiation between models of different spatial dimensionality is very important. Models of lowest spatial dimensionality are named “homogeneous models”. Here, only spatially averaged variable values are calculated - any spatial variations are disregarded. Higher dimensional models are referred to as “inhomogeneous models”. Here, the variables are derived as functions of one, two or three space coordinates. However, for electrochemical systems the phrasing is used in a slightly different way as any electrochemical system by definition contains individual parts that can not be lumped (ionic vs. electronic conductor, anode vs. cathode). Consequently, in electrochemistry the term “homogeneous” is used for a system, in which the double layer of interest (in this thesis the anodic double layer) is considered to be homogeneous. This slight re-definition is advantageous and also adopted in this work because it points out the dominant role of this double layer in understanding the whole system.

Autonomous oscillations are a typical phenomenon arising in homogeneous systems. And in electrochemistry they can originate from different kinds of instability. Depending on the kind of instability, very different behavior in the higher dimensional systems (very different patterns) can be anticipated. Among these possible patterns are globally coupled oscillations, waves, spirals, chaos and others. However, before one can specify this expectation it is important to characterize the homogeneous system precisely.

## 1.4 Aims of the Work and Proceeding

The oscillations observed during the electrochemical  $H_2, CO$  oxidation in a PEMFC have an interesting technical impact that motivates further investigation of the system. Maybe, in the future, the findings give rise to new or altered processes during the conversion of chemical energy (stored in the form of hydrocarbons) into electrical energy with a PEMFC. But presently, the insight into the system is insufficient. It is the main goal of this work to develop a precise understanding of the electrochemical  $H_2, CO$  oxidation in a PEMFC.

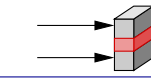
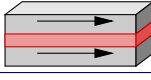
terminology	fundamentals	theoretical analysis	experimental analysis	summary
The anodic double layer voltage is <b>homogeneous</b> . 	section 2.1	section 2.2	section 2.3	section 2.4
The anodic double layer voltage is <b>inhomogeneous</b> . 	sections 3.1-3.2	section 3.3	section 3.4	section 3.5

Figure 8: Structure of the thesis. The main goal of this work - to develop a sound theoretical understanding of the electrochemical  $H_2, CO$  oxidation in a PEMFC - is formed by the four puzzle pieces.

The proceeding in this work is illustrated with the help of Fig. 8. The main goal - to develop a precise understanding of the electrochemical  $H_2, CO$  oxidation in a PEMFC - can be seen as puzzle which is composed out of four pieces. In the work, the more simple pieces are discussed first: Therefore, the homogeneous electrochemical  $H_2, CO$  oxidation in a PEMFC is investigated theoretically in section 2.2. Afterwards, the experimental studies are presented in section 2.3. In chapter 3, the more difficult system - the inhomogeneous electrochemical  $H_2, CO$  oxidation in a PEMFC - is studied. Thereby, in section 3.3, the system is again investigated theoretically first. Then, the related experiments are presented in section 3.4. At the beginning of each chapter, fundamentals are introduced which lay beneath the theoretical understanding of the phenomena that will be found. At the end of each chapter the results are summarized. The conclusions are collected in chapter 4.

Consequently, the task to understand the electrochemical  $H_2, CO$  oxidation in a PEMFC, splits into four sub-tasks. The sub-tasks are

1. Section 2.2: A mathematical model for spatially homogeneous electrochemical  $H_2, CO$  oxidation in a PEMFC shall be developed and analyzed. Thereby, the model should on the one hand reproduce the main experimental features. But on the other hand it should also be simple enough to identify the origin of the oscillations. Model predictions that are crucial shall be identified and collected for subsequent experiments.

2. Section 2.3: Experiments on the spatially homogeneous electrochemical  $H_2, CO$  oxidation in a PEMFC shall be carried out. The results shall be compared to the model predictions and help to identify the origin of the oscillations.

Thereby, the main difficulty lies in the three dimensional nature of the experiments. The experimental conditions need to be chosen such that a spatially homogeneous system is well approximated. However, as will be shown, there are situations in which an intrinsic instability will lead to an inhomogeneous patterning of the active area. In these situations, the PEMFC behavior can not be modeled with the homogeneous model.

3. Section 3.3: A mathematical model for electrochemical  $H_2, CO$  oxidation in a PEMFC shall be developed and analyzed under the assumption that the gases and the double layer voltages are well mixed in any direction but in the direction of gas flow (1D model). The model shall, on the one hand, be capable to predict the main phenomena occurring in the spatially extended system. But on the other hand, it should also be simple enough to identify the main processes that lead to the occurrence of different effects. The model should also help to guide the experiments by identifying the parameters that control the main processes.

4. Section 3.4: Experiments on the electrochemical  $H_2, CO$  oxidation in a PEMFC shall be carried out. The results shall be compared to the model predictions and qualitatively different phenomena shall be identified. In addition, the influence of the parameters that are predicted by the model to control the transitions between them should be validated.

To treat this task, a new measurement device needs to be applied. The device incorporates parallel flow channels and a segmented anode current collector. It allows to measure the individual electric currents that pass through the segments and therefore enables to screen the electric current distribution along the gas flow direction. These experiments will be the first experiments reported in literature in which this technique is applied in order to systematically investigate nonlinear instabilities in a PEMFC.



## 2 $H_2, CO$ Oxidation in a PEMFC: The Homogeneous System

Oscillations of internal states under fixed parameter conditions (no periodic perturbation from outside) are named autonomous oscillations. Autonomous oscillations have been found in all fields of fundamental research (e.g.: physico-chemical [111, 112], biological (see sources in [113]) and hydrodynamical systems [114]). The most prominent biological oscillator is probably the heart. Its cyclic contraction distributes oxygen from the lung into the body while transporting  $CO_2$  towards the lung. But oscillations are not the only puzzling processes in many natural system. Other phenomena that are frequently observed are bistability (two stable states exist for the same set of parameters), stationary patterns, oscillatory patterns, waves and pulses. Such phenomena appear frequently also in electrochemical systems [115–118]. The system considered in this thesis is only one example out of this field.

The mathematical description and understanding of the above mentioned phenomena (in general) is the aim of nonlinear dynamics, a relatively young research field which was established by Henry Poincaré at the end of the 19th century. As nonlinear dynamic research is not bound to specific systems but instead to mathematical equations, it is intrinsically interdisciplinary. However, often phrases are used that indicate the field in which the phenomenon occurs, such as “nonlinear hydrodynamics“, “mathematical biology“, etc.. Probably the most fundamental result of nonlinear dynamics is that none of the phenomena can be mathematically reproduced with linear equation systems. As the phrase “nonlinear dynamics” suggests, nonlinear terms are necessary. Their presence does not intrinsically guarantee any of the mentioned phenomena, but without them none can be found.

Generally in nonlinear dynamics, it is differentiated between spatially homogeneous (0D) and spatially inhomogeneous (1D, 2D, 3D) systems. Spatially homogeneous systems are described by a finite (mostly small) set of ordinary differential equations (ODEs). The phenomena which might occur are bistability, oscillations and temporal chaos. Spatially inhomogeneous systems are described by a finite set of partial differential equations (PDEs) and can be approximated with a finite (mostly large) set of ODEs (e.g.: via discretization). As a consequence of the discretization, each inhomogeneous system can be understood as being composed of a number of small homogeneous systems with interactions between them. Due to these interactions more complex behavior compared to homogeneous systems, like pattern formation, can occur. Pattern formation is further treated in chapter 3. This chapter shall provide a deep insight into the homogeneous<sup>9</sup> electrochemical  $H_2, CO$  oxidation in a PEMFC. The aim is to identify the fundamental nonlinearities that might provoke pattern formation.

Therefore, in the first section (Sec. 2.1) the fundamentals of nonlinear dynamics in homogeneous electrochemical systems are introduced: Initially, the precondition for instabilities in electrochemical systems (a branch of negative differential resistance in the Faradaic current curve) is rationalized. Then, two general system types, named S-NDR type and N-NDR type, are differentiated and their potential behavior is depicted. This classification is helpful in order to categorize the homogeneous electrochemical  $H_2, CO$  oxidation later. In the second section (Sec. 2.2) a simple dynamic two-

---

<sup>9</sup>In this thesis “homogeneous” means that the anodic double layer voltage is homogeneous. Therefore, in the homogeneous model the compartments are not lumped together and the electric potential in the electrolyte and the wiring also varies along the current path.

variable-model for homogeneous electrochemical  $H_2$ ,  $CO$  oxidation in a PEMFC is derived. Through analysis of the model, the system is classified as a rather exotic S-NDR/HN-NDR hybrid system. Various phenomena are depicted and the criteria for their occurrence are discussed. In the third section (Sec. 2.3) experiments are carried out in a specifically designed PEMFC. The so-called “differential design” is advantageous in order to validate the predictions of the homogeneous model. However, the results are not only discussed with respect to the model predictions but they are also related to literature results obtained for the electrochemical  $H_2$ ,  $CO$  oxidation in conventional (liquid electrolyte) systems. In the final section (Sec. 2.4), the findings of the theoretical and experimental analysis are summarized.

## 2.1 Nonlinear Dynamics in Electrochemical Systems: Fundamentals in a Nutshell

The scope of this section is to introduce the reader into the fundamentals of nonlinear dynamics of homogeneous electrochemical systems that form the basis of the sections 2.2-2.3.

The procedure is the following: Firstly, the ODEs that describe a conventional electrochemical system and the necessary terminology are introduced. Then, the stability of the steady state is analyzed with the help of a general two dimensional model. As a result, it appears that a negative differential resistance (NDR) is a prerequisite for nonlinear phenomena in electrochemical systems. After differentiation between two types of NDR, related nonlinear phenomena are depicted. Finally, the connection to PEMFC is established by considering the differences compared to conventional electrochemical setups.

### 2.1.1 The Homogeneous Electrochemical System

In electrochemical systems the double layer voltage “ $\Delta\varphi$ ” is one of the most important variables. The double layer is visualized in Fig. 9a. It consists of an ordered stable structure of ions and polar molecules at the catalyst surface. The double layer extends a few nanometers (depending on the amount of ions) into the electrolyte, where its structure becomes more and more unordered. In solutions with very high or very low pH value, the thickness of the double layer is less than one nm. The plane until which the double layer extends is named outer Helmholtz plane [119].

The double layer voltage describes the difference of the electrical potential between the catalyst surface and the outer Helmholtz plane (Fig. 9a). The following equation can be derived from the equivalent circuit shown in Fig. 9b with the help of Kirchhoff’s node law

$$C_{dl} \frac{d\Delta\varphi}{dt} = I - J_F(\Delta\varphi, x_i) \quad \text{with } i \in [1..n]. \quad (10)$$

The left term stands for a capacitive current that charges (discharges) the double layer of capacitance  $C_{dl}$ . The terms at the right hand side,  $I$  and  $J_F$ , represent the current approaching (leaving) through the electrolyte and the current that is consumed (produced) in a number of electrochemical reactions. Generally, the reaction rate  $J_F$  is an exponential function of  $\Delta\varphi$  and also depends on other local variables  $x_i$ . Such variables could, for example, be the coverage of adsorbents and species concentrations. The evolution of these (chemical) variables follow from mass balances of the general ODE form

$$C \frac{dx_j}{dt} = f_j(\Delta\varphi, x_i) \quad \text{with } j \in [1..n], \quad (11)$$

whereby  $C$  represents a material capacitance. The functions  $f_j$  are determined by mass transport and the consumption of species  $j$ . They might include additional nonlinear terms. Therefore, the

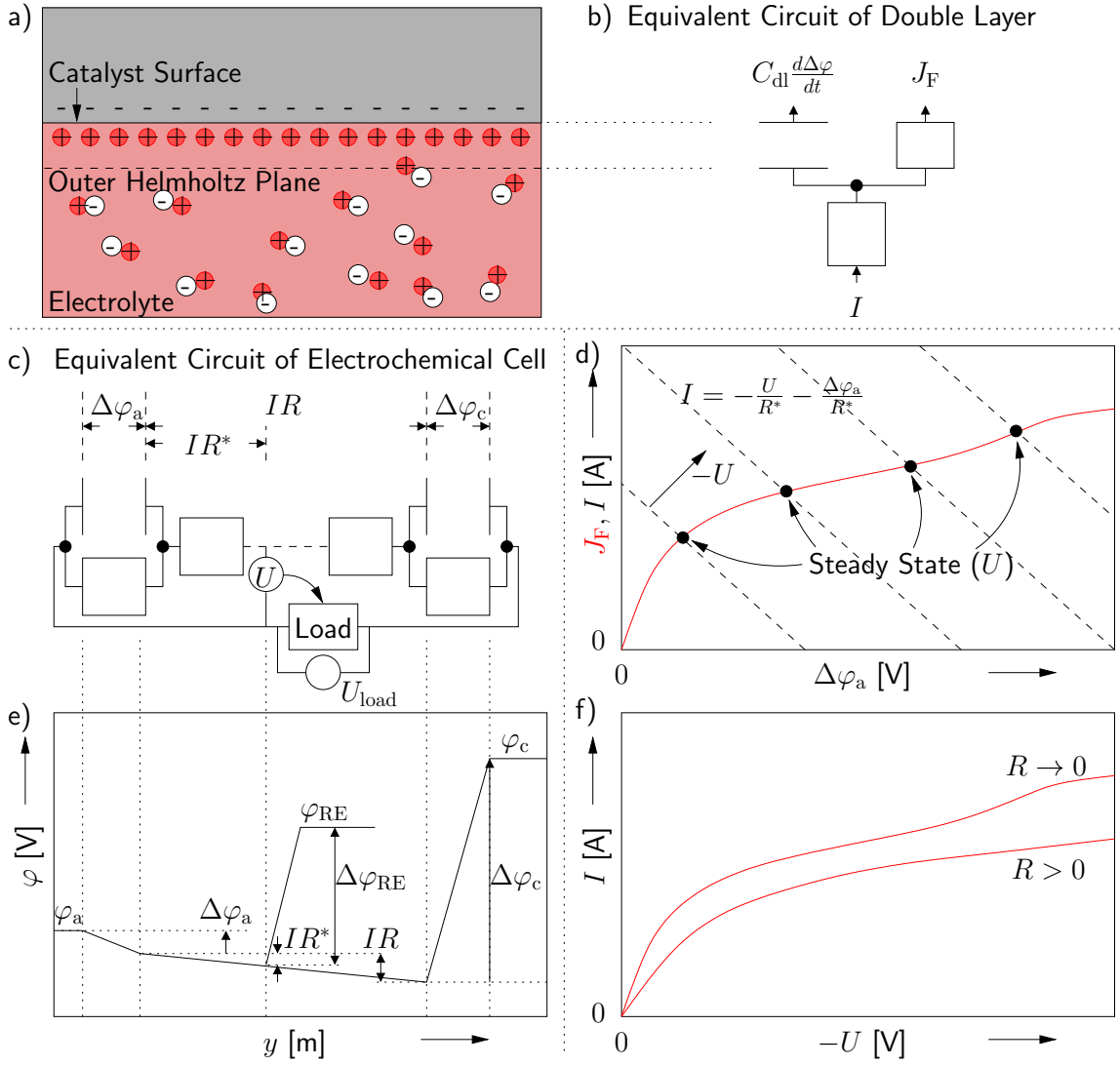


Figure 9: Fundamentals of electrochemical systems. a: Sketch of a differentially small area element of the catalyst surface with the adjacent double layer; b: The equivalent circuit for the double layer; c: The equivalent circuit for the whole electrochemical cell including a reference electrode and e: the potential distribution in the cell; d: The steady state of the system, understood as the intersection of the load line and the Faradaic current curve (see Eq. (15)). The polarization curve follows from sampling the cell voltage  $U$  at a given resistance  $R^*$ . f: The polarization curve.

essential nonlinearities in electrochemical systems usually arise from mass transport and reaction kinetics. Nonlinear phenomena resulting from hydrodynamics or heat transport are seldom.

In case the chemical subsystem (Eqs. (11)) is stationary, the values of the chemical variables at the steady state  $x_i^{ss}(\Delta\varphi_a)$  follow from

$$0 = f_j(\Delta\varphi, x_i^{ss}) \quad \text{with } j \in [1..n]. \quad (12)$$

Single electrode double layer voltages cannot be measured. As can be seen from Fig. 9c, the voltage of a system measured by a load,  $U_{load}$ , comprises always a second electrode (named counter electrode: CE) and a potential loss across the electrolyte in case of nonzero currents. Typically, a reference electrode (RE) is implied which measures the voltage  $U$ . In that way the contribution of the counter electrode and the largest part of the electrolyte is corrected. Thereby, a focusing on the

interesting working electrode (WE) is achieved. Of course, a RE has a double layer, too. But as only a tiny current passes through it in order to allow the voltage measurement, its double layer voltage is constant for all currents passing from WE to CE. If a  $H_2$ -RE is used where the double layer voltage is defined to be zero, then, according to Kirchhoff's loop law, it follows for  $U$  (see Fig. 9c,e) that

$$U = \varphi_{RE} - \varphi_a = \Delta\varphi_{RE} - \Delta\varphi_a - IR^* = -\Delta\varphi_a - IR^*, \quad (13)$$

and accordingly

$$I = -\frac{U + \Delta\varphi_a}{R^*}, \quad (14)$$

with  $R^*$  being the Ohmic resistance between the outer Helmholtz layers of working and reference electrode. If the variables  $x_i$  are in steady state, the solution of Eq. (12),  $x_i^{ss}$ , can be inserted into Eq. (10). Including additionally Eq. (14), it follows that

$$C_{dl} \frac{d\Delta\varphi_a}{dt} = -\frac{U + \Delta\varphi_a}{R^*} - J_F(\Delta\varphi_a, x_i^{ss}(\Delta\varphi_a)). \quad (15)$$

The both terms at the right hand side of Eq. (15) play very important roles throughout the rest of this manuscript. To address them individually they are specifically named. While the first term is referred to as "load line", the second term is addressed as "Faradaic current curve". Both terms relate to properties of different system components: While the load line resembles the current that passes through the electrolyte, the Faradaic current curve describes the current created by the electrochemical reactions in the double layer. Consequently, also both terms have a different appearance: While the load line usually decreases linearly with increasing double layer voltage (for a given  $U$ ), the shape of the Faradaic current curve depends on the details of the reaction network and the kinetic constants. A strictly decreasing load line and the most often occurring type of Faradaic current curve are sketched in Fig. 9d.

The intersection of load line and Faradaic current curve marks the steady state. The two most important parameters to influence the steady state are the voltage  $U$  and the resistance  $R^*$ .  $U$  can be directly controlled by the load if a feedback loop is arranged (the arrangement is then called "a potentiostat").  $R^*$  can in some range be altered by implementing additional resistance. It is worth to depict the influence of  $U$  and  $R^*$ .

A variation of the cell voltage  $U$  is indicated in the diagram Fig. 9d. Evidently, only the load line is influenced by  $U$  - it is shifted upwards. If  $U$  is scanned by the experimentalist with the help of the load, the Faradaic current curve is sampled and the so-called "polarization curve"  $I(U)$  is obtained (please note that for anodic reactions the current increases with decreasing voltage  $U$ ). The polarization curve represents the dependence of the steady state current on  $U$ . The resulting polarization curve for the example sketched in Fig. 9d is illustrated in Fig. 9f.

Similarly,  $R^*$  influences only the load line and not the Faradaic current curve. But differently, by manipulating  $R^*$ , not only the intersection with the current axis is altered, but also the load lines slope. Please note that for almost any  $R^*$  the load line is strictly decreasing. But there are two exceptions. The one exception follows if  $R^*$  is increased to approach an infinitely large value (this case could experimentally be approximated through implementation of another very large series resistance). Then, the load line aligns horizontally. This scenario is also referred to as galvanostatic operation mode. The other exception follows from a decrease of  $R^*$  towards zero. In this case the potential drop across the electrolyte becomes negligible and the load line aligns vertically. In this



limit the double layer voltage is no longer determined by Eq. (15) but it is directly defined by the cell voltage ( $R^* \rightarrow 0 \Rightarrow \Delta\varphi_a = U$ ).

The qualitative outcome of a measurement depends on the slope of the load line and the shape of the Faradaic current curve. The different emerging phenomena are presented in subsection 2.1.5. However, in order to understand these scenarios, initially, the stability of the steady state in an electrochemical system needs to be discussed comprehensively. Therefore, in the subsection 2.1.2 the stability of a steady state in a general two variable system is rehearsed, leading to the differentiation between nodes and saddles. Then, in subsection 2.1.3, the special pre-conditions for the occurrence of saddles in electrochemical systems are analyzed. It will become evident that saddles can be caused by two different sources, giving rise to the definition of two different classes of nonlinear electrochemical systems in subsection 2.1.4. Finally, the resulting phenomena are depicted in subsection 2.1.5.

### 2.1.2 The Stability of the Steady State

Assume a simple two variable system of  $\Delta\varphi_a$  and  $x$ , whereby the ODEs are given by the general form

$$C_{dl} \frac{d\Delta\varphi_a}{dt} = -\frac{U + \Delta\varphi_a}{R^*} - J_F(\Delta\varphi_a, x), \quad (16)$$

$$C \frac{dx}{dt} = f(\Delta\varphi_a, x). \quad (17)$$

The linearization<sup>10</sup> around the steady state  $\Delta\varphi_a^{ss}$  and  $x^{ss}$  with  $\delta\Delta\varphi_a = \Delta\varphi_a - \Delta\varphi_a^{ss}$  and  $\delta x = x - x^{ss}$  reads

$$\frac{d}{dt} \begin{pmatrix} \delta\Delta\varphi_a \\ \delta x \end{pmatrix} = |A|^{ss} \begin{pmatrix} \delta\Delta\varphi_a \\ \delta x \end{pmatrix} = \begin{vmatrix} A_{11} & A_{12} \\ A_{21} & A_{22} \end{vmatrix}^{ss} \begin{pmatrix} \delta\Delta\varphi_a \\ \delta x \end{pmatrix}, \quad (18)$$

with the Jacobian elements  $A_{ij}$  being given by

$$\begin{aligned} A_{11} &= -\frac{1}{C_{dl}} \left( \frac{1}{R^*} + \frac{\partial J_F}{\partial \Delta\varphi_a} \Big|_{x^{ss}} \right) & A_{12} &= -\frac{1}{C_{dl}} \frac{\partial J_F}{\partial x} \Big|_{\Delta\varphi_a^{ss}} \\ A_{21} &= \frac{1}{C} \frac{\partial f}{\partial \Delta\varphi_a} \Big|_{x^{ss}} & A_{22} &= \frac{1}{C} \frac{\partial f}{\partial x} \Big|_{\Delta\varphi_a^{ss}} \end{aligned} \quad (19)$$

The eigenvalues follow from

$$\lambda_{1,2} = \frac{(A_{11} + A_{22}) \pm \sqrt{(A_{11} + A_{22})^2 - 4(A_{11}A_{22} - A_{12}A_{21})}}{2}. \quad (20)$$

When evaluating Eq. (20) with respect to several values of the trace of  $A$  ( $A_{11} + A_{22}$ ) and its determinant ( $A_{11}A_{22} - A_{12}A_{21}$ ), different scenarios are possible. They are collected in Fig. 10a. Depending on the differently colored areas, the trajectories in the local state space (the space spanned by  $\delta\Delta\varphi_a$  and  $\delta x$ ) change their characteristics qualitatively. In the first quadrant, below the parabola, the system yields an unstable node because both eigenvalues are positive. In the region above the parabola the real parts are positive identical and the imaginary part is non-zero giving rise to an oscillatory unstable node. In the third and fourth quadrant one eigenvalue is negative while the other one is positive and the state is an unstable saddle. The only quadrant in which the steady state is stable is the second quadrant. Here, both eigenvalues are negative.

<sup>10</sup>The linearized system, spanned by  $\Delta\varphi_a$  and  $x$ , is topologically equivalent to the original system if all eigenvalues have nonzero real parts (see Hartmann-Grobmann theorem).

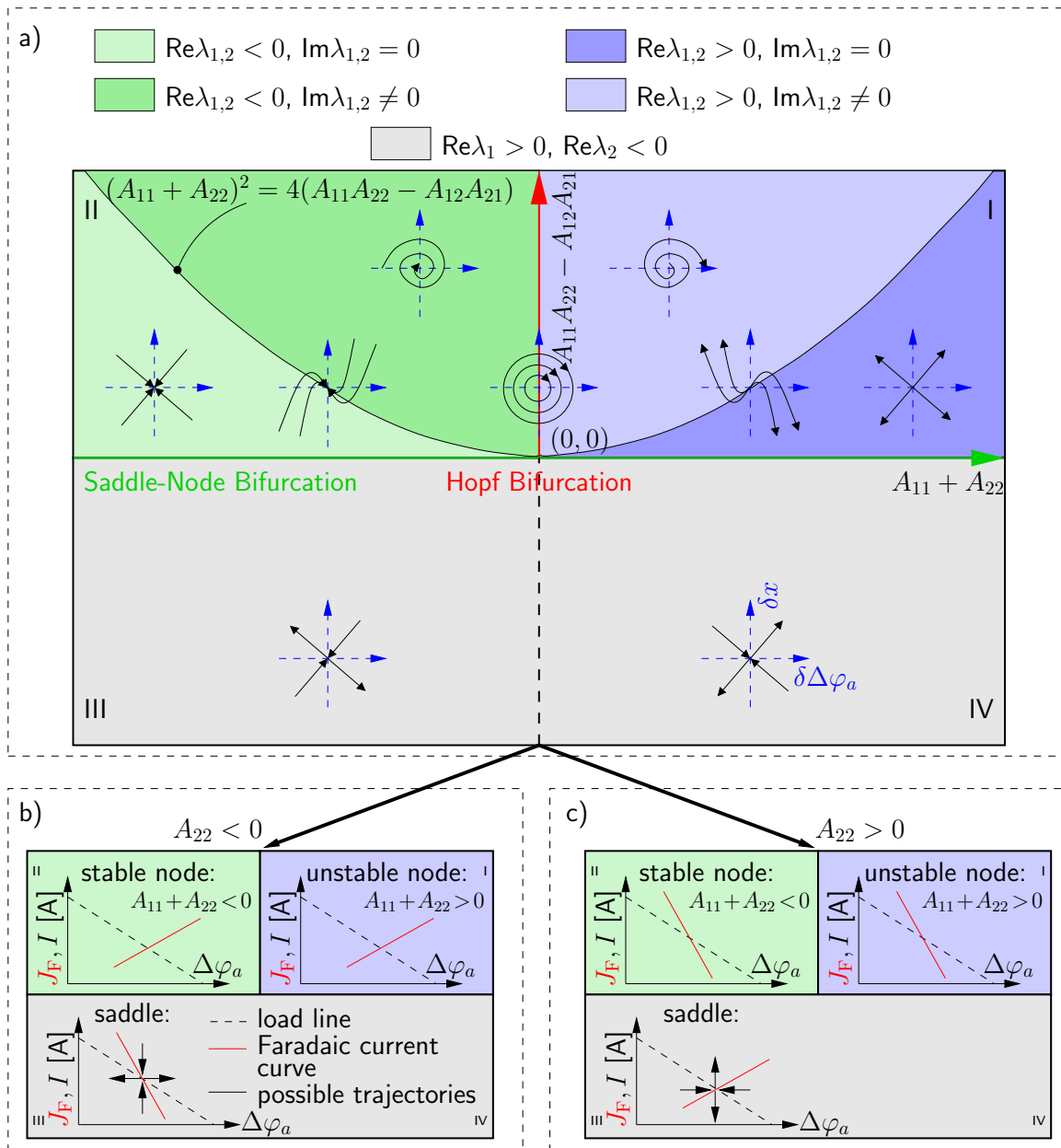


Figure 10: a) Collection of possible scenarios in a two variable system for varying trace and determinant of  $A$ ; The small coordinate systems depict the state space close the steady state. b-c): The conditions that determine the stability of the steady state in a) translated into requirements of how load line slope and Faradaic current curve need to intersect if  $A_{22} < 0$  or  $A_{22} > 0$ , respectively. For the indicated trajectories in b-c, it was assumed that  $A_{12}A_{21} < 0$ .

For a changing parameter (e.g. the cell voltage  $U$ , resistance  $R^*$ , concentrations) the  $A_{ij}$  elements vary and the trajectory in the state space changes accordingly. The characteristic points at which, upon a parameter change, the stability of the steady changes are called bifurcations. At a bifurcation, a quadrant boundary in Fig. 10a is crossed. Two different bifurcations have to be differentiated. If the system crosses from the second into the first quadrant (turning from a stable node into an unstable node) the bifurcation is named a Hopf (or loop) bifurcation. If the steady state crosses from the third into the second quadrant (turning from a saddle into a stable node) the bifurcation is named saddle-node bifurcation.

### 2.1.3 Two Different Saddles

All the depicted forms of the steady state can arise in electrochemical systems but the saddle plays a key role. Therefore, in this subsection, the properties of saddles in electrochemical system shall be evaluated. Basically, the criterion for the occurrence of a saddle

$$A_{11}A_{22} - A_{12}A_{21} < 0 \quad (21)$$

can be translated into a specific requirement for the electrochemical system — a requirement that sensitively depends on the sign of  $A_{22}$ .

#### *Electrochemical Autocatalysis*

Let us start with considering the case  $A_{22} < 0$ , representing a system in which the chemical variable is named to be autoinhibitory. After dividing Eq. (21) by  $A_{22}$  and inserting the conditions (19) one finds<sup>11</sup>

$$0 < A_{11} - \frac{A_{12}A_{21}}{A_{22}} = -\frac{1}{C_{dl}} \left( \frac{1}{R^*} + \left. \frac{\partial J_F}{\partial \Delta \varphi_a} \right|_{x^{ss}} + \left. \frac{\partial J_F}{\partial x} \right|_{\Delta \varphi_a^{ss}} \frac{\delta x}{\delta \Delta \varphi_a} \right). \quad (22)$$

In the limit of differentially small deviations from the steady state ( $\delta \rightarrow d$ ) the bracket in Eq. (22) can be reformulated

$$\frac{1}{R^*} + \left. \frac{\partial J_F}{\partial \Delta \varphi_a} \right|_{x^{ss}} + \left. \frac{\partial J_F}{\partial x} \right|_{\Delta \varphi_a^{ss}} \frac{\delta x}{\delta \Delta \varphi_a} = \frac{1}{R^*} + \frac{dJ_F}{d\Delta \varphi_a}, \quad (23)$$

finally leading to the result

$$\frac{dJ_F}{d\Delta \varphi_a} < -\frac{1}{R^*}. \quad (24)$$

Eq. (24) is a condition for how load line and Faradaic current curve have to intersect in order to yield a saddle. The result is illustrated in Fig. 10b. As can be seen, the saddle forms only if the slope of the Faradaic current curve is smaller than the slope of the load line. As the load line slope is generally negative, this argument includes the fact that any system exhibiting such a saddle contains a branch in the Faradaic current curve with a negative slope. If one defines the differential resistance  $Z_F$  via

$$\frac{1}{Z_F} = \frac{dJ_F}{d\Delta \varphi_a}, \quad (25)$$

the requirement (24) includes that the state need to be at a branch of negative differential resistance (NDR). Thus, a saddle forms if

$$Z_F < 0 \quad \text{and} \quad |Z_F| < R^*. \quad (26)$$

A second interesting aspect can be seen when Eq. (18) is re-considered. It follows that

$$\frac{1}{\delta \Delta \varphi_a} \frac{d}{dt} \delta \Delta \varphi_a = A_{11} - \frac{A_{12}A_{21}}{A_{22}} > 0. \quad (27)$$

<sup>11</sup>In the derivation the quasistationarity of  $\delta x$  was assumed:

$$\frac{\partial \delta x}{\partial t} = A_{21} \delta \Delta \varphi_a + A_{22} \delta x = 0 \quad \Rightarrow \quad \frac{A_{21}}{A_{22}} = -\frac{\delta x}{\delta \Delta \varphi_a}$$

Strictly speaking, one would need to separate between the cases  $A_{12}A_{21} \geq 0$  during the analysis of Eq. (27). However, due to simplicity, only the smaller-as case should be considered here. Then, in order to guarantee Eq. (27),  $A_{11}$  has to be larger than zero. Or in other words, a saddle in a system with an autoinhibitory chemical variable ( $A_{22} < 0$ ) is usually caused by an electrochemical autocatalysis ( $A_{11} > 0$ ). Asking for the origin of this feedback, one can follow the argumentation of Koper [120]. Under the assumption of the following approach for the Faradaic current curve

$$J_F(\Delta\varphi_a, x) = n \cdot A(\Delta\varphi_a) \cdot k(\Delta\varphi_a) \cdot x, \quad (28)$$

with  $n$  representing the number of electrons released in the reaction,  $A$  standing for the available surface area and  $k$  being the reaction constant, the element  $A_{11}$  follows to be

$$A_{11} = -\frac{1}{C_{dl}} \left( \frac{1}{R^*} + nxk \frac{\partial A}{\partial \Delta\varphi_a} \Big|_{x^{ss}} + nxA \frac{\partial k}{\partial \Delta\varphi_a} \Big|_{x^{ss}} \right). \quad (29)$$

Evidently, as  $n, F, x, k$  are larger than zero, at least one of the terms  $\partial A / \partial \Delta\varphi_a$  and  $\partial k / \partial \Delta\varphi_a$  needs to be smaller than zero in order to obtain  $A_{11} > 0$  and the related NDR. Evaluating these conditions, it follows that this kind of NDR can either be caused by a surface blockage (e.g. potential dependent species adsorption) or by a potential dependent increase in activation energy (e.g. due to adsorbents or catalyst desorption).

#### Chemical Autocatalysis

Oppositely, the scenario  $A_{22} > 0$  stands for a system in which the chemical variable is said to behave autocatalytically. Here, the analogue treatment leads to the following results

$$\frac{dJ_F}{d\Delta\varphi_a} > -\frac{1}{R^*} \quad (30)$$

and

$$\frac{1}{\delta\Delta\varphi_a} \frac{d}{dt} \delta\Delta\varphi_a = A_{11} - \frac{A_{12}A_{21}}{A_{22}} < 0. \quad (31)$$

The conclusions from these equations are depicted in Fig. 10c. Thereby, the first conclusion (from Eq. (30)) is that the steady state is a saddle if the slope of the Faradaic current curve is larger than the load line slope (opposite to the scenario in which  $A_{22} < 0$ ). The second conclusion (from Eq. (31)) is that, at this saddle, the double layer voltage acts stabilizing and that  $A_{11} < 0$  (as long as  $A_{12}A_{21} < 0$ ). The trajectory close to the saddle will therefore not deviate parallel to the double layer voltage axes, but either towards smaller or larger  $x$  values (which are connected to different current densities). Possible origins of a chemical autocatalysis can be found when considering a general transport-reaction-equation of the form

$$C \frac{dx}{dt} = D(x) - \frac{A(\Delta\varphi_a)}{F} \cdot k(\Delta\varphi_a, x) \cdot x, \quad (32)$$

with  $F$  being the Faradaic constant and  $D(x)$  being some function controlling the transport towards the electrode. The  $A_{22}$  element then follows to be

$$A_{22} = \frac{1}{C} \left( \frac{\partial D}{\partial x} \Big|_{\Delta\varphi_a^{ss}} - \frac{A}{F} x \frac{\partial k}{\partial x} \Big|_{\Delta\varphi_a^{ss}} - \frac{A}{F} k \right). \quad (33)$$

Accordingly, the chemical autocatalysis can be caused by  $\frac{\partial D}{\partial x} > 0$  or  $\frac{\partial k}{\partial x} < 0$ . The first scenario might arise in case of  $x$ -dependent diffusion, while the second situation might, for example, result from interactions of  $x$ -molecules at the catalyst surface (e.g. via Temkin kinetics).

### 2.1.4 Adjacent to the Saddle

As depicted above, there are two principally different saddles depending on which of the system variables behaves autocatalytic. But what happens if the system's state is initially prepared close to such a saddle? Let us again start the consideration with the system that fulfills  $A_{22} < 0$  (and consequently  $A_{11} > 0$ ). As was shown above, a state that is initially prepared close to the saddle would exceed either towards larger or smaller double layer voltage, thereby speeding up the further apart the saddle is (see Eq. (27)). Without additional nodes for stabilization the state would leave towards infinity, leading to unphysical situations. Therefore, the NDR branch of a realistic Faradaic current curve need to be embraced by two branches of positive slope. Such a curve is depicted in Fig. 11a. As can be seen, apart from the saddle, two other steady states are formed by additional intersections of the load line with the Faradaic current curve. As the slope of the Faradaic current curve at the other intersections is more positive than the load line slope these steady states are nodes. Whether these nodes are stable or unstable is a question that is discussed in the next subsection. Here, at next, the other saddle ( $A_{22} > 0$ ) shall be addressed.

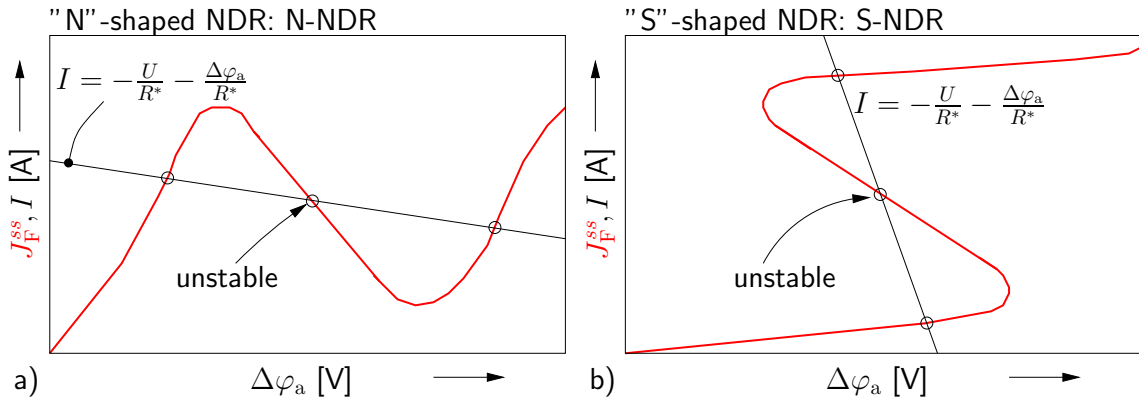


Figure 11: Faradaic current curves with a negative differential resistance (NDR) are differentiated between N-NDR (a) and S-NDR (b) type.

In the other case, when  $A_{22} > 0$  (and consequently  $A_{11} < 0$ ), the evolution of the double layer voltage proceeds towards the stabilization of the saddle-value and the chemical variable deviates. Therefore, in realistic systems two nodes have to be at higher and lower  $x$  (for the double layer voltage of the saddle) in order to prevent the state from approaching infinity. A realistic Faradaic current curve, that fulfills this requirement, is depicted in Fig. 11b. Apart from the centered saddle two additional steady states are formed. These steady states shall be nodes. Accordingly,  $A_{22}$  needs to be smaller than zero there.

Obviously, both Faradaic current curves contain a centered NDR branch. But while the first example has the shape of an "N" and is therefore referred to as N-NDR, the second example is referred to as S-NDR due to its "S-shape". The two curves stand for the two principally different origins of nonlinear instabilities. While in the N-NDR system  $A_{22} < 0$  and  $A_{11} > 0$ , in the S-NDR system  $A_{22} > 0$  and  $A_{11} < 0$ .

This subsection shall be finished with a final comment: It seems that Eq. (30) can not only be fulfilled with an S-shaped Faradaic current curve but also with a Z-shaped curve. The reason why such systems are not counted to the class of nonlinear electrochemical systems follows from the fact that no qualitative changes of the steady state can be induced by changing the electrochemical

parameters  $R^*$  and  $U$ : While in N-NDR and S-NDR systems the stability of saddles can be altered via the slope of the load line such a change cannot be induced in a Z-NDR system. The central branch of the Z, at which the steady state is a saddle, is never accessible. Therefore, Z-NDR curves are counted as nonlinear chemical systems and are not treated further in this thesis.

### 2.1.5 Bistability, Oscillations and Excitability

Above, it was discussed under which circumstances a steady state might be a saddle. It was found that an NDR branch in the Faradaic current curve is of major importance. A classification of homogeneous nonlinear electrochemical systems was motivated based on an S or N-shaped appearance of the Faradaic current curve and stems from Krischer [121]. The shape is indicative for the origin of the instability. In the following, both systems are analyzed while changing the load line parameters  $U$  and  $R^*$ . Occurring bifurcations lead to the appearance (disappearance) of bistability and oscillations.

The analysis bases on the interpretation of the  $I(\Delta\varphi_a)$  diagram. From condition (24) one can see that in an N-NDR system a steady state at the NDR-branch is definitely unstable once  $-1/R^*$  becomes larger than the slope of the Faradaic current curve. However, the steady state is not necessarily stable once  $-1/R^*$  is smaller than the slope of the Faradaic current curve. Instead, if  $A_{11} + A_{22}$  is larger than zero, the steady state remains unstable (see Fig. 10). In S-NDR systems it is similar. If  $-1/R^*$  is larger than the slope of the Faradaic current curve, the steady state is not necessarily stable. Instead, again, the stability depends on the sum of  $A_{11}$  and  $A_{22}$ . These relations are also depicted in Fig. 12a-b. Here, adjacent steady states lie also on the NDR branch and have unsettled stability.

#### *Bistability*

Scenarios as depicted in Figs. 12a-b lead to bistable, non-oscillatory systems if the outer steady states are stable ( $A_{11} + A_{22} < 0$ ): For the given set of voltage  $U$  and resistance  $R^*$  two stable steady states appear and it depends on the history of the system whether it is in the low or high current state. If one would perform a slow upward (downward) scan in  $U$  in the N-NDR system, starting in the stable state at high (low)  $\Delta\varphi_a$ , a discontinuity would appear upon reaching  $U_{sn1}$  ( $U_{sn2}$ ) leading to a jump from the low current to the high current state (reversely for the upward scan). For the S-NDR system it is different: If one would perform a slow downward (upward) scan in  $U$ , starting in the stable state at high (low)  $\Delta\varphi_a$ , a discontinuity would appear upon reaching  $U_{sn2}$  ( $U_{sn1}$ ) leading to a jump from the low current to the high current state (reversely for the upward scan). The points at which, upon a parameter change (e.g.  $U$ ), the discontinuities appear, are the saddle-node bifurcations ( $U_{sn1}$  and  $U_{sn2}$ ). Naturally, the values of  $U_{sn1}$  and  $U_{sn2}$  strongly depend on  $R^*$ . This relationship is qualitatively presented by the continuous curves in the two parameter extensions in Fig. 12.

For parameter pairs  $(R^*, U)$  at which three intersection of load line and Faradaic current curve occur, the state is in the gray regime. Otherwise, for a system with one intersection, the state is in the white area. The lines that separate both areas are the saddle node bifurcations. The point at which the both saddle node bifurcations coincide is named "cusp". Please note the two limiting cases for small and large  $R^*$ : As can be seen from Eq. (13), the potentiostatic control descends into strict potentiostatic control for  $R^* \rightarrow 0$  and the load line aligns vertically. In this situation the S-NDR system is bistable in the maximal possible voltage interval (Fig. 12d for  $R^* \rightarrow 0$ ) while the N-NDR is not bistable anymore (Fig. 12c). Oppositely, for galvanostatic control ( $R^* \rightarrow \infty$  while keeping the ratio  $U/R^* = I_{\text{load}}$  constant) the load line aligns horizontally. In that case, the S-NDR system does not

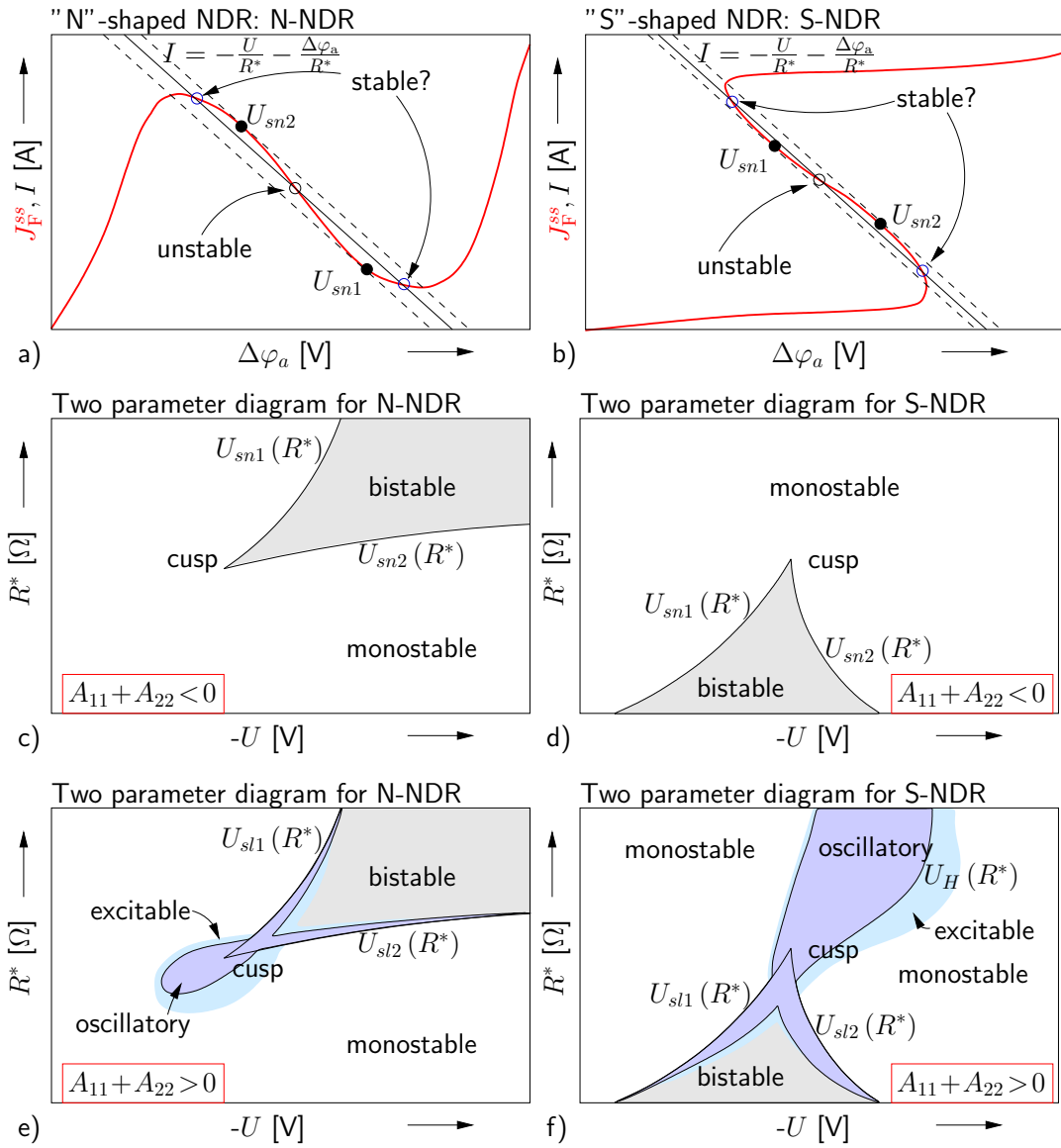


Figure 12: a: N-NDR and b: S-NDR system with unstable central steady state and unsettled stability of the outer steady states. Illustrative two parameter extensions: c-d: For the case that the trace of  $A$  is always negative only bistable behavior can occur; e-f: oscillations demand that  $A_{11} + A_{22} > 0$ . Compare also with Fig. 10.

express bistability anymore while the width N-NDR bistable regime is maximal.

### Oscillations

Scenarios as depicted in Figs. 12a-b lead to oscillatory behavior if the outer steady states are unstable ( $A_{11} + A_{22} > 0$ ): For the given set of  $U$  and  $R^*$  the inner steady state is unstable due to the saddle, but the outer steady states are unstable as well. As there are no other stable steady states, in that situation the only physical solution is that a trajectory terminates in a periodic orbit around one of the outer intersections of load line and Faradaic current curve. When scanning the cell voltage  $U$ , the oscillations start only once a Hopf bifurcation ( $U_H$ ) is crossed and extinct once the orbit intersects with the saddle (saddle-loop bifurcation:  $U_{sl1}$  and  $U_{sl2}$ ). In N-NDR systems, an orbit also forms at lower resistances when only the central intersection at the NDR-branch remains. These oscillations



lead to the extended oscillatory region around the tip of the cusp in Fig. 12e. However, for further decreasing  $R^*$  the double layer voltage is more and more controlled directly by the load, such that no oscillations can happen in the strict potentiostatic case. S-NDR systems behave equivalently for increasing  $R^*$ . However, as there is no maximal resistance at which the oscillations extinct, bifurcation diagrams like the one shown in Fig. 12 arise.

Here, it is necessary to introduce a specific oscillatory system. There exists a third type of system that can be understood as a subtype of N-NDR systems — the "hidden N-NDR", HN-NDR. This kind of system lives only in the upper two quadrants of Fig. 10. In an HN-NDR system, the NDR is superimposed by at least one other slow potential dependent process (e.g. chemisorption) such that the NDR branch cannot be seen in the steady state curve. However, at a faster time scale compared to the time scale of this slow chemical species, the system behaves like an N-NDR system. As a consequence, an HN-NDR system cannot exhibit bistability but oscillations for sufficiently large  $R^*$ . It might also happen, that only a part of NDR branch is hidden. This scenario arises when the double layer voltage interval of the slow chemisorption does not completely overlap with the NDR branch.

To elucidate the importance of S-NDR and N-NDR oscillations it is enlightening to consider the influence of the time constants  $C_{dl}$  and  $C_t$  in Eqs. (16)-(17). After renormalization of the Jacobian elements (Eq. (19)) with

$$\tilde{A}_{1j} = C_{dl}A_{1j}, \quad \tilde{A}_{2j} = CA_{2j} \quad (34)$$

the new elements  $\tilde{A}_{ij}$  are independent of the time constants. The eigenvalues follow to be

$$\lambda_{1,2} = \frac{(\tilde{A}_{11} + \epsilon\tilde{A}_{22}) \pm \sqrt{(\tilde{A}_{11} + \epsilon\tilde{A}_{22})^2 - 4\epsilon(\tilde{A}_{11}\tilde{A}_{22} - \tilde{A}_{12}\tilde{A}_{21})}}{2C_{dl}} \quad \text{with} \quad \epsilon = \frac{C_{dl}}{C}. \quad (35)$$

As can be seen from Eq. (35) a change of  $\epsilon$  (while keeping  $C_{dl}$  constant) has different effects on S-NDR and N-NDR systems as  $\tilde{A}_{22}$  has different signs. In S-NDR systems ( $\tilde{A}_{22} > 0$ ) a decreasing  $\epsilon$  diminishes the trace of the Jacobian (pushing it eventually below zero) and it reduces the determinant of the Jacobian (never passing zero). Therefore, it might easily lead to a shift from the first into the second quadrant of Fig. 10 and stabilize the instable node. In N-NDR systems the opposite is the case ( $\tilde{A}_{22} < 0$ ): A decrease in  $\epsilon$  leads to shift from the second quadrant into the first quadrant, therefore destabilizing the steady state. In real electrochemical systems  $\epsilon$  is in the order of  $10^{-3} - 10^0$  (in the properly rescaled system). Accordingly, it is reasonable that N-NDR oscillations are observed frequently, while no S-NDR oscillations are known.

Two remarks shall finish this part. While the first remark is focused on terminology, the second remark is referred to chaotic motion.

Regularly, in oscillatory systems the terms of activator and inhibitor are used to differentiate the two variables. As the sum  $A_{11} + A_{22}$  is positive, at least one variable contains an autocatalytic feedback. This variable is named activator, while the autoinhibitory variable is referred to as inhibitor. As in S-NDR systems the chemical variable  $x$  is intrinsically autocatalytic,  $x$  is the activator and  $\Delta\varphi_a$  is the inhibitor. Oppositely, in (H)N-NDR systems, where  $x$  is intrinsically autoinhibitory,  $x$  is the inhibitor while  $\Delta\varphi_a$  is the activator.

In a two dimensional state space, chaos cannot occur. As was shown by Poincaré and Bendixon [122, 123], all bound trajectories in a realistic two state system terminate in a stable node or a loop.



Chaotic motion requires at least three variables. Different routes to chaos have been found in the recent years [124], among which the Feigenbaum route via a period doubling cascade is probably the best known. A second route to chaos is the intermittency route (Manneville and Pomeau) in which the rate of statistically distributed bursts of irregular motion increases with an external control parameter. The third route was found by Ruelle, Takens and Newhouse. In this scenario a system starts to exhibit broad band noise after a third Hopf bifurcation (during the first two bifurcations two incommensurate frequencies appear). However, as chaotic motion has only limited relevance in this work, a sophisticated introduction can be avoided here.

### Excitability

A system is excitable if a small perturbation (e.g. a small change in the load line) of a stable steady state leads (due to an autocatalysis) to a large excursion in state space, finally reaching the stable steady state again. Such a scenario can arise close to an oscillatory region (indicated in Figs. 12e-f). However, note that a trajectory which is caused by the perturbation depends strongly on the strength and the direction of the perturbation. Furthermore, a “large excursion” is a very inaccurate definition. Accordingly, no clear boundary can be drawn to separate between excitable and non-excitable systems. Therefore, the excitable region in the Figs. 12e-f only serves as indication.

### 2.1.6 Adaption to PEMFCs

Compared to conventional electrochemical systems, PEMFCs comprise some specific differences that influence the system behavior. Among these is the lack of a reference electrode, a very low Ohmic resistance and better mass transport (influencing the transport function  $D(x)$ , see Eq. (32)). As is shown below, these differences tend to support N-NDR related phenomena and to circumvent S-NDR related effects.

First of all, it is evident that by controlling the electrochemical system in Fig. 9c in absence of a RE, the double layer voltage of the undesired counter electrode influences the measurement. Thereby, the counter electrode’s influence depends on the current passing through the system. The ODEs describing a system with a constant oxidant concentration in the cathode read

$$C_{dl,a} \frac{d\Delta\varphi_a}{dt} = -\frac{U_{load} - \Delta\varphi_c + \Delta\varphi_a}{R} - J_{Fa}(\Delta\varphi_a, x_i) \quad \text{with } i \in [1..n], \quad (36)$$

$$C_{dl,c} \frac{d\Delta\varphi_c}{dt} = -\frac{U_{load} - \Delta\varphi_c + \Delta\varphi_a}{R} - J_{Fc}(\Delta\varphi_c), \quad (37)$$

$$C \frac{dx_j}{dt} = f_j(\Delta\varphi_a, x_i). \quad (38)$$

The indices “a” and “c” separate between anode and cathode specific parameters/functions. Eq. (36) is almost identical to Eq. (15) but contains the influence of the cathodic double layer voltage  $\Delta\varphi_c$  and the full system resistance  $R$  instead of  $R^*$ .

Of course, the cathodic double layer voltage can also cause NDRs and related phenomena in the same way as the anode does. However, for hydrogen evolution and oxygen reduction no such behavior is known. Consequently, the cathodic Faradaic current curves do not possess NDR branches. Under the assumption that for these two reactions the cathode behaves quasi steady ( $\frac{d\Delta\varphi_c}{dt} \approx 0$ ) it can be seen that the cathodic double layer behaves like a non-Ohmic resistor as found from solving Eq. (37). Namely, when entering the result,  $\Delta\varphi_c(\Delta\varphi_a)$ , into Eq. (36), a modified load line could be identified that is no longer direct proportional to  $\Delta\varphi_a$  but has a curvature depending on the details of

the cathodic Faradaic current curve. Therefore, the general stationary impact of a counter electrode is to shift and disturb the two parameter bifurcation diagrams that were shown in Figs. 12c-f.

The thin electrolyte membrane has also some (small) influence. While in typical rotating disk (or ring) setups the electrolyte resistance  $R^*$  can be varied via the acidic concentration between approximately  $10^{-1} \Omega\text{cm}^2 - \infty$  (for a minimum distance of 1 mm between working and reference electrode) [119], the resistance in PEMFC is very restricted to values between  $10^{-1} \Omega\text{cm}^2$  and  $10^0 \Omega\text{cm}^2$  (for a  $100 \mu\text{m}$  thick membrane). Therefore, the internal PEMFC resistance (electrolyte and counter electrode) seems to be comparable to the typical Ohmic resistance in systems with liquid electrolytes. Accordingly, the load line slope has also a similar value.

Mass transport in PEMFCs distinguishes from mass transport in conventional liquid electrolytes because the diffusion coefficient is much higher ( $10^{-10} - 10^{-9} \text{m}^2\text{s}^{-1}$  in liquids and  $10^{-6} - 10^{-5} \text{m}^2\text{s}^{-1}$  in gases). The resulting enhanced species supply translates into larger electric currents, blowing up a hypothetical Faradaic current curve along the current axes by a factor  $10^4$ ! However, the double layer voltage interval of a fictive NDR region is not affected. As a consequence, the slope of the NDR branch is decreased also by a factor of  $10^4$ . Therefore, it might be speculated whether S-NDR related phenomena are less likely to be seen and whether N-NDR related phenomena might be noticed more regularly in a PEMFC compared to a liquid electrolyte system.

## 2.2 $\text{H}_2, \text{CO}$ Oxidation in a Homogeneous PEMFC - Theory

The classification of homogeneous electrochemical  $\text{H}_2, \text{CO}$  oxidation in a PEMFC, according to the scheme presented above, is a very important first step for two reasons. On the one hand, the proper classification supports the identification of the fundamental nonlinearities and allows a deeper insight into the system. But on the other hand, the classification is also essential to understand the phenomena that can appear in spatially extended systems. As will be shown in chapter 3, different patterns are expected depending on whether a system is of S-NDR or N-NDR type.

Once, the electrochemical  $\text{H}_2, \text{CO}$  oxidation in a PEMFC has already been classified [101] to be of HN-NDR type. Another time, a very similar system, namely the electrochemical  $\text{H}_2, \text{CO}$  oxidation at a rotating disk electrode in sulfuric electrolyte, was concluded to be a hybrid system [125], showing characteristics of S-NDR and HN-NDR type. The main goal in this section is to resolve this discrepancy. Therefore, at next, a mathematical model for the homogeneous electrochemical  $\text{H}_2, \text{CO}$  oxidation is developed. Then, the model is analyzed. Key findings are collected for experimental validation in the following section. The results that are presented in the sections 2.2-2.3 were preliminary published by the author in [126].

### 2.2.1 Modeling

In order to investigate the homogeneous electrochemical  $\text{H}_2, \text{CO}$  oxidation in a PEMFC theoretically, in this subsection a physically motivated model for a spatially lumped  $\text{PtRu}$  PEMFC anode is introduced. The model was motivated earlier [110] and has been derived from [2] (which itself bases on an initial RDE model [127]). As the original formulation of [2] is more intuitive, it is initially outlined briefly. Afterwards, the reduced model is introduced. This subsection is finished with the discussion of the applicability of the reduced model.

The model derived in [2] bases on the reaction network sketched in Tab. 2. It describes the temporal evolution of five dynamic variables with the help of ODEs (Tab. 3: (E1)-(E4), (E6)). These quantities are the anode overvoltage  $\eta_a$  ( $\eta_a = \Delta\varphi_a - \Delta\varphi_a^0$ , with  $\Delta\varphi_a^0$  being the open circuit double layer voltage), the surface coverage of the respective species  $\theta_{CO}$ ,  $\theta_{OH}$ ,  $\theta_H$  and the molar fraction of CO in the reaction zone  $x_{CO}$ . For evaluation of the five ODEs the fraction of free surface sites  $\theta_0$  and the flow rate in the reaction zone  $F^{out}$  are needed. They follow from two algebraic equations (Tab. 3: (E5), (E7)). The model is completed by a set of parameters (Tab. 4). For a detailed description of the model, the reader is referred to [110].

Reaction	Rate law
$\frac{1}{2}H_2 + *$ $\leftrightarrow$ $*H$	$r_T = k_{H2,ad} (p\theta_0^2 - K_{H2,ad}\theta_H^2)$
$*H$ $\leftrightarrow$ $* + H^+ + e^-$	$r_V = k_V\theta_H 2 \sinh\left(\frac{F\eta_a}{2RT}\right)$
$CO + *$ $\leftrightarrow$ $*CO$	$r_{CO,ad} = k_{CO,ad} (x_{CO}p\theta_0 - K_{CO,ad}\theta_{CO})$
$H_2O + *$ $\leftrightarrow$ $*OH + H^+ + e^-$	$r_{H2O,dis} = k_{H2O,dis} \left( \theta_0 \exp\left(\frac{F\eta_a}{2RT}\right) - K_{OH}\theta_{OH} \exp\left(-\frac{F\eta_a}{2RT}\right) \right)$
$*CO + *OH \rightarrow 2* + CO_2 + H^+ + e^-$	$r_{CO,ox} = k_{CO,ox}\theta_{CO}\theta_{OH} \exp\left(\frac{F\eta_a}{2RT}\right)$

Table 2: Anodic reaction network and rate equations in the presence of  $H_2$ ,  $CO$  mixtures (taken from [2]). “\*” represents a catalyst site of the  $Pt$ -alloy considered.

Charge balance	$c_{dl,a} \frac{d\eta_a}{dt} = i - F(r_V + r_{H2O,dis} + r_{CO,ox})$	(E1)
Material balances of anode surface	$\gamma c_t^* \frac{d\theta_H}{dt} = r_T - r_V$	(E2)
	$\gamma c_t^* \frac{d\theta_{OH}}{dt} = r_{H2O,dis} - r_{CO,ox}$	(E3)
	$\gamma c_t^* \frac{d\theta_{CO}}{dt} = r_{CO,ad} - r_{CO,ox}$	(E4)
	$\theta_0 = 1 - \theta_{CO} - \theta_H - \theta_{OH}$	(E5)
Material balances of anode compartment	$\frac{dx_{CO}}{dt} = \frac{1}{Ah_{ga}} (x_{CO}^{in} F^{in} - x_{CO} F^{out}) - r_{CO,ad} \frac{RT}{ph_{ga}}$	(E6)
	$F^{out} = F^{in} - A \frac{r_T}{2} \frac{RT}{p}$	(E7)

Table 3: Five ordinary differential equations and two algebraic equations form the core of the model [2]. The model is completed by the rate approaches given in Tab. 2 and the set of parameters given in Tab. 4.

Param.	Value	Param.	Value	Param.	Value	Param.	Value
$k_{H2,ad}$	$4.11 \cdot 10^{-4} \frac{\text{mol}}{\text{m}^2 \text{Pa s}}$	$K_{OH}$	$3.45 \cdot 10^6 \frac{\text{mol}}{\text{m}^2 \text{s}}$	$F^{in}$	$48.1 \cdot \frac{p^\theta T}{p T^\theta} \frac{\text{cm}^3}{\text{min}}$	$A$	$5 \cdot 10^{-4} \text{m}^2$
$K_{H2,ad}$	$5.07 \cdot 10^4 \text{Pa}$	$k_V$	$4.15 \cdot 10^{-1} \frac{\text{mol}}{\text{m}^2 \text{s}}$	$x_{CO}^{in}$	108 ppm	$h_{ga}$	$5.26 \cdot 10^{-4} \text{m}$
$k_{CO,ad}$	$1.53 \cdot 10^{-4} \frac{\text{mol}}{\text{m}^2 \text{Pa s}}$	$k_{CO,ox}$	$5.70 \cdot 10^{-5} \frac{\text{mol}}{\text{m}^2 \text{s}}$	$p$	$2.958 \cdot 10^5 \text{Pa}$	$i$	$0.3 \cdot 10^4 \frac{\text{A}}{\text{m}^2}$
$K_{CO,ad}$	$2.03 \cdot 10^{-2} \text{Pa}$	$c_{dl,a}$	$900 \frac{\text{F}}{\text{m}^2}$	$T$	315 K	$F$	$9.6485 \cdot 10^4 \frac{\text{As}}{\text{mol}}$
$k_{H2O,dis}$	$8.29 \cdot 10^{-5} \frac{\text{mol}}{\text{m}^2 \text{s}}$	$\gamma c_t^*$	$2.2 \cdot 10^{-3} \frac{\text{mol}}{\text{m}^2}$	$R$	$8.3145 \frac{\text{J}}{\text{molK}}$		

Table 4: List of applied parameters for the base case taken from [2].

*The Reduced Model - Motivated by Hanke-Rauschenbach et al. (2009) [110]*

After evaluating the full model, it was suggested in [110] to reduce the dimensionality of the state space by assuming that three of the five dynamic states are in quasi steady state ( $\theta_H$ ,  $\theta_{OH}$  and  $x_{CO}$ ). Accordingly, the respective ODEs (Eqs. (E2),(E3) and (E6)) are replaced by the following algebraic equations

$$\theta_H : \quad 0 = r_T - r_V \quad (39)$$

$$\theta_{OH} : \quad 0 = r_{H_2O,dis} - r_{CO,ox} \quad (40)$$

$$x_{CO} : \quad 0 = \frac{1}{Ah_{ga}} (x_{CO}^{in} F^{in} - x_{CO} F^{out}) - r_{CO,ad} \frac{RT}{ph_{ga}}. \quad (41)$$

Starting from this assumption, explicit solutions for  $\theta_H$ ,  $\theta_{OH}$  and  $x_{CO}$  (see Eqs. (49),(50) and (46)) as functions of  $\theta_{CO}$  and  $\eta_a$ , can be found. Therefore, the reduced model consists only of two ODEs and a set of help variables. The ODEs describe the evolution of the CO coverage and the anode overvoltage and read

$$\gamma c_t^* \frac{d\theta_{CO}}{dt} = r_{CO,ad} - r_{CO,ox} \quad (42)$$

$$c_{dl,a} \frac{d\eta_a}{dt} = i - F (r_V + 2r_{CO,ox}) \quad \forall i < i_F, \quad (43)$$

with  $i$  being the current density applied by the galvanostat. Please note that Eq. (43) holds only for currents smaller than the Faradaic limit current, which is given by

$$i_F = 2F \frac{p}{RT} \frac{F^{in}}{A}. \quad (44)$$

To be more precise, the model behavior is not only inaccurate at current densities above  $i_F$  (when there is a lack of fuel) but also at current densities below  $i_F$ : Then, close to complete  $H_2$  consumption, actually the transport of  $H_2$  to the electrode would need to be considered, too. Unfortunately, the introduction of reasonable  $H_2$  transport equations considerably increases the models complexity<sup>12</sup> and is for the purpose of a qualitative description avoided. Above  $i_F$ , the transport limit can be approximated by replacing Eq. (43) with

$$\eta_a \rightarrow \infty \quad \forall i \geq i_F. \quad (45)$$

This alteration marks a very crude generalization of the model proposed in [2] but yields qualitatively the trend in case of fuel starvation. Dynamic behavior close to the Faradaic limit cannot be described with Eq. (45). Therefore, in the upcoming figures (e.g. Fig. 13b)) a (conservative) gray zone at large current densities ( $[0.2 - 1] i_F$ ) is introduced, sketching the region in which the model is quantitatively incorrect.

<sup>12</sup>A sophisticated treatment would imply a Maxwell-Stefan approach, including an implicit (but linear) system of algebraic equations to describe all species ( $H_2$ ,  $CO$ ,  $H_2O$  and  $CO_2$ ) fluxes.

To calculate the rates, necessary to evaluate Eqs. (42)-(43), the CO mole fraction  $x_{\text{CO}}$  and the coverage of all the species need to be given (Tab. 2). They follow from

$$x_{\text{CO}} = x_{\text{CO}}^{\text{in}} \frac{F^{\text{in}}}{F^{\text{out}}} - r_{\text{CO,ad}} \frac{RT}{p} \frac{A}{F^{\text{out}}} \quad (46)$$

$$F^{\text{out}} = F^{\text{in}} - \frac{r_{\text{T}}}{2} A \frac{RT}{p} \quad (47)$$

$$\theta_0 = \sqrt{\left(\frac{Q_3}{2Q_2}\right)^2 + \frac{Q_4}{Q_2} - \frac{Q_3}{2Q_2}} \quad (48)$$

$$\theta_{\text{H}} = 1 - \theta_{\text{CO}} - (1 + Q_1) \theta_0 \quad (49)$$

$$\theta_{\text{OH}} = Q_1 \theta_0, \quad (50)$$

with the  $Q_i$  ( $\theta_{\text{CO}}, \eta_{\text{a}}$ ) being a set of auxiliary quantities

$$Q_1 = \frac{1}{K_{\text{OH}} \exp\left(-\frac{F\eta_{\text{a}}}{RT}\right) + \frac{k_{\text{CO,ox}}}{k_{\text{H}_2\text{O,dis}}} \theta_{\text{CO}}} > 0 \quad (51)$$

$$Q_2 = \frac{p}{K_{\text{H}_2\text{,ad}}} - (1 + Q_1)^2 \quad (52)$$

$$Q_3 = 2(1 + Q_1) \left(1 - \theta_{\text{CO}} + \frac{k_{\text{H,ox}}}{k_{\text{H}_2\text{,ad}} K_{\text{H}_2\text{,ad}}} \sinh\left(\frac{F\eta_{\text{a}}}{2RT}\right)\right) > 0 \quad (53)$$

$$Q_4 = (1 - \theta_{\text{CO}}) \left(1 - \theta_{\text{CO}} + \frac{2k_{\text{H,ox}}}{k_{\text{H}_2\text{,ad}} K_{\text{H}_2\text{,ad}}} \sinh\left(\frac{F\eta_{\text{a}}}{2RT}\right)\right) > 0. \quad (54)$$

The benefit of the given solution is, that it yields explicit solutions of the states which were assumed to be quasistationarity during the model reduction. Accordingly, the model can be numerically integrated much faster than with the initial algebraic equations. For a given pair of  $\Delta\varphi_{\text{a}}$  and  $\theta_{\text{CO}}$ , first the  $Q_j$  are calculated. Then,  $\theta_0$  as well as  $\theta_{\text{H}}$  and  $\theta_{\text{OH}}$  are evaluated. Together with  $x_{\text{CO}}$ , which follows after computing  $F^{\text{out}}$ , the rates in Tab. 2 can be solved. Then, the ODEs Eqs. (42) and (43) can be evaluated.

At this point it is desirable to extend the model in order to implement another ideal load operation mode which is necessary for the model analysis. For the case of strict potentiostatic control,  $\eta_{\text{a}}$  is defined by a potentiostat and the current  $i$  follows from

$$i: \quad 0 = i - F(r_{\text{V}} + 2r_{\text{CO,ox}}), \quad (55)$$

replacing Eq. (43). Therefore, the model contains only one ODE (Eq. (42)) if strict potentiostatic control is investigated.

Above, a reduced model for homogeneous electrochemical  $\text{H}_2, \text{CO}$  oxidation in a PEMFC was introduced. The model bases on the full model developed by Zhang and Datta [2] and on the assumptions suggested by Hanke-Rauschenbach [110]. The main benefit of the reduced model lies in the lower dimensional state space. The lower dimensionality allows to answer the question, whether the system is of S-NDR or HN-NDR type, more easily. Namely, it is very difficult to investigate a five-dimensional state space, while a two dimensional state-space can be analyzed straight forward. However, before proceeding with this analysis, the validity of the reduced model needs to be evaluated. The detailed evaluation can be found in appendix A. Here, only an overview of the procedure and a brief summary of the results might suffice.

To show the validity of the reduced model, it was compared with the full model by heuristic means. Therefore, both models were implemented in MATLAB and solved with an implicit solver for stiff problems “ode15s”. Several time series were derived for varying current density and feed flow rate. Then, the time series of the individual models were compared by means of frequency and amplitude. In addition to the time series analysis, ideas from the geometric theory of ODEs were exploited: “Quasi-integrals” [128] and singular perturbation theory support the quasistationarity assumptions, center manifold theory allows for a rigorous analysis of the onset of Hopf oscillations.

In summary, only minor deviations have been found in the dynamic behavior of the both models at low feed flow rates. These minor deviations follow completely from the assumption that  $x_{\text{CO}}$  is quasi steady. Indeed, the dynamics of the channel CO balance tend to stabilize the oscillatory steady state close to the Hopf bifurcation at the lower current density. Nevertheless, for the purpose of a qualitative system description the model reduction can be considered to be well justified.

### 2.2.2 Model Predictions

In the following section, the reduced model is applied to study the system behavior under different load operation modes. The aim is to characterize the system according to the S-NDR/N-NDR framework and thereby resolve current ambiguities. Firstly, strict potentiostatic control is investigated. Secondly, galvanostatic control is considered. Finally, both operation modes are analyzed for the special case  $k_{\text{H}_2,\text{ad}} = 0$ , which could be understood as switching off hydrogen adsorption. Or in other words, in the gas mixture  $\text{H}_2$  is replaced by an inert gas. These final scenarios form the basement for subsequent experiments.

The following argumentation rests on the nullclines, drawn in the phase portrait, and their dependence on important operation parameters. When looking into Eqs. (42) and (43) (galvanostatic control) in the following way

$$\gamma c_t^* \frac{d\theta_{\text{CO}}}{dt} = g_{F^{\text{in}}, x_{\text{CO}}^{\text{in}}}(\theta_{\text{CO}}, \eta_a), \quad (56)$$

$$c_{\text{dl},a} \frac{d\eta_a}{dt} = f_i(\theta_{\text{CO}}, \eta_a), \quad (57)$$

abbreviations ( $g_{F^{\text{in}}, x_{\text{CO}}^{\text{in}}}$  and  $f_i$ ) are introduced enabling one to focus on these dependencies ( $g$  depends on  $F^{\text{in}}$  and  $x_{\text{CO}}^{\text{in}}$ ,  $f$  depends on the parameter  $i$ ). The two equations obey the form of the Eqs. (16)-(17) which were introduced to depict the properties of S-NDR and N-NDR type Faradaic current curves. The two nullclines of the model,  $\theta_{\text{CO}}^g$  and  $\eta_a^f$ , can be calculated by solving the following equations

$$\theta_{\text{CO}}^g(\eta_a) : \quad 0 = g_{F^{\text{in}}, x_{\text{CO}}^{\text{in}}}(\theta_{\text{CO}}, \eta_a), \quad (58)$$

$$\eta_a^f(\theta_{\text{CO}}) : \quad 0 = f_i(\theta_{\text{CO}}, \eta_a), \quad (59)$$

where the superscripts “g” and “f” stand for a solution of the respective equation (58) and (59). The intersection(s) of the nullclines form the steady state(s). With the help of a numerical stability analysis and dynamic simulations of the reduced model (Eqs. (42)-(54)) the stability of the steady states is evaluated.

#### *H<sub>2</sub>, CO: Strict Potentiostatic Control*

Under strict potentiostatic control the steady states of the system are determined by equation  $g = 0$  for the given overvoltage (blue curve in Fig. 13a). The corresponding  $\theta_{\text{CO}}^g(\eta_a)$  (Fig. 13a) shows a

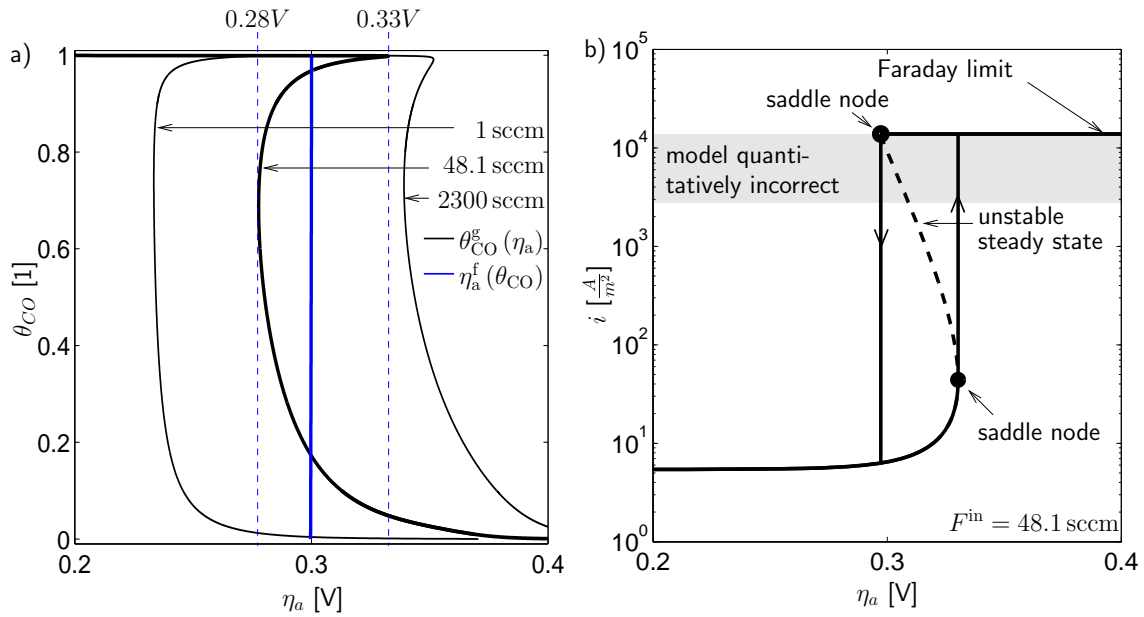


Figure 13: Collected results for strict potentiostatic control. a: The nullclines  $\theta_{CO}^g$  ( $\Delta\varphi_a$ ) for different inlet flow rates  $F^{in}$ ; The solid blue line can be understood as the nullcline  $\eta_a^f$  ( $\theta_{CO}$ ). The intersections of the nullclines show the coexistence of three steady states. The dashed lines mark the potential values of the saddle node bifurcations. b: The Faradaic current curve, resulting from a voltage scan, yields a bistable region (maximum current density inserted due to Faradaic limit, at high current densities the gray zone indicates in which region the model yields quantitatively wrong results). Other parameters can be found in Tab. 4.

switching like behavior of the CO coverage with respect to the overvoltage: While at low  $\eta_a$  the CO coverage is almost one, at high  $\eta_a$  it is almost zero. In between exists a third branch with a positive slope  $\frac{d\theta_{CO}^g}{d\eta_a} > 0$ , such that three different values of CO coverage exist for an intermediate  $\eta_a$  value (e.g. 0.28 – 0.33 V for  $F^{in} = 48.1$  sccm, see Fig. 13a). Additionally, it is interesting to note the influence of the volumetric feed flow rate. By increasing  $F^{in}$  the branch of the stationary  $\theta_{CO}$  with positive slope  $\frac{d\theta_{CO}^g}{d\eta_a} > 0$  disappears at some critical value (at about  $3 \cdot 10^3$  sccm, not shown in Fig. 13).

Commenting on the stability of the steady states, it is found that the steady state at the branch with positive slope  $\frac{d\theta_{CO}^g}{d\eta_a} > 0$  is always unstable while the other two steady states are stable. The system therefore is bistable under strict potentiostatic control. It is either in the passive state (when the CO coverage is close to one and  $H_2$  cannot be consumed) or in the active state (when the CO coverage is close to zero and  $H_2$  can be consumed). At the overvoltage at which  $\frac{d\theta_{CO}^g}{d\eta_a} = \infty$  the steady state undergoes saddle node bifurcations.

When scanning the overvoltage  $\eta_a$ , from  $0.2 \text{ V} \rightarrow 0.4 \text{ V} \rightarrow 0.2 \text{ V}$ , the related Faradaic current curve (Fig. 13b) is obtained. As can be seen, it is S-shaped and contains an unstable branch with negative differential resistance (S-NDR) ending in the two saddle node bifurcation points which mark the transition into the stable branches. The physical interpretation is as follows:

At low overvoltage the system yields small current densities. The finite currents at low  $\eta_a$  arise from hydrogen oxidation on free reaction sites which result from the finite CO desorption rate. As the overvoltage is increased, more  $H_2$  is oxidized but the surface remains deeply poisoned by CO. Increasing the overvoltage beyond the region of bistability (the saddle node bifurcation at 0.33 V), the



autocatalytic CO oxidation sets in: As soon as the rate of water dissociation (which is equivalent to the CO oxidation rate, Eq. (40)) is larger than the rate of CO adsorption, free surface sites are created. Now, as the simultaneous CO consumption leads to the depletion of CO in the anode compartment (the decrease in  $x_{\text{CO}}$  Eq. (46)), further water dissociation and therefore more CO oxidation is in turn supported. This positive feedback in the free surface sites finally ends in an avalanche-like oxidation of CO from the catalyst and out of the compartment. Accordingly, the system jumps into the active state, characterized by the maximum current possible due to complete  $H_2$  and CO oxidation. Increasing the overvoltage beyond this point does not lead to a further current gain.

In the reverse scan the active state is stable down to an overvoltage of  $\eta_a \approx 0.30 \text{ V}$ <sup>13</sup>. Once this limit is exceeded the autocatalytic CO poisoning sets in: As soon as the rate of water dissociation is smaller than the rate of CO adsorption, free surface sites are progressively populated with CO. As the CO oxidation rate decreases, also the CO mole fraction in the reaction zone recovers. The increasing mole fraction at the electrode further supports CO adsorption and in turn decreases the water dissociation/CO oxidation rate. Again, it is this positive feedback in the free surface sites which leads to a change of the system state. The final state after the conversion is characterized by the full CO surface coverage and a CO mole fraction in the compartment that is equivalent to the inlet value.

The discussion in the previous two paragraphs has shown that one of the essential ingredients for a bistability is the possibility of CO depletion in the compartment, which is also in perfect agreement with Fig. 13a, where it can be seen that the bistable  $\eta_a$  range diminishes with increasing feed flow rate. Compared to the RDE scenario it is interesting to note, that a similar condition is necessary there in order to observe a bistability, namely a sufficiently large CO transport resistance (e.g. [129]). But while in RDE experiments the Nernst diffusion layer is the CO reservoir which is depleted (and contains a negligible amount of CO compared to the amount of CO at the surface) when converting from the passive into the active state, in PEMFC experiments the entire compartment acts as a reservoir which is depleted.

The final consideration in this subsection is related to the influence of  $H_2$  onto the S-NDR under strict potentiostatic control. As can be seen from Eq. (42),  $H_2$  influences the stationary values of the CO coverage only weakly. Namely, it diminishes the number of free surface sites, needed to evaluate  $r_{\text{CO,ad}}$  by the amount of  $H$ -adsorbate. And in the overvoltage region of bistability  $\theta_H$  is almost zero. Therefore, under strict potentiostatic control the  $H_2$  oxidation acts only as an indicator of the surface state. Either, there is (almost) no  $H_2$  consumption or there is full  $H_2$  consumption, depending on whether the anode is saturated by CO or free of CO.  $H_2$  has in that sense no mechanistic impact.

### *$H_2, \text{CO}$ : Galvanostatic Control*

In the following, galvanostatic control is studied. Now, the overvoltage becomes a variable of the system according to Eqs. (43) and much insight in the dynamics can be obtained when studying the nullclines of the system. For the parameters of Tab. 4, these are given in Fig. 14a. As the operation mode of the load has only an impact on the  $f = 0$  nullcline, the  $\theta_{\text{CO}}^g$  function under galvanostatic

<sup>13</sup>The other saddle node bifurcation in Fig. 13a occurs at 0.28 V, not matching the saddle node in the Faradaic current curve (Fig. 13b). The reason is that the current connected at 0.28 V is larger than the Faradaic limit, which means that Eq.(45) applies. However, the important point is that the trend of the stationary states  $g = 0$  is correct even if the current connected with the steady state is not. The incorporation of a correct treatment of anodic mass transfer would be a valuable work in the future to remedy this weakness.



control (Fig. 13a) coincides with the  $\theta_{\text{CO}}^g$  curve under strict potentiostatic control. Accordingly, also the Faradaic current curve remains the same, even if the stability changes.

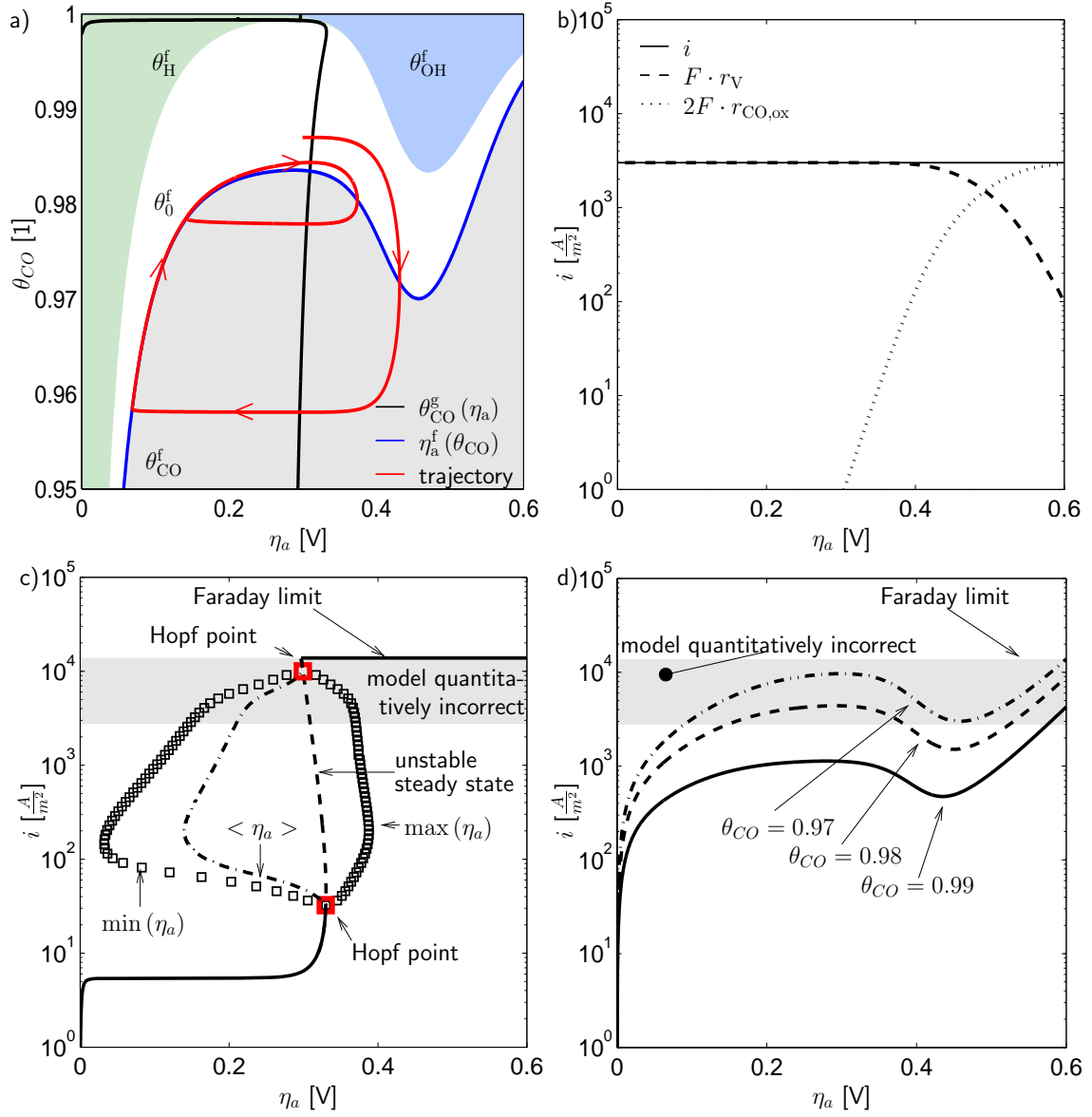


Figure 14: Collected results for galvanostatic control. a: Nullclines in the state space of the reduced model ( $i = 0.3 \text{ A cm}^{-2}$ ) and a trajectory spiraling in the orbit around the unstable steady state; b: Contributions from the different electrochemical oxidation reactions to the total current along the  $\eta_a^f$  nullcline; c: Faradaic current curve with bifurcation points and maximum, minimum and mean overvoltage of the oscillations; d: Faradaic current curve for constant  $\theta_{\text{CO}}$  ( $\theta_{\text{CO}}$  is here set to an arbitrary value and not determined by Eq. 42!) in order to depict the negative differential resistance (N-NDR). Other parameters according to Tab. 4

The nullcline  $f = 0$  has a region with negative slope  $\frac{d\eta_a^f}{d\theta_{\text{CO}}}$  in the range between 97% to 98% CO coverage. The reason for this phenomenon can be found when taking also the coverage of the other species into account ( $\theta_0^f$ ,  $\theta_{\text{H}}^f$  and  $\theta_{\text{OH}}^f$ ) while solving Eq. (59).

The colored areas in Fig. 14a represent these individual coverages as a function of overvoltage. (E.g. at  $\eta_a \approx 0.5 \text{ V}$  the values for the coverages are:  $\theta_{\text{CO}}^f = 0.972$ ,  $\theta_0^f = 0.012$ ,  $\theta_{\text{OH}}^f = 0.016$  and

$\theta_{\text{H}}^{\text{f}} = 0$ .) An  $\text{H}$ -adsorbate forms only at low overvoltage and disappears at about 0.3 V, because it is oxidized easily. Oppositely,  $\text{H}_2\text{O}$  dissociates only at higher overvoltage, leading to the formation of a  $\text{OH}$ -adsorbate above 0.3 V. Accordingly, at low overvoltage  $\theta_{\text{CO}}$  profits from the enhanced free surface and suffers once water dissociation (equivalent to  $\text{CO}$  oxidation, Eq. (40)) sets in. In Fig. 14b it can be seen that with increasing overvoltage also the current from water dissociation/ $\text{CO}$  oxidation grows. At an overvoltage higher than 0.6 V the current is entirely provided by water dissociation/ $\text{CO}$  oxidation.

The exchange between  $\text{H}_2$  and  $\text{CO}$  oxidation as main current carrying reaction is a manifestation of a "hidden N-shaped negative differential resistance" (HN-NDR). This can be easily seen when assuming that the  $\text{CO}$  coverage is fixed at a constant value while solving Eq. (59) for different applied current densities  $i$ . The Faradaic current curve in Fig. 14d is obtained. Clearly, an N-shaped negative differential resistance (N-NDR) is revealed, due to the formation of the  $\text{OH}$ -adsorbate (see again Fig. 14a). However, in the full model  $\theta_{\text{CO}}$  is not an arbitrary constant, but is determined by the solution of the  $g = 0$  nullcline. Therefore, during steady state, the oxidation of  $\text{CO}$  at higher overvoltage leads to a decrease of  $\theta_{\text{CO}}$ , overcompensating the current reduction due to water dissociation. Consequently, the N-NDR is hidden behind a branch of positive slope (or rather behind the S-NDR branch in the present case, see Fig. 14c) and can only be visualized by artificially keeping  $\theta_{\text{CO}}$  constant.

Finally, the dynamic behavior of the reduced model is discussed. The steady state solution is marked by the intersection of the two nullclines (Fig. 14a). For the given parameters the steady state is unstable, forcing the state in an outward spiral until the stable orbit is reached. Fig. 14a depicts a trajectory which does not start at steady state but somewhere else in state space. Nevertheless, the state relaxes into the same stable orbit. In detail, the given trajectory can be looked at as follows: The initial state is set onto the  $\theta_{\text{CO}}$  nullcline giving rise to an increase in  $\eta_{\text{a}}$  alone (not in  $\theta_{\text{CO}}$ ). At a larger overvoltage, water starts to dissociate at the surface, initializing the formation of the  $\text{OH}$  adsorbate. The reduction in available surface sites enhances the overvoltage, as essentially  $\text{H}_2$  oxidation needs to supply the galvanostatic current. However, with increasing overvoltage also the  $\text{CO}$  oxidation rate increases, leading to a reduction of  $\text{CO}$  adsorbate and at some point to an increase of free surface sites again. In turn, the overvoltage decreases and causes the formation of water from surface bound  $\text{OH}$  adsorbate which further increases the number of free sites. This positive feedback in the amount of free surface leads to a sudden drop of the trajectory towards low overvoltage while the electrode frees from  $\text{OH}$ . It stops to fall at a value that is related to the amount of  $\text{CO}$  adsorbate which was not consumed and now hinders hydrogen consumption. Finally, the trajectory follows the  $\eta_{\text{a}}$  nullcline,  $\text{CO}$ , which is delivered by the gas very slowly, adsorbs at the surface and forces  $\eta_{\text{a}}$  to increase up to the point when water dissociation starts to play a role again. The trajectory finally turns into a cycle where the described behavior is less well expressed but the phenomenology remains the same.

The Faradaic current curve is shown in Fig. 14c. As mentioned above, the steady state curve matches the one of strict potentiostatic control (see Fig. 13b) but the dynamic behavior is different. In the current region with an unstable steady state, oscillations appear. They are indicated by their minimum, maximum and mean value. The unstable steady state finally terminates into two Hopf points: Beyond the Hopf points, the steady state is stable.

As an explanation for the cause of the oscillations, a first impression leads one to ascribe them to the HN-NDR, because the orbit in the phase portrait is largely effected by the dissociation of water and also because the extrema along the Faradaic current curve do not coincide with the bistable region (0.30 – 0.33 V). However, a more detailed analysis of the phase portrait, while increasing

the current, reveals that first the CO coverage becomes autocatalytic (the Hopf point appears at a branch with  $\frac{d\theta_{\text{CO}}^g}{d\eta_a} > 0$  and  $\frac{d\eta_a^f}{d\theta_{\text{CO}}} > 0$ <sup>14</sup>). Then, at higher current densities also the overvoltage becomes autocatalytic ( $\frac{d\eta_a^f}{d\theta_{\text{CO}}} < 0$ <sup>15</sup>). In other words, the oscillations appear in presence of the S-NDR branch and in the absence of the HN-NDR branch and oscillations at low current densities could therefore be called “S-NDR oscillations”, but at higher current densities the steady state slips also onto the HN-NDR branch such that oscillations are caused by the S-NDR and the HN-NDR. Siegmeier et al. [125] named these oscillations “hybrid oscillations”. Please note, that at very high feed flow rates (in the absence of the S-NDR), oscillations also appear, which are then referred to as “HN-NDR oscillations”. Also note, that in [125] at values of the specific double layer capacitance typical for bulk metal electrodes and much lower than the values used here (which was taken from [2]) the S-NDR oscillations do not exist anymore, because variations of the double layer potential become much faster than those of the CO coverage. They thus stabilize the S-NDR branch.

The presence of the S-NDR, leading to bistability and oscillations, has never been experimentally validated in PEMFCs, leading to the question, how to find it there.

### *N<sub>2</sub>, CO: Galvanostatic and Strict Potentiostatic Control*

In the previous subsection it has been shown that under galvanostatic control the  $\eta_a$  nullcline contains a branch with  $\frac{d\eta_a^f}{d\theta_{\text{CO}}} < 0$  resulting in an HN-NDR and related oscillations. This phenomenon arises, because water dissociation at high overvoltage inhibits  $H_2$  consumption. Oppositely, for strict potentiostatic control it was shown, that  $H_2$  has almost no influence on the  $\theta_{\text{CO}}^g$  nullcline, but acted only as an indicator for the surface state. In order to focus on the S-NDR instability it is helpful to get rid of the branch with  $\frac{d\eta_a^f}{d\theta_{\text{CO}}} < 0$  in the  $\eta_a^f$  nullcline. This aim can be easily obtained by replacing  $H_2$  with an inert gas (e.g.  $N_2$ ). In terms of the model,  $k_{H_2,ad}$  is set to zero. Nullclines and steady states as well as Faradaic current curves for the two different operation modes are collected in Fig. 15.

For galvanostatic control the nullclines have only one intersection point at high CO coverage (see inset of Fig. 15a). However, this steady state is unstable and surrounded by a stable orbit. Therefore, the related Faradaic current curve Fig. 15b contains two Hopf points with periodic orbits in between. The maximum and minimum overvoltage coincide with the bistable region of the  $\theta_{\text{CO}}^g$  nullcline, indicating that the oscillations are related to the S-NDR (see e.g. [125]). Indeed, applying the same argumentation as in the recent section, the autocatalysis of  $\theta_{\text{CO}}$  and accordingly the S-NDR branch is responsible for the oscillations, meaning that these oscillations are S-NDR oscillations.

For strict potentiostatic control the CO coverage as a function of the overvoltage is again multi-valued, equivalent to the scenario in the  $H_2, CO$  system (Fig. 13a). Accordingly, the Faradaic current curve undergoes hysteresis (Fig. 15d).

Finally, the inlet flow rate for the occurrence of the S-NDR is estimated from experimental studies in order to prepare the experiment. This estimation is necessary, because the hysteresis vanished in the RDE study of Koper [129] at high rotation speeds ( $1.6 \cdot 10^3$  rpm) depicting that the S-NDR forms

<sup>14</sup>This argument is derived from connecting the Jacobian at steady states with the local nullclines. From  $g = 0$  with the solution  $\theta_{\text{CO}}^g(\eta_a)$  it follows, after derivation of  $g = 0$  with respect to  $\eta_a$ , that  $\frac{\partial \theta_{\text{CO}}^g}{\partial \eta_a} = -\frac{\partial g}{\partial \eta_a} / \frac{\partial g}{\partial \theta_{\text{CO}}}$ . As  $\frac{\partial g}{\partial \eta_a} < 0$  for all relevant parameters,  $\theta_{\text{CO}}$  becomes autocatalytic ( $\frac{\partial g}{\partial \theta_{\text{CO}}} > 0$ ) once  $\frac{\partial \theta_{\text{CO}}^g}{\partial \eta_a} > 0$ .

<sup>15</sup>The argumentation is equivalent to the autocatalysis of  $\theta_{\text{CO}}$  but considers the nullcline  $f = 0$  and the precondition  $\frac{\partial f}{\partial \theta_{\text{CO}}} > 0$ .

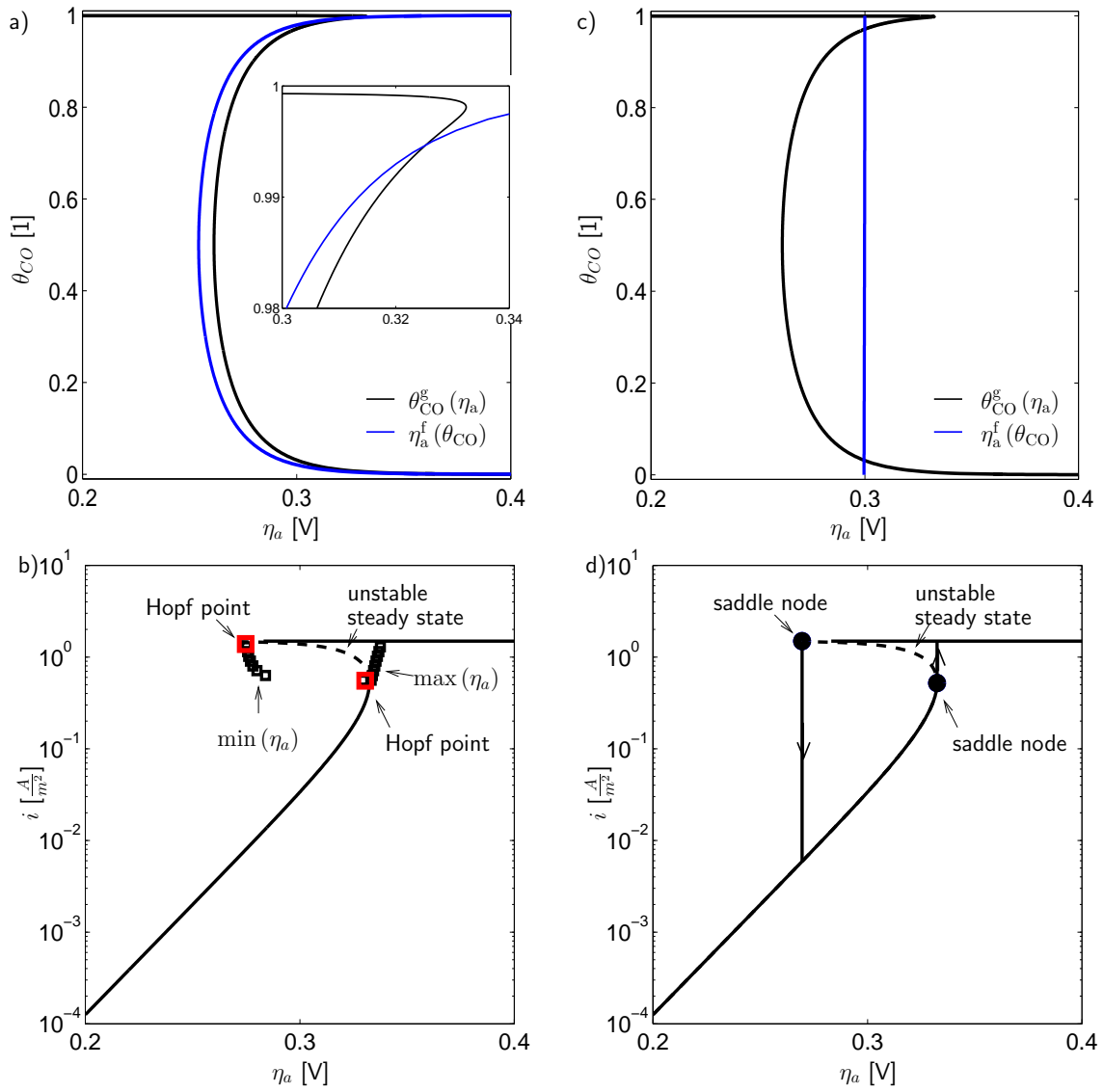


Figure 15: CO oxidation in the absence of  $H_2$  but with the same concentration of an inert gas instead ( $k_{H_2,ad} = 0$ ). a: Nullclines and b: Faradaic current curve for galvanostatic control ( $i = 1 \text{ A m}^{-2}$ ); c: Stationary coverage and d: Faradaic current curve for strict potentiostatic control ( $U = 0.3 \text{ V}$ ). Other parameters according to Tab. 4.

only in presence of a high CO mass transport resistance<sup>16</sup>. By comparing the transport equations for CO oxidation (in the absence of  $H_2$ ) in RDE and PEMFC experiments, this value can be related to an equivalent PEMFC inlet feed flow rate.

With  $k_{H_2,ad} = 0$ , it also follows that  $F^{out} = F^{in}$  (Eq. (47)) and when entering the CO adsorption rate (Tab.2) into Eq. (46), one ends up with:

$$\frac{x_{CO}^{an}}{x_{CO}^{in}} = \left\{ 1 + \frac{RTA}{F^{in}} k_{CO,ad} \theta_0 \right\}^{-1}. \quad (60)$$

<sup>16</sup>Indeed, also the model shows that, beyond a certain critical flow rate in the order of  $10^3 \text{ sccm cm}^{-2}$ , the bistability disappears.

For RDEs in liquid electrolytes a completely equivalent expression for the CO concentration at the double layer  $c_{\text{CO}}^{\text{dl}}$  can be derived [127,129]:

$$\frac{c_{\text{CO}}^{\text{dl}}}{c_{\text{CO}}^{\text{bulk}}} = \left\{ 1 + \frac{1000S_{\text{tot}}\delta}{D_{\text{CO}}}k_{\text{ads,CO}}\theta_0 \right\}^{-1}. \quad (61)$$

where  $S_{\text{tot}}$ ,  $\delta$ ,  $D_{\text{CO}}$  stand for the active area, the thickness of the Nernst diffusion layer and the diffusion coefficient of CO in the liquid electrolyte, respectively. Parameter values were given in [127] and represent a high rotation speed scenario with  $\delta = 10^{-4}$  m ( $28 \cdot 10^3$  rpm). However, as for RDEs  $\delta$  depends on the square root of the angular rotation frequency, the equivalent  $\delta$  from the study of Koper [129] is  $\delta_{\text{K}} = 4.2 \cdot 10^{-4}$  m.

Evidently, the influence of transport in the PEMFC environment (Eq. (60)) can be compared with an RDE environment (Eq. (61)) if  $\theta_0$  is comparable in both cases. Assuming the two right terms in the braces of Eqs. (60)-(61) to be identical, the flux fed into the inlet of the PEMFC  $F^{\text{in}}/A$  need to be as low as  $1.2 \text{ sccm cm}^{-2}$  in order to match the RDE scenario (applying  $\delta_{\text{K}}$ ). Consequently, the experiment should be designed in a way that such small feed flow rates are available.

## 2.3 H<sub>2</sub>,CO Oxidation in an Homogeneous PEMFC - Experiments

The previous section provided a detailed theoretical insight into the homogeneous electrochemical H<sub>2</sub>, CO oxidation in a PEMFC and proposed specific predictions that are experimentally investigated in the present section. The features predicted for N<sub>2</sub>, CO oxidation are: 1) an S-NDR induced hysteresis under potentiostatic control and low feed flow rates that vanishes for increasing feed flow rate and 2) oscillations due to the S-NDR during galvanostatic control. Oppositely, the features predicted for H<sub>2</sub>, CO oxidation are 3) an S-NDR induced hysteresis under strict potentiostatic control and 4) oscillations under galvanostatic operation caused by the HN-NDR.

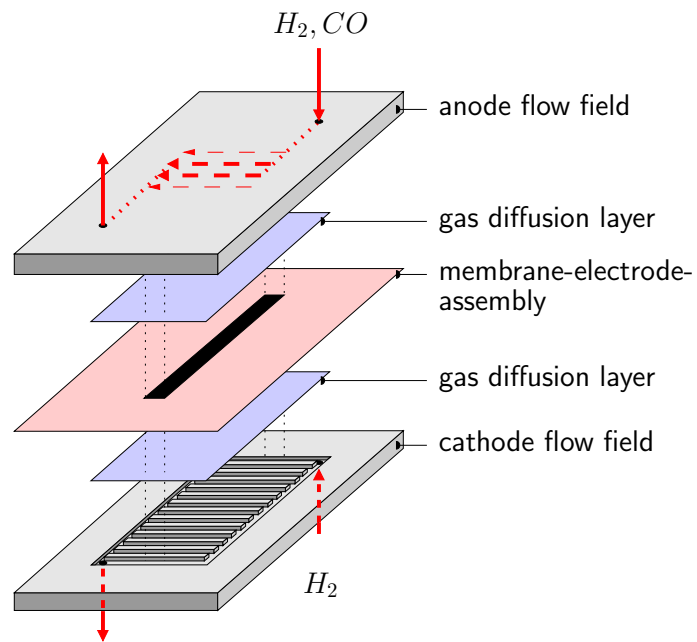
Initially, the experimental procedure and the data preparation are depicted. Afterwards, experiments are carried out to investigate the predictions one after the other.

### 2.3.1 Experimental

A MEA was prepared by spraying both sides of a Nafion 117 polymer membrane with catalytic ink. The ink for the working electrode (WE) was a mixture of 90% Ru/Pt(1:1), purchased from Alfa Aesar, in addition to 10 %wt of Nafion solved in Millipore Water. The ink for the counter electrode (CE) contained pure Platinum but was equivalent in any other respect. The deposited catalyst layers had the dimensions of 1.6 mm · 63 mm resulting in an active area of 1 cm<sup>2</sup>. For a schematic representation of the design, see Fig.16. Although the target was to achieve a Pt loading of 1 mg cm<sup>-2</sup>, it was technically impossible to confirm it. The stripe like catalytic region was chosen in order to avoid effects related to concentration profiles [130] and to approximate the spatially lumped model investigated in the previous sections (as long as the total current is small compared to the Faradaic limit current).

The MEA was then sandwiched between two gas diffusion layers (GDL), followed by two flow field plates with parallel channel configuration. The GDLs consisted of Toray papers (TGP-H-60) treated with PTFE (20%wt PTFE in the Toray paper). The graphite flow field plates contained 21 parallel flow channels. The channels had a width of 1.5 mm, a depth of 2 mm, and 2 mm ribs for distributing the gases. Gold electroplated copper plates were attached to the flow field plates in order to provide the required electrical connection. The cell was braced together by stainless steel plates fixed by 12 screws with a torque of 7 Nm.

Figure 16: Sketch of the differential PEMFC design. Any effects related to concentration profiles in the direction along the flow channel are minimized with the help of the stripe-like catalytic region.



Newly fabricated PEMFCs with low catalyst loading do not reach their best performance directly after assembly. According to Qi et al. [131], the hydration level of the membrane, proton conduction channels and the porosity in the catalyst layer increase during the initial operation. Therefore, the cell was conditioned with the help of a simple dedicated test-stand. The gas flow rates were controlled with rotameters and the gases were humidified with the help of bubbler bottles. To withdraw the current, an external load from STATRON was used. Multimeters were used to monitor both the current and the voltage. During the conditioning process the method of Himanen et al. [132] was followed: The anode of the cell was fed with  $H_2$  in stoichiometric excess while the cathode was fed with  $O_2$  in stoichiometric excess. The cell was operated at 50 mA for 4 hours. Subsequently, the anode and cathode were reversed, after being flushed with  $N_2$  and the cell was left to operate at  $50 \text{ mA cm}^{-2}$  for another 4 hours. Then the current was increased in steps of  $50 \text{ mA cm}^{-2}$  with duration of 20 minutes, after which the corresponding voltage was recorded. This procedure was repeated three times. Afterwards, the cell performance and the polarization curve were reproducible.

A self-made test-stand was specifically designed for the measurements. Premixed  $N_2(5.0)/CO(2.0)$  (1% CO) for the WE in addition to  $H_2$  (5.0) and  $N_2$  (5.0) for the CE were purchased from WEST-FALEN AG. In order to control the flow rates of the gas streams, two mass flow controllers from BRONKHORST were used. They were calibrated in order to provide as low flow rates as  $0.5 - 20 \text{ ml min}^{-1}$ . With the help of an additional rotameter for supplying  $N_2$ , a mixture of 10%  $H_2$  in  $N_2$  was fixed for the CE in order to minimize  $H_2$  diffusion towards the WE. Membrane humidifiers from POMA PURE were applied to set up a dew point temperature of  $32^\circ\text{C}$ . With heated tubes the gas temperatures were increased to  $42^\circ\text{C}$ , in order to avoid condensation in the attached gas lines. Two dew point mirrors from Michell, fixed just before the inlets of the cell, provided an online control of the proper humidification level. The temperature of the fuel cell was controlled by another heating hose to be  $37^\circ\text{C}$ . Electrochemical measurements were recorded with a "Zahner IM6" potentiostat.

As three electrode arrangements in a PEMFC environment are not straight forward to implement and as the hydrogen evolution reaction is fast, a counter electrode forming only  $H_2$  is considered to be free of losses and is therefore also a reasonable reference electrode. However, the double layer potential of such a CE can only be considered to be stable as long as the hydrogen partial pressure is



stable. Therefore, during operation, the CE hydrogen partial pressure should not be too low (otherwise  $H_2$  production would change the partial pressure), but it should be as low as possible to avoid  $H_2$  diffusion to the WE as mentioned above. The present configuration of the CE was determined to be almost free of  $H_2$  diffusion.

As the present CE was operated with 10% hydrogen instead of usual 100% (which would refer to a conventional dynamic hydrogen electrode (DHE)), the CE needs to be electrochemically characterized in order to give the reader a conventional reference potential at hand. For this purpose 100% hydrogen were supplied to the WE and the open circuit voltage (ocv) of that configuration was measured to be  $-31$  mV, which is in full agreement with the Nernst equation for the given two electrode setup. For presentation the measured cell voltage  $U$  is given with respect to the DHE:

$$U_{\text{DHE}} = U + 0.031\text{V}. \quad (62)$$

Additionally, the CE was not perfectly stable during the course of time due to contaminations. Indeed, cell voltage scans to  $-800$  mV<sup>17</sup>, carried out after a few hours at ocv, showed the initial oxidation of surface contaminations evident by the release of a blockage in the reverse scan. Unfortunately, the source of contamination could not be identified. As during the voltage reversal  $H_2$  is pumped to the WE which then need to be removed by diffusion through the gas diffusion layer and subsequent convective drag out of the compartment, experiments can only start once a certain time has passed. Therefore, the experiments were always carried out in the following way:

First, the cell voltage was held at about  $-800$  mV for a 1 – 2 seconds. Afterwards the cell was left at ocv for at least 15 minutes, such that initially an equilibrium with a well-established CO coverage (see e.g. [133]) at the WE was guaranteed. Then the experiments were started.

### 2.3.2 Results and Discussion

In the previous section, it was shown that an S-NDR related bistability is expected during strict potentiostatic operation with  $N_2, CO$  mixtures around the onset overvoltage of CO oxidation. For galvanostatic control, oscillations around the NDR branch are predicted for the parameter values used. Furthermore, as seen in the previous paragraph, the S-NDR should disappear beyond a certain critical flow rate which was in the range of  $1$  sccm  $\text{cm}^{-2}$ . The role of  $H_2$  was found to be diverse. On the one hand, during strict potentiostatic control,  $H_2$  should act only as an indicator for the surface state. On the other hand, a new mechanistic phenomenon, the oscillations related to the HN-NDR instability, are predicted for galvanostatic control. In this section these predictions should be studied one by one.

Therefore, different experiments for the electrochemical CO oxidation (1 % in  $N_2$ ) have been carried out. First, the influence of the voltage scan rate at the lowest possible feed flow rate is investigated (Fig. 17a) in order to test for the S-NDR related hysteresis. Subsequently, galvanostatic scans at the same conditions are discussed (Fig. 17b). Later, the influence of the feed flow rate at a fixed scan rate is studied (Fig. 18). Finally, also the impact of  $H_2$  is considered briefly (Fig. 19).

#### *$N_2, CO$ : "Strict" Potentiostatic Control*

If not stated otherwise, the lower voltage of the cyclic voltammograms (CVs) is  $0.38 V_{\text{DHE}}$  while the

<sup>17</sup>For applied cell voltages smaller than the ocv, hydrogen evolution takes place at the WE, while hydrogen is consumed at the CE. Therefore, in this case, the overvoltage of the CE is scanned and the WE acts (somehow) as a DHE.

upper limit is  $0.66 V_{\text{DHE}}$ . For each specific CV experiment three cycles were recorded in order to overcome initial transients. Always, only the third cycle is presented.

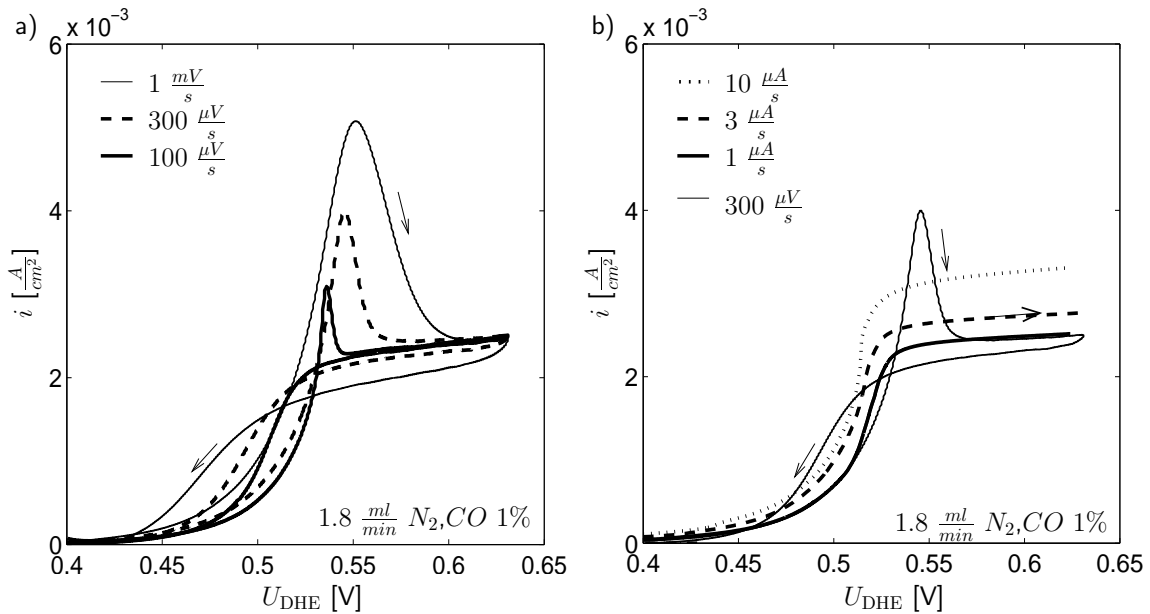


Figure 17: Experimental results of CO oxidation at  $37^\circ\text{C}$  in a PEMFC with differential design.  $\text{H}_2$  is absent. a: The influence of the voltage scan rate at smallest possible feed flow rate; b: The influence of the current scan rate at smallest possible feed flow rate.

Starting with Fig. 17a at the lowest sweep rate<sup>18</sup> of  $100 \mu\text{V s}^{-1}$ , the current in the forward scan is negligible until about  $0.5 V_{\text{DHE}}$ . Afterwards, a steep current growth can be seen, followed by a peak attributed to an avalanche-like oxidation of the CO adsorption layer and the consumption of the CO in the anode compartment. As soon as the CO adsorption layer is oxidized the current stabilizes at the Faradaic limit current (according to Eq. (44)). In the reverse scan the overshoot is absent and the voltage begins to fall steeply at approximately  $0.54 V_{\text{DHE}}$  until the current levels completely off. In comparison this onset voltage has been found in RDE experiments of Gasteiger et al. to be at about  $0.6 V_{\text{RHE}}$  at  $25^\circ\text{C}$  (Fig. 5 in [47]) and about  $0.5 V_{\text{RHE}}$  at  $62^\circ\text{C}$  (Fig. 5 in [134]). Extrapolating in a linear fashion to  $37^\circ\text{C}$  the onset voltage of  $530 \text{ mV}_{\text{RHE}}$  is in reasonable agreement with the present study ( $\approx 500 \text{ mV}_{\text{DHE}}$ ). The hysteresis between  $0.54 V_{\text{DHE}}$  and  $0.57 V_{\text{DHE}}$  is the typical fingerprint of the S-NDR known from RDE and related experiments ([47, 129, 135] and [136]), yielding an active and a passive state at the same voltage. However, remembering that the bistability is a steady state phenomenon, it is worth noting that twice during the course along a cycle the system is not in quasi steady state even if the scan rate is as low as here (It takes about 20 minutes to slip over  $100 \text{ mV}$ !). With the help of faster voltage scans these situations can be investigated.

The first situation in which the state is not quasi steady occurs during (and a bit prior to) the current overshoot in the forward scan. From the consideration of the steady states of the model system (Fig. 15), in this period the CO coverage jumps from almost 1 to almost 0. The CO coverage

<sup>18</sup>At even slower scan rates the hysteresis disappeared and the high current state also showed some noise-like behavior. We attribute the effects to either the formation of unspecific catalyst oxides and/or the influence of altering experimental conditions.



finally reaches steady state again once the current plateau is arrived. In agreement, Fig. 17a shows, that the overshoot is remarkably lowered when applying smaller voltage scan rates.

The second situation in which the state is not steady occurs during the slow decay of the current in the backward scan below  $0.53 V_{\text{DHE}}$ . From the consideration of the steady states of the model system (Fig. 15c), in this period the CO coverage increases from almost 0 to almost 1. CO oxidation, leading to large current densities in the active state, slowly decreases as more CO adsorbs to the surface than water dissociates in a given time. This implies that the slope of the decay increases with decreasing voltage sweep rate as more CO is provided in a certain potential window. Nevertheless, the intimate presence of mass transport during CO poisoning compared to the onset of CO oxidation usually leads to a lower slope of the current in the reverse scan ( $0.53 V_{\text{DHE}} \rightarrow 0.50 V_{\text{DHE}}$ ) compared to the slope of the current in the forward scan ( $0.52 V_{\text{DHE}} \rightarrow 0.57 V_{\text{DHE}}$ ) [47, 129, 134–137]. Therefore, it is interesting to note, that this trend is not reflected here.

Even for a scan rate as low as  $100 \mu\text{Vs}^{-1}$  the current at the onset of CO oxidation in the forward scan does not yield “infinite” slope as expected for very slow scan rates (compare with Fig. 15d). In studies applying a liquid electrolyte much larger slopes at the onset of the CO oxidation are obtained with scan rates as high as  $20 \text{mV s}^{-1}$  [129, 137]! To elucidate the origin of the slow process, hindering the straight onset of CO oxidation, [137] should be taken into account. In their study the authors investigated CO oxidation in a flow cell with a polycrystalline Pt film in sulfuric acid electrolyte and found a much steeper onset of CO oxidation. As it seems unlikely that the reaction kinetics change dramatically when changing from sulfuric acid electrolyte to a wet Nafion membrane, the responsible difference is likely to be found in the mass transport processes. The following paragraphs on estimated characteristic time constants might help to identify the responsible process. A candidate process should elapse in the range of 10 minutes, which is the time needed to scan over  $50 \text{mV}$  (the potential distance between the onset of CO oxidation and the point when the Faradaic limit is crossed first) with the slowest applied scan rate.

Firstly, it is evident that almost all the CO, consumed during the onset of CO oxidation, was surface bound, because the amount of CO in the gas compartment as well as in the feed are comparatively small. Additionally, the time needed to equilibrate a compartment of the given dimension by diffusion is in the order of ten milliseconds ( $D = 10^{-4} \text{m}^2 \text{s}^{-1}$  [138]). Therefore, the amount of CO which is in the gas phase would after consumption of the mono-layer be supplied too quickly to explain the smooth CO oxidation onset. There is also no lack of water (the oxygen source). Even under disregard of the membrane storage,  $10 \text{s}$  of gas feed are sufficient to account for the demand during the transition from passive to active state. In summary, transport in the gas phase seem to be too fast to explain the shallow CO oxidation onset. Therefore, an alternative explanation needs to take into account the electrode surface itself.

Surely, a uniform oxidation of the CO mono-layer (as in liquid electrolytes) would only take place if all the surface bound CO is situated in an electrochemically active region. However, in PEMFC the active region is restricted to the three phase boundary, dividing the electrode into active and inactive areas. CO, bound in inactive areas, needs either to hop along the catalyst (and also between particles) or it needs to perform a desorption-adsorption random walk to find a reactive spot.

The time constant of CO desorption can be estimated from the recovery of a  $\text{H}_2$  oxidation current at a fixed cell voltage of a PEMFC after transient CO exposure. It lies in the range of  $10 - 20 \text{mins}$  (e.g. [100, 139]) and is therefore in the region of interest. However, if desorption and re-adsorption of CO is the dominant CO transport mechanism, the surface transport should not contribute a lot. For

the surface diffusion of CO a value of  $3.6 \cdot 10^{-17} \text{ m}^2 \text{ s}^{-1}$  was reported by Kobayashi et al. [140] for 7 nm Pt particles. Accordingly, the time constant for surface diffusion on the length scale of such a particle lies in the range of 0.1 seconds. But interestingly also a strong dependence of the CO surface diffusion coefficient on the particle diameter was reported [141], such that particles of 1.7 nm size show a CO surface diffusivity about three to four orders smaller compared to the 7 nm particles. Accordingly, the time constant slides into the range of 100 seconds ( $(1.7 \cdot 10^{-9})^2 \text{ m}^2 / 7 \cdot 10^{-21} \text{ m}^2 \text{ s}^{-1}$  [141]). Hopping of CO between particles would further prolong the process. Therefore, in a chain of inactive catalyst particles, especially smaller particles could act as CO collectors which in turn might build the reservoir we are looking for.

#### *N<sub>2</sub>, CO: Galvanostatic Control*

Galvanostatic scans from low to high currents were carried out at the same conditions as the prior experiments (gas composition and inlet flow rate, Fig. 17b) in order to compare the experimental behavior of the system with its theoretical prediction (Fig. 15b). For matching CVs and galvanostatic scans the CV with the intermediate scan rate is given at hand.

The galvanostatic scans follow the potentiostatic forward scan up to the Faradaic limit, but at highest currents the overshoot is absent and replaced instead by a monotonically increasing curve. As the oxidation of the CO adsorption layer is a dynamic transition effect, the galvanostatic scans coincide the better with the Faradaic limit the slower the scan rate is.

However, the main conclusion from Fig. 17b is, that no NDR (and related oscillations) is revealed. At currents close to the Faradaic limit the slope of the polarization curve becomes almost infinite but does not show an NDR and therefore does not agree with the model predictions from the lumped model (Fig. 15b). However, it was found earlier experimentally that the spatially extended system undergoes a domain instability (which cannot be covered by our spatially lumped model) [142], partially even with a simultaneous formation of CO micro islands [136]. In both cases the available surface area is split into active and a passive regions (only on different length scales). As the differential design chosen for the present experiments cannot avoid such intrinsic mechanistic phenomena, such spatial inhomogeneities are likely to occur. Nevertheless, this argument can only be sufficiently discussed in the scope of spatially resolved measurements which are not the objective of the present study.

#### *N<sub>2</sub>, CO: The Influence of the Feed Flow Rate*

The influence of the volumetric inlet flow rate is presented in Fig. 18. As can be seen, the Faradaic limit increases with the feed flow rate. The peak related to the oxidation of the CO mono-layer and the CO from the compartment diminishes with the larger feed flow rates. At highest feed flow rate even a second slope appears far beneath the Faradaic limit ( $U_{\text{DHE}} > 0.6 \text{ V}$  for  $F_{\text{in}} = 20.1 \text{ ml min}^{-1}$ ), showing that the stripping current is superimposed by the current from continuous CO oxidation. The decay of the width of the bistable region with increasing CO transport, as found in RDE experiments (Fig. 5 in [47], Fig. 4 in [129]), is not significant here.

#### *N<sub>2</sub>, H<sub>2</sub>, CO: The Influence of Hydrogen*

Finally, the impact of a small H<sub>2</sub> feed is studied, while the feed flow rate of the N<sub>2</sub>, CO mixture is kept

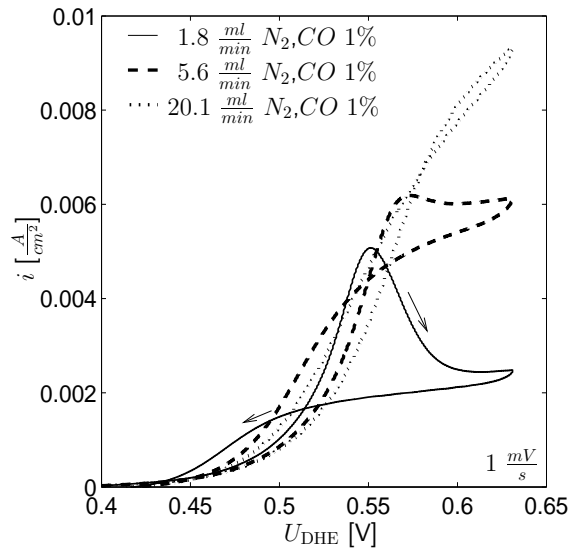


Figure 18: Experimental results for potentiostatic electrochemical CO oxidation at 37°C in a PEMFC with differential design for different feed flow rates.  $H_2$  is absent.

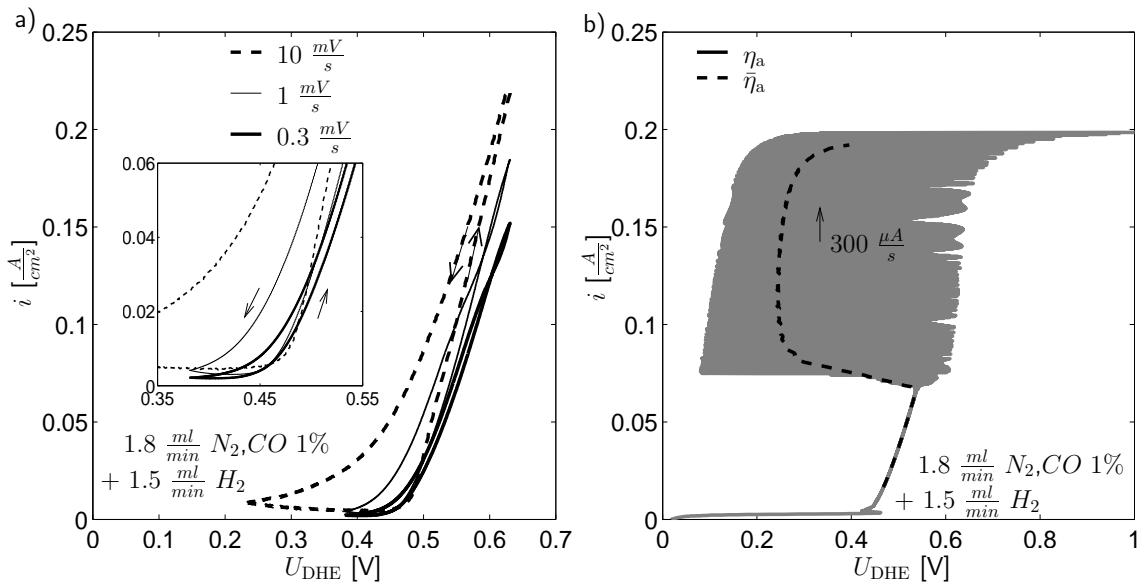


Figure 19: Experimental results for the electrochemical  $H_2, CO$  oxidation at 37°C in a PEMFC with differential design. a: The influence of the voltage scan rate; b: Cell voltage oscillations during a current scan.

constant. In this way, a rather smooth transition between the  $N_2, CO$  system and the  $H_2, CO$  system is carried out. Fig. 19a shows three CVs at different scan rates for a  $N_2, H_2, CO$  mixture. As can be seen from the fastest CV, the forward scan shows an almost linear increase as soon as the onset voltage of CO oxidation is reached. This growth proceeds up to the voltage turning point. Oppositely, in the reverse scan a steep decrease of the current can be seen. The fact, that the backward scan lies always higher than the forward scan, indicates, that also under these conditions ongoing CO oxidation is present. However, by lowering the scan rate to  $1 \text{ mV s}^{-1}$  the hysteresis almost vanishes and totally disappears at even slower scan rates. In other words, when applying  $H_2$  to the  $N_2, CO$  PEMFC system the S-NDR is lost. The reason can be rationalized as follows:

At highest currents considerable voltage losses are related to the CE and the electrolyte. As the currents were small for pure  $CO$  oxidation these losses were negligible. However, as soon as  $H_2$  is applied they become essential. (The losses of the electrolyte and the counter electrode are approximately 30 mV at 200 mA as found from electrochemical impedance spectra.) As was discussed earlier, the main impact of  $H_2$  is to act as an indicator of the surface state. The active state of the system is therefore characterized by a large current, while in the passive state the current is small. As losses shift the polarization curve at high currents towards more positive voltages, the S-NDR branch resulting from  $\eta_a$  is unfolded in the polarization curve, the S-NDR is lost.

The galvanostatic scan, Fig. 19b, follows the CV up to a (supercritical) Hopf bifurcation point at which oscillations set in ( $65 \text{ mA cm}^{-2}$ ). The amplitude of approximately 550 – 600 mV is almost independent of the applied current. The mean voltage, obtained by temporally averaging the time series, depicts the advantage (in terms of PEMFC  $CO$ -tolerance mentioned by [3]) of the galvanostatic control compared to potentiostatic control as the losses related to the presence of  $CO$  are lowered. The kinks in the envelope of the oscillatory regime have no meaning as they are related to the sampling frequency of the time series. As soon as the Faradaic limit is reached, the oscillations die out and the cell voltage shifts towards "infinite" values. As the oscillations are unique for the presence of  $H_2$  and as the S-NDR branch did not show oscillations in the earlier  $N_2, CO$  experiments (Fig. 17b), the underlying mechanism is probably the HN-NDR mechanism as discussed in the theoretical section. Remembering the galvanostatic scans without  $H_2$  and assuming that spatial patterns form also in presence of  $H_2$  it might be interesting to study  $H_2, CO$  oxidation under galvanostatic conditions with a spatially resolved technique.

## 2.4 Summary

In the present chapter the homogeneous electrochemical  $H_2, CO$  oxidation in a low temperature PEMFC was studied with the help of a mathematical model and experiments performed in a differential fuel cell. The scope was to understand the fundamental nonlinearities while classifying the system according to the scheme suggested by Krischer [121] and introduced in section 2.1. Thereby, also a discrepancy was intended to be resolved: While Zhang and Datta classified the system to be of HN-NDR type [101], the conclusion of Siegmeier et al., for homogeneous electrochemical  $H_2, CO$  oxidation in an RDE setup, was that it would be a hybrid of S-NDR and HN-NDR [125].

Initially, a reduced model for homogeneous electrochemical  $H_2, CO$  oxidation was synthesized based on the full model of Zhang and Datta [2] and the model reduction suggested by Hanke-Rauschenbach [110]. The advantage of the reduced model is, that it contains only two variables. It can therefore be dissected straight forward by means of a phase space analysis. It is also suited well for numerical evaluation as it does not contain any implicit equations. By heuristic arguments, the reduced model was shown to be applicable in the relevant parameter region.

In the model analysis, it was found that the steady state Faradaic current curve possesses S-shape as long as the feed flow rate of the fuel gas is sufficiently low. The autocatalytic feedback loop of the  $CO$  coverage, at the NDR branch, is caused by the fact that a decreasing  $CO$  coverage leads to an increasing  $CO$  oxidation rate (because of increasing  $OH$  formation at the free sites  $\Rightarrow \frac{\partial k}{\partial x} < 0$ , see Eq. (33)) and the circumstance that the adsorption rate cannot counterbalance the resulting decrease in  $CO$  surface coverage.

However, in the model analysis it was also found that there exists a second autocatalytic mechanism leading to N-NDR related oscillations. The related autocatalytic feedback loop of the overvoltage stems from the potential dependence of the  $OH$ -formation: An increase in overvoltage will, at the NDR branch of the “N”, lead to a decreasing  $H_2$  oxidation rate ( $\frac{\partial k}{\partial \Delta \varphi_a} < 0$ , see Eq. (29)). But the N-NDR is hidden because of the slow dynamics of the  $CO$  coverage, such that the N-NDR cannot be seen in the steady state curve. Instead, the S-NDR appears. Ultimately, the system can therefore (in full agreement with [125]) be classified as an S-NDR/HN-NDR hybrid.

With the insight obtained in the model analysis, it was possible to design experiments in order to specifically investigate the S-NDR — the yet unproven characteristic — in a PEMFC. Namely, a test-stand was assembled that allows to apply very small feed flow rates. During slow potentiostatic scans and in the absence of  $H_2$  a hysteresis was found. The hysteresis appeared in the potential interval in which water starts to dissociate and is very indicative for the presence of the predicted S-NDR. Galvanostatic scans in the absence of  $H_2$  did not reveal the S-shape, but likely, a spatial instability [136, 142] is responsible for that. In final experiments, the bistability under potentiostatic control disappeared in the presence of  $H_2$ . This behavior can be rationalized accordingly: While the addition of  $H_2$  blows up the Faradaic current curve, the overvoltage interval of the S-related NDR remains constant. Both effects, in combination, lead to a strong decrease of the slope of the NDR branch and as the load line slope is unchanged, the bistable region vanishes. Nevertheless, note that, although the measured polarization curve does not reveal the bistability, the Faradaic current curve still possesses the S-NDR.



### 3 $H_2, CO$ Oxidation in a PEMFC: The Inhomogeneous System

As oscillations and bistability require only a few degrees of freedom they are the simplest manifestations of nonlinear dynamics and occur in homogeneous systems. In a theoretical sense, it can be imagined that the same phenomena also occur at each microscopic reaction site in inhomogeneous electrochemical systems [143]. Qualitatively new phenomena then arise due to the interaction between the differential sites. These phenomena comprise pulses, spirals, fronts, standing waves, synchronized oscillations, space-time chaos and others [115–118, 144, 145], which are shortly referred to as patterns. The most prominent pattern in chemical systems are the so-called Turing structures - stationary, spatially ordered, concentration profiles which are caused by diffusion [146].

Oppositely, in electrochemical systems the most important interactions arise not from species diffusion but due to electric “migration currents” and “mean-field-induced currents”. Mostly, the interactions are just referred to as migration coupling and mean-field coupling. Mean-field coupling arises due to the presence of an external circuit. It describes a global feedback by which any differential system has the same influence on any other. Migration coupling is caused by the charge neutrality of the electrolyte and its range depends (opposite to mean-field coupling) on the electrolyte dimensions [147]. Given a thin but large-area electrolyte, migration coupling acts purely local. In oscillatory systems, both couplings can act synchronizing or desynchronizing, depending, for example, on the algebraic sign of the coupling terms [121]. While synchronization leads to the entrainment of the oscillator frequencies and their phases, desynchronization can cause spatio-temporal turbulence - a scenario in which the local oscillations are characterized by the absence of distinct oscillations frequencies. Spatio-temporal turbulence in an electrochemical system was recently found for the first time [46, 148, 149] and it will be one aspect of this chapter to investigate whether spatio-temporal turbulence can occur during the electrochemical  $H_2, CO$  oxidation in a PEMFC, too.

Generally, during the electrochemical  $H_2, CO$  oxidation in PEMFCs, the  $CO$  concentration at the cell outlet differs from the inlet concentration [150]. Therefore, apart from the two electric coupling terms, a third interaction between reaction sites, caused by the along-the-channel  $CO$  transport, influences the PEMFC system. Yet, the influence of species-transport-along-the-electrode on pattern formation has never been studied, because bulk concentration gradients are unimportant in conventional electrochemical systems. But aperiodic oscillations, that were recently found during the electrochemical  $H_2, CO$  oxidation in a PEMFC, could not be reproduced with a homogeneous model [106, 107]. It will be another aspect in the following chapter to show that the  $CO$  transport can cause (such) aperiodic behavior.

The proceeding in this chapter is chosen to serve three major aims. But before following these aims in the subsections 3.2-3.4, initially, in Sec. 3.1, the impact of the electric field distribution in a PEMFC and the electric circuitry are analyzed in order to depict the origin of the migration coupling and the mean-field coupling. Then, in Sec. 3.2, the first aim is the presentation of a compact overview of patterns that frequently occur in nonlinear electrochemical systems. The importance of this overview lies in the development of an a priori insight and the formulation of a certain pattern-expectation in the considered system. Afterwards, in Sec. 3.3, the second aim is the analysis of a model for the electrochemical  $H_2, CO$  oxidation in an idealized one-dimensional PEMFC (plus sandwich coordinate) under oscillatory galvanostatic control. Qualitatively different patterns are identified. Finally, in Sec. 3.4, the third aim is the presentation of experimental results of pattern formation in a specially



designed PEMFC. Thereby, for the first time, the measurement of the spatial current distribution (via a printed circuit board) is shown to be an applicable tool for the investigation of pattern formation in electrochemical systems. The chapter is finished with a summary of theoretical- and experimental results in Sec. 3.5.

### 3.1 The Role of the Electric Field

The purpose of this section is to derive specific partial differential equations (PDEs) which describe the evolution of the double layer voltages in a PEMFC. The related improvement in transparency leads to an altered understanding of a fuel cell, namely as being composed of local dynamical systems that interact via migration currents and the mean-field currents induced by the external circuit. The results presented below were preliminary published by the author in [151].

Fig. 20 sketches the idealized PEMFC under consideration. The system consists of an electrolyte, the two electrochemical double layers and an embedding electrical control circuit. During the following derivation these three preconditions need to hold: 1) The system can be considered as two-dimensional (the in-plane direction perpendicular to the gas flow direction is assumed to be homogeneous). 2) The conductivity of the membrane is constant in time and space. 3) The dimensions of the electrolyte are such that  $d_m \ll L$ .

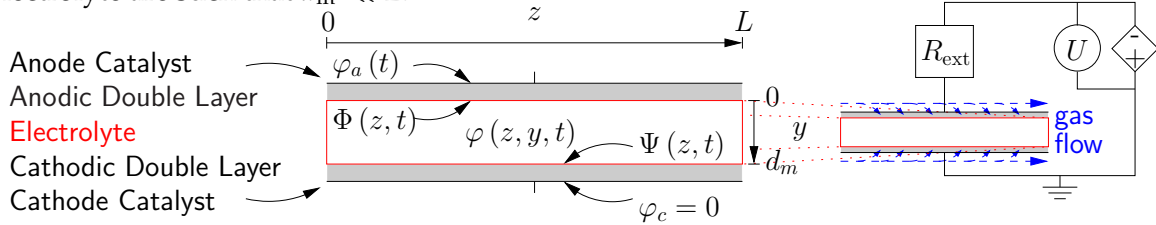


Figure 20: The electric setup of the considered “one dimensional” PEMFC system together with the used abbreviations. Note that for an infinite external resistance ( $R_{\text{ext}} \rightarrow \infty$ ) the operation mode switches from potentiostatic to galvanostatic control when the ratio  $I_{\text{load}} = U/R_{\text{ext}}$  is held constant.

The derivation starts by solving the potential field in the electrolyte and proceeds via the approximation of the current that passes from the electrolyte into the double layer. Afterwards, an equation for the external electric circuit is solved explicitly and entered into the double layer equations to obtain the general result. At the very end some limiting cases are considered to derive the formulas that are needed in the course of this chapter.

#### Analytical Solution for the Charge Transport in the Electrolyte

The distribution of the electric field in an isotropic, two-dimensional electrolyte is given by the Laplace equation and the related boundary conditions

$$\kappa \frac{\partial^2 \varphi}{\partial y^2} + \kappa \frac{\partial^2 \varphi}{\partial z^2} = 0 \quad (\text{Laplace equation}), \quad (63)$$

$$\frac{\partial \varphi}{\partial z} \Big|_{z=0} = \frac{\partial \varphi}{\partial z} \Big|_{z=L} = 0 \quad (\text{left and right boundary condition}), \quad (64)$$

$$\varphi|_{y=0} = \phi(z, t) \quad (\text{boundary condition at top}), \quad (65)$$

$$\varphi|_{y=d_m} = \psi(z, t) \quad (\text{boundary condition at bottom}), \quad (66)$$

whereby  $\kappa$  is the membrane conductivity. Equation (63) is linear and can be solved with the help of a separation ansatz followed by a Fourier series approach for the two remaining ODEs. Incorporating



then the boundary conditions (Eqs. (64)-(66)) one finds the following solution for the potential field in the electrolyte  $\varphi(y, z, t)$

$$\varphi(y, z, t) = \phi_0 - (\phi_0 - \psi_0) \frac{y}{d_m} + 2 \sum_{n=1}^{\infty} \cos\left(\frac{n\pi z}{L}\right) \left( \phi_n A_n + \psi_n \cosh\left(\frac{n\pi d_m}{L}\right) (B_n - A_n) \right), \quad (67)$$

with  $A_n$  and  $B_n$  being the functions

$$A_n(y) = \frac{\sinh\left(\frac{n\pi}{L}(d_m - y)\right)}{\sinh\left(\frac{n\pi d_m}{L}\right)} \quad \text{and} \quad B_n(y) = \frac{\cosh\left(\frac{n\pi}{L}(d_m - y)\right)}{\cosh\left(\frac{n\pi d_m}{L}\right)}. \quad (68)$$

The set of variables  $\phi_n$  and  $\psi_n$  represent the real Fourier transforms of the related boundary condition,  $\phi(z, t)$  and  $\psi(z, t)$ , at frequency  $\frac{n\pi d_m}{L}$

$$\phi_n(t) = \frac{1}{L} \int_0^L \phi(z, t) \cos\left(\frac{n\pi z}{L}\right) dz \quad \text{and} \quad \psi_n(t) = \frac{1}{L} \int_0^L \psi(z, t) \cos\left(\frac{n\pi z}{L}\right) dz. \quad (69)$$

Evaluating Eq. (67) at the anode and at the cathode boundary, the potential follows to be

$$\varphi(z, t)|_{y=0} = \phi_0 + 2 \sum_{n=1}^{\infty} \cos\left(\frac{n\pi z}{L}\right) \phi_n \quad \text{at the anode,} \quad (70)$$

$$\varphi(z, t)|_{y=d_m} = \psi_0 + 2 \sum_{n=1}^{\infty} \cos\left(\frac{n\pi z}{L}\right) \psi_n \quad \text{at the cathode,} \quad (71)$$

which is (of course) the Fourier representation of the boundary conditions.

Finally, two expressions are introduced which are needed below. The first equation (72) describes the current (density) that penetrates the electrolyte from the anode side

$$-\kappa \frac{\partial \varphi}{\partial y} \Big|_{y=0} = -\kappa \left( \frac{\psi - \phi}{d_m} + \frac{d_m}{3} \frac{\partial^2 \phi}{\partial z^2} + \frac{d_m}{6} \frac{\partial^2 \psi}{\partial z^2} \right). \quad (72)$$

The derivation of Eq. (72) can be found in appendix B. Here, it might be sufficient to notice that the derivation bases on the approximation of some hyperbolic functions (that appear during the derivation of  $\frac{\partial \varphi}{\partial y} \Big|_{y=0}$ ) with a Laurent series under the assumption that  $d_m \ll L$ . When the definition of the double layer voltages is implied into Eq. (72)

$$\Delta \varphi_a(z, t) = \varphi_a(t) - \phi(z, t), \quad (73)$$

$$\Delta \varphi_c(z, t) = \varphi_c(t) - \psi(z, t) = -\psi(z, t), \quad (74)$$

whereby the arbitrary “zero-potential” was defined to be at the counter electrode current collector, Eq. (72) can be brought into its final shape

$$-\kappa \frac{\partial \varphi}{\partial y} \Big|_{y=0} = -\kappa \left( \frac{\Delta \varphi_a - \Delta \varphi_c}{d_m} - \frac{\varphi_a}{d_m} + \frac{d_m}{3} \frac{\partial^2 \Delta \varphi_a}{\partial z^2} + \frac{d_m}{6} \frac{\partial^2 \Delta \varphi_c}{\partial z^2} \right). \quad (75)$$

The second expression yields the total current  $I$  per surface area of the electrolyte  $A$  ( $A = L \cdot b$ ,  $b$  is the width of the cell in the dimension which is disregarded in Fig. 20). It follows from integrating Eq. (75)

$$-\kappa \frac{1}{L} \int_0^L \frac{\partial \varphi}{\partial y} \Big|_{y=0} dz = \frac{I}{A} = -\kappa \left( \frac{\overline{\Delta \varphi_a} - \overline{\Delta \varphi_c}}{d_m} - \frac{\varphi_a}{d_m} \right). \quad (76)$$

In Eq. (76), the expressions  $\overline{\Delta\varphi_{a,c}}$  stand for the spatially averaged values of the respective double layer voltages

$$\overline{\Delta\varphi_a} = \frac{1}{L} \int_0^L \Delta\varphi_a dz \quad \text{and} \quad \overline{\Delta\varphi_c} = \frac{1}{L} \int_0^L \Delta\varphi_c dz \quad (77)$$

### The Double Layer Voltages

Generally, the equation for the evolution of the anodic double layer voltage  $\Delta\varphi_a$  follows from Kirchhoffs node law of a differential double layer element (as depicted in Fig. 9) and is given by

$$c_{dl,a} \frac{\partial \Delta\varphi_a(z,t)}{\partial t} = -\kappa \frac{\partial \varphi}{\partial y} \Big|_{y=0}(z,t) - i_{F,a}(z,t). \quad (78)$$

Thereby, the parameter  $c_{dl,a}$  represents the specific electric double layer capacity and the function  $i_{F,a}$  is a placeholder for a current density resulting from electrochemical reactions. For the consideration in this subsection this function is not of interest. If Eq. (75) is inserted into Eq. (78), one obtains

$$c_{dl,a} \frac{\partial \Delta\varphi_a}{\partial t} = -\kappa \left( \frac{\Delta\varphi_a - \Delta\varphi_c}{d_m} - \frac{\varphi_a}{d_m} + \frac{d_m}{3} \frac{\partial^2 \Delta\varphi_a}{\partial z^2} + \frac{d_m}{6} \frac{\partial^2 \Delta\varphi_c}{\partial z^2} \right) - i_{F,a}. \quad (79)$$

Yet, only the potential field between the anodic and the cathodic current collector was described. But finally, also the embedding of the cell into the external circuit need be taken into account. The related equation should yield  $\varphi_a$  (the potential of the anodic current collector) as a function of the load voltage, it follows from Kirchhoff's loop law of the overall circuit (Fig. 20)

$$\varphi_a = -U - R_{ext}I, \quad (80)$$

in which  $U$  stands for the potential difference, measured between the cathode current collector and a resistance  $R_{ext}$  connected to the anode (see Fig. 20). Upon replacing  $I$  in Eq. (80) with Eq. (76) one can solve for  $\varphi_a$ . When the obtained expression is used in Eq. (79) one finally obtains the desired equation for the evolution of the anodic double layer voltage

$$c_{dl,a} \frac{\partial \Delta\varphi_a}{\partial t} = -\frac{U + \Delta\varphi_a - \Delta\varphi_c}{A(R_\Omega + R_{ext})} - i_{F,a} + \frac{d_m^2}{6AR_\Omega L^2} \left( 2 \frac{\partial^2 \Delta\varphi_a}{\partial \zeta^2} + \frac{\partial^2 \Delta\varphi_c}{\partial \zeta^2} \right) + \frac{R_{ext}(\overline{\Delta\varphi_a} - \overline{\Delta\varphi_c} - \Delta\varphi_a + \Delta\varphi_c)}{AR_\Omega(R_\Omega + R_{ext})}. \quad (81)$$

In expression (81) the membrane conductivity  $\kappa$  was avoided in favor of the membrane resistance  $R_\Omega = \frac{d_m}{\kappa A}$ . Similarly, the channel coordinate  $z$  was replaced by the dimensionless variable  $\zeta$  ( $\zeta = \frac{z}{L}$ ). The boundary conditions to Eq. (81) read

$$\frac{\partial \Delta\varphi_a}{\partial \zeta} \Big|_{\zeta=0} = \frac{\partial \Delta\varphi_a}{\partial \zeta} \Big|_{\zeta=1} = 0. \quad (82)$$

The same procedure can be also carried out for the cathode double layer. The result for the cathode double layer voltage follows to be

$$-c_{dl,c} \frac{\partial \Delta\varphi_c}{\partial t} = -\frac{U + \Delta\varphi_a - \Delta\varphi_c}{A(R_\Omega + R_{ext})} - i_{F,c} + \frac{d_m^2}{6AR_\Omega L^2} \left( \frac{\partial^2 \Delta\varphi_a}{\partial \zeta^2} + 2 \frac{\partial^2 \Delta\varphi_c}{\partial \zeta^2} \right) + \frac{R_{ext}(\overline{\Delta\varphi_a} - \overline{\Delta\varphi_c} - \Delta\varphi_a + \Delta\varphi_c)}{AR_\Omega(R_\Omega + R_{ext})}, \quad (83)$$

with the boundary conditions

$$\left. \frac{\partial \Delta \varphi_a}{\partial \zeta} \right|_{\zeta=0} = \left. \frac{\partial \Delta \varphi_a}{\partial \zeta} \right|_{\zeta=1} = 0. \quad (84)$$

In equation (83) the parameters  $c_{dl,c}$  and  $i_{F,c}$  stand for the specific electric double layer capacity and the Faradaic current density at the cathode. Please note the high symmetry between the two equations (81) and (83): Apart from the Faradaic reactions, the only differences appear in the factor controlling the diffusion-like coupling term and in the sign of the capacitive current (due to the reverse embedding of the cathodic double layer into the circuit compared to the anodic double layer).

#### *Interpretation and Limiting Cases*

Eqs. (81)-(84) describe the position dependent evolution of the anodic- and cathodic double layer voltages in the idealized PEMFC setup depicted in Fig. 20. While a part of the equations represents the differential system (in absence of gradients the form of the homogeneous system Eq. (36)-(37) is re-obtained), the last two terms at the right hand side describe coupling interactions between neighbored differential systems: The first of these terms looks like a local diffusion interaction but stems from migration coupling in thin electrolytes [147]. The second term represents a positive global mean-field interaction which arises from the (very) fast information transport via the electric field.

The mechanism of the global interaction can be rationalized when assuming a local degradation of the Faradaic current: Such a local current drop will also reduce the global Faradaic current, leading to a voltage drop across the external resistance. But because a constant voltage  $U$  is ensured by the load, the double layer voltage (and membrane voltage drop) will automatically increase everywhere along the electrode. The direct feedback of any differential current perturbation on the control of any other differential system is the heart of the mean-field interaction. Please note that it can be deactivated by reducing the size of the external resistance, leading to a diffusion (migration) dominated system for  $R_{ext} = 0$ .

An important limiting case of the system (81)-(83) follows when the cathode is negligible ( $\Delta \varphi_c \approx 0$ ). The result, following from Eq. (81), is a single PDE for the anodic double layer evolution which is especially worthy when the potentiostatic operation with a  $H_2$ -fed cathode is considered. The expression is used in the following subsections primarily:

$$c_{dl,a} \frac{\partial \Delta \varphi_a}{\partial t} = -\frac{U + \Delta \varphi_a}{A(R_\Omega + R_{ext})} - i_{F,a} + \frac{d_m^2}{3AR_\Omega L^2} \frac{\partial^2 \Delta \varphi_a}{\partial \zeta^2} + \frac{R_{ext}(\overline{\Delta \varphi_a} - \Delta \varphi_a)}{AR_\Omega(R_\Omega + R_{ext})}. \quad (85)$$

Galvanostatic control follows from Eq. (85) in the limit  $R_{ext} \rightarrow \infty$  while keeping  $-U/R_{ext} = I$  constant

$$c_{dl,a} \frac{\partial \Delta \varphi_a}{\partial t} = \frac{I}{A} - i_{F,a} + \frac{d_m^2}{3AR_\Omega L^2} \frac{\partial^2 \Delta \varphi_a}{\partial \zeta^2} + \frac{1}{AR_\Omega} (\overline{\Delta \varphi_a} - \Delta \varphi_a). \quad (86)$$

### 3.2 Nonlinear Dynamics in Inhomogeneous Electrochemical Systems

In appendix A it is shown that the homogeneous electrochemical  $H_2, CO$  oxidation can be well approximated by two ODEs. It can therefore be argued that the inhomogeneous system is well approximated by the two related PDEs. Accordingly, the discussion of phenomena arising in systems described by only two PDEs is a good starting point. Assume an electrochemical system that is adequately described by the following two partial differential equations (PDEs)

$$c_{dl,a} \frac{\partial \Delta \varphi_a}{\partial t} = -\frac{U + \Delta \varphi_a}{A(R_\Omega + R_{ext})} - i_{F,a}(\Delta \varphi_a, x) + \frac{d_m^2}{3AR_\Omega L^2} \frac{\partial^2 \Delta \varphi_a}{\partial \zeta^2} + \frac{R_{ext}(\overline{\Delta \varphi_a} - \Delta \varphi_a)}{AR_\Omega(R_\Omega + R_{ext})}, \quad (87)$$

$$c_{t,a}^* \frac{\partial x}{\partial t} = f(\Delta \varphi_a, x) + \frac{D}{L^2} \frac{\partial^2 x}{\partial \zeta^2}, \quad (88)$$

whereby  $\Delta \varphi_a$  represents the electrochemical double layer voltage and  $x$  stands for the concentration (or a coverage) of a chemical key species that is involved in the Faradaic reaction network. Please note that Eq. (88) does not include a term that represents convective transport. Indeed, convective transport is an important influence in PEMFCs and also plays a role in one of the phenomena depicted in the course of this chapter. But for the depiction of the fundamentals it is worth to simplify the system to the form above.

The form of the PDE system Eqs. (87)-(88) would be of typical reaction-diffusion type if the global coupling term (last term in Eq. (87)) would be absent. Reaction-diffusion systems appear naturally in chemical and biological systems and have been studied extensively since the beginning of computational research [115–118, 144, 145]. They can express a variety of phenomena arising from the interaction of local dynamics (stemming from the reaction network) and transport (diffusion).

Principally, due to the same mathematical structure, the same phenomena that occur in reaction-diffusion systems can be expected in electrochemical systems whenever the external resistance vanishes. An overview about selected phenomena, which appear in electrochemical nonlinear systems under these conditions, is given in Fig. 21. The patterns are classified based on the differentiation between N-NDR (including HN-NDR) and S-NDR systems, always assuming that  $\frac{d_m^2}{3AR_\Omega} \gg D$  (an assumption that is usually well fulfilled). Other patterns arise when the impact of global coupling is sufficiently strong ( $R_{ext} > 0$ ).

In the course of the following subsections the phenomena, depicted in Fig. 21, are discussed one by one. Thereby, the first subsection illustrates pattern formation in non-oscillatory media while the second subsection introduces phenomena in oscillatory media. The first subsection (on non-oscillatory media) should not be too detailed because in this thesis an HN-NDR system, in which oscillatory behavior is most essential, is predominantly investigated. Nevertheless, there are also a couple of interesting phenomena related to excitable N-NDR media that could be expected during the electrochemical  $H_2, CO$  oxidation in a PEMFC. And, additionally, the S-NDR branch in the system (shown in the previous chapter) might also cause specific non-oscillatory phenomena. Finally, after the overview of non-oscillatory and oscillatory phenomena has been presented, the discussed patterns relevance with respect to the electrochemical  $H_2, CO$  oxidation is summarized briefly.

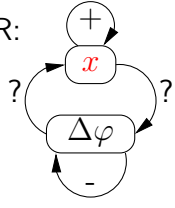
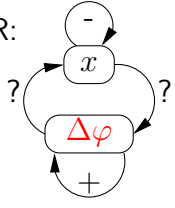
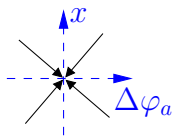
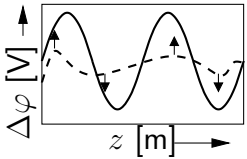
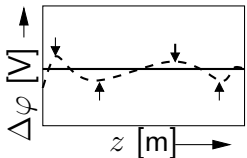
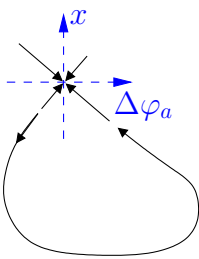
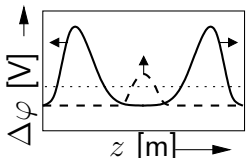
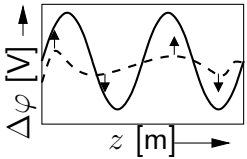
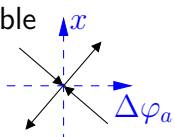
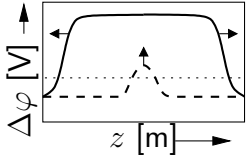
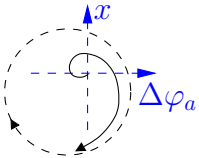
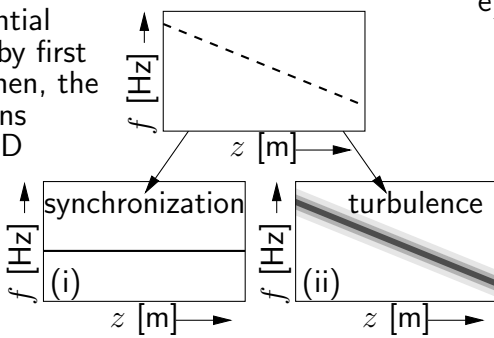
type of differential system regime of the differential system	S-NDR:  activator  inhibitor	N-NDR:  inhibitor  activator
monostable 	The homogeneous steady state is unstable: Any local disturbance leads to the emergence of spatially ordered, time-invariant patterns (Turing-mechanism) 	The homogeneous steady state is stable. 
excitable 	A critical local disturbance of the homogeneous steady state leads to the occurrence of traveling pulses and to the establishment of self-sustaining spiral patterns (in 2D systems). 	a) 
bistable 	A critical local disturbance of one specific of both homogeneous steady states leads to the emergence of travelling fronts that convey the system into the opposite state.	
oscillatory 	In the easiest case the differential oscillators synchronize, whereby first the frequencies entrain (i). Then, the phases align. Resulting patterns comprise waves and spirals (2D system). Under certain circumstances phase- or defect turbulence appears (ii), depending on the sign of the phase-diffusion coefficient.	

Figure 21: Possible phenomena that can occur in inhomogeneous N-NDR and S-NDR systems, depending on the regime. It is assumed that migration of  $\Delta\varphi$  is much larger than the diffusion of  $x$  and that global coupling is absent. Dashed lines represent initial states, solid lines illustrate established profiles after some time. Dotted lines indicate critical thresholds. The numbering a-e was chosen for more convenient reference in the text.

### 3.2.1 Phenomena in Non-Oscillatory Media

The subsection starts with a debate on diffusively coupled differential systems. Then the impact of the global coupling is discussed separately.

*Turing Patterns: Fig. 21a*

The discussion in the field of spatio-temporal pattern formation is often based on a separation of the spatial structure into several Fourier modes. By considering the stability of the modes with respect to small perturbations, spatial bifurcations can be identified. As a fascinating result of such an analysis it was found by Turing that, otherwise stable, homogeneous systems will undergo spatial stationary pattern formation if the inhibitor diffuses faster<sup>19</sup> than the activator [146]. Thereby, the wavelength of the structure is determined by the properties of the reaction-diffusion system and not by the finite size of the system.

Technically speaking, the homogeneous mode becomes unstable with respect to perturbations of a certain wave length, but the process can also be understood in a more intuitive way: The patterning happens, because the activator activates its- and the inhibitors growth at a specific site but the diffusion of the inhibitor is too fast to inhibit the production of the activator effectively, therefore leading locally to large concentrations of the activator. Then, at adjacent sites, more inhibitor (compared to activator) arrives such that the growth of initially little activator can be greatly inhibited. While time proceeds, a stationary pattern, consisting of spots with high amount of activator and inhibitor separated by regions of lower amount, arranges.

As the precondition of a fast diffusing inhibitor (compared to the activator diffusion) is usually well fulfilled in S-NDR systems [152], it is not surprising that Turing patterns were found during the electrochemical oxidation of CO on a Pt ring electrode [153] (a typical S-NDR system as discussed earlier). The first Turing pattern in an electrochemical system was reported not before 2001 [154].

*Pulses and Waves: Fig. 21b-c*

Oppositely, due to the fast activator diffusion in an N-NDR system, the homogeneous mode cannot be destabilized. However, if the differential N-NDR systems are excitable, then a local perturbation of critical extension and height leads to a wide excursion in phase space of the local system. Thereby, due to the diffusive interaction, adjacent reaction sites are being excited too. With some delay they also carry out wide excursions in their local phase space. As a consequence in one-dimensional systems two solitary, shape-invariant pulses form that travel into opposite directions (as depicted in Fig. 21c). Concentric solitary waves are the equivalent pattern in two-dimensional systems. As time passes and the pulses/waves spread (and eventually leave the system), the homogeneous state is re-established.

*Spirals: Fig. 21c*

However, in two-dimensional excitable systems, there exists a phenomenon that (oppositely to the concentric waves) persists in a bound region once one critical perturbation has been applied, and that is the occurrence of spiral waves (see [155] for nice examples). Principally, a spiral can grow from a wave with a broken front (opposite to waves that emerged from a local perturbation and which formed a closed ring). As the speed of the wave motion depends on the local front curva-

<sup>19</sup>Here, a properly rescaled system is considered. For a comprehensive analysis, see [113].

ture, the wave starts to curl at the ends of the broken front. Each broken end emerges to a spiral tip. Typically, the tip of a spiral rotates on a circle around a “core” (a region which remains always unexcited), following the direction of the spiral’s arm concavity. But also inward rotating spirals, so-called “antispirals”, are reported [156].

Under certain circumstances the core can also move (on straight paths or circles). Then, due to the so-called “meandering instability”, the tip performs more complicated meandering walks in the two dimensional plane [157]. In combination with another instability (see Eckhaus instability below, Eq. (97)), spiral chaos can be also found (e.g. in the Belousov-Zhabotinsky-reaction [158]). An introduction about the large amount of work that has been dedicated to spirals can be found in [155, 159].

The earliest experimental examples of spirals have been found in the Belousov-Zhabotinsky-reaction [160]. Other (very beautiful) examples were found in the 90’s during the catalytic oxidation of CO at well defined Pt surfaces under vacuum conditions by Ertl et. al [161]. A very prominent example for spiral formation in excitable media is believed to occur in the heart: Ventricular flutter is an arrhythmia stemming from the formation of a spiral in the heart tissue that disturbs the natural pacemaker. Ventricular fibrillation is believed to stem from the breakdown of this single spiral into spiral chaos [162, 163]. The use of a defibrillator resets the heart tissue and gives the responsibility for homogeneous contraction back to the pacemaker [164].

#### *Fronts: Fig. 21d*

When the homogeneous system is bistable, one of both states is more stable than the other. The more stable state is named globally stable state, while the other one is referred to as the metastable state. Considering a small perturbation that is applied onto the homogeneous metastable state, one will find that it dies out. But when the perturbation is sufficiently large, then it will grow until the value of the global steady state is reached locally. The spatial region which connects both stable states will develop a constant shape that travels along the space (across the surface) with constant speed and is named a “front”. It moves in such a way that the region of the globally steady state is widened. Extensive studies on front motion in different models are collected in various text books [113, 159, 165].

#### *The Impact of Global Coupling*

The impact of global coupling onto electrochemical S-NDR systems (as depicted in Fig. 21a) was investigated theoretically in [166]. As a result it was found that, apart from the Turing instability, another instability might occur which leads to the formation of two stationary domains. Such stationary domains have been found during the electrochemical CO oxidation at a polycrystalline Pt surface. They were experimentally investigated with the help of spatially resolved attenuated total reflection Fourier transform infrared spectroscopy (ATR-FTIRS) [136, 142]. While the one domain refers to a state of active CO oxidation, the second domain is inactive. Under galvanostatic control, when the global coupling is maximal, the size of domains adjusts to the current demanded. Accordingly, the active domain expands at the same rate as the inactive domain shrinks when the current is increased.

In non-oscillatory N-NDR systems the global coupling can effect pulses, waves and spirals. As all phenomena rely on the same principle, namely that an excitation preserves through lateral transmission (as depicted in Fig. 21c), it is reasonable to discuss the impact of global coupling onto all of these phenomena at the same time. Due to the different impact of a positive activator coupling onto regions with activator concentration below- and above average value, a positive global activa-



tor coupling increases the activator concentration in the unexcited region, but decreases the activator concentration in the excited region. In that way, the coupling is trying to equalize excited and unexcited regions. As a consequence, every pulse, wave or spiral can be brought to extinction at some large global coupling strength. A different influence of global activator coupling on spiral motion was investigated in [167, 168]. It was found that a positive global coupling can also cause a drift of the spiral core.

For bistable N-NDR systems (as depicted in Fig. 21d), the influence of a positive global activator (double layer voltage) coupling onto front motion was investigated theoretically in [147, 169]: An accelerated front motion was observed which in the most extreme case lead to a spontaneous global change of the metastable- into the globally stable state. The motivation for the theoretical research arose from earlier experimental results which reported accelerated [170] and decelerated front motion [171], whereby the deceleration and eventual stabilization of the fronts was shown to be caused by a negative global activator coupling<sup>20</sup> [172]. No studies on the influence of a positive inhibitor (double layer voltage) coupling in a bistable S-NDR systems are reported, but it is reasonable to expect that a positive global inhibitor coupling in S-NDR systems acts like a negative global activator coupling in N-NDR systems (and reverse) and therefore leads to decelerated front motion.

### 3.2.2 Phenomena in Oscillatory Media

In this subsection, phenomena that occur in oscillatory media are introduced. These phenomena comprise synchronization, turbulence and a few others. Synchronized and turbulent scenarios principally differ in their amplitude spectra. An amplitude spectrum yields the local oscillation frequency and its amplitude (gray scale) as function of the space coordinate. Typical spectra are sketched in Fig. 21e: While the upper amplitude spectrum depicts a distribution in the absence of coupling (when each reaction site behaves like an individual), the lower spectra are characteristic for a globally synchronized scenario (i: with one specific frequency for all reaction sites) and a turbulence regime (ii: characterized by a broad distribution of frequencies at any reaction site).

To depict the reason for this contrary behavior, the Complex Ginzburg-Landau Equation (CGLE) is considered. The CGLE is the standard generic equation in the field of synchronization. After its introduction, the CGLE is analyzed with respect to plane wave solutions. The reason for this analysis is to motivate the condition at which all stable waves break down (Benjamin-Feir-Newell condition), or in other words, to motivate the condition at which spatio-temporal turbulence emerges. Afterwards, other patterns that are frequently found in oscillatory electrochemical systems are depicted briefly.

#### *The Complex Ginzburg-Landau Equation*

The Complex Ginzburg-Landau Equation (CGLE) is a generic cubic equation that describes the evolution of a field of identical oscillators in the vicinity of a supercritical Hopf bifurcation, where oscillations have small amplitudes. It can be rigorously derived from reaction-diffusion systems (without global coupling) that are at the onset of oscillations [173] and it is one of the most studied equations in the world of physics [174]. It reads

$$\frac{\partial A}{\partial t} = (1 - i\omega_0) A - (1 + i\alpha) |A|^2 A + (1 + i\beta) \nabla^2 A, \quad (89)$$

<sup>20</sup>A negative global activator coupling arises when the reference electrode is placed between working electrode and counter electrode, a scenario that is not relevant in PEMFCs.



with

$$A(z, t) = \rho(z, t) \exp(i\Phi(z, t)), \quad (90)$$

whereby here only the one spatial dimension  $z$  shall be taken into account.  $A(z, t)$  is a field of complex oscillation amplitudes,  $\rho(z, t)$  describes the real amplitudes and  $\Phi(z, t)$  the respective phases (see also Fig. 22). The parameter  $\omega_0$  stands for the (real) oscillation frequency of the linearized oscillator.  $\alpha$  and  $\beta$  represent two real parameters that are closely linked to the detailed model from which the CGLE is derived<sup>21</sup>.

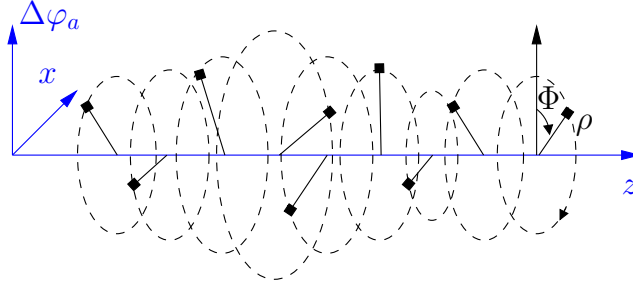


Figure 22: Idea of the complex Ginzburg Landau Equation (CGLE). The CGLE describes the spatio-temporal evolution of a field of identical oscillators close to a supercritical Hopf bifurcation. Here, for simple representation, the local oscillators do not interact and have time-independent amplitudes.

When a transformation of Eq. (89) into a rotating coordinate system is carried out according to  $A \rightarrow A \exp(-i\omega_0 t)$ , then  $i\omega_0 A$  in Eq. (89) disappears and the form is obtained which is mostly analyzed in literature

$$\frac{\partial A}{\partial t} = A - (1 + i\alpha) |A|^2 A + (1 + i\beta) \nabla^2 A. \quad (91)$$

Eq. (91) can be understood as a diffusively coupled network of the simplest oscillators, whereby the first term at the right hand side causes the destabilization of the steady state and the second (cubic) term leads to the stabilization of a limit cycle. Eq. (91) predicts several patterns depending only on the two parameters  $\alpha$  and  $\beta$ . But, before the results of Eq. (91) are described, two comments should be given on the wider context of the CGLE.

Firstly, note that in some limit of Eq. (91) other well studied equations can be obtained. These are the real Ginzburg-Landau equation (important in the field of superconductivity) and the non-linear Schrödinger equation (important in the field of water waves and optics). Secondly, note that recently a rigorous expansion of the CGLE towards a non-local CGLE (NCGLE) was presented [175]. The expansion also accounts for non-local and global migration currents in electrochemical systems and it appears that the range of the non-local migration coupling acts like a size-scaling factor for a variety of patterns: The larger the coupling range, the larger the patterns typical length scale. Other expansions of the CGLE are collected in [176].

<sup>21</sup>A procedure to derive  $\alpha$  and  $\beta$  from electrochemical model equations was recently published in [175].

### Oscillations and Plane Waves

The most simple solution of Eq. (91) is the homogeneous oscillation. It follows if the spatial gradient is negligible. In that case the space-independent Stuart-Landau equation is obtained

$$\frac{dA}{dt} = A - (1 + i\alpha) |A|^2 A. \quad (92)$$

Inserting the approach  $A(t) = \rho(t) \exp(-i\Phi(t))$  into Eq. (92), the two ODEs for the real and imaginary part read

$$\frac{d\rho}{dt} = \rho(1 - \rho^2), \quad (93)$$

$$\frac{d\Phi}{dt} = \alpha\rho^2. \quad (94)$$

The first equation (93) describes the (real) amplitude evolution and has only one meaningful steady state for  $\rho = 1$ . The second equation describes the evolution of the phase, which for  $\rho = 1$  continuously increases (with frequency  $\alpha$ ) as time passes by. Please note that, as the equation describes the phase evolution in a frame that rotates with frequency  $\omega_0$ , this evolution arises purely from the nonlinear terms.

Almost as simple is the solution of Eq. (91) for plane waves of the form  $A = \rho \exp(i[kz - \omega t])$ , with  $k$  representing the wave number ( $|k| \in [0,1]$ ). Entering this approach into Eq. (91) the stationary amplitude  $\rho$  and the related frequency  $\omega$  follow to be

$$\rho = \sqrt{1 - k^2}, \quad (95)$$

$$\omega = \alpha + k^2(\beta - \alpha). \quad (96)$$

It appears that  $\rho$  and  $\omega$  depend on the wave number. For  $k = 0$  (infinite wavelength) the homogeneous oscillation is re-obtained. However, as found by stability analysis, this plane wave is unstable whenever [173,174]

$$k^2 > k_{\text{EI}}^2 = \frac{1 + \alpha\beta}{3 + 2\alpha^2 + \alpha\beta}. \quad (97)$$

Eq. (97) is also referred to as the Eckhaus instability criterion. It says that each wave with a wave number larger than a critical value is unstable with respect to long-wave-length perturbations.

### Space-Time Chaos

Please note that criterion Eq. (97) also includes that no stable plane wave solutions exist (for any value of  $k$ ) if the numerator in Eq. (97) falls below zero

$$0 > 1 + \alpha\beta. \quad (98)$$

This special criterion is named Benjamin-Feir-Newell instability. Different patterns might arise, depending on whether the instability appears super- or subcritical. In the first case, so-called phase turbulence, that is the occurrence of plane waves with small local phase variations, arises. In the second case, so-called defect turbulence appears. Defect turbulence is characterized by the local breakages of the amplitude, indicating phase singularities (phase shifts by  $2\pi$ ) between neighboring sites [173,174]. For an overview of the characteristics space time patterns, see [176,177].

The meaning of condition Eq. (98) can be also rationalized when focusing on the phase distribution alone. When restricting the real amplitude to its steady state value, a general equation for the phase  $\Phi$  can be derived from the CGLE [173]. It reads

$$\frac{\partial \Phi}{\partial t} = \alpha + (1 + \alpha\beta) \nabla^2 \Phi + (\alpha - \beta) (\nabla \Phi)^2, \quad (99)$$

which reduces to the uniform oscillation if spatial gradients are absent. Of special importance is the coefficient that controls the phase diffusion,  $1 + \alpha\beta$ . A positive value of  $1 + \alpha\beta$  leads to stable plane wave solutions, while a negative value of  $1 + \alpha\beta$  leads to phase repulsion — the origin of space-time chaos. In the regime of phase turbulence, a proper description of the phases requires the extension of Eq. (99) according to

$$\frac{\partial \Phi}{\partial t} = \alpha + (1 + \alpha\beta) \nabla^2 \Phi + (\alpha - \beta) (\nabla \Phi)^2 - \frac{1}{2} \beta^2 (1 + \alpha^2) \nabla^4 \Phi, \quad (100)$$

yielding the so-called Kuramoto-Shivansky equation [173]. However, in the regime of defect turbulence the behavior of the CGLE is not captured anymore by Eq. (100), simply because the assumption  $\rho \approx 1$  does not hold anymore.

#### *Other Phenomena*

Apart from plane waves and spatio-temporal turbulence, other solutions of the CGLE in two spatial dimensions are spiral waves (i.e. spirals do not only appear in excitable systems but also in oscillatory media), target patterns, breathing domains and phase clusters.

In the context of spiral waves, the Eckhaus instability has to be further subdivided into convective- and absolute Eckhaus instability. In the first case, a spatially fixed perturbation decays, while a perturbation that is advected with the wave grows and leads to amplitude variations or phase singularities (as mentioned earlier). In the second case, even localized perturbations grow and lead to one of the turbulence regimes. The associated consequence of spiral waves is their breakup into turbulence [178].

In experimental systems, shortly before an oscillatory bifurcation of the homogeneous system occurs, the medium is often excitable. Then, it might appear that due to local inhomogeneities, limited surface areas, named pacemakers, are already oscillatory. In that case, local oscillations continuously produce disturbances which travel as pulses (or rather concentric waves) through the excitable media. The results are so-called target patterns as they appear, in a snapshot of the surface, as encircling rings. The same patterns might also arise when a fast oscillating pacemaker is embedded into a slower oscillating media. Sometimes, the pacemaker does not arise due to an inhomogeneity of the medium but due to the nonlinearity of the system itself [178]. The first target patterns were observed in the Belousov-Zhabotinsky-reaction [179]. Target patterns were also found during CO oxidation at Pt, during Rayleigh-Bénard convection, in colonies of bacteria and in many other systems (see [178] for a comprehensive overview).

Another phenomenon in S-NDR systems is the occurrence of standing waves. Standing waves arise through a so-called “wave instability”, which is a secondary bifurcation occurring at the intersection of a Turing-like instability (including domains) and a Hopf bifurcation. A nice example of a standing wave can be found in [180]. When a domain bifurcation (arising due to galvanostatic control) intersects with the Hopf bifurcation then also breathing domains can arise [181]. The difference to a standing wave is that the values oscillate around the steady state values of the domain structure

and not around the homogeneous steady state. In systems containing an S-NDR, phase clusters can also appear. They represent standing waves without fixed spatial wavelength and their mechanism is still under discussion [182].

### 3.2.3 Preliminary Expectations

A large variety of patterns can occur in non-oscillatory and oscillatory media. Some patterns appear in S-NDR systems (Turing- and domain instabilities) while others are expressed in N-NDR systems (homogeneous oscillations, phase- and defect turbulence, etc.). During the electrochemical  $H_2, CO$  oxidation, the difficulty is that the system is of S-NDR and HN-NDR type simultaneously (as was shown in the previous chapter). Therefore, it is reasonable to expect very complex behavior, being a result of the individual instabilities occurring in the subsystems.

In an S-NDR system under positive global inhibitor coupling, in which the load line intersects the NDR branch under such an angle that only one intersection occurs, different phenomena (as depicted above) might appear: Oscillations of the homogeneous mode can coexist/interact with Turing patterns. Secondary bifurcations from Turing- and Hopf bifurcation can cause standing waves and phase clusters. However, as was depicted in Sec. 2.1, the time constants in the system are such that any oscillatory behavior due to the S-NDR is unlikely. Accordingly, only Turing- patterns have a pronounced relevance.

Oppositely, oscillations are very likely (and are known) in the HN-NDR subsystem. The homogeneous oscillation is very likely to dominate when the global coupling is very strong (for large external resistance and galvanostatic control). If the global feedback is weak (potentiostatic control with small external resistance), then, depending on the system parameters, phase- and defect turbulence can be expected to play a role, too.

A medium is often excitable when it is close to an oscillatory- or saddle-node instability. Therefore, it can be expected that phenomena like pulses, waves and spirals (and related secondary bifurcations) occur in the environment of the NDR branch, too. Fronts do not play a role as long as a bistable system setup cannot be arranged.

## 3.3 $H_2, CO$ Oxidation in an Inhomogeneous PEMFC - Theory

In the following section a model for spatially distributed electrochemical  $H_2, CO$  oxidation is presented and analyzed. Parts of this subsection were preliminary published by the author in [108, 151]. The PEMFC setup under consideration is sketched in Fig. 23. The model is appropriate to describe the behavior of a galvanostatically controlled “one-dimensional” PEMFC with a highly active cathode ( $H_2$  evolution) and is built upon three pillars. The first pillar is the partial differential equation (PDE) that describes the spatio-temporal evolution of the anodic double layer, developed in Sec. 3.1 (Eq. (86)). The second pillar is the simplified homogeneous model that was developed in Sec. 2.2 and which describes the reaction network, active at each reaction site. The third pillar is a set of equations for the mass transport in the anode channel. Altogether, the model captures the essential dynamics in the spatially distributed system.

After presenting the model in the first subsection, in the second subsection the model is numerically analyzed in the oscillatory regime. Qualitatively different patterns are identified.

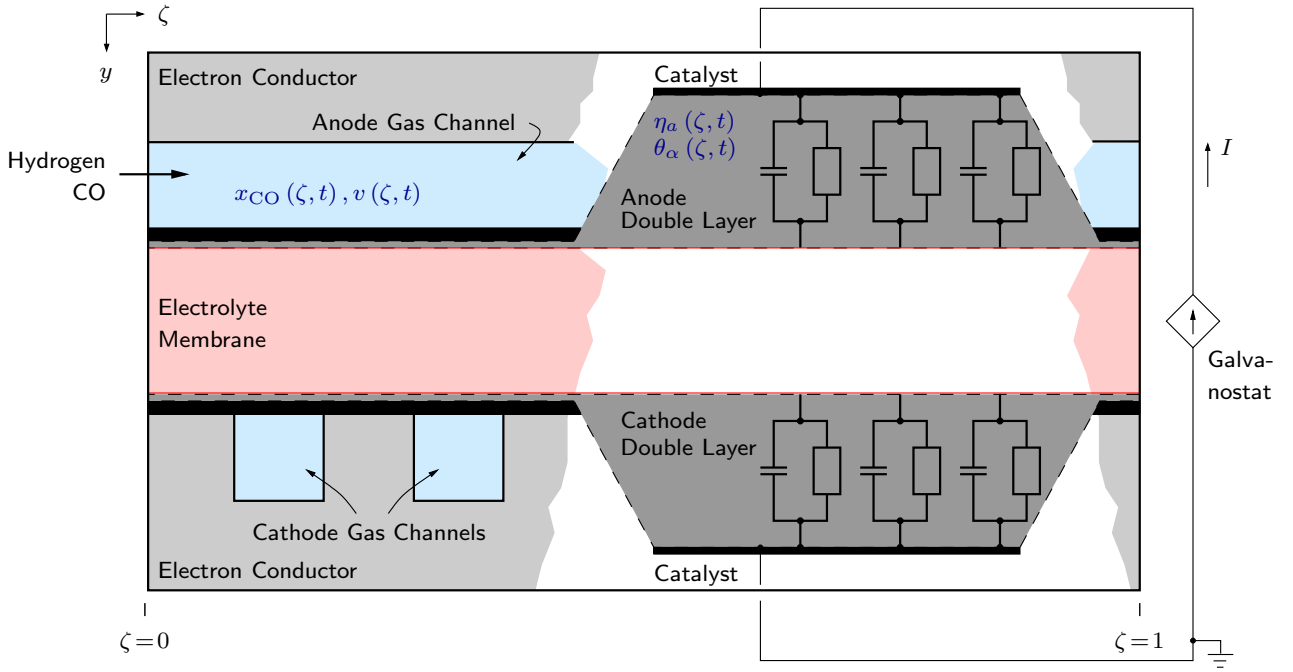


Figure 23: The setup of the considered “one dimensional” PEMFC system.

### 3.3.1 Modeling

Kinetic parameters are not introduced again. Their meaning is equivalent to their intent in Sec. 2.2. Operation conditions and design parameters partly deviate from the values used in the homogeneous model and are collected in Tab. 5.

operating conditions		design parameters	
$F_{in}$	$10^2 \cdot \frac{p^\theta T}{p T^\theta} \frac{\text{cm}^3}{\text{min}}$	$A$	$5 \cdot 10^{-5} \text{ m}^2$
$x_{\text{CO},in}$	$10^3 \text{ ppm}$	$L$	$2.5 \cdot 10^{-2} \text{ m}$
$p$	$2.958 \cdot 10^5 \text{ Pa}$	$b$	$A/L$
$T$	$315 \text{ K}$	$h_{ga}$	$2 \cdot 10^{-3} \text{ m}$
$\frac{I}{A}$	$3 \cdot 10^3 \frac{\text{A}}{\text{m}^2}$	$d_m$	$127 \cdot 10^{-6} \text{ m}$
$\kappa$	see text		

Table 5: Operating conditions and design parameters

#### The Model

The variables with the most dynamic relevance are, according to the model reduction carried out in Sec. 2.2, the CO coverage and the anode overvoltage. Under the assumption that the CO surface diffusion is negligible, the local CO coverage follows from the ODE (which needs to be evaluated at each reaction site)

$$\gamma c_t^* \frac{\partial \theta_{\text{CO}}}{\partial t} = r_{\text{CO},ad} - r_{\text{CO},ox}. \quad (101)$$

For galvanostatic control and a highly active cathode, the anodic overvoltage follows from entering the overvoltage definition,  $\eta_a := \Delta\varphi_a - \Delta\varphi_a^0$ , into Eq. (86)

$$c_{dl,a} \frac{\eta_a}{\partial t} = \frac{I}{A} - i_{F,a} + \frac{d_m \kappa}{3L^2} \frac{\partial^2 \eta_a}{\partial \zeta^2} + \frac{\kappa}{d_m} (\bar{\eta}_a - \eta_a), \quad (102)$$

with the boundary conditions

$$\frac{\partial \eta_a}{\partial \zeta} \Big|_{\zeta=0} = \frac{\partial \eta_a}{\partial \zeta} \Big|_{\zeta=1} = 0. \quad (103)$$

The function  $i_{F,a}$  in Eq. (102) can be written as (see Eq. (43) for reference)

$$i_{F,a} = F (r_V + 2r_{CO,ox}) \approx Fr_V, \quad (104)$$

whereby in the second step the CO oxidation rate was neglected. This simplification is reasonable, because the CO oxidation rate will generally be at least two orders smaller than the  $H_2$  oxidation rate due to small CO concentrations applied in the following modeling study. The reaction rates, necessary to evaluate Eqs. (101) and (104) were formulated already in Tab. 2 and are re-stated here

$$r_V = k_V \theta_H (Q_i) 2 \sinh \left( \frac{F\eta_a}{2RT} \right). \quad (105)$$

$$r_{CO,ad} = k_{CO,ad} (x_{CO} p \theta_0 - K_{CO,ad} \theta_{CO}), \quad (106)$$

$$r_{CO,ox} = k_{CO,ox} \theta_{CO} \theta_{OH} \exp \left( \frac{F\eta_a}{2RT} \right). \quad (107)$$

The coverages  $\theta_0$ ,  $\theta_H$  and  $\theta_{OH}$  have been shown to follow from

$$\theta_0 = \sqrt{\left( \frac{Q_3}{2Q_2} \right)^2 + \frac{Q_4}{Q_2}} - \frac{Q_3}{2Q_2}, \quad (108)$$

$$\theta_H = 1 - \theta_{CO} - (1 + Q_1) \theta_0, \quad (109)$$

$$\theta_{OH} = Q_1 \theta_0, \quad (110)$$

whereby the  $Q_i$  form a set of help variables

$$Q_1 = \frac{1}{K_{OH} \exp \left( -\frac{F\eta_a}{RT} \right) + \frac{k_{CO,ox}}{k_{H_2O,dis}} \theta_{CO}} > 0, \quad (111)$$

$$Q_2 = \frac{p}{K_{H_2,ad}} - (1 + Q_1)^2, \quad (112)$$

$$Q_3 = 2(1 + Q_1) \left( 1 - \theta_{CO} + \frac{k_{H,ox}}{k_{H_2,ad} K_{H_2,ad}} \sinh \left( \frac{F\eta_a}{2RT} \right) \right) > 0, \quad (113)$$

$$Q_4 = (1 - \theta_{CO}) \left( 1 - \theta_{CO} + \frac{2k_{H,ox}}{k_{H_2,ad} K_{H_2,ad}} \sinh \left( \frac{F\eta_a}{2RT} \right) \right) > 0, \quad (114)$$

that need to be evaluated at each reaction site. During the model reduction in Sec. 2.2 that lead to the construction with the  $Q_i$  variables, it was always assumed that the molar  $H_2$  fraction is one. The same assumption is also valid here. Of course, the assumption of a constant  $H_2$  concentration will fail when the current is higher than the Faradaic limit. Therefore, in Sec. 2.2 the Faradaic limit was taken into account as an additional equation that was implied when the current approached it. Oppositely, in the following analysis it is ensured that the current never exceeds the Faradaic limit. It is therefore not

necessary to state this equation here again. Please also note, that this (rather labyrinthine) solution structure is very advantageous for fast computation as it involves only explicit equations.

The only remaining un-determined variable, necessary to evaluate Eq. (106), is the local molar CO fraction,  $x_{\text{CO}}$ . In the model reduction carried out in Sec. 2.2 it was argued that the material balance for the determination of  $x_{\text{CO}}$  is a good candidate for a quasistationarity reduction<sup>22</sup>. Therefore, in the following analysis  $x_{\text{CO}}$  will be determined by

$$0 = -\frac{p}{RTL} \frac{\partial}{\partial \zeta} (x_{\text{CO}} v) - \frac{r_{\text{CO,ad}}}{h_{\text{ga}}}, \quad \text{with the boundary condition } x_{\text{CO}}(\zeta=0, t) = x_{\text{CO,in}}(t) \quad (115)$$

and the local gas velocity  $v$  following from

$$0 = -\frac{p}{RTL} \frac{\partial v}{\partial \zeta} - \frac{1}{2} \frac{r_{\text{V}}}{h_{\text{ga}}}, \quad \text{with the boundary condition } v(\zeta=0, t) = \frac{1}{h_{\text{gab}}} F_{\text{in}}(t). \quad (116)$$

This previous equation completes the model as no unknown functions appear. Please note that Eq. (115) is an implicit equation as also  $r_{\text{CO,ad}}$  depends on the molar CO fraction. However, when the model is spatially discretized, it can be also converted into an explicit equation, suitable for fast computation. An explicit solution follows also for the velocity field upon discretization.

Finally, before starting with the analysis of the model, it is worth to depict two limitations, which lead to the circumstance that some patterns cannot be modeled.

Firstly, the model allows only for galvanostatic control. This constraint helps to guarantee that the Faradaic limit is never exceeded, but it naturally also restricts the parameter space. As the system is an S-NDR/HN-NDR system no bistability can ever occur. Therefore, also no front motion can be found. The possibility for domain- and Turing patterns persist upon this constraint.

Secondly, the diffusion of  $\theta_{\text{CO}}$  is neglected. The impact of this simplification is that Turing structures which might be realistic, cannot be found (see chapter 14 in [113]). Of course, if a diffusion term would be added, then the model would not necessarily provide all requirements for Turing patterns as the instability also depends on the properties of the reaction-diffusion system. Oppositely, domains can still appear. They do not depend on the activators diffusion constant in the S-NDR system but on the system size.

As a conclusion on these limitations one can say, that the model is tailored to the essential HN-NDR related phenomena, i.e. to phenomena in oscillatory media caused by a positively coupled activator.

### *Numerical Simulation and Validation of the Model*

The model was discretized with the Finite Volume Method and solved using the software tool MATLAB. The number of discrete elements was chosen relatively large ( $n = 400$ ) in order to suppress numerical diffusion. As initial conditions, homogeneous profiles were chosen such that the anode surface was almost completely covered with CO (99%) while the rest was occupied with  $H_2$ . Sampling a couple of simulations started from random inhomogeneous profiles confirmed the independence of the results of the initial conditions. The model was evaluated for a time span of 600 s. The first 200 s were cut off to make sure that only the cyclic steady state was used for analysis. Simulations were carried out on a Desktop PC "Dell Optiplex 760". The results are presented as space time plots of the anode overvoltage (e.g. Fig. 25a) and amplitude spectra (e.g. Fig. 25c).

<sup>22</sup>Indeed, it was shown in [183] that this assumption can, under certain circumstances, fail. A discussion on the dynamic impact of the CO channel balance is part of this subsection.



The model was validated by comparing the results (for the parameters presented in Tab. 5 and varying conductivity) with results obtained from a second, more rigorous, model [183]. Basically, the second model was derived from first principals and avoids most of the assumptions made above. Therefore, the second model is in the following referred to as “full model”. In detail, the full model disregards the assumptions on quasistationarity that lay beneath the construction with the  $Q_i$  variables, it takes into account a realistic rate approach for a cathodic oxygen reduction and it contains the determination of the potential field in the electrolyte via the Laplace equation. However, this second model is rather in-transparent and allows only for slow numerical integration. As the introduction of this second model would therefore have no other purpose as to confirm the model presented above, its presentation is avoided here. The comparison was part of [108]. Note, that there exists also scenarios in which the full model yields different behavior compared to the model presented above. This discrepancy is also discussed in the next subsection.

### 3.3.2 Model Predictions

Within this section simulation results of the minimal model will be presented while the model is systematically analyzed. The discussion is started with the separation of the conductivity into  $\kappa_y$  and  $\kappa_z$  in order to control the coupling terms individually.

$$+ \frac{\kappa_z d_m}{3L^2} \frac{\partial^2 \eta_a}{\partial \zeta^2} \quad \text{Migration-Coupling} \quad (117)$$

$$+ \frac{\kappa_y}{d_m} (\bar{\eta}_a - \eta_a) \quad \text{Mean-Field-Coupling} \quad (118)$$

The realistic situation can be re-obtained by setting  $\kappa_y = \kappa_z$ . The analysis is based on the investigation of the term’s influence on the amplitude spectra: Four limiting cases of the model are considered and sketched in Tab. 6 as overview. Simulation results including the case studies are classified according to their long time behavior and collected in Fig. 24. After the subsequent presentation of the four cases, finally the dynamic impact of the channel CO mass balance is discussed. It provides another scenario.

#### Case 1: Material Coupling

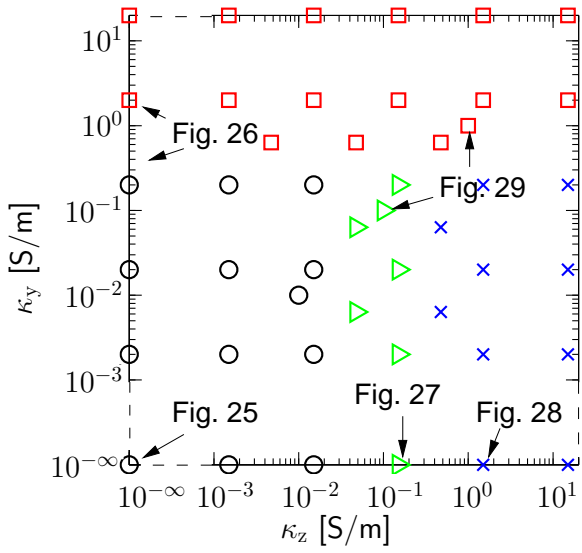
In the first case the conductivities  $\kappa_y$  and  $\kappa_z$  are small enough to neglect mean-field- and migration coupling. The dynamic state-equations left over are

$$\gamma C_t^* \frac{\partial \theta_{CO}}{\partial t} = r_{CO,ad}(x_{CO}, \theta_{CO}, \eta_a) - r_{CO}(\theta_{CO}, \eta_a) \quad (119)$$

$$c_{dl} \frac{\partial \eta_a}{\partial t} = \frac{I}{A} - Fr_H(\theta_{CO}, \eta_a) \quad (120)$$

Essentially, the structure of these equations is the same as in the homogeneous model (see Sec. 2.2). But in comparison, the CO content  $x_{CO}$  is here a function of  $\zeta$  while in the spatially lumped model it was a scalar value. As other terms depend purely on local values, this one dimensional system can be understood as a chain of oscillators coupled only via the CO mass balance of the channel.

Fig. 25 collects the results for this scenario. Access to the figures is gained by starting with Fig. 25c. It can be seen that the frequency decreases along the channel and concluded from Fig. 25e that this is due to the oxidation of CO. Interestingly, the experimentalist would hardly measure any oscillation of  $\bar{\eta}_a$  in that situation (Fig. 25b,d) because any differential system oscillates with a unique frequency



- uncoupled oscillations
- mean-field coupling induced synchronization
- ▷ migration coupling induced synchronization
- × migration coupling induced spatio-temporal turbulence

Cases	$\kappa_y$	$\kappa_z$
1. <i>Material Coupling</i>	$= 0$	$= 0$
2. <i>Material- and Mean-Field Coupling</i>	$> 0$	$= 0$
3. <i>Material- and Migration Coupling</i>	$= 0$	$> 0$
4. <i>Material-, Migration- and Mean-Field Coupling</i>	$= \kappa_z$	$> 0$

Figure 24: Parameter map of the one dimensional PEMFC-model with respect to the different parameters  $\kappa_z$  and  $\kappa_y$ . Qualitative different long time behavior are encoded by different symbols, colors shall help to guide the eye.

Table 6: Different coupling phenomena influence the dynamic state equation of the anode overvoltage (Eq. (102)). As  $\kappa_y$  and  $\kappa_z$  control the phenomena, four qualitatively different cases are chosen to study the effects independently.

(Fig. 25c). Accordingly, phase shifts between adjacent reaction sites grow in time and destroy any initial order. The apparent spatial coherence seen in Fig. 25a is a misleading effect of the depiction. There is no fixed phase relation along the channel.

Additionally, the influence of the channel CO mass balance (Eq. (115)) on the dynamic behavior was elucidated. The balance yields the local  $x_{CO}$  values. When these values are replaced in Eq. (101) by their temporal mean value  $\langle x_{CO} \rangle_t$  the Eqs. (115)-(116) are cut off. Comparing the frequency curves calculated with- and without fluctuations of  $x_{CO}$  (Figs. 25c and 25g) it is evident that the  $x_{CO}$ -fluctuations have no influence on the globally coupled oscillations.

Finally, it need to be clearly stated that the real system cannot express such behavior. The oscillations appear in the simulation due to the finite size of the discrete elements. The attempt to increase the model accuracy by increasing the number of discrete elements brings the problem to the point: Firstly, in the limit of microscopic element size the macroscopic rate approach, chosen above, is no longer valid. And secondly, there is no reason for the formation of synchronized regions at any length scale. Accordingly, if there is no length scale at which oscillations of unique frequency occur, then oscillations can never be measured and their existence is only hypothetical. However, the hypothetical individual oscillators can explain the other patterns emerging below.

#### Case 2: Material Coupling and Mean-Field Coupling

This situation considers the influence of the positive mean-field coupling term ( $\kappa_y > 0$ ) and neglects migration coupling ( $\kappa_z = 0$ ). It is known that global coupling with a positive sign leads to synchronization of reaction sites with frequencies around the mean-field-frequency [173, 184].

Indeed, it can be seen from Fig. 26 that mean-field coupling leads to synchronization in the present system, too. Once a certain critical  $\kappa_y^{\min}$  is exceeded (ca. 0.24 S/m for the given parameters) some of

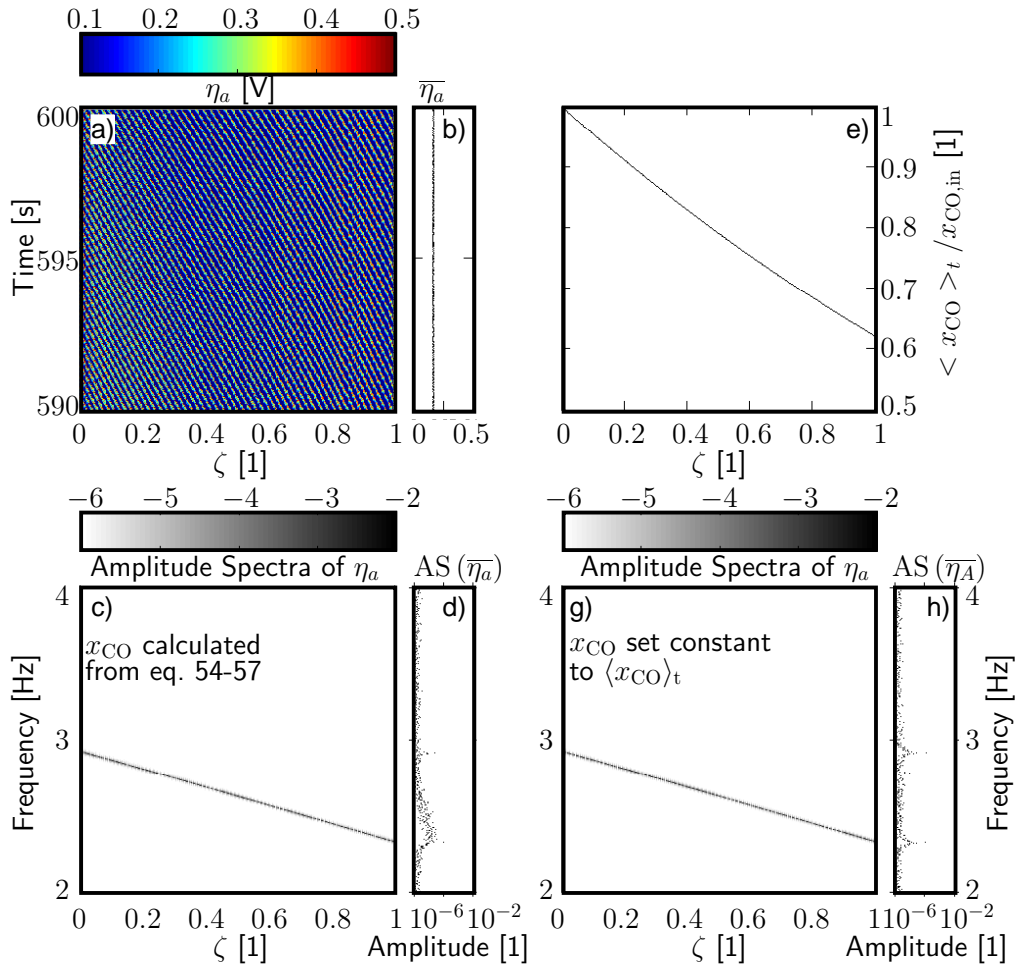


Figure 25: Scenario arising with negligible electrical couplings  $\kappa_y = \kappa_z = 0$ . a: Anode double layer potential and b: its mean value; e: Temporal average of the CO content along the channel; c: Amplitude spectra for  $x_{CO}$  being calculated dynamically and g:  $x_{CO}$  being replaced by its constant temporal mean value  $\langle x_{CO} \rangle_t$ ; d-h: Amplitude spectra (AS) of the respective mean anode overvoltage at the side.

the differential oscillators synchronize at a frequency  $f$  (Fig. 26d) and build a homogeneous oscillating parcel (Fig. 26a,c). The phases of the entrained oscillators are confined within a region of  $1/2f$  (see front-shape in Fig. 26a) and form waves that run along the spatial coordinate. The rest of the PEMFC shows quasi-periodic oscillations characterized by two incommensurate frequencies (Fig. 26c) (the intimate- and the mean-field frequency) and their integer combinations [185]. From Fig. 26b one can see that  $\bar{\eta}_a$  shows oscillations as soon as the synchronization starts.

For larger  $\kappa_y$  the synchronized PEMFC part extends until the whole PEMFC is oscillating with a single frequency (Fig. 26e-h) at some other critical value  $\kappa_y^{\max}$  (ca. 0.40 S/m for the given parameters). Rising  $\kappa_y$  further, lowers the homogeneous oscillation frequency and entrains the phases even harder. One can also identify a small part of the cell, close to the outlet in Fig. 26e, which oscillates with double period. However, this effect is considered to be of minor importance and has not been studied further.

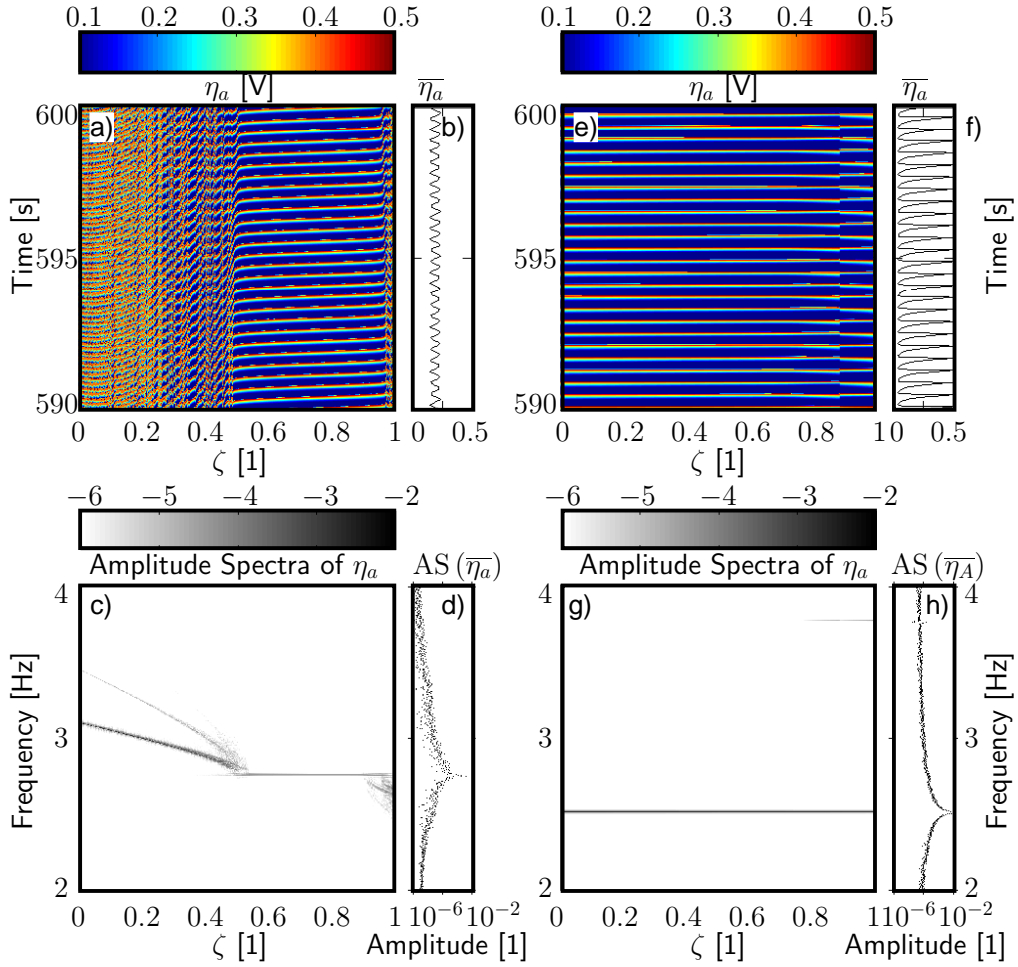


Figure 26: Influence of mean-field coupling on the anode overvoltage and related amplitude spectra for different  $\kappa_y$  ( $0.30 \frac{S}{m}$  left,  $2.00 \frac{S}{m}$  right).

### Case 3: Material Coupling and Migration Coupling

This case investigates the influence of the migration coupling term ( $\kappa_z > 0$ ) and neglects mean-field coupling ( $\kappa_y = 0$ ). Different from the procedures carried out for the first two cases it is helpful to further subdivide the investigation of migration coupling. The discussion starts therefore with the exploration of the influence of the  $x_{CO}$ -gradient on a weakly coupled system. Then, the situation with larger couplings is studied. The gradient is controlled via the volumetric feed flow rate.

At low  $\kappa_z$  and a weak  $x_{CO}$ -gradient (large  $F_{in}$ ) the frequencies of differential oscillators are locked (Fig. 27a-d. But opposite to the mean-field coupling scenario, here waves are initiated at the inlet and travel downstream (Fig. 27a, giving rise to a continuously increasing phase shift along the channel. Or in other words, the wave continuously decelerates while traveling downstream. And it seems that there is a critical wave velocity. Namely, at larger  $x_{CO}$ -gradients the differential oscillators close to the outlet do not entrain anymore (Fig. 27e-h). Instead, in that area some locally restricted waves evolve which travel downstream and then leave the system. Due to the transient nature of these events the amplitude spectra show blurred signals in the outlet region.

At higher  $\kappa_z$  the behavior significantly changes (Fig. 28): Assuming an infinite volumetric inlet flow rate, one achieves a system without any  $x_{CO}$ -gradient. Considering the stability of a homogeneous oscillation in that situation, it is found that any perturbation (random variation of the dy-

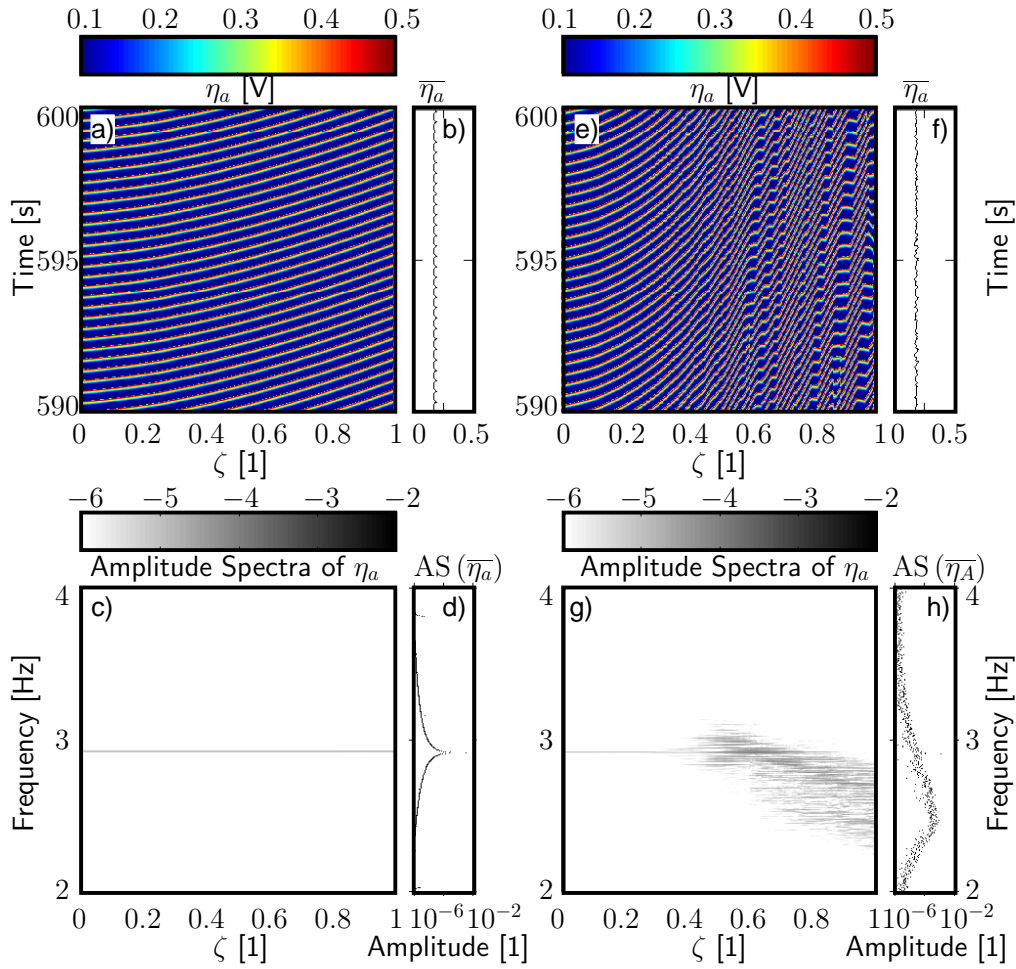


Figure 27: Influence of weak migration coupling ( $\kappa_z = 0.15 \frac{\text{S}}{\text{m}}$ ) on the amplitude spectra for different  $x_{\text{CO}}$  gradients (left:  $F_{\text{in}} = 10^3 \text{sccm}$ ; right:  $F_{\text{in}} = 10^2 \text{sccm}$ ).

dynamic state variables) dies out if it is small. However, once the amplitude of the perturbation is large enough, fronts start traveling along the system and leave a turbulent pattern in the created cone (Fig. 28a-d). Thereby, close to the perturbation the disturbed fronts first become wavy and then develop defects. Or in other words, it follows the typical mechanism of the Benjamin-Feir instability [176].

Now, while going back one step and forgetting any perturbation, the situation with applied  $x_{\text{CO}}$ -gradient is considered by setting  $F_{\text{in}}$  to the value of interest. If starting the simulation from spatially homogeneous conditions spatio-temporal turbulence puts through little time later, when plane waves in the outlet region become unstable (Fig. 28e-f) and consequently drive the whole system again into the spatio-temporal turbulent state.

#### Case 4: Material-, Mean-Field- and Migration Coupling — The Realistic Situation

In the previous section it was shown that mean-field- and migration coupling lead to antithetic behavior by varying  $\kappa_y$  and  $\kappa_z$  independently. However, in practice  $\kappa_y = \kappa_z$ . Then, the question arises which of the both coupling terms dominates the cell behavior. From the experimental point of view the membrane conductivity can be influenced indirectly via the membrane humidity. Conductivities



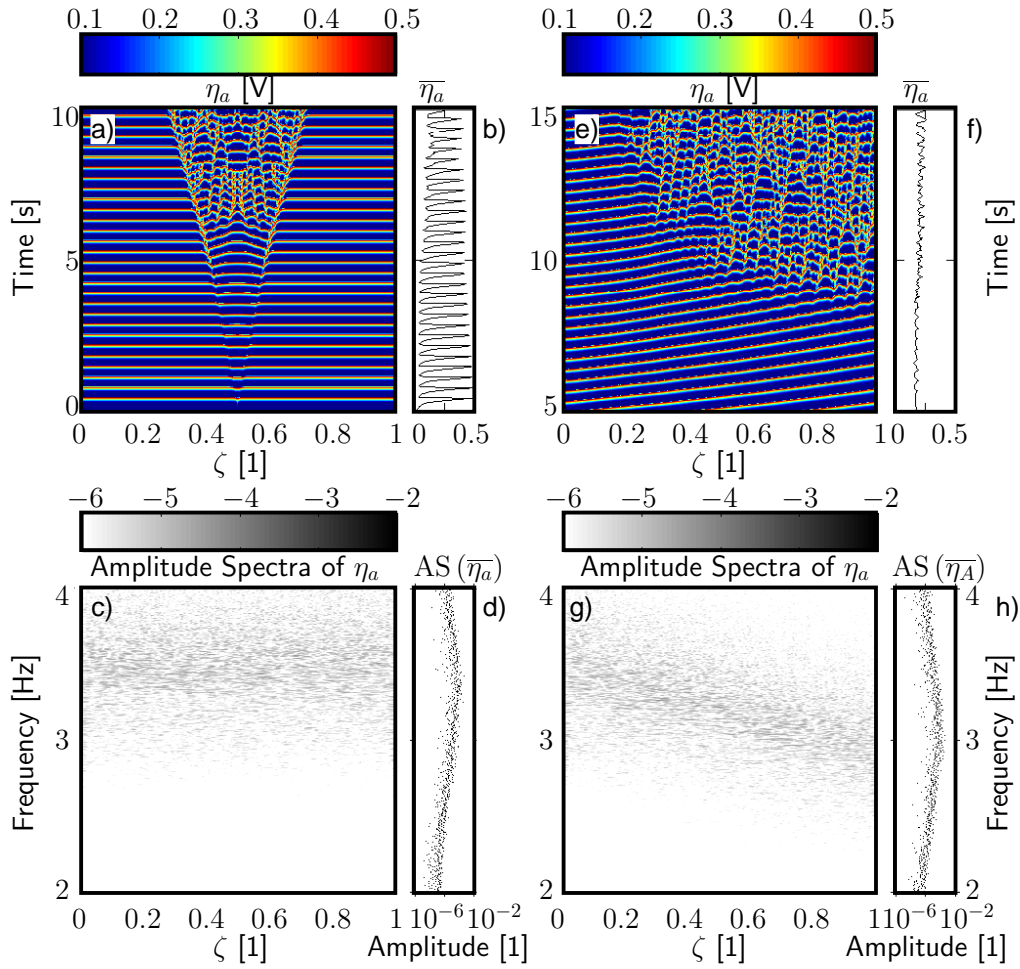


Figure 28: Influence of strong migration coupling ( $\kappa_z = 1.5 \frac{S}{m}$ ) on the amplitude spectra for different  $x_{CO}$  gradients (left:  $F_{in} = 10^{\infty}$  sccm and strong artificial perturbation at  $z = L/2, t = 0$ ; right:  $F_{in} = 10^2$  sccm).

between 0.01 to 20 S/m for Nafion are reasonable [186]. In the present paragraph the cell behavior is studied for varying conductivity and  $\kappa_y = \kappa_z = \kappa$ .

The influence of  $\kappa$  on the amplitude spectra is shown in Fig. 29. At low value the amplitude spectra at the outlet are dominated by traveling local planar waves introduced by migration coupling (compare with Fig. 27). However, at higher conductivities mean-field coupling dominates the PEMFC behavior.

Consequently, it seems that the defect turbulence observed in Fig. 28 can not be found in real experiments. Nevertheless, this possibility cannot be excluded. In fact, it is about the proper choice of system dimensions to push the region of turbulence on the line where  $\kappa_y = \kappa_z$  (Fig. 24). Indeed, the both transformations given in Tab. 7 convert the model equivalently. That implies that changing the system parameters according to transformation 1 rises the influence of migration coupling in the same way as transformation 2 does. Therefore, for small currents and small volumetric inlet flow rates chaos might occur in relatively short channels. However, note here, that the model is strictly valid only for the case with  $L \gg b$  and under galvanostatic control. As was discussed earlier in Sec. 3.1 mean-field coupling is also reduced under potentiostatic control.

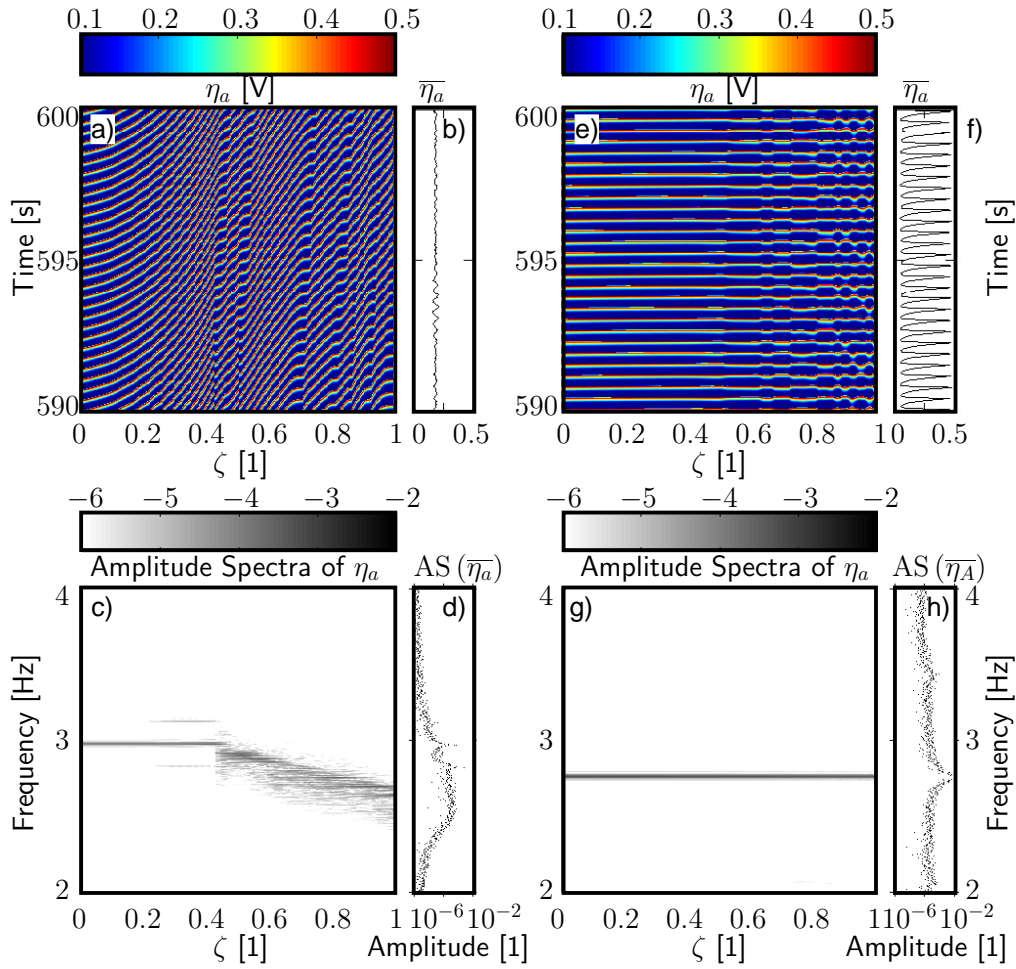


Figure 29: Influence of mean-field- and migration coupling on the amplitude spectra for different  $\kappa = \kappa_y = \kappa_z$  (left:  $0.10 \frac{\text{S}}{\text{m}}$ ; right:  $1.00 \frac{\text{S}}{\text{m}}$ ).

Transformation 1		Transformation 2	
$L$	$\rightarrow L/s$	$\kappa_z$	$\rightarrow s^2 \cdot \kappa_z$
$I$	$\rightarrow I/s$		
$h_{ga}$	$\rightarrow h_{ga}/s$		
$F_{in}$	$\rightarrow F_{in}/s$		

Table 7: The both transformations convert the minimal model in the same way. Migration coupling can therefore be supported by changing the system dimensions and the operating parameters.

#### Dynamic Impact of the Channel CO Mass Balance

In the paper of Hanke-Rauschenbach et al. [183], the full model (mentioned earlier) was investigated and a pattern was found that is qualitatively different from the patterns discussed, yet. The pattern arose from the homogeneous oscillation (Fig. 26) when the feed flow rate was decreased sufficiently. One characteristic of the new behavior was that, in the time series of  $\bar{\eta}$ , two maxima (indexed with  $k$  and  $k+1$ ) per period appeared. When introducing  $\tau_k$  as the time between them

$$\tau_k = t \left( \text{Max}(\bar{\eta}_a(t))_{k+1} \right) - t \left( \text{Max}(\bar{\eta}_a(t))_k \right), \quad (121)$$



then the new behavior can be characterized by  $\tau_{k+2} - \tau_k = 0$  while  $\tau_{k+1} - \tau_k \neq 0$ . Oppositely, for the simple homogeneous oscillations  $\tau_{k+1} - \tau_k = 0$ .

A pattern with such a characteristic was not found with the reduced model. During the stepwise investigation of the different assumptions that lay beneath the reduced model, the origin of the discrepancy was identified. The discrepancy can be resolved if the local molar CO fraction is calculated via

$$\frac{p}{RT} \frac{\partial x_{\text{CO}}}{\partial t} = -\frac{p}{RTL} \frac{\partial}{\partial \zeta} (x_{\text{CO}} v) - \frac{r_{\text{CO,ad}}}{h_{\text{ga}}}, \quad \text{with the boundary condition } x_{\text{CO}}(\zeta=0) = x_{\text{CO,in}}, \quad (122)$$

instead of using Eq. (115). The term that provokes the new behavior is  $\frac{p}{RT} \frac{\partial x_{\text{CO}}}{\partial t}$ . Or in other words, qualitatively new phenomena are caused by the dynamic impact of the channel CO mass balance.

With the modified reduced model, the new behavior (found in [183]) can be reproduced if, for example, the current is changed for a given feed flow rate. Fig. 30a depicts the  $\tau_k$  during a slow scan of the current density. The oscillations set in at a current density of  $\approx 0.1 \text{ A cm}^{-2}$ . The first period  $\tau_1$  has a length of 0.63 s. Up to  $0.26 \text{ A cm}^{-2}$  subsequent  $\tau_k$  have the same length, thus  $\tau_{k+1} - \tau_k = 0$ . The related spatio-temporal behavior is, in the interval between  $\approx 0.1 \text{ A cm}^{-2}$  and  $0.26 \text{ A cm}^{-2}$ , qualitatively the same as in Fig. 26. At  $0.26 \text{ A cm}^{-2}$ , the bifurcation appears and  $\tau_k$  splits into two branches. Here,  $\tau_{k+1}$  starts to deviate from  $\tau_k$ , indicating that a full period is only completed once two maxima have happened. However, by increasing the current further, it becomes apparent that the bifurcation is followed by several other bifurcations. Namely, at  $\approx 0.33 \text{ A cm}^{-2}$  the time series becomes aperiodic (evident by the multiple values of  $\tau_k$  for a given current), at  $\approx 0.43 \text{ A cm}^{-2}$   $\tau_k$  abruptly starts to express three specific values and above  $\approx 0.53 \text{ A cm}^{-2}$  the time series becomes aperiodic again. Furthermore, in the current interval between  $\approx 0.32 \text{ A cm}^{-2}$  and  $\approx 0.43 \text{ A cm}^{-2}$  there seem to be different attractors: While in the upward current scan (red markers) two distinct  $\tau_k$  values are found, three values appear in the downward scan (black markers).

In the Figs. 30b-e, four different spatio-temporal patterns of the CO concentration in the channel are given. The different patterns represent short cutouts of the overall scan (Fig. 30a). In addition to each of the patterns, the time series of the spatially averaged anode overvoltage is given at the side. As can be seen from the course of the overvoltage, the pattern in Fig. 30b belongs to the simple periodic oscillations, the patterns in Figs. 30c-d relate to the oscillations with two and three distinct periods and the pattern in Fig. 30e is connected with the aperiodic case. All scenarios have in common that the CO concentration, at any time, continuously decreases from the inlet of the PEMFC ( $\zeta = 0$ ) towards the outlet of the PEMFC ( $\zeta = 1$ ) due to ongoing electrochemical CO oxidation. Thereby, the CO concentration at the outlet decreases with increasing current (from b to e).

The interesting aspect in the Figs. 30c-d is the appearance of downstream traveling CO shock fronts. The white dashed line in Fig. 30c indicates one of them. Their evolution can be understood in the following way: Imagine an ignition (short excursion of  $\bar{\eta}_a$  into the CO oxidation range) that cleans the surface from CO to a homogeneous minimum value (e.g. at  $t = t_0$  in d). Such a clean surface will briefly adsorb the CO that is still present in the channel but it will not be saturated due to its high capacity. Simultaneously, a bulk of fresh CO enters the cell with the gas velocity. At the front of this bulk, the electrode surface is passivated, thereby sharpening the front profile continuously [183].

The oscillations with the multiple ignitions per period seem to arise from the interaction of the homogeneous oscillations with the CO shock fronts. As was pointed out in [183], the new behavior

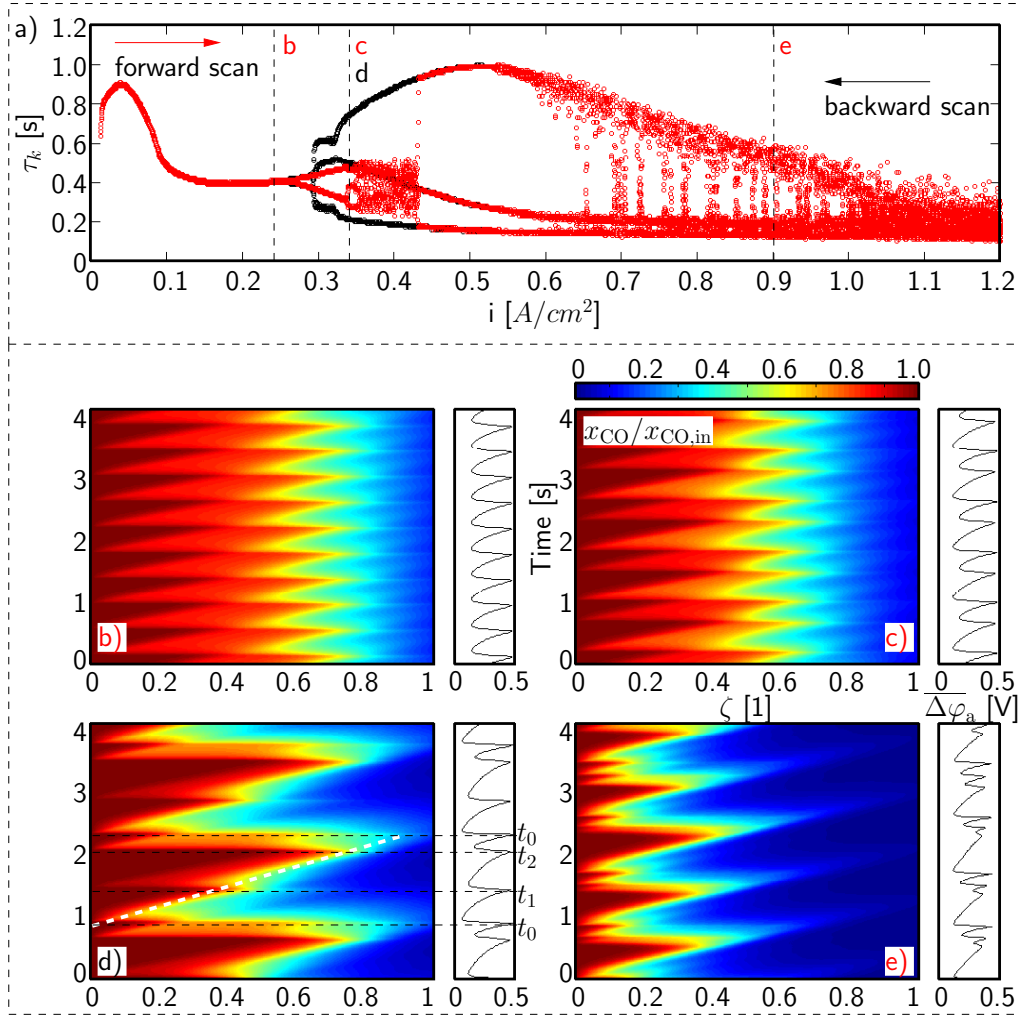


Figure 30: Simulated influence of a slow scan in the current density (scan rate  $1/3000 \text{ A s}^{-1} \text{ cm}^{-2}$ ) on the mean-field coupled homogeneous oscillations. a:  $\tau$  is the period between subsequent maxima in the time series of  $\overline{\Delta\varphi_a}$ . Apart from the oscillations with a single maximum per period, at larger current densities also oscillations with two or three maxima per period are predicted as well as chaotic oscillations. b-e: Space-time plots of  $x_{\text{CO}}$  at selected current densities (b:  $0.24 \text{ A/cm}^2$ ; c:  $0.32 \text{ A/cm}^2$  in the forward scan; d:  $0.32 \text{ A/cm}^2$  in the backward scan; e:  $0.9 \text{ A/cm}^2$ ); The white dashed line indicates the motion of one of the CO shock fronts. For the simulation  $F_{\text{in}} = 16 \text{ sccm}$ . Eq. (115) was replaced by Eq. (122). Other parameters as in Tab. 5.

only appears if the time that is needed by the front to pass the PEMFC is larger than the oscillation period in the absence of the front. Therefore, it is not surprising that the new behavior is seen for decreasing CO supply [183] and for increasing CO consumption (as above). In both cases the front speed is diminished. Another important point in the explanation of Fig. 30 might be that, on the one side, the homogeneous oscillation depends mainly on spatially averaged values but that, on the other side, the spatial profile is very inhomogeneous. Lets rationalize this idea by considering one period of the oscillation with the three ignitions per period ( $t_0 \rightarrow t_1 \rightarrow t_2 \rightarrow t_3$ ) in Fig. 30d.

At  $t = t_0$ , shortly after the last ignition, the channel is free of CO, but the electrode is (again) covered with some CO. A homogeneous CO coverage might be assumed for simplicity. As time proceeds and CO covers the catalyst from the inlet, the average CO coverage increases high enough, so

that  $H_2O$  can dissociate and that  $CO$  can be oxidized at  $t = t_1$ . However, in this ignition only very little  $CO$  adsorbate will be removed in the passivated inlet region, because rather much surface at the outlet is free for  $H_2O$  dissociation and hereafter  $H_2$  oxidation. Accordingly, the large increase in  $\eta_a$  originating from too much  $CO$  in the inlet region is quickly counteracted by  $H_2$  oxidation in the region downstream. After this insufficient ignition, only little  $CO$  can be adsorbed by the catalyst in the inlet region, because it is still saturated. Therefore, the new  $CO$  front does not start at the cell inlet but (approximately) at the point up to which the electrode was previously passivated. As the passivated region expands, the average  $CO$  coverage increases again. When the  $H_2O$  dissociation is "triggered" the second time (at  $t_2$ ), then the  $CO$  coverage at the outlet is even lower than in the last ignition, due to  $CO$  removal at  $t_1$ . Accordingly, the  $H_2$  oxidation rate is even higher at the outlet (compared to the prior ignition) and the  $CO$  oxidation is even smaller in the passivated region. Only once the front has traveled far enough, the overvoltage can sufficiently increase to yield an effective  $CO$  oxidation everywhere. Then the whole process repeats.

### *Current Density Patterns*

Yet, only space-time plots of the anode overvoltage and the molar  $CO$  fraction in the channel were introduced. This choice was appropriate for the illustration of the different patterns and the mechanisms in the system. However, the results depicted in the next chapter rely on the measurement of the spatial current distribution. It is therefore desirable to depict the current patterns that are associated with the qualitatively different space-time plots identified above. The current entering locally the electrode  $i_a$  follows from by Eq. (75)

$$i_a = \frac{I}{A} + \frac{d_m \kappa}{3L^2} \frac{\partial^2 \eta_a}{\partial \zeta^2} + \frac{\kappa}{d_m} (\bar{\eta}_a - \eta_a) . \quad (123)$$

Qualitatively different current patterns, derived from data presented previously, are collected in Fig. 31.

Starting the explanation with Fig. 31a-b it can be seen that the current distribution is flapping when the oscillators are synchronized due to mean-field coupling: After an ignition has occurred the current decreases at the inlet (green to blue) and increases at the outlet (green to red). The flapping results from enhanced passivation at the inlet (which decreases the current locally) and the constant current constraint (which forces an increase in current density downstream).

The same trend is also seen when the channel  $CO$  dynamics become important (Fig. 31c-d). But oppositely, in this case the whole cell does not recover equally well after an oscillation period. Instead, the inlet region remains poisoned and more current passes through the cleaner outlet region.

The other two scenarios (Fig. 31e-d and Fig. 31g-h) depict the impact of (local) migration coupling. As there is no important global feedback, the patterns simply resemble the space-time plots of the overvoltage. However, note that during defect turbulence (Fig. 31g-h) the current deviations from average are very high.

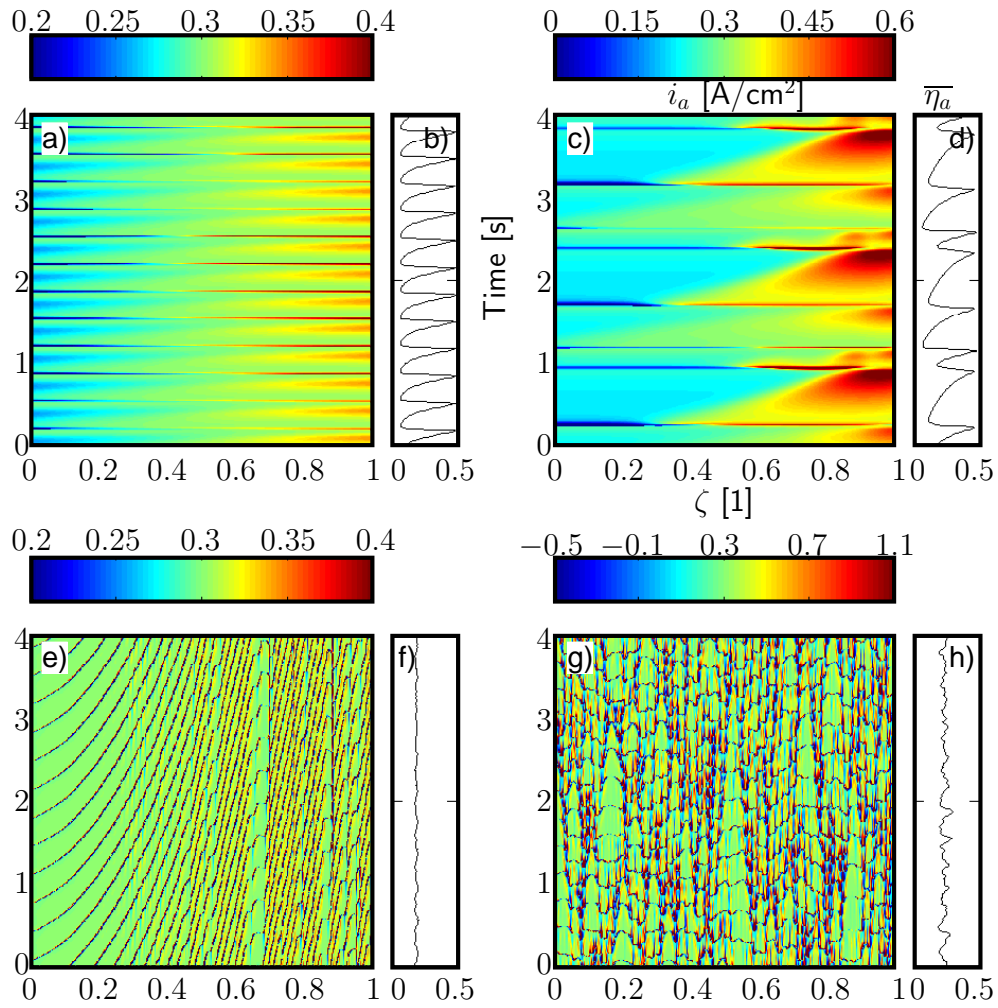


Figure 31: The current patterns that are associated with qualitatively different space-time plots. a-b: The homogeneous oscillation originating from strong mean-field coupling and large CO supply - refers to Fig. 30b; c-d: Interaction of the homogeneous oscillation with CO shock fronts originating from strong mean-field coupling and channel CO dynamics - refers to Fig. 30d; e-f: Waves and broken fronts arising from weak (local) migration coupling - refers to Fig. 27e-h; g-h: Turbulence caused by strong (local) migration coupling - refers to Fig. 28e-h.

### 3.4 H<sub>2</sub>,CO Oxidation in an Inhomogeneous PEMFC - Experiments

The previous section provided a detailed theoretical insight into spatially distributed electrochemical H<sub>2</sub>, CO oxidation in a PEMFC and derived specific predictions. The predictions were presented in the form of spatio-temporal current density patterns in Fig. 31 and represent two scenarios dominated by (global) mean-field coupling and two other scenarios dominated by (local) migration coupling. The scope of this subsection is the experimental validation of the predicted patterns. The results presented in this section were preliminary published by the author in [151].

Initially, the experimental procedure and the data preparation are depicted. Afterwards, experiments are carried out to investigate the predictions one after the other. Thereby, first the behavior is analyzed under galvanostatic control. Then, potentiostatic control is investigated.

#### 3.4.1 Experimental

In this subsection, first the fuel cell setup for the distributed current density measurement is introduced. Then, the preparation of the membrane electrode assembly is described. Afterwards, the used test-stand is sketched and the conditioning procedure depicted. Finally, the setup and the applied parameters for the following experiments are given.

##### *Measurement Device*

The measurement of the current distribution in a PEMFC has been proven to be a very helpful tool to investigate spatial inhomogeneities [187]. With its help, flow field design and operation conditions have been successively optimized in recent years (e.g. [188]). Several methods to measure the current distribution are reported in the literature. The three most important techniques are either based on the application of (1) a printed circuit board (PCB) [189, 190], (2) a resistor network [191, 192], or (3) an array of Hall effect sensors [193, 194]. The PCB technique was introduced in 1998 by Cleghorn et al. [189] and is based on the replacement of one current collector by a PCB. The PCB is segmented, whereby each segment has an individual electrically isolated pathway for current collection. The big advantages of the PCB technology compared to the other techniques are its simple implementation and its high spatial and temporal resolution.

For the present study, a device for the measurement of the current distribution, based on PCB technology, has been developed by S++ Simulation Services (Fig. 32a-b). The working principle is sketched in Fig. 32c-d. It is based on the measurement of voltages across multiple shunt resistors which are integrated into the PCB (trade name: Current Scan Shunt). The resistance of an individual shunt resistor is  $\approx 7 \text{ m}\Omega$ .

The device is constructed as follows: Initially, the shunt resistors are prepared by etching a special foil with a very low temperature coefficient. Then, the foil is embedded into a printed circuit board referred to as sensor plate. Afterwards, the shunt resistors are connected with vias to the contact segments on the top and the bottom of the sensor plate. A multiplexer, responsible to read out 8 shunts successively, is connected to the segments. The multiplexer signal is amplified and passed into an analogue digital converter. Finally, the signal is sent to the PC via USB interface. After calibration the actual current density profile is obtained.

In Fig. 32a-b the sensor plate is shown. Six parallel gas channels are machined into it. They are 14.4 cm in length and 4 mm in width (2 mm land and 2 mm channel). Each channel is equipped with 80 contact segments (and 10 multiplexers). Each segment is divided into two sub-segments left and



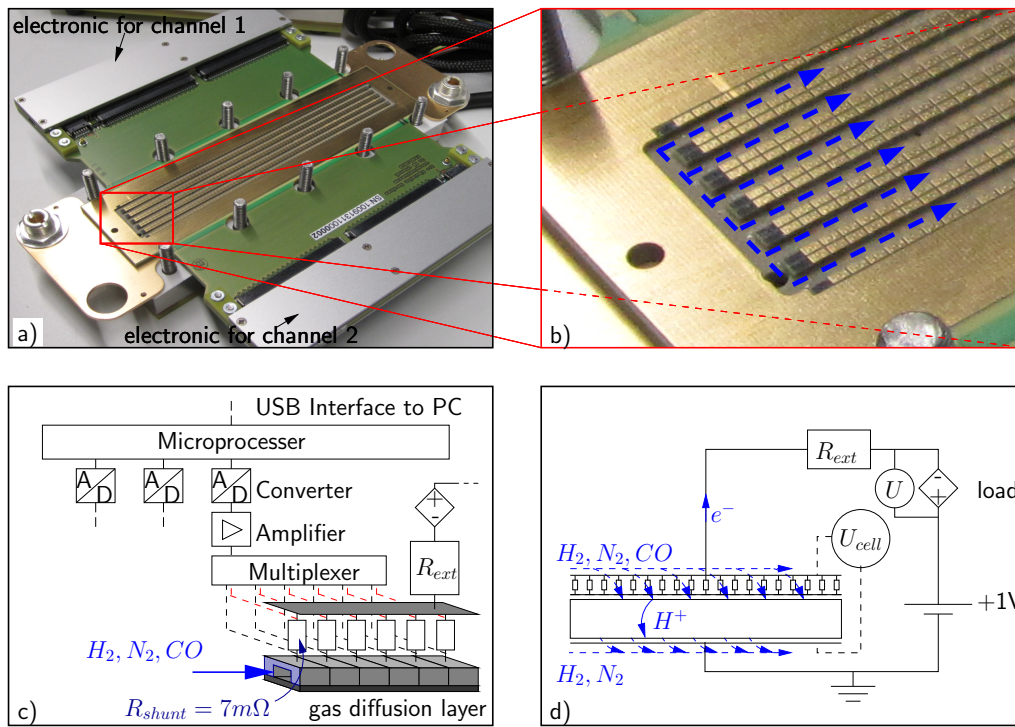


Figure 32: a: The segmented anode flow field with 80 segments per channel (channel length: 14.4 cm); The both inner channels are used for current distribution measurement, while the outer channels serve for homogenization. b: Each segment consists of two sub-segments that face across the channel. c: The scheme depicts how the current is read out with the help of small shunt resistors. d: The setup shows how the cell was implemented into the test-stand.  $R_{ext}$  stands for the line resistances.

right of the channel (Fig. 32b). The sub-segments were first galvanically plated with gold and then covered with a highly conductive anti-corrosive carbon varnish (not shown). The active area of a segment is  $1.8 \cdot 4 \text{ mm}^2$ . Only the two inner channels are connected to read-out electronics (Fig. 32a), the other channels are equipped with shunt resistors due to symmetry reasons. The minimum sampling time for a complete scan is 15 ms. The data is stored in ASCII format and analyzed with MATLAB for presentation.

#### Fuel Cell Preparation and Conditioning

After initial activation of a Nafion membrane in hydrogen peroxide (5% in  $H_2O$ ), subsequent boiling in sulphuric acid (1M), and final storage in Millipore water, the membrane (for thickness see Tab. 8) was spray-coated with the catalyst ink. The cathode catalyst ink was composed of  $Pt$ , purchased from Alfa Aesar, and 10 wt% Nafion (related to dry catalyst) dissolved in sufficient Millipore water. The anode catalyst contained  $PtRu$  50/50 instead of pure  $Pt$  but was identical in the other respects. The anode catalyst loading was chosen to be  $2 \text{ mg cm}^{-2}$  and  $1 \text{ mg cm}^{-2}$  for the cathode. The spray painted area was  $(144 \cdot 22) \text{ mm}^2$  in size.

The fuel cell was then assembled with the prepared MEA and  $200 \mu\text{m}$ -thick Toray papers that were surrounded by  $170 \mu\text{m}$  PTFE-sealing. The cell was then connected to a FuelCon test-stand which allows for convenient automatic control of the cell conditions via a predefined user interface. In short, each of the two gas lines contained several mass flow controllers for different gases (plus additional

valves for the full shut down of the inlets) followed by bubbler bottles, heating hoses between the bubblers and the cell (temperature always 5 K higher than cell temperature), a water collector in the cathode line and backpressure valves.

During conditioning, the cell was fed with  $1000 \text{ ml min}^{-1}$  hydrogen and  $1500 \text{ ml min}^{-1}$  air and held at  $60^\circ\text{C}$  cell temperature ( $\text{rH} = 100\%$ ). Then, the cell voltage was set to  $0.85 \text{ V}$  for 15 mins before it was held at  $0.60 \text{ V}$  for 10 mins and finally at open circuit voltage (ocv) for 3 mins. This cycle was carried out five times. Afterwards, the gas lines were flipped and the cycle was carried out five times again.

### Experimental Procedure

For the following experiments, the two inlets of the anode side were set up with  $\text{H}_2$  (purity: 5.0) and a mixture of  $\text{N}_2$  and 1%  $\text{CO}$  (purity: 4.8 for the  $\text{N}_2$ ). Usually, the feed flow rates were  $180$  and  $20 \text{ ml min}^{-1}$ , respectively. On the cathode side, a  $\text{H}_2, \text{N}_2$  mixture was used for most of the experiments. The  $\text{H}_2$  to  $\text{N}_2$  ratio was chosen to be 10% in order to minimize  $\text{H}_2$  diffusion towards the anode but still to guarantee a well-defined electrode. In addition, two experiments were also carried out with an air-fed cathode. To avoid any uncertainty the important operational parameters for all experiments are collected in Tab. 8. Please note, that a thicker membrane was applied in the case of the air-fed cathode. The reason for this choice will become clear in the discussion. Throughout all the experiments the cell was operated in co-flow arrangement.

	$T_{\text{cell}}$ [ $^\circ\text{C}$ ]	$T_{\text{dp}}$ [ $^\circ\text{C}$ ]	$p$ [bar]	$F_{\text{H}_2, \text{in}}^{\text{a}, \theta}, F_{(\text{N}_2, \text{CO}), \text{in}}^{\text{a}, \theta}$ [ $\text{ml min}^{-1}$ ]	$F_{\text{H}_2, \text{in}}^{\text{c}, \theta}, F_{\text{N}_2, \text{in}}^{\text{c}, \theta}$ [ $\text{ml min}^{-1}$ ]	$d_{\text{m}}$ [ $\mu\text{m}$ ]
Fig. 33	37	32	1.1	40, 40	20, 180	89
Fig. 34	37	32	1.1	180, 20	20, 180	89
Fig. 35	37	32	1.1	variable	20, 180	89
Fig. 36	37	32	1.1	126, 14	20, 180	89
Fig. 37	variable	variable	1.1	180, 20	20, 180	89
Figs. 38-39	37	32	1.1	180, 20	20, 180	89

	$T_{\text{cell}}$ [ $^\circ\text{C}$ ]	$T_{\text{dp}}$ [ $^\circ\text{C}$ ]	$p$ [bar]	$F_{\text{H}_2, \text{in}}^{\text{a}, \theta}, F_{(\text{N}_2, \text{CO}), \text{in}}^{\text{a}, \theta}$ [ $\text{ml min}^{-1}$ ]	$F_{\text{air}, \text{in}}^{\text{c}, \theta}$ [ $\text{ml min}^{-1}$ ]	$d_{\text{m}}$ [ $\mu\text{m}$ ]
Figs. 40-41	37	32	1.1	180, 20	1000	179

Table 8: Operating conditions for the following experiments.  $T_{\text{dp}}$  and  $p$  stand for the dew point temperature and the backpressure in both gas lines,  $F_{\text{H}_2, \text{in}}^{\text{a}, \theta}$  and  $F_{(\text{N}_2, \text{CO}), \text{in}}^{\text{a}, \theta}$  represent the feed flow rate of  $\text{H}_2$  and the  $\text{N}_2, \text{CO}$  mixture at the inlet at standard conditions. Oppositely, the differently indexed  $F_{i, \text{in}}^{\text{c}, \theta}$  represent the type of feed gas ( $i \in [(\text{N}_2, \text{CO}), \text{N}_2, \text{air}]$ ) and its feed flow rate into the cathode.  $d_{\text{m}}$  mimics the membrane thickness.

As the electric load of the test-stand (Höcherl and Hackl ZS Electronic Load) can only work passively, an additional voltage supply device (Statron Power Supply 2257.8, maximum voltage:  $4.0 \text{ V}$ , maximum current:  $100 \text{ A}$ ) was used if the  $\text{H}_2$ -fed cathode was applied (Fig. 32d). Its negative pole was attached to the cathode while the positive pole was connected to the load. The source was operated in current limiting mode with a set-up voltage of  $1.000 \text{ V}$ . In initial tests it was assured that the



voltage is stable for varying currents up to 30 A (maximal deviation < 10 mV). For operation with an air-fed cathode, the source was removed from the circuit.

The load allowed for galvanostatic- as well as for potentiostatic control. The total resistance of all lines was measured to be  $7 \pm 1 \text{ m}\Omega$ . For impedance measurements at 1 kHz a RCL meter (Fluke PM6303A Automatic RCL Meter) was used while the system was at ocv.

### 3.4.2 Results and Discussion: Galvanostatic Control

In this subsection, the results of galvanostatic electrochemical  $H_2, CO$  oxidation for a single pre-defined current are presented first to familiarize the reader with the principal information of such a measurement and also to sketch basic behavior. Next, current scans are introduced as a method to quickly search for bifurcation points. Afterwards, qualitatively different behaviors occurring under the influence of varied current and feed flow rate will be considered in detail. Finally, results are presented for varying humidity.

#### Behavior at Constant Current

Fig. 33 shows the spatio-temporal plots of the current density distributions in the two screened channels as well as the time series of the cell voltage and the average current in the observed cell area during galvanostatic control.

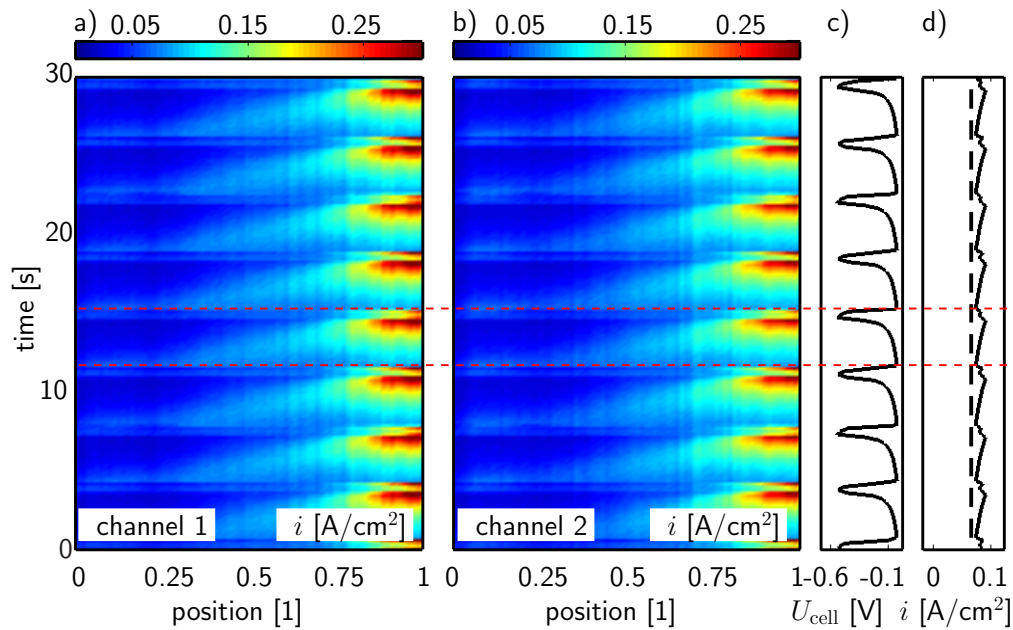


Figure 33: Experimental results for galvanostatic electrochemical  $H_2$  oxidation in a PEM fuel cell under influence of 5000 ppm  $CO$  for an integral current of 2 A. a-b: The spatio-temporal evolution of the current density in the two channels under observation; c: The related time series of the cell voltage; d: The related time series of the mean current density, averaged about the both channels (continuous line), as well as the setup current density (dashed line).

In Fig. 33c it can be seen that the cell voltage oscillates within a period of several seconds and has an amplitude of 500 mV typical for  $PtRu$  catalyst [95]. This time series resembles the information that is obtained with a conventional fuel cell (without spatially distributed current measurement).

Assuming a homogeneous system, this time series was successfully modeled [2, 109] and is well understood (see chapter 2). From the model perspective, the phenomenon can be rationalized as follows:

Whenever the cell voltage has recovered from minimal values (e.g. at  $t = 11$  s in Fig. 33) the electrochemical active surface has minimum  $CO$  coverage. From then on, as  $CO$  enters the cell with the feed stream,  $CO$  adsorbs onto the  $PtRu$  and hinders the oxidation of  $H_2$ . Because the current is set to be constant, the anodic overvoltage (a driving force for  $H_2$  oxidation) needs to increase. This leads to a decrease in the cell voltage. At a specific overvoltage (approx. 350 mV on  $PtRu$  [47, 126]) dissociation of water begins. This has two different effects. On one hand this process leads to a further reduction in the surface available for  $H_2$  oxidation but on the other hand it also provides the reactant for the oxidation of  $CO$ . As long as the overvoltage is further increasing the total coverage (by oxides and  $CO$ ) increases, too - even if the  $CO$  coverage is quickly falling. However, the oxidation of  $CO$  proceeds autocatalytically, meaning that surface freed from  $CO$  will immediately support water dissociation and enhance the  $CO$  oxidation. At the point in time when the  $CO$  oxidation rate exceeds that of water dissociation more surface is freed from  $CO$  compared to what is lost due to oxide formation, therefore freeing up space for  $H_2$  oxidation. The decreasing overvoltage in turn leads to quick formation of water from surface oxides (the reverse reaction of water dissociation) and enhances the  $H_2$  oxidation rate leading to a further drop in overvoltage. A minimum in overvoltage is reached (maximum in cell voltage) once the  $H_2$  oxidation equilibrium is established on the less  $CO$  contaminated catalyst. From this point the cycle repeats itself. The part of the period during which  $CO$  is oxidized (when the overvoltage is sufficiently large) will be called "ignition" in the rest of the manuscript. An oscillation-period (interval between red marks in Fig. 33) is thought to start, and to end, at the end of an ignition.

However, compared to the picture of a homogeneous system, where it is believed that the local current density is spatially homogeneous during an oscillation-period, it can be clearly seen in Fig. 33a-b that the current locally oscillates with the same period as the cell voltage. Connecting the spatio-temporal plot of the current with the explanation of the cycle given above, it can be concluded that the current in the inlet region diminishes after the maximum cell voltage has been reached. This indicates that  $CO$  poisoning begins at the inlet of the cell and proceeds downstream. Simultaneously to the current decrease at the inlet, the current in the outlet region increases because of the constant current constraint assured by the load. The result is a current distribution that is flapping with the same period as the cell voltage oscillates.

Finally, note the following two aspects: Firstly, due to the fact that the current distribution of the both channels is almost identical, only one channel will be presented in the rest of the galvanostatic discussion. Secondly, the spatially averaged current density of the two channels oscillates itself (Fig. 33d) and does not coincide with the expected value (predefined by the setup current through the load, the dashed line in Fig. 33d). Likely, this kind of deviation is caused by inhomogeneities in connection with the galvanostatic constraint. Thus, in the  $CO$  adsorption phase, a more severe current degradation in one channel is compensated by a less severe current degradation in the other channels (e.g. by the two screened ones, see Fig. 33d). Oppositely, in the  $CO$  oxidation phase, this altered current distribution is revoked (Fig. 33d). The discrepancy between the setup current density and the measured value in the observed region is even more enhanced at larger currents and can lead to deviations of up to 30% (e.g. Fig. 34a).

### Influence of Current Density and Feed Flow Rate

In order to search for the bifurcations that were predicted in section 3.3.2, at next the current density is scanned. Of course, the scan rate needs to be sufficiently low in order to avoid transient effects. Therefore, an appropriate current scan rate is validated from integral information before the feed flow rate is varied. Spatially resolved data are taken into account later.

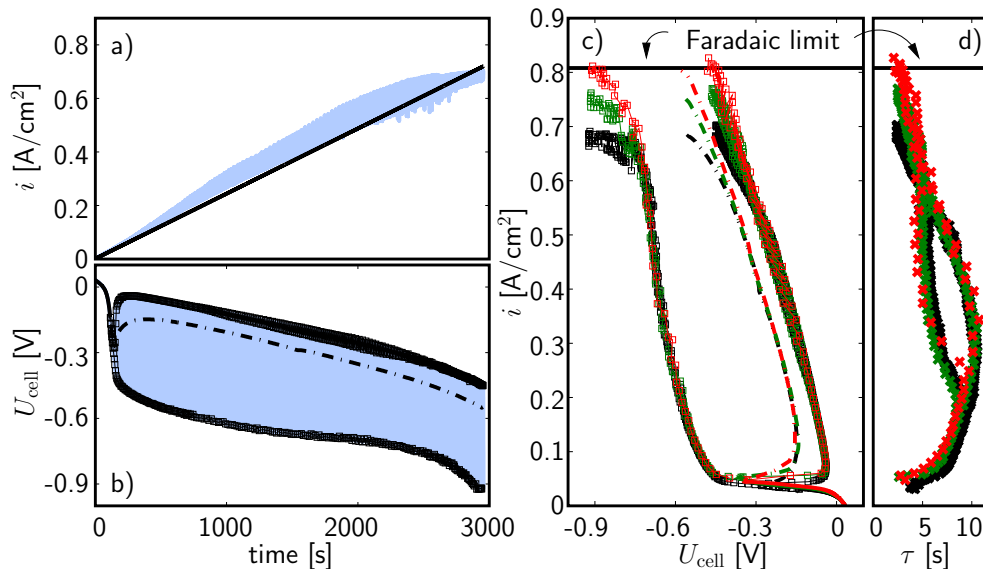


Figure 34: Integral experimental results for galvanostatic electrochemical  $H_2, CO$  oxidation while performing current scans. a: The trajectory of the calculated average current density in the observed cell area (blue line) and the setup value (black line - scan rate of  $28 \text{ A}/3600 \text{ s}$ ); b: The related trajectory of the cell voltage (blue), the extrema (black boxes) and the temporal average (dash dotted line); c: Polarization curves and d: Oscillation periods for different scan rates (red:  $28 \text{ A}/400 \text{ s}$ , green:  $28 \text{ A}/1200 \text{ s}$ , black:  $28 \text{ A}/3600 \text{ s}$ ).

Fig. 34a-b shows the average current density and the cell voltage in the observed region during a slow scan of the applied current. The current density in the observed region follows the defined value up to a current density of  $0.05 \text{ A cm}^{-2}$  (Fig. 34a). In that interval the cell voltage quickly drops to about  $-0.35 \text{ V}$  (Fig. 34b) due to a lack of free catalyst surface for  $H_2$  oxidation in the course of enhanced  $CO$  blockage (e.g. [109]). At  $-0.35 \text{ V}$  the behavior changes as the dissociation of  $H_2O$  becomes important, allowing the oxidation of  $CO$ . However, soon the system loses stability and starts to oscillate (The  $CO$  is only oxidized during the ignition phase of the oscillations). As the current scan in Fig. 34a-b is carried out very slowly, too many oscillations are carried out per current interval to resolve the cell voltage trajectory. Instead, a homogeneously colored blue surface appears. Apart from the time series of the cell voltage itself, the branches that represent the extrema and the temporal average in the oscillatory regime are given in addition to the branch of stable cell voltage at current densities below  $0.05 \text{ A cm}^{-2}$ .

The derived polarization curve is shown in Fig. 34c. Additionally, polarization curves for two significantly higher scan rates are depicted. For higher transparency the trajectories of the cell voltage are omitted. From the polarization curves, no differences can be seen except at high current densities, when the current approaches the Faradaic limit and  $H_2$  is drawn from the anode outlet tube. In

addition to the polarization curves, the periods,  $\tau$ , of the oscillations are shown in Fig. 34d in the form of a  $\tau(i)$  diagram ( $\tau$  is defined to be the time between subsequent maxima of the cell voltage trajectory). This figure was found to be very sensitive to various cell conditions; thus it is adequate for the comparison of different scan rates. Here, a period doubling bifurcation is found at approximately  $0.25 \text{ A cm}^{-2}$  with a small shift towards positive current density for the largest scan rate (Fig. 34d). This indicates that the two lower scan rates are sufficiently low in order to consider the system as being in a steady (oscillatory) state. However, for subsequent scans the lowest scan rate of  $28 \text{ A h}^{-1}$  is chosen in order to obtain a more dense  $\tau(i)$  diagram.

The influence of the feed flow rate onto the integral oscillatory behavior is collected in Fig. 35. As can be seen in Fig. 35a, a cascade of period doubling bifurcations is well expressed for small feed flow rates. The bifurcations diminish with increasing feed flow rate until they disappear at

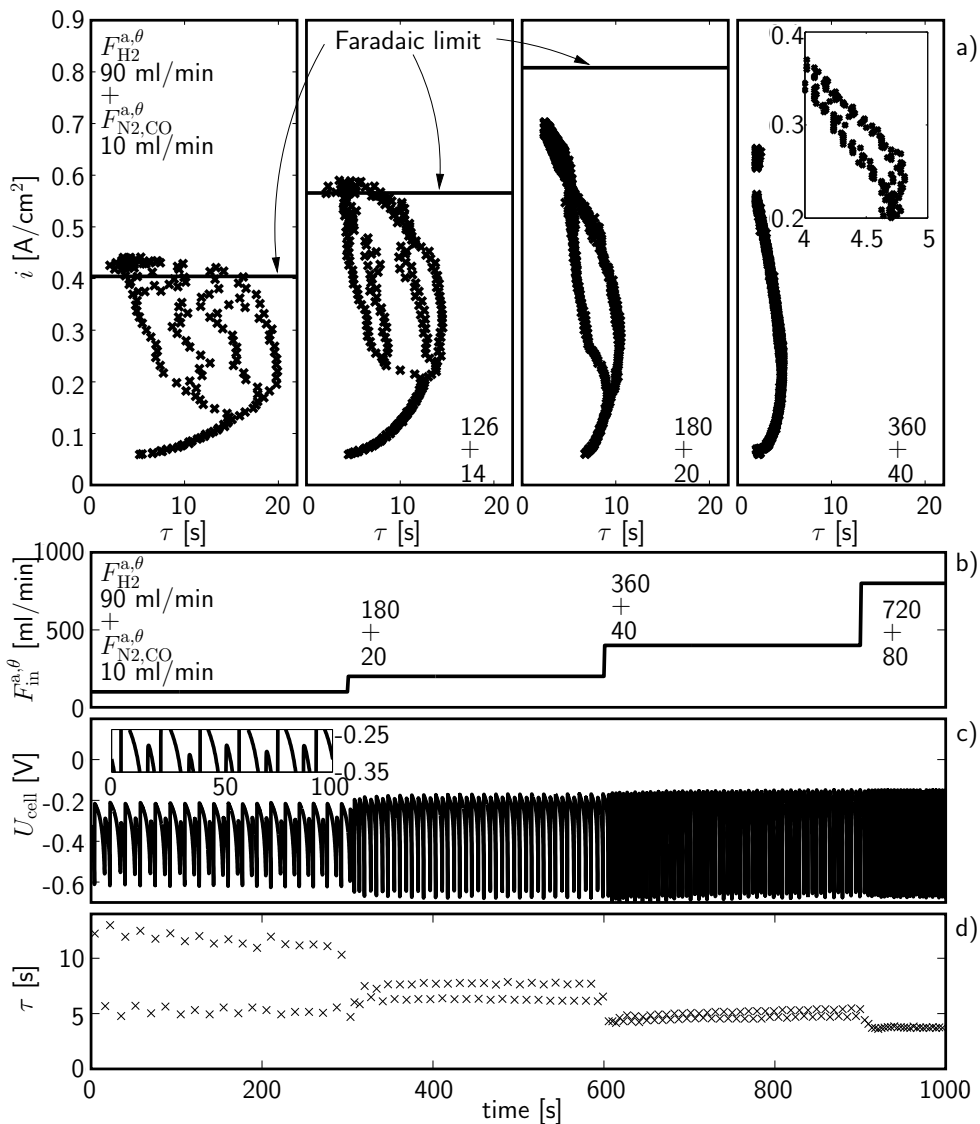


Figure 35: a: shows the change of the homogeneous oscillation period during slow current scans for different feed flow rates. b: For a fixed cell current of  $0.31 \text{ A cm}^{-2}$  steps in the total feed flow rate are carried out. The measured time series of the cell voltage and the related oscillation periods are depicted in c-d. In all experiments the  $\text{CO}$  inlet concentrations was 1000 ppm.

about  $400 \text{ ml min}^{-1}$ . In Fig. 35b the current is held constant while the feed flow rate is increased stepwise. Of course, the trend is the same: The increase of feed flow rate leads to the homogenization of subsequent periods. However, it turns out that the regime with the four fold period does not survive longer than a couple of minutes. Thus the occurrence of this regime in the Fig. 35a (and Fig. 36b) needs to be considered as transient.

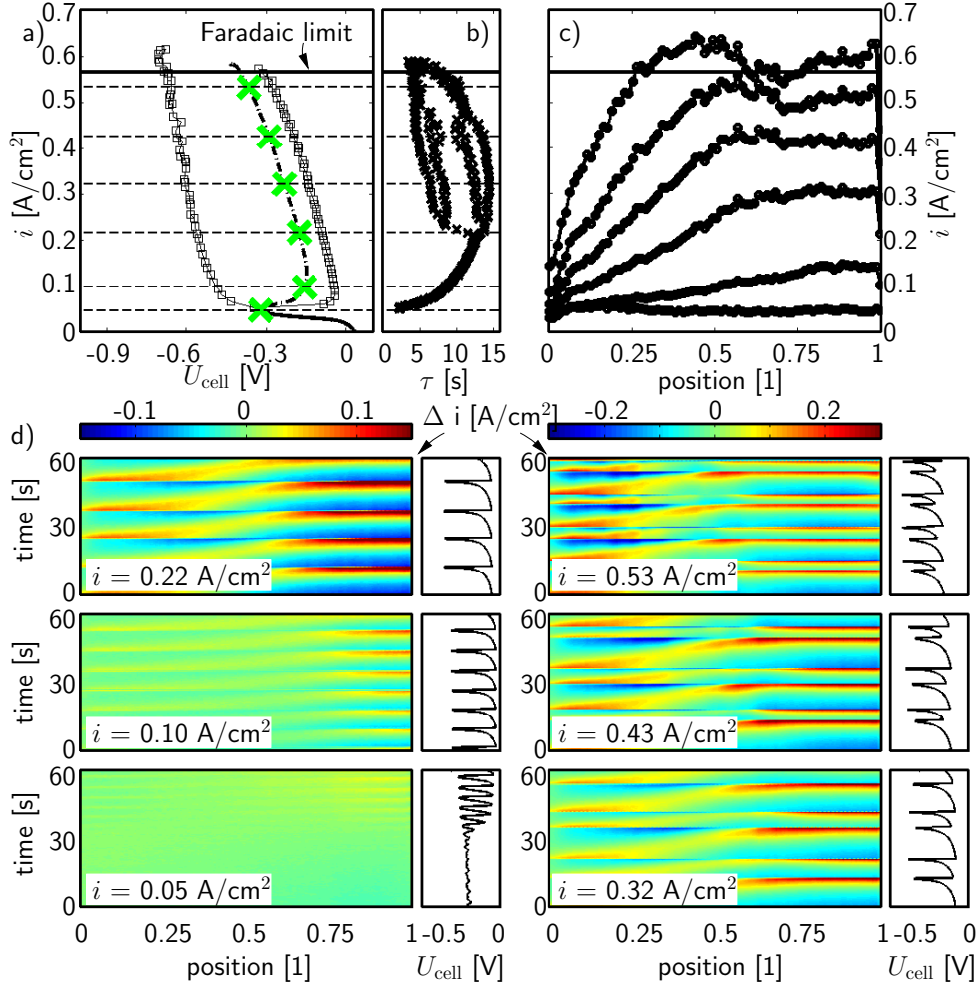


Figure 36: Collected experimental results for a current scan during electrochemical  $H_2, CO$  oxidation. a: Polarization curve; b: Periods; c: Temporally smoothed profiles to see the average trend during the current scan. d: Spatio-temporal plots of the measured spatially distributed current signal (corrected for its temporal space dependent average) starting with the current value given in the plots. The definition of  $\Delta i$  is given in Eq. (124). Scan rate:  $28 \text{ A}/3600 \text{ s}$

Fig. 36 gives an overview of the spatio-temporal results obtained at a constant total feed flow rate of  $140 \text{ ml min}^{-1}$ . The green crosses in the polarization curve (Fig. 36a) mark the position at which the average profiles of the current distribution in Fig. 36c are shown. These profiles reflect the temporally smoothed current distribution while changing the global current. Looking at these profiles a general trend can be observed: At the lowest current, before the onset of oscillations, the current distribution is rather homogeneous. This indicates that no  $CO$  is oxidized and that  $H_2$  oxidation occurs on a homogeneously poisoned surface. At higher currents, the current density increases initially at the outlet. The effect can be rationalized by considering the  $CO$  concentration: As  $CO$  is oxidized its

concentration gradually decreases along the channel and accordingly the coverage of  $CO$  is smaller at the outlet. At currents larger than  $0.2 \text{ A cm}^{-2}$  a plateau appears in the outlet region coinciding with a first period doubling bifurcation apparent from Fig. 36b. The high plateau indicates that the  $CO$  coverage in the corresponding region is in average rather low and homogeneous. An explanation might be that almost all  $CO$  is oxidized in the region upstream and that in the plateau region mainly  $H_2$  is consumed. This idea will be further discussed in the following paragraphs.

Fig. 36d shows six excerpts of the spatially distributed measurement that were recorded during the scan. But instead of showing the current distribution, only the deviation from the local average  $\Delta i(z, t)$  is depicted.

$$\Delta i(z, t) = i(z, t) - \frac{1}{T} \int_0^T i(z, t) dt. \quad (124)$$

Thereby,  $T$  is the length of the considered time window (60 s in Fig. 36d). The setup current density at which the excerpts start, is given at the side.

At the lowest current density it can be seen how the system behaves at the onset of the oscillations. While the cell voltage starts to oscillate, the current distribution is rather flat, meaning that the homogeneous state of the system becomes unstable first. With increasing current then also the current distribution starts flapping. At low currents two subsequent oscillations have roughly the same period (see Fig. 36b). But at approximately  $0.20 \text{ A cm}^{-2}$  a first period doubling bifurcation appears before another one happens at about  $0.25 \text{ A cm}^{-2}$ . At high currents it is difficult to draw clear conclusions due to the influence of the transport limit. However, it seems that at about  $0.4 \text{ A cm}^{-2}$  the system starts to behave aperiodic.

When considering the cell voltage in Fig. 36d ( $0.32 \text{ A cm}^{-2}$ ) in detail, please note that, compared to the longer periods, the short periods always end with a more negative minimum, indicating that at the end of a short period more  $CO$  is oxidized. Consequently, from the spatio-temporal plot, it can be seen that at the end of each long period (e.g. at  $t = 59 \text{ s}$ ) the current increase at the outlet is larger compared to the end of a shorter period (e.g. at  $t = 46 \text{ s}$ ). This behavior shows that at the end of long periods only little  $CO$  is present at the outlet leading to a large  $H_2$  oxidation rate. Therefore, the onset of the plateau in the smoothed current profile (Fig. 36c) might indicate the point between an upstream region in which  $CO$  is oxidized during every ignition and a downstream region in which  $CO$  is oxidized only during every second ignition. In the temporal average, then the downstream part of the cell would lead to major  $H_2$  oxidation, while the upstream part is more concerned with  $CO$  oxidation. Therefore, the onset of the plateau in the smoothed current profile (Fig. 36c) might indicate the point between an upstream region which is more concerned with  $CO$  oxidation and a downstream region of the cell that is preliminary oxidizing  $H_2$ .

The pattern need to be compared with the theoretical prediction that occurred due to the influence of the channel  $CO$  balance at decreasing feed flow rate. The characteristic current patterns were presented in Figs. 31c-d and arise from the interaction of the homogeneous oscillation with  $CO$  shock fronts. The patterns appeared when the velocity of the shock was sufficiently diminished (by rising the  $CO$  consumption via an increase in the current density or decreasing the feed flow rate). Then, the time that the front needed to pass the PEMFC exceeded the period of the homogeneous oscillation. Let us check whether this true in the given experiment (Fig. 36). The “unperturbed” homogeneous oscillation period can be found at the largest feed flow rate. From Fig. 35a the minimum period of the homogeneous oscillation at  $400 \text{ ml min}^{-1}$  is found to be 2 s. The time that a fictive  $CO$  shock front needs to pass the channel cannot be seen so easily. But as a front has to travel slower than the  $H_2$  bulk,



the residence time mimics an upper estimate. With the parameters applied for the given experiment (Fig. 36), the residence time follows to be 1.6 s. Therefore, the necessary condition for the occurrence of shock fronts is fulfilled. Another agreement between experiment and model regards the qualitative course of the cell voltage (compare the cell voltage at  $0.4 \text{ A cm}^{-2}$  in Fig. 36 with Fig. 31d). Indeed, the feature of an extended period that follows a more negative cell voltage (a more positive anodic overvoltage) during the prior oxidation phase is also reflected by the model. Discrepancies mainly arise during quantitative comparison. Finally, as the residence time is slower than the oscillation period and as the current pattern as well as the cell voltage trajectory qualitatively agree with the predicted scenario, it seems reasonable to conclude that this period doubling cascade is caused by CO shock fronts.

### *Influence of the Membrane Conductivity*

As illustrated in Sec. 3.3, the membrane resistance (conductivity) is expected to be a reasonable parameter to switch between qualitatively different spatio-temporal behavior. The regime dominated by strong mean-field coupling, evident in the results above, is expected to suddenly change into a spatio-temporal chaotic regime when decreasing the membrane conductivity (increasing the membrane resistance). The purpose of this section is the attempt to experimentally validate this prediction.

The membrane conductivity was changed by varying the cell temperature  $T_{\text{cell}}$  and the dew point temperature  $T_{\text{dp}}$ . At each specific pair of temperatures a galvanostatic scan was carried out with a scan rate of  $28 \text{ A h}^{-1}$ . The scan was interrupted once the cell voltage fell below  $-1 \text{ V}$ . Several values were extracted to characterize the results, these values are: the averaged oscillation period (averaged about the whole scan), the current density at which the oscillations set in and the maximum current density that was obtained in the scan (most likely the cell voltage was minimum then). Furthermore, the highest period doubling bifurcation of the scan was taken in order to see the change of the oscillation behavior: "1T" is for oscillations with one maximum period, "2T" is for oscillations with two maxima period and so forth. Fig. 37 collects the results.

From the information depicted in Fig. 37 three general trends can be derived that have major influence on the results. Firstly, for increasing cell temperature the oscillation period dramatically decreases. When the dew point temperature is set to  $37^\circ\text{C}$  the period drops from 6.1 s at  $37^\circ\text{C}$  cell temperature to less than 0.3 s at  $60^\circ\text{C}$  cell temperature (The temporal resolution during these scans was about 150 ms. Therefore, 0.3 s represents the technical limit. Likely, the oscillations were faster than this.). This behavior was already observed during the initial finding of the oscillations in PEMFCs [2] and attributed to the change in the CO adsorption [92]. Secondly, for increasing cell temperature there is a shift of the Hopf point towards larger current densities. It can be explained with an altered CO adsorption/desorption behavior in addition to improved  $\text{H}_2$  adsorption [92]. Thirdly, for decreasing  $rH$  it was found that the maximum current density that can be driven through the cell, also decreases. For an  $rH$  of 75% the maximal current density is larger than  $0.6 \text{ A cm}^{-2}$ . It decreases to  $0.24 \text{ A cm}^{-2}$  at 30%  $rH$ . This trend cannot be explained by an increased electrolyte resistance alone and was also present in subsequent experiments in the absence of CO (not shown), indicating that this effect has to do with anode dry out. Anode dry out is known to influence conventional PEMFC operation ( $\text{H}_2/\text{O}_2$ ) during operation with poorly humidified gases [78, 195]. For co-flow configuration the typical fingerprint is then the following: Close to the inlet the current density as well as the water content in the anode gas is high. Downstream, the anode gas humidity quickly decreases due to the drag of water towards the cathode. Accordingly the current density also diminishes. Op-



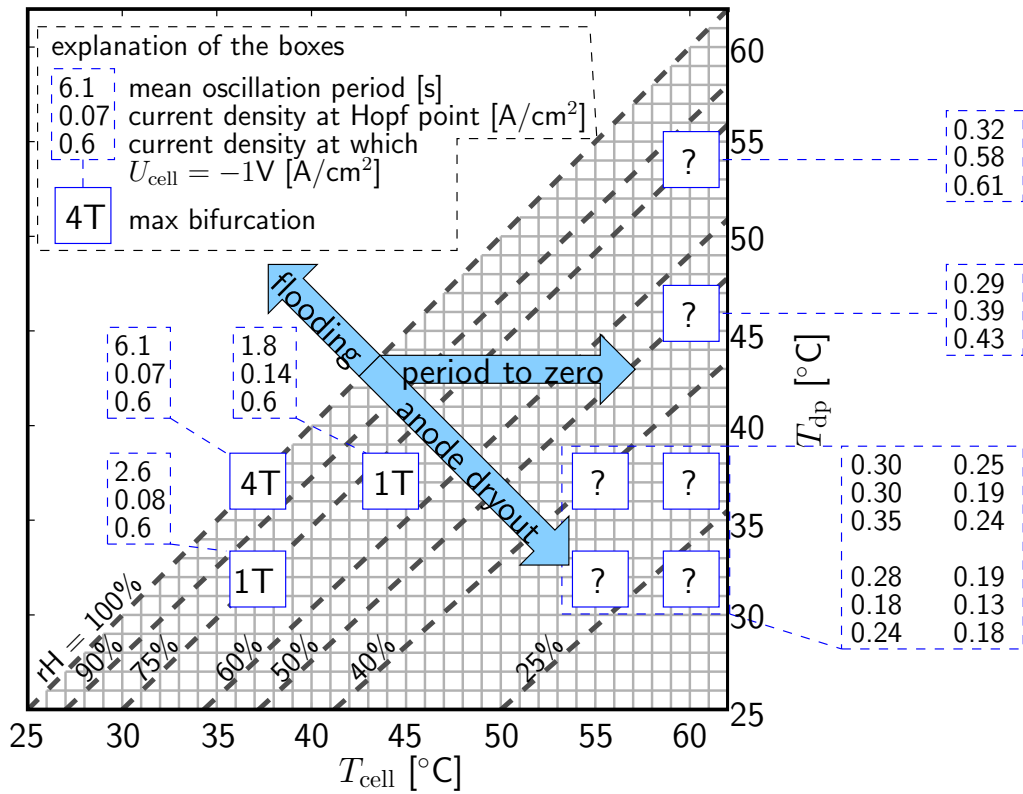


Figure 37: Collected results of galvanostatic scans at various cell- and dew point temperatures. The blue continuous boxes are centered around the pair of temperatures which define the measurement conditions. In the box the highest period doubling bifurcation is written. In the dashed boxes other characteristics of the scans are collected. Additionally, critical influences are indicated that hinder the investigation at high cell temperature (fast oscillations), low conductivity (anode dry out) and high water feed (flooding). Scan rate: 28 A/3600 s.

positely, due to water production at the cathode in conventional PEMFC operation, also the back diffusion enhances such that the anodic  $rH$ , as well as the current density, recovers towards the end of the channel once a minimum has been passed. However, as in the present study the current continuously diminishes along the channel it is likely that this is due to the  $H_2$ -fed counter electrode used in the present study at which no water production appears.

The final conclusion of studying the influence of the membrane resistance is that no spatio-temporal turbulence, like that predicted in Sec. 3.3, was found. Arguing about the discrepancy between the experiment and the model, it need to be stated that the model was very simplistic with respect to the water balance. In fact, in the model it was assumed that the gases are saturated at any time and at any place and that the membrane conductivity is also constant in space and time. No water drag and no back diffusion were included because the focus has been on the electrochemical  $H_2, CO$  oxidation. Under these pre-conditions the assumption that the current can be kept stable while the resistance is raised lead to the appearance of spatio-temporal turbulence (if the system dimensions were chosen properly). In the experiment these preconditions fail because of anode dry out. In this case the maximum current quickly drops with falling  $rH$  and therefore impedes the idea to decrease the current sufficiently in order to find spatio-temporal turbulence. However, as will

be shown in the following section, potentiostatic experiments offer an opportunity to search for this regime at high conductivities when anode dry out is absent.

### 3.4.3 Results and Discussion: Potentiostatic Control

No waves and no spatio-temporal turbulence were found during galvanostatic control. Instead, mean-field coupling was always dominant. However, potentiostatic experiments offer an option to diminish mean-field coupling, while leaving migration coupling (that might lead to chaos) unchanged. To see this, Eq. (85) is re-called. Thereby, the anode double layer voltage is replaced in favor of the anode overvoltage

$$c_{dl,a} \frac{\partial \eta_a}{\partial t} = -\frac{U + \eta_a}{A(R_\Omega + R_{ext})} - i_{F,a} + \frac{d_m^2}{3AR_\Omega L^2} \frac{\partial^2 \eta_a}{\partial \zeta^2} + \frac{R_{ext}(\bar{\eta}_a - \eta_a)}{AR_\Omega(R_\Omega + R_{ext})}. \quad (125)$$

Compared to galvanostatic control (Eq. (86)), the new variables  $R_{ext}$  and  $U$  stand for an external resistance (lines etc.) and the load voltage, respectively (see Fig. 32c-d). Galvanostatic control can be re-obtained from Eq. (125) if  $I_{load} = -U/R_{ext}$  is kept constant while increasing the external resistance to infinite values ( $R_{ext} \rightarrow \infty$ ). In that case also the factor controlling the mean-field coupling term becomes maximal (for a given  $R_\Omega$ ). Oppositely, the influence of the global coupling term vanishes for decreasing external resistance and disappears for  $R_{ext} \rightarrow 0$ . Therefore, the control of  $R_{ext}$  during potentiostatic operation allows to diminish mean-field coupling alone while leaving migration coupling unchanged. This is in contrast to the change of  $R_\Omega$  (membrane conductivity) during galvanostatic control, where both coupling terms were affected.

As in the model analysis (Sec. 3.3) a dominant migration coupling term lead to the occurrence of waves (Fig. 31c-d) and spatio-temporal turbulence (Fig. 31g-h), it is reasonable to assume that these scenarios are more easily found with potentiostatic control compared to galvanostatic control. The only necessary pre-condition is that the homogeneous potentiostatic system can also oscillate at lower  $R_{ext}$  (steeper load line, see first term r.h.s. in Eq. (85)).

In the present section, results of potentiostatic electrochemical  $H_2, CO$  oxidation are presented. Initially, the behavior during a voltage scan is depicted. Then, the response to voltage steps is shown. Finally, the impact of the counter electrode is investigated. For this reason the  $H_2, N_2$  mixture, that was up to then fed into the counter electrode compartment, is replaced by air. In that way the behavior of a conventional PEMFC under potentiostatic operation with  $H_2, CO$  mixtures is illustrated.

#### Scanning the Cell Voltage

Fig. 38 collects the results for a voltage scan with a scan rate of 1 V/2000 s. In Fig. 38a the polarization curve can be seen. The branch at high cell voltages (beyond  $-0.35$  V) is characterized by a very little slope, while the branch at lower cell voltage (beneath  $-0.35$  V) shows a very steep decrease. The slope of this last branch can be explained almost entirely with the membrane losses. Accordingly, the change in the (spatially averaged) anodic double layer voltage is minor.

Current density profiles at specific cell voltages (indicated in Fig. 38a with colored crosses) are depicted in Fig. 38b. In comparison with Fig. 36c here the profiles are not smoothed but represent the true current distribution at that time. In general an increase in current profile towards the outlet of the cell can be seen at voltage sufficient for  $CO$  oxidation (below  $-0.35$  V). This trend is the more pronounced the lower the cell voltages. The effect relates to the diminishing  $CO$  mole fraction due to cumulative  $CO$  oxidation. However, in a certain voltage interval the profiles show spikes (e.g. red

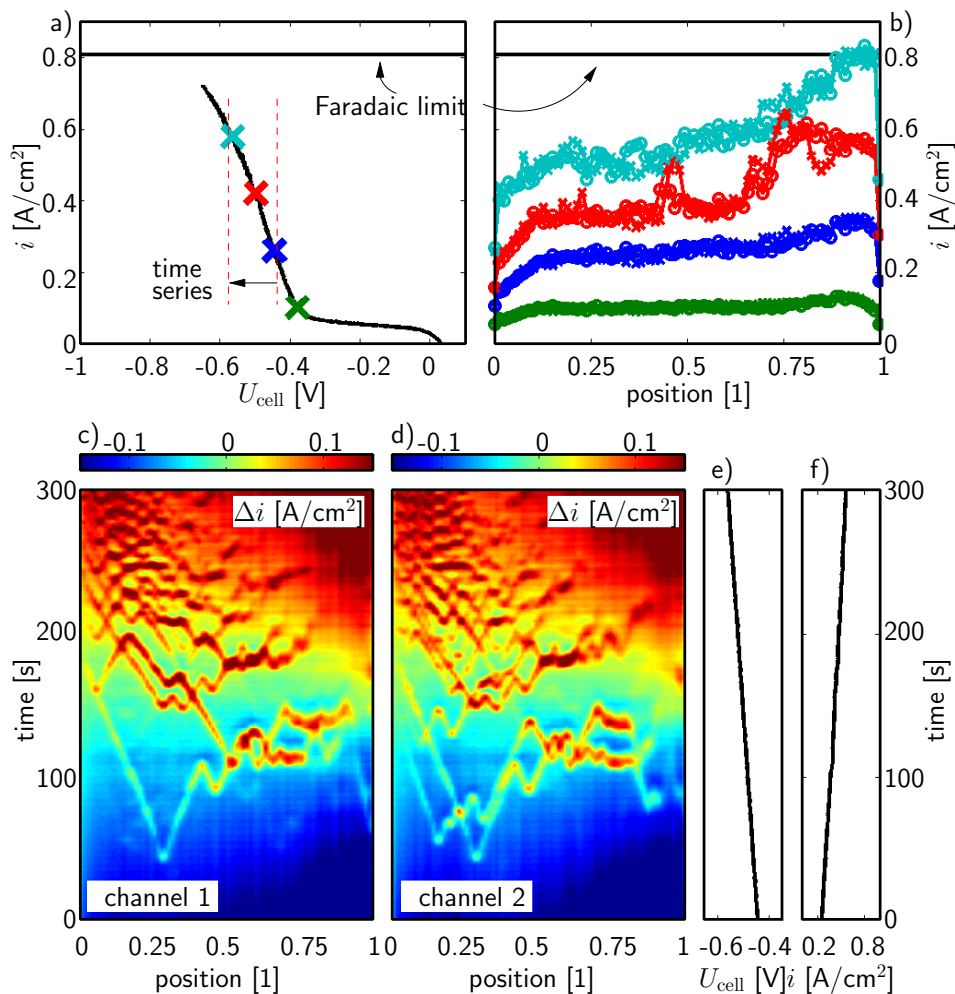


Figure 38: Collected experimental results for a voltage scan during potentiostatic electrochemical  $H_2, CO$  oxidation. a: Polarization curve; b: Current density profiles at specific moments.  $\times$  and  $\circ$  represent the individual channels. c-d: Spatio-temporal plots of the measured spatially distributed current (corrected for its temporal space dependent average); e-f: Cell voltage and average current density in the observed region. Scan rate: 1 V/2000 s.

curve in Fig. 38b) while the integral polarization curve (Fig. 38a) is smooth. The meaning of these spikes is clarified in the Figs. 38c-d which show the current density deviations from the local average in the time interval depicted in Fig. 38a.

Globally, the spatio-temporal plots turn from blue at high cell voltages ( $-0.44$  V) to red at low cell voltages ( $-0.58$  V) due to the increasing current density. However, apart from that, several straight lines can be seen which depict the propagation of pulses. Apparently, below a certain cell voltage ( $-0.46$  V in the present configuration) current bumps form at arbitrary positions that soon split into two pulses that travel in the down- and upstream direction. Thereby, the pulses seem to be very local objects as they do not appear necessarily in both channels simultaneously (e.g. compare Fig. 38c with d at 50 s). As the traveling speed is independent from the direction (about 1.7 cm/min) and much slower than the gas velocity (about 90 cm/min) they likely represent objects restricted to the active area. Another interesting observation is that some of the pulses extinguish each other (Fig. 38c at 120 s at the position 0.4) while in other situations they seem to cross without noticing (Fig. 38c at 160 s at

the position 0.4). However, it is difficult to conclude that these pulses truly cross. It could also be that the pulse in-plane extension is much smaller than the individual segments of the measurement board. In that case it would seem that they cross while they pass each other closely. Crossing pulses would indicate that the present understanding of electrochemical  $H_2, CO$  oxidation is incomplete, for the following reason: After the pulse has crossed a certain place, the  $CO$  coverage is lower at that place and this site is necessarily not excitable until a sufficient  $CO$  surface coverage has recovered. Therefore, left and right of the position where two pulses intersect the surface would not be excitable, too.

### Stepping the Cell Voltage

Fig. 39 collects the integral signals and the spatio-temporal plots of one of the two channels after stepping through the voltage. After each of the steps, a characteristic overshoot in the current can be seen (Fig. 38b). The related irregularities in the cell voltage (Fig. 38a) are a consequence of the control loop of the load. The overshoot indicates the presence of  $CO$  oxidation (more effective at the outlet: see Fig. 38c) and is absent at cell voltages that are larger than  $-0.4$  V. Late after the residence time (about 1.5 s) has passed, the overshoot disappears (more than 20 s), indicating that after a rather effective ignition, triggered by the step, it takes some time to supply sufficient  $CO$  to passivate the surface again.

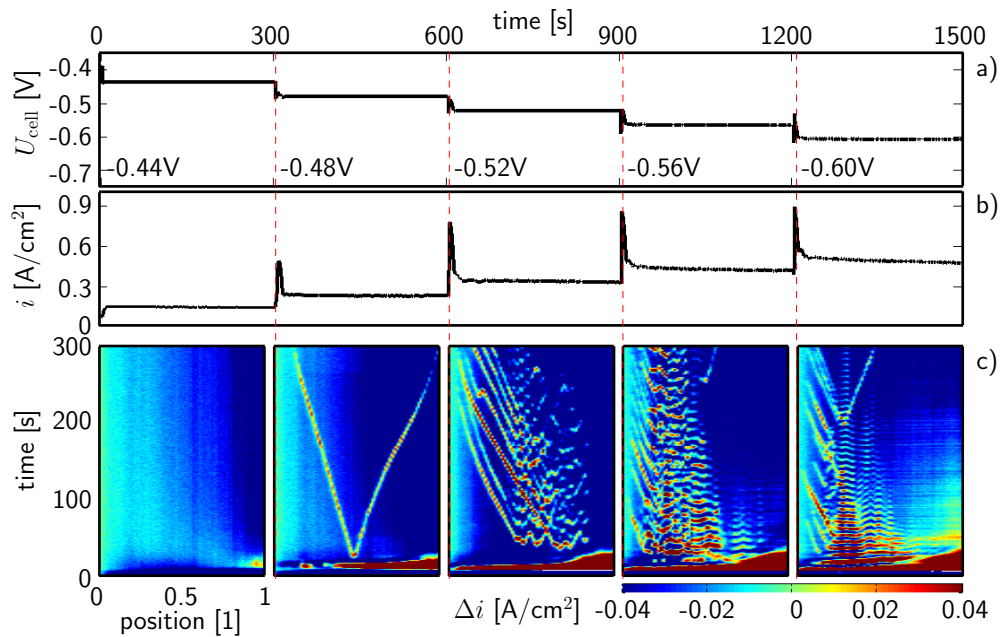


Figure 39: Collected experimental results for sudden steps of the voltage during potentiostatic electrochemical  $H_2, CO$  oxidation. a: The defined cell voltage profile; b: The related average current density in the observed region; c: Spatio-temporal plots of the measured spatially distributed current signal (corrected for its temporal space dependent average) for one of the two channels beginning at the voltage step.

Apart from this general feature, other phenomena can be also identified. First of all, the second step in Fig. 39a to  $-0.48$  V triggers two pulses that are formed by the splitting of a single perturbation at the center of the channel (Fig. 39c). While the pulse that moves upstream travels with constant

speed, the pulse that travels downstream undergoes some velocity variation. The reason for this alteration is unclear and also no general feature.

After the next step to  $-0.52$  V, in the center of the channel some oscillations are found that die out in the course of minutes. The spatial variation in this central part is rather unordered. Evidently, these small oscillations trigger a bunch of pulses that travel upstream. Some of these pulses travel a little faster than others and again it seems that some cross each other without interaction. However, as discussed above it might be caused by the finite spatial resolution of the measurement device. It is likely that the pulses only pass each other closely.

At lower cell voltage two general observations can be made. The one is, that after the step a part of the channel starts to oscillate homogeneously (with a stricter phase relation between adjacent sites than after the steps before). But also these structures are unstable and crumble as time passes. The other trend is that the region of the channel, in which some structure appears, shifts upstream, leaving at low cell voltages a major downstream part of the cell non-oscillatory. It is unlikely that in this region absolutely no CO is present on the surface, but it seems that the local concentration is low enough to stabilize the downstream part.

#### *The Influence of the Counter Electrode*

Finally, the influence of a counter electrode should be depicted with the help of two experiments. Compared to the potentiostatic experiments presented above, air is fed into the counter electrode compartment while the anode configuration is left unchanged. The first experiment is a voltage scan and the results are collected in Fig. 40. The second experiment is a single step of the cell voltage and the results are shown in Fig. 41.

The polarization curve during the scan (Fig. 40) starts at an open circuit potential of 0.9 V. For decreasing cell voltage the current initially increases very slowly before the much steeper slope indicates the onset of CO oxidation. This general course is, apart from the shift along the cell voltage axis, identical to the behavior found with the  $H_2$ -fed counter electrode (Fig. 38). However, at about 0.2 V a maximum current is reached at which rather strong fluctuations of the current are observed. In other experiment the onset of these oscillations appeared before the maximum was reached. It can therefore not be attributed to this specific feature. The low maximum current density of  $0.2 \text{ A cm}^{-2}$  in comparison with the high current densities obtained for the  $H_2$ -fed counter electrode (Fig. 36a) indicates the appearance of ongoing flooding. While the differences in the separate channel profiles at 0.30 V (red curves) and 0.24 V (cyan curves) given in Fig. 40b can be explained with minor flooding, the initial decrease of current along the profiles at lowest cell voltage (0.16 V blue curves) is likely to be caused by more severe flooding. However, the subsequent current increase at the position 0.75 (in the blue curve) marks a front of an upstream traveling pulse.

The related spatio-temporal patterns are presented in the Figs. 40c-d. The sequence starts at the time when the cell voltage is 0.15 V. Clearly, a pulse that starts at the outlet of the cell quickly travels upstream. The speed of this pulse is much faster than in the scenarios with the  $H_2$ -fed cathode (here:  $30 \text{ cm min}^{-1}$ ). Once it crossed, the sites are not excitable for a short time (3 – 4 s). In that time no fluctuations appear at the position where the pulse has just passed. After the delay some oscillations appear and adjacent sites synchronize. However, the in phase-regions (the connected red regions in Figs. 40c-d) bend weakly, indicating phase turbulence. At other sites (e.g. Fig. 40c at  $x = 0.4$  and  $t = 35$  s) discontinuities can be observed, indicating defect turbulence. Also note the difference between the both channels, indicating phase changes also in the direction perpendicular to the gas flow.



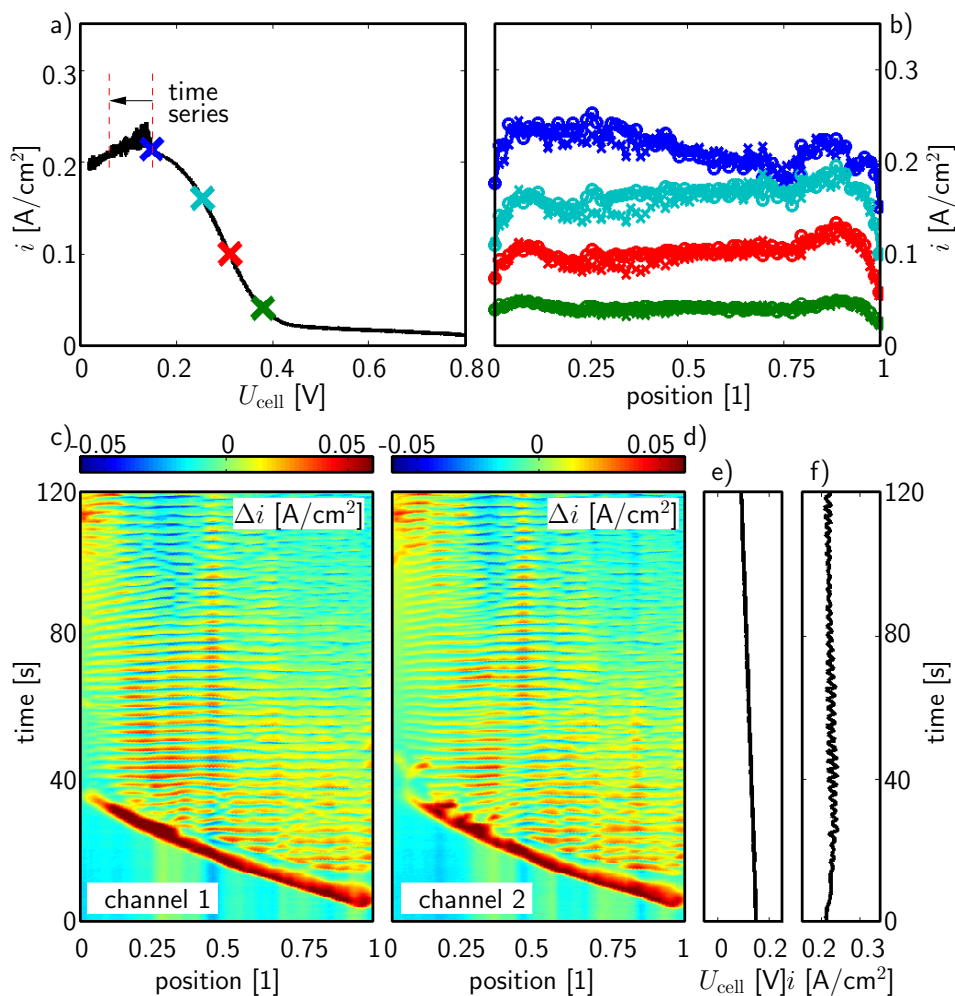


Figure 40: Collected experimental results for a voltage scan during potentiostatic electrochemical  $H_2$ ,  $CO$  oxidation with an air-fed counter electrode. a: Polarization curve; b: Current density profiles at specific moments during the scan;  $\times$  and  $\circ$  represent the individual channels. c-d: Spatio-temporal plots of the measured spatially distributed current signal (corrected for its temporal space dependent average) for both channels; e-f: Cell voltage and average current density in the observed region; Scan rate: 1 V/2000 s.

Both scenarios, phase- and defect turbulence, are typical for a Benjamin-Feir instability [177,196,197] in which a plane wave becomes unstable due to phase repulsion of adjacent oscillators. Although the Benjamin-Feir instability has experienced some numerical investigation [197–199], experimental evidence is seldom yet. The only experimental result (to our knowledge) depicting phase and defect turbulence in electrochemical systems was reported on the oscillatory electrochemical  $H_2$  oxidation in acidic electrolyte with a  $Pt$  ring [148,149].

Finally, a simple step from ocv into the oscillatory regime ( $U_{\text{cell}} = 0.12$  V) was carried out. The corresponding spatio-temporal plot of one of the channels is given in Fig. 41, together with an excerpt that presents the behavior in larger detail at the end of the time series. Again, phase- and defect turbulence is found. Some of the defects are encircled.

In comparison with the potentiostatic experiments with the  $H_2$ -fed counter electrode the discrepancies in the patterns can be speculated to mainly originate from two differences: Firstly, the differ-

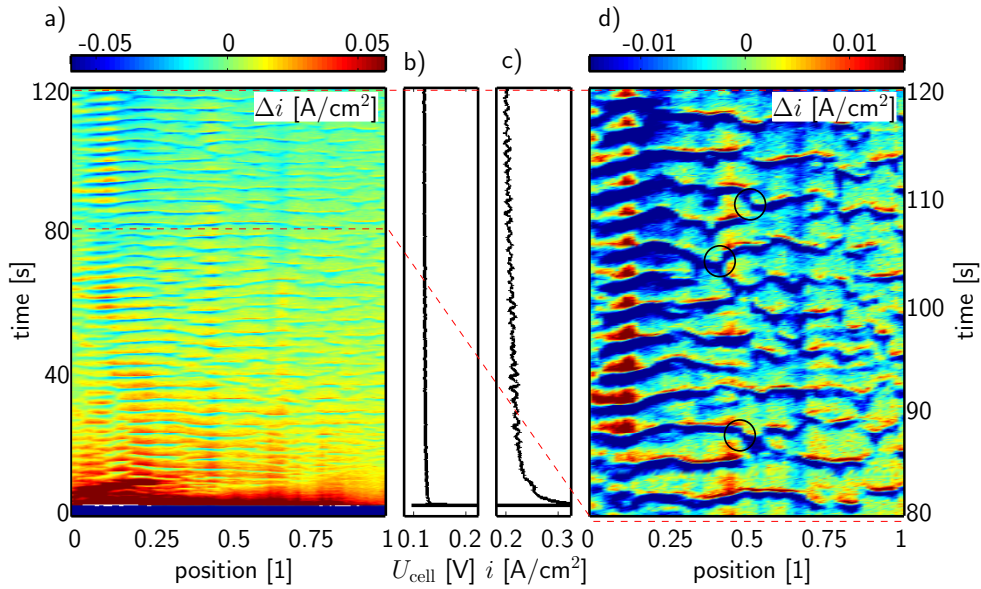


Figure 41: a: Space-time plots of the measured spatially distributed current signal (corrected for its temporal space dependent average) of one arbitrary channel after a step into the voltage regime at which  $CO$  can be oxidized. b: The cell voltage; c: The average current density in the observed two-channel-region; d: Magnified spatio-temporal plot of the last 40 s: In this experiment, the cathode was fed with air.

ence might be associated to the along-the-channel profile of the membrane resistance and therefore be caused by the water production in case of the air-fed cathode. Secondly, the more expressed oscillations in case of the air-fed cathode might relate to the larger cathode overvoltage as the electrode is more lossy compared with the cathode at which  $H_2$  evolution occurs. In the following, these candidates should be inspected in more detail.

Regarding the lower membrane resistance in case of water production at the cathode, it can be seen from Eq. (125) that the influence of both coupling terms is enhanced. However, in Fig. 39 it seems that the outlet region of the cell is not only not oscillatory unstable but even not excitable as no pulses travel in that direction. This fact indicates that the oscillations in the downstream part are not inhibited by the coupling terms but by the dynamics of the local systems.

Indeed, the membrane resistance has an impact on the homogeneous system, too (first term at right hand side of Eq. (85)). For a homogeneous HN-NDR system, a decreasing Ohmic resistance would in fact drive the system towards extinction of the oscillations (see Fig. 12e), oppositely to what is seen above. Additionally, the influence of changing membrane resistance should also be very small, as during the experiments with the air-fed cathode the membrane implied was as double as thick as in the case with the  $H_2$ -fed cathode. In fact, a 1 kHz-impedance of about  $7 \pm 2 \text{ m}\Omega$  for the first and  $9 \pm 2 \text{ m}\Omega$  for the later experiment were measured. Therefore, an altered membrane resistance is probably not the reason for the changed behavior.



Considering the impact of the cathode overvoltage with the help of Eqs. (36)-(37), the overvoltage  $\eta_{a,c}$  ( $\eta_{a,c} = \Delta\varphi_{a,c} - \Delta\varphi_{a,c}^0$ ) of the homogeneous system is given by

$$c_{dl,a} \frac{d\eta_a}{dt} = \frac{(\Delta\varphi_c^0 - \Delta\varphi_a^0 - U) - \eta_a + \eta_c}{A(R_\Omega + R_{ext})} - i_{F,a}, \quad (126)$$

$$-c_{dl,c} \frac{d\eta_c}{dt} = \frac{(\Delta\varphi_c^0 - \Delta\varphi_a^0 - U) - \eta_a + \eta_c}{A(R_\Omega + R_{ext})} - i_{F,c}. \quad (127)$$

with  $\Delta\varphi_{a,c}^0$  standing for the equilibrium double layer voltages at the anode/cathode. The term  $(\Delta\varphi_c^0 - \Delta\varphi_a^0 - U)$  represents the difference between open circuit cell voltage and actual cell voltage. For both implied cathodes it is always positive and increases with decreasing voltage  $U$ . The first term at the right hand side of Eq. (126) is the load line (see Fig. 9d and related text). It yields the current, passing through the potentiostat, as a function of the anodic overvoltage. The new aspect of the load line above, is that in conventional electrochemical system no influence on  $\eta_c$  can be found due to the application of reference electrodes. However, using an explicit expression for  $i_{F,c}$ , Eq. (127) would yield an equation of the form  $\eta_c(\eta_a)$  that could be entered into Eq. (126) to obtain an anodic load line similar to the conventional type (dependent only on  $\eta_a$ ). The load line is such an interesting object, because its slope determines (for a given  $i_{F,a}$ ) if the HN-NDR system can oscillate or not (Fig. 12e). For an HN-NDR system it is true that, the steeper the load line is (the smaller  $R_\Omega + R_{ext}$  is), the smaller is the voltage interval in which oscillations occur. At some critical slope the oscillations will extinct. Assuming the most simple rate approach for the Faradaic cathodic current  $i_{F,c} = -k\eta_c$ , with  $k$  representing some positive constant, it follows from the steady state condition applied to Eq. (127) that

$$\eta_c = a\eta_a - b, \quad (128)$$

with  $a$  and  $b$  being some positive constants that vanish for infinite  $k$ . Entering this expression into Eq. (126), it becomes apparent that the slope of the load line is flattened. So, a lossy counter electrode ( $k < \infty$ ) acts in this respect like an additional series resistance, supporting oscillations in the HN-NDR system. Likely, it is this relation that leads to the enhanced oscillatory behavior when an air-fed CE is applied (Fig. 40-41) compared to the  $H_2$ -fed CE (Fig. 38-39).

### 3.5 Summary

In the present chapter the spatially distributed electrochemical oxidation of  $H_2$ ,  $CO$  mixtures in a low temperature PEMFC was studied with the help of a mathematical model and experiments performed in a segmented cell.

The model, presented in Sec. 3.3, predicts pattern formation in a galvanostatically controlled one-dimensional PEMFC. The simplistic view connected with this new model allows to understand pattern formation phenomena in the sense that the system can be seen as a chain of interacting oscillators. Three interaction mechanisms have been identified. It is predicted that they cause qualitatively different PEMFC behavior. The three different interaction mechanisms between the individual oscillators arise due (1)  $CO$  transport along the channel, (2) local migration currents and (3) global mean-field-induced currents.

The qualitatively different PEMFC behavior expresses in the form of four distinct spatio-temporal current patterns and the related time series of the cell voltage. The four scenarios are characterized accordingly:

1. In the first scenario, caused by dominant mean-field coupling, the cell voltage oscillates with one minimum per period. Although the total current is constant in time, the current density profile along the PEMFC is not. Instead, as a consequence of the  $CO$  transport, the profile is flapping with the frequency of the cell voltage oscillation.
2. In the second scenario, caused by dominant mean-field coupling and the channel  $CO$  dynamics, the cell voltage expresses oscillations with two or three minima per period or is even aperiodic. For a given feed flow rate and increasing global current, the cell voltage expresses a characteristic period-doubling-like cascade. The current density patterns that are related to the more complex oscillations were shown to be a result from the flapping of the first scenario with downstream traveling  $CO$  shock fronts.
3. The third scenario is caused by dominant migration coupling: Plane waves were observed in the current pattern. Due to  $CO$  transport, the waves travel downstream. Plane waves result (as the first scenario) from frequency entrainment of the individual reaction sites but (opposite to the first scenario) their phases do not align. As a consequence, no oscillations might be found in the cell voltage although the double layer voltage oscillates at any reaction site.
4. In the fourth scenario, migration coupling leads to spatio-temporal turbulence in the current pattern. Thereby, the emergence of the pattern is in line with the behavior caused by the Benjamin-Feir instability. Namely, after a perturbation has been applied to the unstable plane wave, initially, the wave fronts become wavy (indicating phase repulsion of adjacent oscillators) and then defects (breakages in the fronts) occur. The cell voltage oscillates chaotically.

Experiments on the spatially distributed electrochemical  $H_2$ ,  $CO$  oxidation in a PEMFC, presented in Sec. 3.4, were carried out with the help of a printed circuit board (PCB) for distributed current measurements. These experiments are, to the authors knowledge, the first experiments in which this technique has been implied to investigate nonlinear pattern formation. Results were reported for varying cell temperatures, feed gas conditions, cathode electrode setups and load operation modes.

Thereby, three of the four predicted scenarios were found. A fourth experimentally observed pattern was not predicted. The findings are in detail:

1. For galvanostatic control and large feed flow rate, homogeneous oscillations (evident by the oscillating cell voltage) are found. The current distribution is flapping and one minimum appears per period in the time series of the cell voltage. This finding agrees qualitatively well with the first predicted scenario and proves the importance of mean-field coupling experimentally.
2. For galvanostatic control and decreasing feed flow rate, the oscillatory time series of the cell voltage expresses a period doubling. A whole period-doubling cascade is found when the cell current is scanned for a given feed flow rate. Both findings are in good agreement with the second predicted scenario and prove the importance of the channel CO dynamics experimentally. However, there are also considerable deviations between the predicted and the experimental behavior. For example, the predicted oscillations with three ignitions per period did not appear in the experiment.
3. For potentiostatic control and with an air-fed cathode, spatio-temporal turbulence appears. The pattern is in qualitative agreement with the fourth predicted scenario and proves the importance of migration-coupling experimentally. As the turbulence pattern contains wavy fronts and defects, it is likely to be caused by the Benjamin-Feir instability.
4. The plane waves that are characteristic for dominant migration coupling in the Benjamin-Feir stable regime (according to the third prediction) are not found.
5. During potentiostatic experiments with a  $H_2$ -fed cathode, current pulses were seen. The pulses were not noticed in the modeling study. But this is not surprising, because the pulses likely originate from the excitability of the system under non-oscillatory conditions - a case which was not investigated theoretically.

## 4 Conclusions and Outlook

This work was motivated by the observation of periodic cell voltage oscillations during the electrochemical oxidation of  $H_2, CO$  mixtures in a PEMFC. The oscillations have two interesting aspects. Namely, on the scientific side, the phenomenon is indicative for more complex pattern formation at different conditions. And, on the technical side, the oscillations substantially decrease the power losses which are caused by the presence of  $CO$ . In combination, it might therefore be argued whether there exist other phenomena in this system which are technically even more beneficial.

The main goal of this work was to develop a sound theoretical framework that describes the nonlinear phenomena that occur during the electrochemical  $H_2, CO$  oxidation in a PEMFC for a variety of parameters. Thereby, it was separated between a differentially small PEMFC and a PEMFC with considerable lateral extension. For each system, an individual model was developed and analyzed. Experiments, dedicated to the results of these analyses, were carried out in order to verify the key findings. The experiments include the measurement of spatio-temporal current profiles with a printed circuit board — a technique which was never used for the study of nonlinear pattern formation beforehand.

The key finding of the analysis of the small PEMFC was that the oscillations stem from an autocatalytic behavior of the double layer voltage. This feedback is caused by a potential dependent surface passivation by  $OH$ . However, in addition, also an autocatalytic behavior of the  $CO$  surface coverage was found. The related feedback is caused by enhanced  $CO$  oxidation with decreasing amount of  $CO$  adsorbate. As the  $OH$  species plays the key role in both autocatalytic feedback loops, they are ultimately coupled and lead to a wide oscillatory parameter range.

The key finding of the analysis of the spatially extended system is that the system can be understood as a chain of interacting oscillators. Thereby, it appeared that the oscillations observed in the small PEMFC are a result of a dominant mean-field interaction — a global coupling which originates from the external circuit. The oscillations represent a spatio-temporal pattern in which the frequencies and the phases of the local oscillations are globally entrained. Or in other words, the reaction sites oscillate homogeneously.

In addition to the mean-field coupling, two other interaction mechanisms between the individual oscillators were identified. They lead to the occurrence of patterns which have not been noticed beforehand. The one mechanism is  $CO$  transport. Thereby, any  $CO$  consumption upstream is noticed downstream. The impact of such a convective influence on electrochemical pattern formation was, to the authors knowledge, never studied before. In the given system,  $CO$  transport was found to cause  $CO$  shock fronts which perturb the homogeneous oscillations. As a consequence, the PEMFC shows more complex behavior compared to the homogeneous oscillations if the  $CO$  supply is diminished or if the  $CO$  consumption is increased. Namely, the cell voltage oscillation might express several minima per period or it might even be aperiodic.

The third interaction mechanism between individual oscillators is migration coupling. It stems from lateral currents in the membrane and was predicted to cause waves and spatio-temporal turbulence. In this work only the turbulent scenario was found. Thereby, the system seems to be the second electrochemical example which expresses this behavior.

The main parameters, that were identified to control the system behavior, can be grouped into three sets. The first parameter set controls the load line (cell voltage, membrane resistance, external resistance), the second set controls the local Faradaic current curve and the material coupling ( $CO$  content, cell temperature, feed flow rate) and the third set defines the strength of mean-field coupling and migration coupling (membrane diameter, membrane resistance, external resistance). It should also be highlighted that migration-coupling is also influenced by the system dimensions. Accordingly, spatio-temporal turbulence is more prone to be expressed in short cells with thick electrolyte.

From the technical perspective, it was known already that the pattern with the globally entrained oscillations improves the PEMFC  $CO$  tolerance. In this work, other patterns were found which are not dominated by mean-field coupling. But none of them did, in the experiments, provide additional benefits in this respect: In the scenario arising from the channel  $CO$  dynamics, the average cell voltage loss is not significantly different compared to the simple periodic, globally entrained oscillations. Oppositely, in the spatio-temporal turbulent pattern arising from migration coupling, the benefit of the improved cell voltage is even absent. Arguing about the mechanistic reason of this observation, one tends to conclude that migration coupling is technically less interesting than mean-field coupling. But this conclusion cannot be drawn. Namely, when comparing the turbulent pattern found in this work with the homogeneous oscillation seen in this work, one should be aware that the first pattern occurred during potentiostatic control while the second pattern appeared during galvanostatic control. Consequently, not only the coupling influence were different but also the load line: The turbulent regime stands for a scenario with a steeper load line and a negligible mean-field coupling, while the globally entrained oscillations represent a scenario with a flat load line and dominant mean-field coupling. A conclusion about the technical impact of the coupling terms would desire a clear experimental separation between load line slope and the pre-factors that control the spatial couplings. One could, for example, keep the total resistance  $R_{ext} + R_{\Omega}$  constant, while changing the ratio  $R_{ext}/R_{\Omega}$ . In this way the load line would be left unchanged while the mean-field coupling would be altered.

On the other side, the technical significance of the coupling terms (and the related patterns), for the purpose to clean the  $H_2$  from  $CO$ , is even more unclear. In the discussion in the last two paragraphs, only the temporally averaged cell voltage was considered to be technically relevant. But in order to evaluate the potential of the patterns with respect to deep  $CO$  removal, additionally, the  $CO$  selectivity needs to be regarded. It is therefore desirable to clarify the influence of the coupling terms not only in relation to the temporally average cell voltage but also towards the selectivity.

As a final comment, electrochemical  $H_2$ ,  $CO$  oxidation at  $Pt$  alloys is a system of outstanding complexity. Usually, electrochemical systems that possess an autocatalytic chemical variable are rather rare. The given system is a real curiosity in this respect: The system does not only incorporate an autocatalytic chemical variable, but it also contains an autocatalytic electrochemical variable, simultaneously. As a consequence, a large variety of patterns can be expected. Few have been found in this work. However, the author truly believes that this system can express many other astonishing phenomena and that the study of these phenomena will not only enhance our understanding of the origin of natural complexity, but that it might also teach us new ways to engineer complex systems.

## Appendix A: Model Reduction via Quasistationarity

In the following, the original model Tab. 3 for the oxidation of  $H_2/CO$  mixtures at a  $PtRu$  anode [2] is compared with the reduced model Eqs. (42)-(54) motivated in [110] for a wide range of experimental control parameters. A few time series of the two models are shown in Fig. 42a. In the end, systematic parameter scans for the two models are carried out. Bifurcation diagrams, eigenvalues and oscillation frequencies as well as amplitudes are compared.

### Heuristics of the Model Reduction: Quasi-Integrals

The reduction of the full 5-dimensional system, which is of the form

$$\dot{w} = W(w, z, p), \quad \dot{z} = Z(w, z, p) \quad (129)$$

with  $w = (\theta_H, \theta_{OH}, x_{CO})^T, z = (\theta_{CO}, \eta_a)^T$  for a parameter vector  $p$ , to the 2-dimensional system

$$\dot{z} = Z(w, z, p)|_{W(w,z,p)=0} =: Z^*(z, p) \quad (130)$$

is based on numerical tests whether certain scalar-valued functions are suited as ‘quasi-integrals’ [128]. The homotopy argument from singular perturbation theory linking quasi-integrals and quasistationarity to slow invariant manifolds for systems of the form

$$\varepsilon \dot{w} = W(w, z, p), \quad \dot{z} = Z(w, z, p) \quad (131)$$

for sufficiently small  $\varepsilon > 0$  can be found in [128]. In our present setup, there are five candidates for quasi integrals  $I_\alpha$ . They are defined as the ratios of all terms (rates) with a minus sign divided by all terms (rates) with a plus sign in a respective ODEs in Tab. 3:

$$I_{\theta_H} = \frac{r_V + r_T^b}{r_T^f} \quad (132)$$

$$I_{\theta_{OH}} = \frac{r_{CO,ox} + r_{H_2O,dis}^b}{r_{H_2O,dis}^f} \quad (133)$$

$$I_{x_{CO}} = \frac{x_{CO} F^{out} + \frac{RTA}{p} r_{CO,ad}^f}{x_{CO}^{in} F^{in} + \frac{RTA}{p} r_{CO,ad}^b} \quad (134)$$

$$I_{\theta_{CO}} = \frac{r_{CO,ox} + r_{CO,ad}^b}{r_{CO,ad}^f} \quad (135)$$

$$I_{\eta_a} = \frac{F \left( r_V + r_{CO,ox} + r_{H_2O,dis}^f \right)}{i + F r_{H_2O,dis}^b} \quad (136)$$

with the superscripts <sup>f</sup> and <sup>b</sup> standing for the forward- and backward contributions to the related net reaction rate (see Tab. 2). For the oscillatory regime, it is argued in [128], that whenever such a ratio  $I_\alpha$  is ‘almost always’ close to 1 during the course of oscillations (once the transient phase has passed), the  $\omega$ -limit sets of such trajectories are confined to a slow invariant manifold close to  $\{I_\alpha = 1\}$ . With the present definition (Eqs. (132)-(136)) such a manifold  $I_\alpha = 1$  is equivalent to the assumption of quasistationarity of the respective dynamic state  $\alpha$ . In other words, if the approach to  $I_\alpha = 1$  in the transient initial phase is fast (as it would be the case for small  $\varepsilon$  in (131)) and if  $I_\alpha$  is ‘almost always’ sufficiently close to 1 during the course of oscillations the ODE describing the temporal evolution of the species  $\alpha$  might be assumed to be quasistationary.

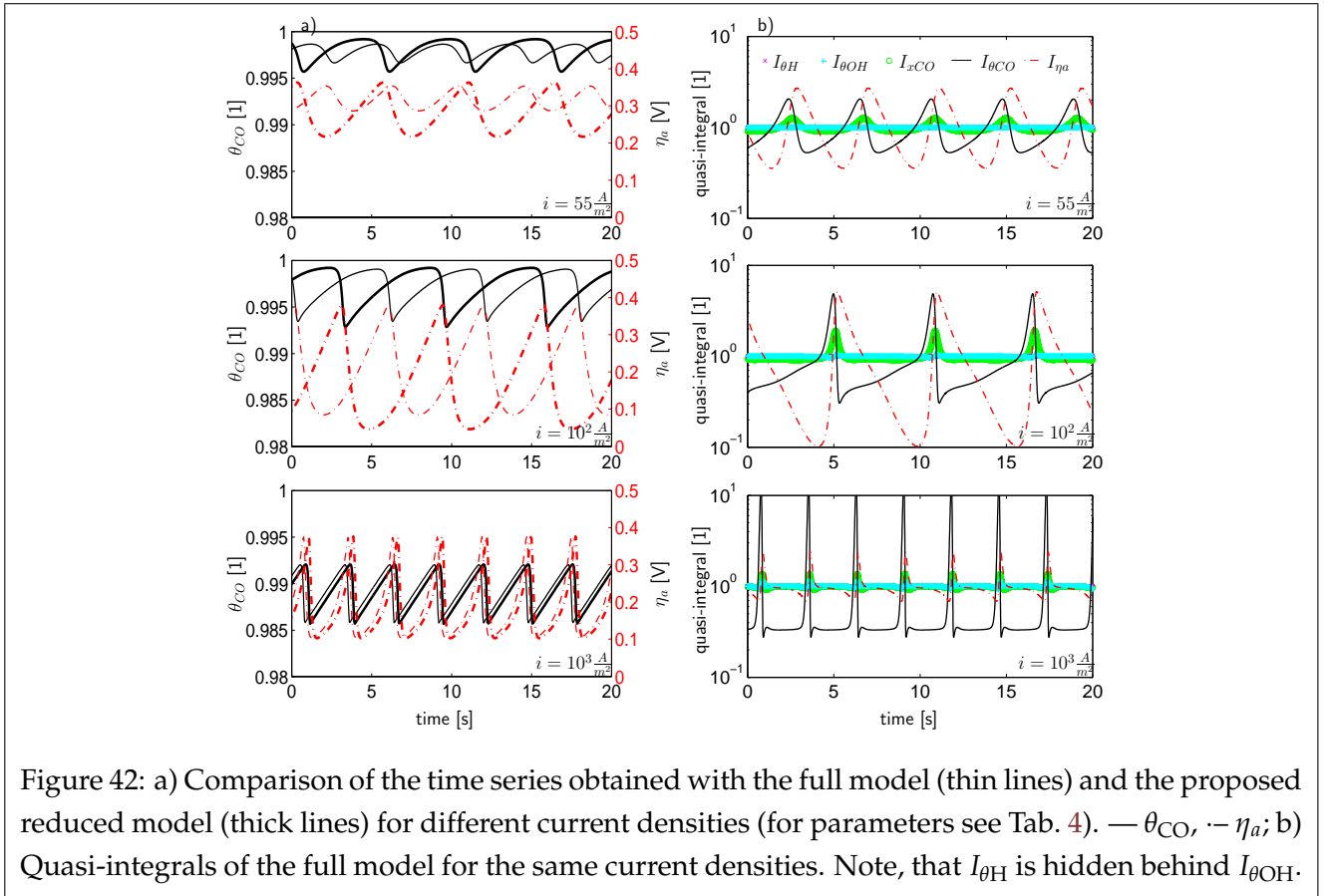


Figure 42: a) Comparison of the time series obtained with the full model (thin lines) and the proposed reduced model (thick lines) for different current densities (for parameters see Tab. 4). —  $\theta_{CO}$ , - -  $\eta_a$ ; b) Quasi-integrals of the full model for the same current densities. Note, that  $I_{\theta H}$  is hidden behind  $I_{\theta OH}$ .

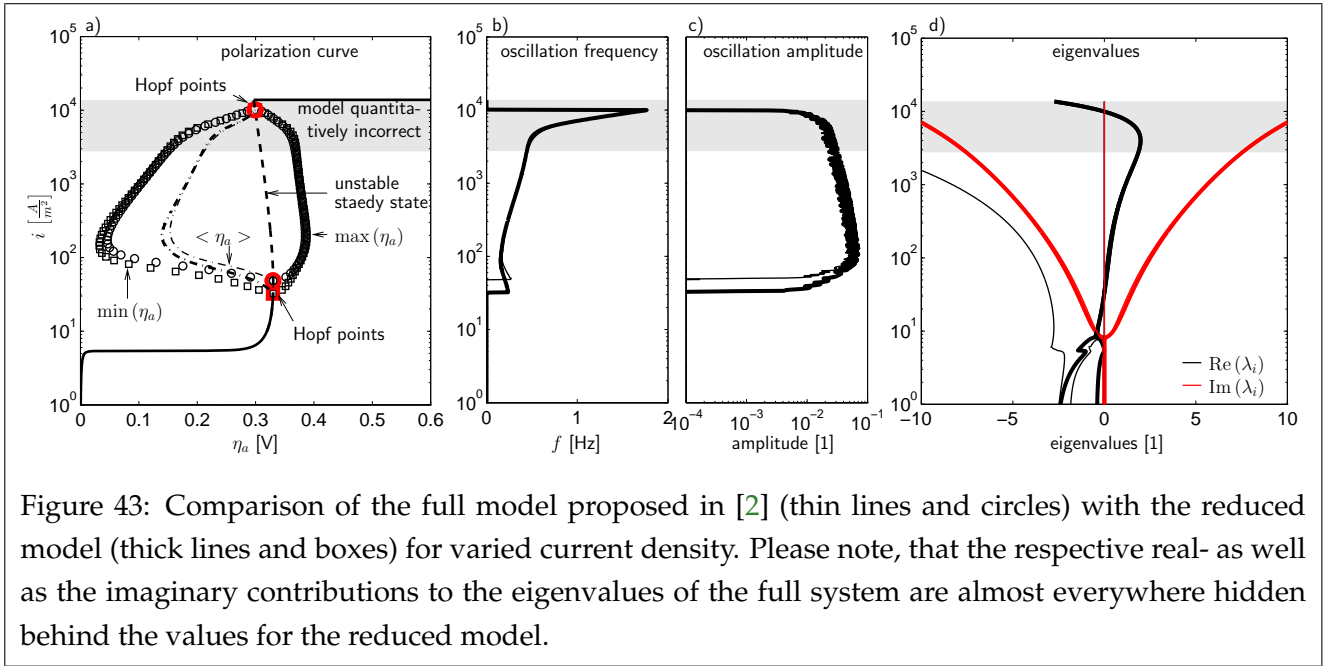
The five quasi-integrals (Eqs. (132)-(136)) for different current densities spanning the whole oscillation region are gathered in Fig. 42b.

It can be seen that  $I_{\theta H}$  and  $I_{\theta OH}$  show only very small deviations from unity. Thus they might be considered as well-suited candidates for quasi-integrals and thus for quasistationarity. The candidate  $I_{xCO}$  shows deviations from unity that are larger than the ones for  $I_{\theta H}$  and  $I_{\theta OH}$ , but much smaller than the ones for  $I_{\theta CO}$  and  $I_{\eta a}$ . Our heuristic argument for the oscillatory regime can be summarized as follows: The reduction to a 3-dimensional system in  $x_{CO}$ ,  $\theta_{CO}$  and  $\eta_a$  seems legitimate, a reduction to a 2-dimensional system in  $\theta_{CO}$  and  $\eta_a$  seems promising.

The comparison of the bifurcation diagrams for the full 5-dimensional system (Eq. (129)) and the reduced 2-dimensional system (Eq. (130)) in Fig. 43 shows good agreement. Fig. 43 collects the polarization curves with the respective frequencies and amplitudes of the two models. In addition, the eigenvalues with largest real parts are given. The current density was varied from  $1 \frac{\text{A}}{\text{m}^2}$  to  $1.38 \cdot 10^4 \frac{\text{A}}{\text{m}^2}$ . So one can compare the models at the unstable steady states. The upper limit marks the maximum Faradaic current assuming full  $H_2$  conversion for the given inlet flow rate. It is evident that both models match even quantitatively well. Deviations due to the model reduction occur only at low current densities: After the model reduction, the bifurcation point is shifted to lower current densities due to the assumption of quasistationarity of  $x_{CO}$ . As, for highest flow rates,  $x_{CO}$  need to be  $x_{CO}^{\text{in}}$  in both models, the approximation by the reduced model is generally better the higher the flow rate.

All in all, the 2-dimensional model (Eqs. (42)-(54) or the generic form Eq. (130)) still possesses all the bifurcation mechanisms that can be observed in the original 5-dimensional system (129) (Tab. 3). In this respect, our model reduction is considered to be sound.





#### Heuristics of the Model Reduction: Hopf Bifurcations

The above quasi-integrals are tailored to the  $\omega$ -limit sets in the oscillatory regime, so to say, to oscillations of higher amplitudes. Now we investigate whether our chosen reduction to the  $(\theta_{CO}, \eta_a)$ -plane is suited well for the bifurcation of periodic orbits at steady states of Hopf type (oscillations of small amplitudes). Since the Hopf orbits necessarily lie on a 2-dimensional center manifold that is tangent to the critical eigenspace – corresponding to pure imaginary eigenvalues – we will compute such critical eigenspaces and their deviations from the  $(\theta_{CO}, \eta_a)$ -plane.

The full model consists of five ODEs. Consequently at steady states, one has (generically) five different eigenvalues  $\lambda_i$  with 5-dimensional eigenvectors  $\vec{\mu}_i$ . These might be complex quantities. At Hopf bifurcation points, one pair of conjugate-complex eigenvalues of the form  $\sigma \pm i\beta$  is crossing the imaginary axis. In the presence of Hopf limit cycles the steady state is unstable, characterized by two eigenvalues with identical real parts  $\sigma > 0$  and non-vanishing imaginary parts  $\pm i\beta$  (see Fig. 43d). Let the two corresponding eigenvectors be  $\vec{\mu}_1$  and  $\vec{\mu}_2$  where the second one is just the complex conjugate of the first. The corresponding real eigenspace is then spanned by the real and imaginary part, e.g. by  $\vec{v}_1 = \frac{\text{Re}\vec{\mu}_1}{\|\text{Re}\vec{\mu}_1\|}$  and  $\vec{v}_2 = \frac{\text{Im}\vec{\mu}_1}{\|\text{Im}\vec{\mu}_1\|}$  of unit length. The length  $r_j$  of the projection of  $\vec{v}_j$  to the  $(\theta_{CO}, \eta_a)$ -plane is given for  $j = 1, 2$  by

$$r_j = \sqrt{\frac{v_{j,\theta_{CO}}^2 + v_{j,\eta_a}^2}{v_{j,\theta_{CO}}^2 + v_{1,\eta_a}^2 + v_{j,\theta_{OH}}^2 + v_{j,\theta_H}^2 + v_{j,x_{CO}}^2}}. \quad (137)$$

For all current densities considered in this appendix, the  $r_j$ 's were always larger than 0.995 indicating that the critical eigenspaces are “almost” parallel to the  $(\theta_{CO}, \eta_a)$ -plane. So one could rigorously prove that the reduced system for the onset of Hopf oscillations is one in  $(\theta_{CO}, \eta_a)$ -coordinates.

## Appendix B: Derivation of Eq. (72)

Here, the derivation of Eq. (72) is described in greater detail. Evaluating the local gradient of the electrolyte potential at the anode  $\frac{\partial \phi}{\partial y}|_{y=0}$  with the help of Eq. (67) one finds

$$\frac{\partial \phi}{\partial y}|_{y=0} = \frac{\psi_0 - \phi_0}{d_m} + 2 \sum_{n=1}^{\infty} \cos\left(\frac{n\pi z}{L}\right) \frac{n\pi}{L} \cdot \left( -\phi_n \coth\left(\frac{n\pi d_m}{L}\right) - \psi_n \left( \sinh\left(\frac{n\pi d_m}{L}\right) - \cosh\left(\frac{n\pi d_m}{L}\right) \coth\left(\frac{n\pi d_m}{L}\right) \right) \right). \quad (138)$$

If the electrolyte is very thin compared to its length the terms at the right hand side can be approximated by their second order Laurent series expansion

$$-\coth\left(\frac{n\pi d_m}{L}\right) \approx -\frac{L}{n\pi d_m} - \frac{n\pi d_m}{3L} \quad (139)$$

$$-\sinh\left(\frac{n\pi d_m}{L}\right) \approx -\frac{n\pi d_m}{L} \quad (140)$$

$$\cosh\left(\frac{n\pi d_m}{L}\right) \coth\left(\frac{n\pi d_m}{L}\right) \approx \frac{L}{n\pi d_m} + \frac{5n\pi d_m}{6L}. \quad (141)$$

Implying Eqs. (139)-(141) into Eq. (138) it follows after rearranging that

$$\frac{\partial \phi}{\partial y}|_{y=0} = \frac{1}{d_m} \left( \psi_0 + 2 \sum_{n=1}^{\infty} \cos\left(\frac{n\pi z}{L}\right) \psi_n \right) - \frac{1}{d_m} \left( \phi_0 + 2 \sum_{n=1}^{\infty} \cos\left(\frac{n\pi z}{L}\right) \phi_n \right) - \frac{d_m}{6} \left( 2 \sum_{n=1}^{\infty} \cos\left(\frac{n\pi z}{L}\right) \psi_0 \left(\frac{n\pi}{L}\right)^2 \right) - \frac{d_m}{3} \left( 2 \sum_{n=1}^{\infty} \cos\left(\frac{n\pi z}{L}\right) \phi_n \left(\frac{n\pi}{L}\right)^2 \right). \quad (142)$$

Noticing that the first two brackets represent the Fourier series of the boundary conditions  $\psi$  and  $\phi$  and the last two brackets their second derivative with respect to  $z$  it finally follows

$$\frac{\partial \phi}{\partial y}|_{y=0} = \frac{\psi - \phi}{d_m} + \frac{d_m}{3} \frac{\partial^2 \phi}{\partial z^2} + \frac{d_m}{6} \frac{\partial^2 \psi}{\partial z^2}, \quad (143)$$

which after multiplication with  $-\kappa$  yields Eq. (72).

## References

- [1] Bundesministerium für Wirtschaft und Technologie. Die Energiewende in Deutschland. [www.bmwi.de](http://www.bmwi.de) (2012).
- [2] J. X. Zhang and R. Datta, *J. Electrochem. Soc.*, 149, A1423–A1431 (2002).
- [3] J.X. Zhang and R. Datta, *Electrochem. Solid-State Lett.*, 7, A37–A40 (2004).
- [4] J. Zhang and R. Datta, *J. Electrochem. Soc.*, 152, A1180–A1187 (2005).
- [5] G. Sandstede, E.J. Cairns, V.S. Bagotsky, and K. Wiesener, in *Handbook of Fuel Cells*, W. Vielstich, A. Lamm, and H.A. Gasteiger, editors, John Wiley and Sons, New York (2003).
- [6] F. Barbir. *PEM Fuel Cells: Theory and Practice*. Elsevier Academic Press, Burlington (2005).
- [7] W. Vielstich, A. Lamm, and H.A. Gasteiger, editors. *Handbook of Fuel Cells*. John Wiley and Sons, New York (2003).
- [8] M.M. Mench. *Fuel Cell Engines*. John Wiley and Sons, New Jersey (2008).
- [9] Q.F. Li, R.H. He, J.O. Jensen, and N.J. Bjerrum, *Chem. Mater.*, 15, 48964915 (2003).
- [10] A. Hamnett, in *Handbook of Fuel Cells, 1st Vol.*, W. Vielstich, A. Lamm, and H.A. Gasteiger, editors, John Wiley and Sons, New York (2003).
- [11] C Kittel. *Introduction to Solid State Physics, 7th edition*. John Wiley and Sons, New Jersey (1996).
- [12] S.J. Paddison, *Annu. Rev. Mater. Res.*, 33, 289319 (2003).
- [13] M. A. Hickner, *J. Polymer Sci. B: Polymer Phys.*, 50, 9–20 (2012).
- [14] C.N. Sun, K.L. More, and T.A. Zawodzinski. Investigation of Transport Properties, Microstructures, and Thermal Behaviour of PEFC Catalyst Layers. In *ECS Trans.*, volume 33, p. 1207 – 1215 (2010).
- [15] A.J. Bard and L.R. Faulkner. *Electrochemical Methods 2nd ed.* John Wiley and Sons, New York (2000).
- [16] U.S. Department of Energy. Hydrogen and Fuel Cells Program Plan. [www.hydrogen.energy.gov/pdfs/program\\_plan2011.pdf](http://www.hydrogen.energy.gov/pdfs/program_plan2011.pdf) (2011).
- [17] FuelCellToday. Industry Review 2012. [www.fuelcelltoday.com/analysis/industry-review/2012/the-industry-review-2012](http://www.fuelcelltoday.com/analysis/industry-review/2012/the-industry-review-2012) (2012).
- [18] K. Sundmacher, *Ind. Eng. Chem. Res.*, 49, 10159–10182 (2010).
- [19] FuelCellToday. Industry Review 2011. [www.fuelcelltoday.com/analysis/industry-review/2011/the-industry-review-2011](http://www.fuelcelltoday.com/analysis/industry-review/2011/the-industry-review-2011) (2011).
- [20] Y. Wang, K.S. Chen, J. Mishler, S.C. Cho, and X.C. Adroher, *Applied Energy*, 88, 981–1007 (2011).
- [21] California Fuel Cell Partnership. DOE Targets. [cafcp.org/progress/technology/doetargets](http://cafcp.org/progress/technology/doetargets) (2012).

- [22] U.S. Department of Energy: Energy Efficiency and Renewable Energy (DOE: EERE). Status of Hydrogen Storage Technologies. [www1.eere.energy.gov/hydrogenandfuelcells/storage/tech\\_status.html](http://www1.eere.energy.gov/hydrogenandfuelcells/storage/tech_status.html) (2012).
- [23] Linde, Daimler, EnBW, OMV, Shell, Total, Vattenfall and the NOW GmbH. Major Companies Sign Up to Hydrogen Infrastructure Built-Up Plan in Germany. [www.the-linde-group.com/en/news\\_and\\_media/press\\_releases/news2009\\_09\\_10.html](http://www.the-linde-group.com/en/news_and_media/press_releases/news2009_09_10.html) (2009).
- [24] search in the www with the help of google. [www.google.de](http://www.google.de) (2012).
- [25] European Commission for Research and Innovation. EU support for Research on Fuel Cells and Hydrogen. [ec.europa.eu/research/energy/eu/research/fch/support/index\\_en.html](http://ec.europa.eu/research/energy/eu/research/fch/support/index_en.html) (2012).
- [26] U.S. Department of Energy: Energy Efficiency and Renewable Energy (DOE: EERE). Technical Plan - Fuel Cells. [www1.eere.energy.gov/hydrogenandfuelcells/mypp/pdfs/fuel\\_cells.pdf](http://www1.eere.energy.gov/hydrogenandfuelcells/mypp/pdfs/fuel_cells.pdf) (2012).
- [27] R. Borup, J. Meyers, B. Pivovar, Y.S. Kim, R. Mukundan, N. Garland, D. Myers, M. Wilson, F. Garzon, D. Wood, P. Zelenay, K. More, K. Stroh, T. Zawodzinski, X.J. Boncella, J.E. McGrath, O.M. Inaba, K. Miyatake, M. Hori, K. Ota, Z. Ogumi, S. Miyata, A. Nishikata, Z. Siroma, Y. Uchimoto, K. Yasuda, K. Kimijima, and N. Iwashita, *Chem. Rev.*, 107, 3904–3951 (2007).
- [28] U.S. Department of Energy: Energy Efficiency and Renewable Energy (DOE: EERE). Mass Production Cost Estimation for Direct H<sub>2</sub> PEM Fuel Cell Systems for Automotive Applications: 2010 Update. [www1.eere.energy.gov/hydrogenandfuelcells/pdfs/dti.80kW\\_fc\\_system\\_cost\\_analysis\\_report\\_2010.pdf](http://www1.eere.energy.gov/hydrogenandfuelcells/pdfs/dti.80kW_fc_system_cost_analysis_report_2010.pdf) (2010).
- [29] M.K. Debe. Advanced Cathode Catalysts and Support for PEM Fuel Cells. In *2010 Hydrogen Program Annual Merit Review and Peer Evaluation Meeting* (2010).
- [30] U.S. Department of Energy. Hydrogen and Fuel Cell Activities, Progress, and Plans: Report to Congress. [www.hydrogen.energy.gov](http://www.hydrogen.energy.gov) (2009).
- [31] M.K. Debe, *Nature*, 486, 43–51 (2012).
- [32] X.Z. Yuan, H. Li, S.S. Zhang, J. Martin, and H.J. Wang, *J. Pow. Sources*, 196, 9107 – 9116 (2011).
- [33] H. Liu, H.A. Gasteiger, A. Laconti, and J. Zhang, *ECS Transactions*, 1, 283–293 (2006).
- [34] F.D. Coms. The chemistry of fuel cell membrane chemical degradation. In *ECS Transactions*, volume 16, p. 235–255 (2008).
- [35] F.A. Bruijn, V.A.T. Dam, and G.J.M. Janssen, *Fuel Cells*, 8, 3–22 (2008).
- [36] L. Gublera and W.H. Koppenolb, *J. Electrochem. Soc.*, 159, B211–B218 (2012).
- [37] D.E. Curtin, R.D. Lousenberg, T.J. Henry, P.C. Tangeman, and M.E. Tisack, *J. Power Sources*, 131, 41–48 (2004).
- [38] Y.H. Lai, C.K. Mittelsteadt, C.S. Gittleman, and D.A. Dillard, *ASME Conference Proceedings*, 2005, 161–167 (2005).

- [39] W. Liu, K. Ruth, and G. Rusch, *J. New Mat. Electrochem. Sys.*, 4, 227–232 (2001).
- [40] F.Q. Liu, B.L. Yi, D.M. Xing, J.R. Yu, and H.M. Zhang, *J. Mem. Sci.*, 2012, 213–223 (2003).
- [41] X. Zhu, H. Zhang, Y. Zhang, Y. Liang, X. Wang, and B. Yi, *J. Phys. Chem. B*, 110, 1424014248 (2006).
- [42] J. Malis, M. Paidar, and K. Bouzek. Properties of Nafion Membrane at Elevated Temperature and Pressure. In *Electromembrane Processes and Materials (Cesky Krumlov/Czech Republic)* (2012).
- [43] S.H. Almeida and Y. Kawano, *JTAC*, 58, 569–577 (1999).
- [44] S. Zhang, X.Z. Yuan, J.N.C. Hin, H. Wang, K.A. Friedrich, and M. Schulze, *J. Pow. Sources*, 194, 588–600 (2009).
- [45] N. Zamel and X. Li, *Progress in Energy and Combustion Science*, 37, 292329 (2011).
- [46] V. Hamilton. *Spatiotemporal Pattern Formation During Electrochemical Oxidation of Hydrogen on Platinum*. PhD thesis, Freie Universität Berlin (2003).
- [47] H.A. Gasteiger, N.M. Markovic, and P.N. Ross, *J. Phys. Chem.*, 99, 8290–8301 (1995).
- [48] E. Antolini, *J. Sol. St. Electrochem.*, 15, 455–472 (2011).
- [49] Z. Chen, W. Deng, X. Wang, and Y. Yan, *ECS Transactions*, 11, 1289–1299 (2007).
- [50] C.A. Reiser, L. Bregoli, T.W. Patterson, J.S. Yi, J.D. Yang, M.L. Perry, and T.D. Jarvi, *Electrochem. Solid-State Lett.*, 8, A273–A276 (2005).
- [51] J.P. Meyers and R.M. Darling, *J. Electrochem. Soc.*, 153, A1432–A1442 (2006).
- [52] C. Wang, G.F. Wang, D. van der Vliet, K.C. Chang, N.M. Markovic, and V.R. Stamenkovic, *Phys. Chem. Chem. Phys.*, 12, 6933–6939 (2010).
- [53] C. Wang, M.F. Chi, G.F. Wang, D. van der Vliet, D.G. Li, K. More, H.H. Wang, J.A. Schlueter, N.M. Markovic, and V.R. Stamenkovic, *Adv. Func. Mat.*, 21, 147–152 (2011).
- [54] J.X. Wang, H. Inada, L.J. Wu, Y.M. Zhu, Y.M. Choi, P. Liu, W.P. Zhou, and R.R. Adzic, *J. Am. Chem. Soc.*, 131, 17298–17302 (2009).
- [55] S. Ball, S.L. Burton, J. Fisher, R. OMalley, B. Tessier, B.R.C. Theobald, D. Thompsett, W.P. Zhou, D. Su, Y. Zhu, and R. Adzic, *ECS Trans.*, 25, 1023–1036 (2009).
- [56] E. Proietti, F. Jaouen, N. Lefevre, M. and Larouche, J. Tian, J. Herranz, and J.P. Dodelet, *Nature Communication*, 2 (2011).
- [57] T.E. Wood, Z. Tan, A.K. Schmoeckel, D. O'Neill, and R. Atanasoski, *J. Pow. Sources*, 178, 510–516 (2008).
- [58] B. Bahar, C. Cavalca, S.J.C. Cleghorn, J. Kolde, D. Lane, M. Murthy, and G. Rusch, *JNMES*, 2, 179–182 (1999).
- [59] J.A. Kolde, B. Bahr, M.S. Wilson, T.A. Zawodzinski, and S. Gottesfeld, *Electrochemical Society Proceedings*, 95-23, 193–201 (1995).

- [60] R.L. Perry. Analysis of the Durability of PEM FC Membrane Electrode Assemblies in Automotive Applications Through the Fundamental Understanding of Membrane and MEA Degradation Pathways DE-EE0003772 2010: DOE Hydrogen Program Fuel Cell Project Kick-Off. [www1.eere.energy.gov/hydrogenandfuelcells/pdfs/10\\_dupont\\_perry.pdf](http://www1.eere.energy.gov/hydrogenandfuelcells/pdfs/10_dupont_perry.pdf) (2010).
- [61] D.J. Jones and J. Roziere, *Adv. Polym. Sci.*, 215, 219264 (2008).
- [62] S. Hamrock. Membranes and MEAs for Dry, Hot Operating Conditions. [www.hydrogen.energy.gov/pdfs/progress10/v\\_d\\_2\\_hamrock.pdf](http://www.hydrogen.energy.gov/pdfs/progress10/v_d_2_hamrock.pdf) (2010).
- [63] M. Watanabe, H. Uchida, Y. Seki, M. Emori, and P. Stonehart, *J. Electrochem. Soc.*, 143, 3847–3852 (1996).
- [64] J.S. Wainright and M.H. Litt, in *Handbook of Fuel Cells, 4th Vol.*, W. Vielstich, A. Lamm, and H.A. Gasteiger, editors, John Wiley and Sons, New York (2003).
- [65] K. Lee, J.J. Zhang, H.J. Wang, and D.P. Wilkinson, *J. Appl. Electrochem.*, 36, 507–522 (2006).
- [66] W.M. Zhang, P. Sherrell, A.I. Minett, J.M. Razal, and J. Chen, *Energy Environ. Sci.*, 3, 1286–1293 (2010).
- [67] D.A. Masten and A.D. Bosco, in *Handbook of Fuel Cells, 4th Vol.*, W. Vielstich, A. Lamm, and H.A. Gasteiger, editors, John Wiley and Sons, New York (2003).
- [68] T. E. Springer, T. A. Zawodzinski, and S. Gottesfeld, *J. Electrochem. Soc.*, 138, 2334 (1991).
- [69] Y. Sone, P. Ekdunge, and D. Simonsson, *J. Electrochem. Soc.*, 143, 1254–1259 (1996).
- [70] J. St-Pierre, D.P. Wilkinson, S. Knights, and M.L. Bos, *J. New Mater. Electrochem. Systems*, 3, 99 (2000).
- [71] F. Barbir, in *Handbook of Fuel Cells, 4th Vol.*, W. Vielstich, A. Lamm, and H.A. Gasteiger, editors, John Wiley and Sons, New York (2003).
- [72] F.N. Buechi, in *Handbook of Fuel Cells, 4th Vol.*, W. Vielstich, A. Lamm, and H.A. Gasteiger, editors, John Wiley and Sons, New York (2003).
- [73] A. Heinzl and C. Hebling, in *Handbook of Fuel Cells, 4th Vol.*, W. Vielstich, A. Lamm, and H.A. Gasteiger, editors, John Wiley and Sons, New York (2003).
- [74] D.M. Chen, W. Li, and H. Peng, *J. Pow. Sources*, 180, 461–467 (2007).
- [75] S.H. Jung, S.L. Kim, M.S. Kim, Y. Park, and T.W. Lim, *J. Pow. Sources*, 170, 324–333 (2007).
- [76] Z. Mirza. Development of Thermal and Water Management System for PEM Fuel Cell. [www.hydrogen.energy.gov/pdfs/review10/fc066\\_mirza\\_2010\\_p\\_web.pdf](http://www.hydrogen.energy.gov/pdfs/review10/fc066_mirza_2010_p_web.pdf) (2010). Presentation of a DOE Funded Project.
- [77] D. Wheeler, J. Yi, R. Fredley, D. Yang, T. Patterson, and L. VanDine, *J. New Mat. Electrochem. Sys.*, 4, 233–238 (2001).
- [78] Q. Dong, M.M. Mench, S. Cleghorn, and U. Beuscher, *J. Electrochem. Soc.*, 152, A2114–A2122 (2005).

- [79] J.D. Holladay, J. Hu, D.L. King, and Y. Wang, *Cat. Tod.*, 139, 244–260 (2009).
- [80] O. Korotkhik and R. Farrauto, *Cat. Tod.*, 62, 249–254 (2000).
- [81] R. Farrauto, S. Hwang, L. Shore, W. Ruettinger, J. Lampert, T. Giroux, Y. Liu, and O. Ilinich, *Annu. Rev. Mater. Res.*, 33, 1–27 (2003).
- [82] E.D. Park, D. Lee, and H.C. Lee, *Catalysis Today*, 139, 280 (2009).
- [83] S. Balasubramanian, C.E. Holland, and J. W. Weidner, *Electrochem. Solid-State Let.*, 13, B5–B7 (2010).
- [84] H.A. Gasteiger, J.E. Panels, and S.G. Yan, *J. Power Sources*, 127, 162171 (2004).
- [85] L.P.L. Carette, K.A. Fredrich, and U. Stimming, *Phys. Chem. Chem. Phys.*, 3, 320–324 (2001).
- [86] C.G. Farrell, C.L. Gardner, and M. Ternan, *J. Pow. Sources*, 171, 282–293 (2007).
- [87] B.C. Glenn and J.H. Saunders, *J. Electrochem. Soc.*, 159, B165–B172 (2012).
- [88] P. Stonehart and G. Kohlmayr, *Electrochimica Acta*, 17, 396 (1972).
- [89] M.W. Breiter, *J. Electroanal. Chem.*, 65, 623–634 (1975).
- [90] W. Vielstich, in *Encyclopedia of Electrochemistry*, A.J. Bard, M. Stratmann, and E.J. Calvo, editors, volume 2, chapter 5.2, Wiley, Weinheim (2003).
- [91] O.A. Petrii, *J. Solid State Electrochem.*, 12, 609–642 (2008).
- [92] T. Kadyk, S. Kirsch, R. Hanke-Rauschenbach, and K. Sundmacher, *Electrochimica Acta*, 56, 10593–10602 (2011).
- [93] S. Wilhelm, W. Vielstich, H.W. Buschmann, and T. Iwasita, *J. Electroanal. Chem.*, 229, 377–384 (1987).
- [94] P.P. Lopes and E.A. Ticianelli, *J. Electroanal. Chem.*, 664, 110–116 (2010).
- [95] R. Hanke-Rauschenbach, M. Mangold, and K. Sundmacher, *Reviews in Chemical Engineering*, 27, 23–52 (2011).
- [96] W. Gu, D.R. Baker, Y. Liu, and H.A. Gasteiger, in *Handbook of Fuel Cells, 6th Vol.*, W. Vielstich, A. Lamm, and H.A. Gasteiger, editors, John Wiley and Sons, New York (2009).
- [97] M.C. Deibert and D.L. Williams, *J. Electrochem. Soc.: Electrochem. Tech.*, 116, 1290–1292 (1969).
- [98] S. Szpak, *J. Electrochem. Soc.: Technical Notes*, 117, 1056 (1970).
- [99] B. Rohland and V. Plzak, *J. Pow. Sources*, 84, 183–186 (1999).
- [100] M. Murthy, M. Esayian, A. Hobson, S. MacKenzie, W.K. Lee, and J.W. Van Zee, *J. Electrochem. Soc.*, 148, A1141 (2001).
- [101] J.X. Zhang, J.D. Fehribach, and R. Datta, *J. Electrochem. Soc.*, 151, A689 (2004).
- [102] N. Wagner and M. Schulze, *Electrochimica Acta*, 48, 3899–3970 (2003).



- [103] A.H. Thomason, T.R. Lalk, and A.J. Appleby, *J. Pow. Sources*, 135, 204 (2004).
- [104] H. Lu, L. Rhiko-Struckmann, R. Hanke-Rauschenbach, and K. Sundmacher, *Top. Catal.*, 51, 89 (2008).
- [105] H. Lu, L. Rhiko-Struckmann, R. Hanke-Rauschenbach, and K. Sundmacher, *Electrochimica Acta*, 54, 1184 (2009).
- [106] A. Mota, P.P. Lopes, E.A. Ticianelli, E.R. Gonzalez, and Varela H., *ECS Trans.*, 25, 81 (2009).
- [107] A. Mota, P.P. Lopes, E.A. Ticianelli, E.R. Gonzalez, and Varela H., *J. Electrochem. Soc.*, 157, B1301–B1304 (2010).
- [108] S. Kirsch, R. Hanke-Rauschenbach, and K. Sundmacher, *J. Electrochem. Soc.*, 158, B44–B53 (2011).
- [109] P.P. Lopes, E.A. Ticianelli, and H. Varela, *J. Pow. Sources*, 196, 84–89 (2011).
- [110] R. Hanke-Rauschenbach, C. Weinzierl, M. Krasnik, L. Rihko-Struckmann, H. Lu, and K. Sundmacher, *J. Electrochem. Soc.*, 156, B1267–B1275 (2009).
- [111] R.M. Noyes and R.J. Field, *A. Chem. Res.*, 10, 273–280 (1977).
- [112] R.F. Ludlow and S. Otto, *Chem. Soc. Rev.*, 37, 101–108 (2008).
- [113] J.D. Murray, editor. *Mathematical Biology*. Springer, New York (1989).
- [114] C.W. Rowley, T. Colonius, and A.J. Basu, *J. Fluid Mech.*, 455, 315–346 (2002).
- [115] R. Imbihl, *Prog. Surf. Sci.*, 44, 185–343 (1993).
- [116] G. Ertl, *Surf. Sci.*, 299, 742–754 (1994).
- [117] J.L. Hudson and T.T. Tsotsis, *Chem. Engin. Sci.*, 49, 1493–1572 (1994).
- [118] K. Krischer, in *Modern Aspects of Electrochemistry*, No. 32, B.E. Conway, J.O'M. Bockris, and R.E. White, editors, p. 1–141, Kluwer Academic/Plenum Publishers (2003).
- [119] C.H. Hamann and W. Vielstich. *Elektrochemie*, 4. Auflage. WILEY-VCH, Weinheim (2005).
- [120] M.T.M. Koper, in *Advances in Chemical Physics*, Vol. 92, I. Prigogine and S.A. Rice, editors, Wiley, New York (1996).
- [121] K. Krischer, in *Advances in Electrochemical Science and Engineering*, 8th Vol., R.C. Alkire and D.M. Kolb, editors, p. 89, Wiley-VCH, Weinheim (2003).
- [122] H. Poincaré, *Oeuvres Paris*, 1 (1892).
- [123] I. Bendixon, *Acta Mathematica (Springer Netherlands)*, 24, 1–88 (1901).
- [124] H.G. Schuster and W. Just. *Deterministic Chaos*. Wiley, Weinheim (2005).
- [125] J. Siegmeier, N. Baba, and K. Krischer, *J. Phys. Chem. C*, 111, 13481–13489 (2007).

- [126] S. Kirsch, R. Hanke-Rauschenbach, A El-Sibai, D. Flockerzi, K. Krischer, and K. Sundmacher, *J. Phys. Chem. C*, 115, 25315–25329 (2011).
- [127] P. Strasser, M. Eiswirth, and G. Ertl, *J. Chem. Phys.*, 107, 991–1003 (1997).
- [128] R. Straube, D. Flockerzi, S.C. Mueller, and M.J.B. Hauser, *J. Phys. Chem. A*, 109, 441–450 (2005).
- [129] M.T.M. Koper, T.J. Schmidt, N.M. Marković, and P.N. Ross, *J. Phys. Chem. B*, 105, 8381–8386 (2001).
- [130] T. Kadyk, R. Hanke-Rauschenbach, and K. Sundmacher, *J. Electroanal. Chem.*, 630, 19–27 (2010).
- [131] Z. Qi and A. Kaufman, *J. Pow. Sources*, 111, 181–184 (2002).
- [132] O. Himanen, T. Hottinen, M. Mikkola, and V. Saarinen, *Electrochimica Acta*, 52, 206–214 (2006).
- [133] T. Vidakovic, M. Christov, and K. Sundmacher, *Electrochimica Acta*, 52, 5606–5613 (2007).
- [134] H.A. Gasteiger, N.M. Markovic, and P.N. Ross, *J. Phys. Chem.*, 99, 16757–16767 (1995).
- [135] P. Strasser, M. Lübke, F. Raspel, M. Eiswirth, and G. Ertl, *J. Chem. Phys.*, 107, 979–990 (1997).
- [136] P. R. Bauer, A. Bonnefont, and K. Krischer, *Chem. Phys. Chem.*, 11, 3002–3010 (2010).
- [137] D. Zhang, O. Deutschmann, Y.E. Seidel, and R.J. Behm, *J. Phys. Chem. C*, 115, 468–478 (2011).
- [138] B.E. Poling, J.M. Prausnitz, and J.P. O’Connell. *The Properties of Gases and Liquids 5th ed.* McGraw-Hill, New York (2000).
- [139] J. Divisek, H.-F. Oetjen, V. Peinecke, V.M. Schmidt, and U. Stimming, *Electrochimica Acta*, 43, 3811–3815 (1998).
- [140] T. Kobayashi, P.K. Babu, L. Gancs, J.H. Chung, E. Oldfield, and A. Wieckowski, *J. Am. Chem. Soc.*, 127, 14164 (2005).
- [141] F. Maillard, M. Eikerling, O.V. Cherstiouk, S. Schreier, E. Savinova, and U. Stimming, *Faraday Discuss.*, 125, 357–377 (2004).
- [142] R. Morschl, J. Bolten, A. Bonnefont, and K. Krischer, *J. Phys. Chem. C*, 112, 9548–9551 (2008).
- [143] J. Christoph and M. Eiswirth, *Chaos*, 12, 215–230 (2002).
- [144] I.R. Epstein and K. Showalter, *J. Phys. Chem.*, 100, 13132–13147 (1996).
- [145] R. Imbihl, *Surf. Sci.*, 603, 1671–1679 (2009).
- [146] A.M. Turing, *Phil. Trans. Royal Soc. London S. B-Bio. Sci.*, 237, 37–72 (1952).
- [147] N. Mazouz, G. Flatgen, and K. Krischer, *Phys. Rev. E*, 55, 2260–2266 (1997).
- [148] H. Varela, C. Beta, A. Bonnefont, and K. Krischer, *Phys. Rev. Lett.*, 94 (2005).
- [149] H. Varela, C. Beta, A. Bonnefont, and K. Krischer, *Phys. Chem. Chem. Phys.*, 7, 2429–2439 (2005).

- [150] D.J.L. Brett, P. Aguiar, N.P. Brandon, and A.R. Kucernak, *Int. J. Hydrogen Energy*, 32, 863–871 (2007).
- [151] S. Kirsch, R. Hanke-Rauschenbach, B. Stein, R. Kraume, and K. Sundmacher, *J. Electrochem. Soc.*, 160, F436–F446 (2013).
- [152] N. Mazouz and K. Krischer, *J. Phys. Chem. B*, 104, 60816090 (2000).
- [153] A. Bonnefont, H. Varela, and K. Krischer, *J. Phys. Chem. B*, 109, 34083415 (2005).
- [154] Y.J. Li, J. Osolonovitch, N. Mazouz, F. Plenge, K. Krischer, and G. Ertl, *Science*, 291, 2395–2398 (2001).
- [155] E. Meron, *Phys. Rep.-Rev. Sec. Phys. Lett.*, 218, 1–66 (1992).
- [156] Y.F. Gong and D.J. Christini, *Phys. Rev. Lett.*, 90 (2003).
- [157] D. Barkley, *Phys. Rev. Lett.*, 72, 164–167 (1994).
- [158] A.L. Belmonte, Q.Y. Ouyang, and J.M. Fleselles, *J. de Phys. II France*, 7, 1425–1468 (1997).
- [159] R. Kapral and K. Showalter, editors. *Chemical Waves and Patterns*. Kluwer Academic Publishers, Dordrecht (1995).
- [160] A.T. Winfree, *Science*, 175, 634 (1972).
- [161] S. Jakubith, H.H. Rotermund, W. Engel, A. von Oertzen, and G. Ertl, *Phys. Rev. Lett.*, 65, 3013–3016 (1990).
- [162] F.H. Fenton, E.M. Cherry, H.M. Hastings, and S.J. Evans, *Chaos*, 12, 852–892 (2002).
- [163] E.M. Cherry and F.H. Fenton, *New J. Phys.*, 10 (2008).
- [164] A.V. Panfilov, A.C. Muller, V.S. Zykov, and J.P. Keener, *Phys. Rev. E*, 61, 4644–4647 (2000).
- [165] P. Gray and S.K. Scott, editors. *Chemical Oscillations and Instabilities*. Clarendon Press, Oxford (1994).
- [166] K. Krischer, N. Mazouz, and G. Flatgen, *J. Phys. Chem. B*, 104, 7545–7553 (2000).
- [167] V.S. Zykov, A.S. Mikhailov, and S.C. Muller, *Phys. Rev. Lett.*, 78, 3398–3401 (1997).
- [168] O.U. Kheowan, V.S. Zykov, O. Rangsiman, and S.C. Muller, *Phys. Rev. Lett.*, 86, 2170–2173 (2001).
- [169] G. Flatgen and Krischer K., *Phys. Rev. E*, 51, 3997–4003 (1995).
- [170] R. D. Otterstedt, P. J. Plath, N. I. Jaeger, J.C. Sayer, and J. Hudson, *Chem. Eng. Sci.*, 51, 1747–1756 (1996).
- [171] R. D. Otterstedt, P. J. Plath, N. I. Jaeger, and J. L. Hudson, *J. Chem. Soc. Faraday Trans.*, 92, 2933–2939 (1996).
- [172] P. Grauel, J. Christoph, G. Flatgen, and K. Krischer, *J. Phys. Chem. B*, 102, 10264–10271 (1998).

- [173] Y. Kuramoto. *Chemical Oscillations, Waves, and Turbulence*. Dover Publication, Inc., Mineola, New York (1984).
- [174] I.A. Aranson and L. Kramer, *Rev. Mod. Phys.*, 74, 99–143 (2002).
- [175] V.G. Morales and K. Krischer, *Phys. Rev. Lett.*, 100 (2008).
- [176] V.G. Morales and K. Krischer, *Contemporary Physics*, 53, 79–95 (2012).
- [177] A. Pikovsky, M. Rosenblum, and J. Kurths. *Synchronization*. Cambridge University Press, Cambridge (2001).
- [178] M. Stich. *Target Patterns and Pacemakers in Reaction-Diffusion Systems*. PhD thesis, Technische Universität Berlin (2003).
- [179] A.N. Zaikin and A.M. Zhabotinsky, *Nature*, 225, 535–537 (1970).
- [180] P. Strasser, J. Christoph, W.-F. Lin, M. Eiswirth, and J. Hudson, *J. Phys. Chem. A*, 104, 1854–1860 (2000).
- [181] F. Plenge, P. Rodin, E. Scholl, and K. Krischer, *Phys. Rev. E*, 64 (2001).
- [182] N. Baba and K. Krischer, *Chaos*, 18 (2008).
- [183] R. Hanke-Rauschenbach, S. Kirsch, R. Kelling, C. Weinzierl, and K. Sundmacher, *J. Electrochem. Soc.*, 157, B1521–B1528 (2010).
- [184] S.H. Strogatz, *Physica D*, 143, 1–20 (2000).
- [185] J.M.T. Thompson and H.B. Stewart. *Nonlinear Dynamics and Chaos*. Wiley-VCH, Weinheim (1997).
- [186] C. Yang, S. Srinivasan, A.B. Bocarsly, S. Tulyani, and Benziger J.B., *J. Mem. Sci.*, 237, 145 (2004).
- [187] M. Schulze, E. Gülzow, S. Schonbauer, T. Knori, and R. Reissner, *J. Power Sources*, 173, 1927 (2007).
- [188] L.C. Perez, L. Brandao, J.M. Sousa, and A. Mendes, *Renewable Sustainable Energy Rev.*, 15, 169–185 (2011).
- [189] S.J.C. Cleghorn, C.R. Derouin, M.S. Wilson, and S. Gottesfeld, *J. Appl. Electrochem.*, 28, 663–672 (1998).
- [190] D.J.L. Brett, S. Atkins, N.P. Brandon, and V. Vesovic, *Electrochem. Comm.*, 3, 628–632 (2001).
- [191] J. Stumper, S.A. Campbell, D.P. Wilkinson, and M.C. Johnson, *Electrochimica Acta*, 43, 3773–3783 (1998).
- [192] Z. Liu, Z. Mao, B. Wu, L. Wang, and V.M. Schmidt, *J. Pow. Sources*, 141, 205–210 (2005).
- [193] Ch. Wieser, A. Helmbold, and E. Gülzow, *J. Appl. Electrochem.*, 30, 803–807 (2004).
- [194] A.B. Geiger, R. Eckl, A. Wokaun, and G.G. Scherer, *J. Electrochem. Soc.*, 151, A394–A398 (2004).

- [195] Y. Wang and C.Y. Wang, *Electrochimica Acta*, 51, 3924–3933 (2006).
- [196] T.B. Benjamin and J.E. Feir, *J. Fluid. Mech.*, 27, 417–430 (1967).
- [197] B.I. Shraiman, A. Pumir, W. VanSaarloos, P.C. Hohenberg, H. Chate, and M. Holen, *Physica D*, 57, 241–248 (1992).
- [198] J.T. Stuart and R.C. Diprima, *Proc. Roy. Soc. - Math. Phys. Eng. Sci.*, 362, 27–41 (1978).
- [199] H. Segur, D. Henderson, J. Carter, J. Hammack, C.M. Li, D. Pheiff, and K. Socha, *J. Fluid Mech.*, 539, 229–271 (2005).

## Publications and Statements on Authorship

This dissertation contains material that has previously been published by the author elsewhere. The following list gives a detailed overview. A statement on authorship is enclosed.

- [1] R. Hanke-Rauschenbach, S. Kirsch, R. Kelling, C. Weinzierl, and K. Sundmacher. Oscillations and Pattern Formation in a PEM Fuel Cell with Pt/Ru Anode Exposed to  $H_2/CO$  Mixtures. *J. Electrochem. Soc.*, 157:B1521–B1528, 2010. [DOI-link: <http://dx.doi.org/10.1149/1.3469570>].

The author contributed to the development of the published material through discussion and numerical evaluation.

- [2] S. Kirsch, R. Hanke-Rauschenbach, and K. Sundmacher. Analysis of Spatio-Temporal Pattern Formation in a PEM Fuel Cell with Pt/Ru Anode exposed to  $H_2/CO$  Mixtures. *J. Electrochem. Soc.*, 158:B44–B53, 2011. [DOI-link: <http://dx.doi.org/10.1149/1.3507263>].

The author developed and implemented the model. He carried out the simulations and he evaluated the results in cooperation with R. Hanke-Rauschenbach. He also wrote the manuscript.

- [3] T. Kadyk, S. Kirsch, R. Hanke-Rauschenbach, and K. Sundmacher. Autonomous potential oscillations at the Pt anode of a PEM Fuel Cell under CO poisoning. *Electrochimica Acta*, 56:10593–10602, 2011. [DOI-link: <http://dx.doi.org/10.1016/j.electacta.2011.05.005>].

The author generated and evaluated the model data presented in the manuscript. He also wrote the modeling part of the manuscript.

- [4] R. Hanke-Rauschenbach, S. Kirsch, and K. Sundmacher. Spatiotemporal pattern formation in an electrochemical membrane reactor during deep CO removal from reformat gas. In *21st European Symposium on Computer Aided Process Engineering*, volume 29, pages 201–205, 2011. [DOI-link: <http://dx.doi.org/10.1016/B978-0-444-53711-9.50041-9>].

The author was involved in the evaluation of the model data. The author also contributed to the manuscript by providing figures and parts of the text.

- [5] S. Kirsch, R. Hanke-Rauschenbach, A El-Sibai, D. Flockerzi, K. Krischer, and K. Sundmacher. The S-Shaped Negative Differential Resistance during the Electrooxidation of  $H_2/CO$  in Polymer Electrolyte Membrane Fuel Cells: Modeling and Experimental Proof. *J. Phys. Chem. C*, 115:25315–25329, 2011. [DOI-link: <http://dx.doi.org/10.1021/jp206660y>].

The author planned the experiments and carried them out in cooperation with A. El-Sibai. The author carried out the reduction and the simulation of the mathematical model and analyzed the experimental data as well as the mathematical data. He also wrote the manuscript.

- [6] S. Kirsch, R. Hanke-Rauschenbach, B. Stein, R. Kraume, and K. Sundmacher. The Electro-Oxidation of  $H_2, CO$  in a Model PEM Fuel Cell: Oscillations, Chaos, Pulses. *J. Electrochem. Soc.*, 160:F436–F446, 2013. [DOI-link: <http://dx.doi.org/10.1149/2.002306jes>].

The author planned the experiments and carried them out. He analyzed the experimental data and he also wrote the manuscript.

## Student Theses

The following student theses were prepared in the process-system-engineering group at the Max Planck Institute for Dynamics of Complex Technical Systems Magdeburg under the supervision of the author:

Name	Title
R. Kelling	“Modelltheoretische Untersuchung von Orts-Zeit-Mustern bei der elektrochemischen präferentiellen Oxidation von $CO$ aus $CO/H_2$ -Gemischen in einem Membranreaktor” 2009, Otto-von-Guericke-Universität Magdeburg Studiengang: Systemtechnik und technische Kybernetik
A. El-Sibai	“Measurement of S-NDR type oscillations in the $H_2, H_2O, CO N_2, H_2O$ system” 2011, Otto-von-Guericke-Universität Magdeburg Studiengang: Chemical and Process Engineering



# Curriculum Vitae

## Personal

---

Name: Kirsch, Sebastian  
Date of birth: September, 23th 1982  
Place of birth: Plauen/Germany  
  
e-Mail: BastlKirsch@gmx.de



## Education and Civil Service

---

8/1989 - 6/1993      Elementary school "An der Pandorfhalle" in Gera

8/1993 - 6/2001      Secondary School "Georg-Christoph-Lichtenberg Gymnasium" Gera  
Degree:                General Qualification for University Entrance

9/2001 - 9/2002      Civil service in the municipality of Rauda

10/2002 - 9/2008     *Bayrische Julius-Maximilians Universität Würzburg*  
Degree:                Dipl. Phys. Univ.  
Thesis:                Correlations of Dielectric and Rheological Properties of PUR-based Electro-  
Rheological Fluids  
Supervisor:           Prof. Dr. Vladimir Dyakonov

9/2005 - 6/2006      *Heriot-Watt-University Edinburgh*  
Degree:                Master of Physics in Physical Science with Honors of the First Class  
Thesis:                Simultaneous Multi-Plane Imaging with a Distorted Diffraction Grating  
Supervisor:           Prof. Dr. Richard Warburton

11/2008 - 12/2012    *Max-Planck-Institut for the Dynamics of Complex Technical Systems Magdeburg*  
Degree:                Dr.-Ing.  
Thesis:                Electrochemical Oxidation of H<sub>2</sub>,CO Gas Mixtures in Polymer-Electrolyte-  
Membrane Fuel Cells  
Supervisor:           Prof. Dr.-Ing. Kai Sundmacher  
Awards:                Young Scientist Poster Award (2nd Indo German Workshop 2012)  
Student Oral Presentation Award (Electromembrane Processes and Technol-  
ogy Conference 2012)

## Schriftliche Erklärung

Ich erkläre hiermit, dass ich die vorliegende Arbeit ohne zulässige Hilfe Dritter und ohne Benutzung anderer als der angegebenen Hilfsmittel angefertigt habe. Die aus fremden Quellen direkt oder indirekt übernommenen Gedanken sind als solche kenntlich gemacht.

Insbesondere habe ich nicht die Hilfe einer kommerziellen Promotionsberatung in Anspruch genommen. Dritte haben von mir weder unmittelbar noch mittelbar geldwerte Leistungen für Arbeiten erhalten, die im Zusammenhang mit dem Inhalt der vorgelegten Dissertation stehen.

Die Arbeit wurde bisher weder im Inland noch im Ausland in gleicher oder ähnlicher Form als Dissertation eingereicht und ist als Ganzes auch noch nicht veröffentlicht.

Magdeburg, den 1.1.2013

Sebastian Kirsch